Title
Cancer Nano-Theranostics with High Contrast MRI

Author
Ray, Sayoni

Publication Date
2019

Peer reviewed|Thesis/dissertation

UNIVERSITY OF CALIFORNIA

Los Angeles

Cancer Nano-Theranostics with High Contrast MRI

A dissertation submitted in partial satisfaction of the

requirements for the degree Doctor of Philosophy

in Chemistry

by

Sayoni Ray

2019

ABSTRACT OF THE DISSERTATION

Cancer Nano-Theranostics with High Contrast MRI

by

Sayoni Ray

Doctor of Philosophy in Chemistry

University of California, Los Angeles, 2019

Professor William M. Gelbart, Co-Chair
Professor Charles M. Knobler, Co-Chair

One of the holy grails in cancer therapy is to simultaneously image and deliver drugs to the tumor site. The first part of the thesis has developed new ideas in cancer theranostics and the second part is about the development of a novel contrast agent for risk-free imaging of the tumor. In the first project of the thesis, I have discussed the development of a liposome-based cargo delivery strategy that can simultaneously monitor alternating magnetic field–induced drug release by observing the change in MRI relaxation parameter R_1, and the location and condition of liposomal site (such as tumor) from MRI parameter R_2. However, the loading of a contrast agent in liposomes generally results in poor contrast and suffers from various artifacts in *in vivo* experiments, compared to the use of free contrast agent. Thus, the second project of my work in this part demonstrates the effective filtering of artifacts and contrast enhancement to obtain high quality sensitive imaging of the tumor site in a mouse model using paramagnetic liposomes, a novel pulsing sequence in active-feedback MRI, and robust data analysis. The second part of my work is about using a self-replicating viral-RNA molecule derived from Nodamura, an insect virus,

to express and amplify ferritin, leading to increased iron content of the cells in the form of ferrihydrite that acts as a novel contrast agent. In summary, my thesis is about the development of cancer theranostics and a novel contrast agent. In the last part of the thesis, I have reviewed the current development of rapidly growing state of the art magnetic resonance cancer theranostics for commonly used polymer-based nanovehicles.

The dissertation of Sayoni Ray is approved.

Jeffrey I. Zink

Michael Albert Thomas

Charles M. Knobler, Committee Co-Chair

William M. Gelbart, Committee Co-Chair

University of California, Los Angeles

2019

To

My Parents, Sister and Shubhrangshu

TABLE OF CONTENTS

Chapter 3: High-contrast Background-free Magnetic Resonance Molecular Imaging

Part II. Use of Natural Iron Content in the Body for MR Contrast Enhancement for Early Theranostics

Chapter 4: Contrast and Sensitivity Enhancement for Early Tumor Detection Using a Ferritin Replicon

Part III. Review on Current Trends of Magnetic Resonance Cancer Theranostics with Different Nanoparticles

Chapter 5: Dendrimer- and Copolymer-based Nanoparticles for Magnetic Resonance Cancer Theranostics

List of Figures

List of Tables

Acknowledgements

It is an immense pleasure to take this opportunity to thank all the persons who made this work possible and kept me motivated with their continuous enthusiasm, support and encouragements in the journey of my graduate life over the past years. I like to express my sincere gratitude and deepest respect to my PhD advisors and mentors —Professor Yung-Ya Lin, Professor William M. Gelbart and Professor Charles M. Knobler for their endless support, advice, guidance and providing me a unique opportunity to work across disciplines. I am so thankful to Prof. Lin for his supervision and encouragement in each of my PhD projects and specially for introducing me to the world of magnetic resonance imaging. I deeply appreciate his guidance to become an independent self-motivated researcher. I sincerely acknowledge Prof. Gelbart for his continuous support throughout my PhD life. His patience, hard work and enthusiasm in science are truly inspirational and any conversation with him always brought hope, even during the most difficult time of my graduate life. I found him always ready to advice me on both scientific and non-scientific issues. His constant encouragement, thoughtful insights and discussions on my projects helped me immensely to complete my PhD thesis. I particularly want to thank Prof. Knobler for his interest in my projects. I am grateful to him for carefully reading and correcting my scientific writings as well as for his thoughtful suggestions. My sincere thanks go to Professor Jeffrey Zink and Professor Albert M. Thomas for serving on my doctoral committee. I greatly appreciate their insightful comments and interesting discussions to improve the quality of my work. I want to specially thank Prof. Zink for collaborating with me and providing me the opportunity to learn magnetic heating and drug delivery experiments, which opened up a new direction of research to me. I am extremely grateful for allowing me in his lab and for stimulating discussions.

During my years at UCLA, I had the privilege of knowing and working with many exceptional people. I wholeheartedly express my special thanks to Dr. Chao-Hsiung Hsu for performing extensive *in vivo* studies for my projects. I thank him for his guidance and for teaching me fundamentals of important technical skills. Long hours of conversation and working with him, helped me to grow up as a research scientist. I want to thank Dr. Zhao Li for her contribution in experiments, scientific writing, and performing theoretical simulations. My special

acknowledgements go to my collaborators in different projects, Ms. Chi-An Cheng, Mr. Wei Chen and Mr. Jerrell Tisnado. I thank Chi-An and Wei for their immense help in magnetic heating experiments. Without their help and support, I could not successfully complete the project. Special thanks to Jerrell for carrying out extensive biological work in ferritin project and sharing his skills with me. I want to thank Ms. Fang-Chu Lin for her contributions in experiment and anaysis. It was such an enjoyable experience to work with all of you, and I feel very lucky to work with all of you during my graduate life at UCLA. I want to specially thank my wonderful fellow labmates and sweet friends at UCLA, Chencai Wang, Huimin Yang, Tanya Kim, Youyuan Zhang, Jingwen Yao, Sheba Plamthottam, Natcha Wattanatorn, and Richard Sportsman for all the fun conversation and memorable time we spent together. It would have been very difficult to survive at UCLA without all of you.

I am highly obliged to all the funding agencies —National Science Foundation (NSF), NSF-EAPSI, University of California Cancer Research Award, Hirshberg Foundation for Pancreatic Cancer Research, and Taiwan Ministry of Science and Technology whose support made this work possible. My sincere thanks to UCLA for providing me the opportunity for graduate study. I want to thank the journals where my work was published and chapter 5 is a reproduction of the publication: 'Ray, S.; Li, Z.; Hsu, C.-H.; Hwang, L.-P.; Lin, Y.-C.; Chou, P.-T.; Lin, Y.-Y. Dendrimer- and Copolymer-Based Nanoparticles for Magnetic Resonance Cancer Theranostics. Theranostics 2018, 8 (22), 6322–6349. doi:10.7150/thno.27828'. Chapter 2 is a reproduction of a manuscript submitted to the journal Nanotheranostics: 'Ray, S; Cheng, C-A; Chen, W; Li, Z; Zink, J; Lin, Y-Y. Magnetic Heating Stimulated Cargo Release with Dose Control using Multifunctional MR and Thermosensitive Liposome'. Chapter 3 is a version of 'Ray, S; Hsu, C.-H.; Lin F-C; Lin, Y-Y. High-contrast Background-free Magnetic Resonance Molecular Imaging. *In preparation*'. I sincerely acknowledge the contribution of all my coauthors and specific details of their contributions in each project have been listed at the end of each chapter in the acknowledgement section.

Above all, I want to thank my family for their endless guidance and love over the years. I have no word to express my gratitude to my father for fostering my excitement about science from a young age and supporting me in every possible way in the toughest time of my graduate life. His all-time inspiration kept me motivated in pursuing research. I learned the true meaning of

perseverance and motivation from him. I never met a person like him, who always remained so excited about scientific discussion and provided thoughtful insights. Often these discussions stimulated new ideas and directions in my research. I am deeply indebted to my mother who supported and encouraged me in every step of my life. She handled me with extreme patience, understanding and affection in difficult times of my graduate study. I cannot imagine myself to be here without them! I want to express special thanks to my dearest sister Srijita for making my journey easier with her love, encouragement, affection and fun conversations. Finally, I wish to convey big thanks to my sweetheart Shubhrangshu for taking keen interest in my studies, giving helpful advices and guidance in research works, and always providing me strong mental support. I want to thank him for his understanding, help and insightful comments in all my projects. Without his help and continuous support, it would have been very hard to survive during the long years of graduate life. I feel extremely blessed to have all of you in my life, which make it possible to achieve what I am today.

VITA

Education

- MS Chemistry, University of California, Los Angeles (UCLA), December 11, 2015
- M.Sc. Chemistry, Indian Institute of Technology (IIT) Kanpur, India, July 5, 2013
- B.Sc. (Hons) Chemistry, University of Calcutta, India, July 25, 2011

Honors & Awards

- Fellowship 2 from CLINAM European Foundation for Clinical Nanomedicine (2018)
- Award Nominee for Women in Molecular Imaging Network (WMIN) Scholar at WMIC 2018
- ISMRM Trainee (Educational) Stipend from International Society for Magnetic Resonance in Medicine (ISMRM) (2017 & 2018) WMIC Student Travel Stipend 2018
- Pauley Fellowship from the University of California, Los Angeles (2016-2017)
- Student/Trainee member in WMIS 2018 & ISMRM 2017-2018
- National Science Foundation's (NSF) East Asia and Pacific Summer Institutes (EAPSI) fellow (2016)
- Hanson-Dow Distinguished Teaching Assistant award from the Department of Chemistry and Biochemistry, University of California, Los Angeles (2015)
- UCLA Doctoral Student Travel Grant from the University Of California, Los Angeles (2015 & 2017)
- Departmental fellowship from the Department of Chemistry and Biochemistry, University of California, Los Angeles (2013-2016)
- Lectureship through National Eligibility Test (NET), University Grants Commission, India (2013)
- Innovation in Science Pursuit for Inspired Research (INSPIRE) scholarship from the Department of Science &Technology (DST), Govt. of India (2008-2012)
- Visiting Student Research Program fellow (VSEPR) at Tata Institute of Fundamental Research (TIFR), Mumbai, India (2012)

Publications and Presentations

- **S. Ray**, Z. Li, C.-H. Hsu, et al "*Dendrimer and Copolymer-based Nanoparticles for Magnetic Resonance Cancer Theranostics*". *Theranostics*. 2018; 8(22):6322-6349
- **S. Ray**, C.-A. Cheng, W. Chen, et al, "*Magnetic Heating Stimulated Cargo Release with Dose Control using Multifunctional MR and Thermosensitive Liposome*" *(*Submitted in *Nanotheranostics*)
- **S. Ray**, C.-H. Hsu, Z. Li, et al, "*High-contrast Background-free Magnetic Resonance Molecular Imaging*" (in preparation)
- H. Chandra, R. Sharma, Satyanarayan, R. V. Raman, **S. Ray**, A. S. R. Koti, "*Multiple Unfolding Pathways of Leucine Binding Protein (LBP) Probed by Single-molecule Force Spectroscopy (SMFS)*". *JACS.* 2013; 135(39):14768–14774
- **S. Ray**, C.-A. Cheng, W. Chen, et al, "*Real-time simultaneous monitoring of tumor site and alternating magnetic field controlled drug release with dual modal MRI and thermosensitive multifunctional liposomes*" presented at CLINAM 2018, Basel, Switzerland
- **S. Ray**, C.-H. Hsu, Z. Li, et al, "*High-contrast in vivo cancer MR imaging in mouse models utilizing paramagnetic liposomes and nonlinear active-feedback difference technique*" presented at WMIC 2018, Seattle, US
- **S. Ray**, C.-H. Hsu, Z. Li, et al, "*Early Cancer Detection using Paramagnetic Liposome by a Novel Contrast Mechanism with Active-feedback Magnetic Resonance Imaging*" presented at ISMRM 2017, Honolulu, US
- **S. Ray**, C.-H. Hsu, F.-C. Lin, Z. Li, et al "*Contrast Enhancement for Early Cancer Imaging by Gd-Nanoparticles and Active Feedback MRI*" presented at ICIS 2015, London, UK
- **S. Ray**, C.-H. Hsu, Z. Li, et al "*A Synergistic Approach for Early Cancer Detection and Targeted Therapy by Sensitive Detection of Gadolinium-liposomal Nanoparticles with Active-feedback Magnetic Resonance Imaging*" presented at Glenn T. Seaborg Symposium 2017, Los Angeles, US
- **S. Ray**, C.-H. Hsu, Z. Li, et al, "*Early Cancer Detection using Paramagnetic Liposome with Active-feedback Magnetic Resonance Imaging*" presented at Glenn T. Seaborg Symposium 2016, Los Angeles, US
- H. Chandra, R. Sharma, Satyanarayan, R. V. Raman, **S. Ray**, A. S. R. Koti, "*Multiple Unfolding Pathways of Leucine Binding Protein (LBP) as revealed by SM-AFM* " presented at National Fluorescence Workshop in single molecule spectroscopy 2012, Kolkata, India

Chapter 1

Introduction

Cancer is a major cause of death worldwide. Every year, the number of deaths due to cancer is increasing in the United States and there would be about 2.5 million cancer cases by 2030, as illustrated in **Figure 1.1**. The prognosis for the cancer patients is rather poor (~35% death), making it the second highest leading cause of death (**Figure 1.2**) in US just behind the cardiovascular disease. Thus, cancer research seeks a lot a serious attention in biomedical research.

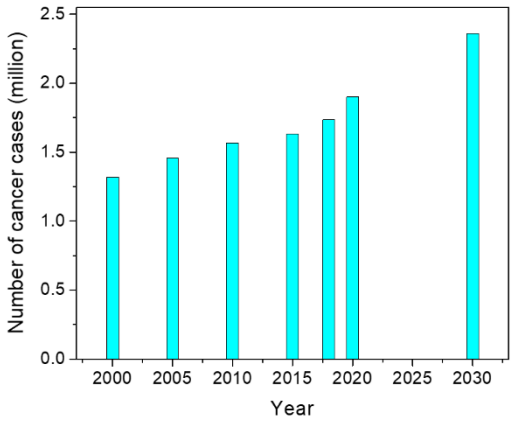

Figure 1.1. Trends of cancer statistics: Statistical data and prediction for cancer cases in US for different years. (Data is taken from following websites https://www.cancer.gov, https://www.cdc.gov/cancer, https://www.medicalnewstoday.com, https://gis.cdc.gov/Cancer)

While, there are numerous efforts in the cancer research field, recently theranostic[1–4] nanomedicine seeks a special attention in the biomedical community. Theranostics, consists of the simultaneous detection, therapy and online monitoring of the therapy; it is a rapidly growing young platform in biomedical research. The success of this approach usually relies on three factors 1) accurate detection 2) specific targeting of the tumor cells and 3) controlled therapy

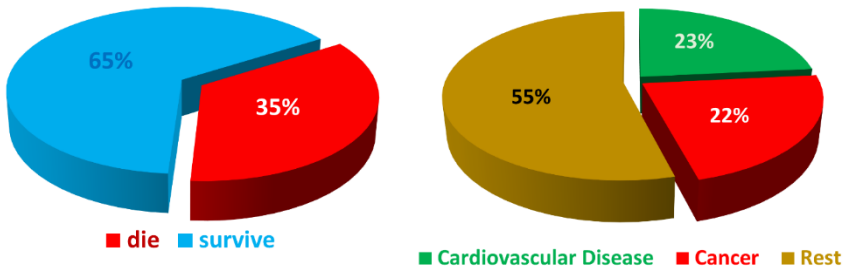

Figure 1.2. Cancer, a leading cause of death: Pie charts are showing the trend of cancer death in US and compared number of deaths due to other diseases. (Data is taken from following websites https://www.cancer.gov, https://www.cdc.gov/cancer, https://www.medicalnewstoday.com, https://gis.cdc.gov/Cancer)

(might include drug/gene delivery) at the target site . **Figure 1.3** demonstrates an overall scheme of this approach. Since theranostics requires the flexibility of simultaneous detection and therapy, a suitable nanoparticle capable of carrying both a detection agent and a cancer drug or suitable gene for therapeutic purpose is necessary.[5–8] The development of suitable, safe and biocompatible nanovehicles providing the flexibility of preferential targeting of different cancers is required for successful theranostics. This approach relies on two kinds of specific targeting— active and passive. Active targeting[9] is dependent on the bioconjugation of specific ligands to overexpressed moieties in particular cancers; passive targeting depends on the longer circulation in blood stream and preferential accumulation in cancer cells by the enhanced permeability and retention (EPR) effect.[10,11] Nanoparticles having a dimension of a hundred to a few hundred nanometers, could achieve significant passive targeting.[12,13] Since the nanovehicles contain the cancer drugs and deliver them to the tumor site, thus limiting its exposure to the healthy cells, the theranostics methods have the potential of much fewer side effects compared to the traditional chemotherapy. In addition to being minimally invasive, this method is expected to be much less expensive compared to surgical procedures. In spite of the significant potential of the theranostic method, it faces many challenges such as finding a suitable nanoparticle with all functionality, detection

sensitivity, safety, biocompatibility etc.[1,14] This thesis addresses some of these concerns of the theranostic approach.

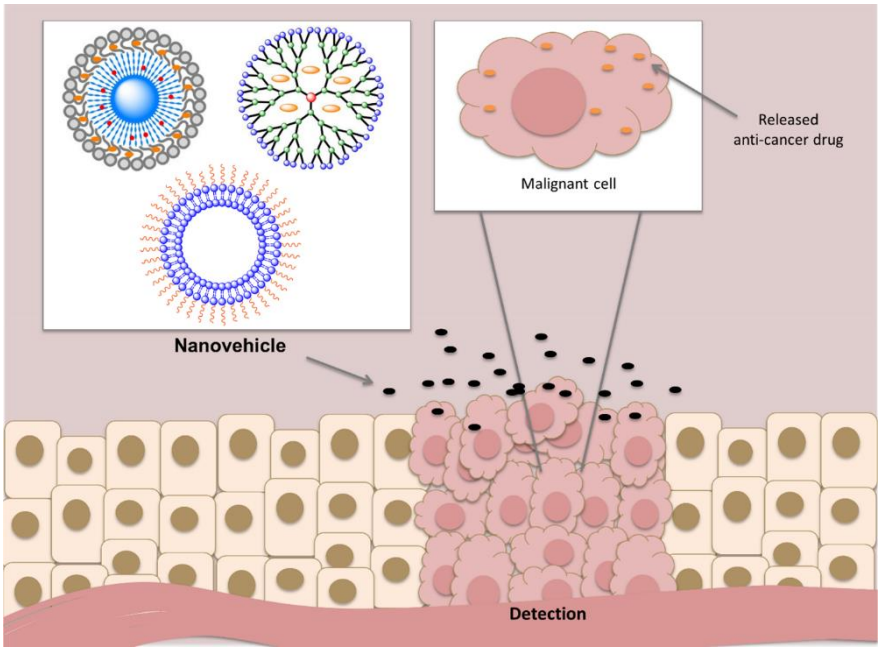

Figure 1.3. Graphical scheme for theranostics: Schematic diagram illustrating theranostic approach to cancer cells. It shows a simultaneous approach of targeting malignant cells, controlled drug delivery and MRI detection with different nanovehicles.

I have chosen magnetic resonance imaging (MRI) as a diagnostic platform for theranostics, because it employs low-energy, non-ionizing radiation and has a deep penetration capability. It is considered very safe, widely used worldwide and generally favored over other imaging techniques such as computed tomography (CT) and positron emission tomography (PET) that use ionizing radiation or other methods like fluorescence, which have limited penetration capability.[4,15] While MRI has advantages over other methods of imaging modality, it is limited by low thermal polarization, contrast and sensitivity. Hence, contrast agents[16] are often used to improve the detection sensitivity. Contrast agents are a special class of complexes that attach to the tumor site and cause enhanced change of local relaxation parameters in MRI. However, there is a problem of

toxicity associated with them and poor contrast still remains a major drawback of the MRI techniques. The approach of this thesis is to improve contrast, sensitivity and safety of MRI techniques by developing suitable nano-constructs capable of carrying both the contrast agent and drugs and developing new MRI techniques as well.

There are two major components to theranostics — therapy and detection. The first part of my thesis describes the theranostics approach with a liposome nanomaterial. Liposomes[17–23] are one of the ideal candidates for carrying cargo inside the human body because of its biocompatible nature, tunable size and functional versatility. They are composed of self-assembled spherical lipid bilayers and are capable of carrying both hydrophilic drugs in their aqueous cores and hydrophobic moieties in the interior of the lipid membrane. Such biodegradable and long-circulating nanovehicles can be engineered to attach conjugating moieties or polyethylene glycol (PEG) for active and passive targeting respectively. Another great advantage of liposomes comes from their thermosensitive behavior near the membrane lipid melting temperature (T_m), as permeability of liposome is greatly enhanced there. Hence, a clever choice of the lipid formulation could manipulate this temperature slightly above the body temperature to use it for hyperthermia, heat-induced activation of cancer drug or controlled drug delivery purposes.[18,19,21,23–25] Finally, liposomes are already FDA-approved nanovehicles and are used clinically for different purposes.[6,24,26–32] As safety is a major concern in this field, liposomes provide a safe and biocompatible platform with diverse functionality to start with theranostic applications. The first project in the thesis describes the online monitoring of a controlled dose regulated drug delivery process and my second project shows a novel analytical technique to improve the MRI detection of paramagnetic nanovehicles.

The second part of my thesis deals with improving the sensitivity and contrast of early MRI detection of a small tumor. The detection of a tiny malignant tumor at the very early stage of its

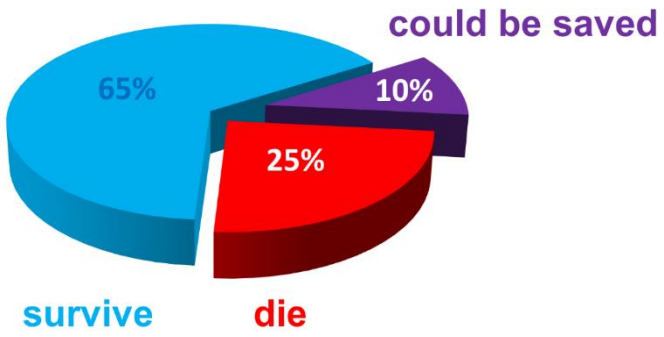

Figure 1.4. Potent advantages of early detection: Early tumor detection could save ~30 % of cancer deaths, which is ~ 10% total cancer patients (based and approximated from assumptions) and can improve prognosis of cancer patients.

development significantly increases the treatment options and could save a significant percentage (~30%) of those who die of the disease (**Figure 1.4**). However, MRI techniques lack the necessary sensitivity to small differences in the characteristics of the tissue pathology of early tumor growth because of the rapid development of blood vessels associated with the growth of tumor that does not appreciably affect the relaxation parameters. Hence, theranostic research must try to develop new techniques capable of detecting early tumor growth as well as detecting and destroying them at an early stage. Most commonly used contrast agents are metal chelates, but the use of such exogenous contrast agents is often limited by their probable toxicity to different organs, their extent of penetration and restriction in dosage etc. Thus, the use of foreign contrast agents for early tumor detection might not be advisable and the development of an endogenous nontoxic contrast agents to improve the sensitivity of MRI detection is urgently required. In this context, endogenous MR reporter genes[33–37] could be ideal candidates for early tumor detection, compared to the exogenous contrast agents. Recent studies indicate, MR reporter gene ferritin[38–53] could be exploited as a good

contrast agent for its capability of highly conserved iron storage. In this work, I specifically seek to utilize a self-replicating viral RNA molecule derived from Nodamura,[54–56] an insect virus to express and amplify the MR reporter gene ferritin that should increase the iron content of the cells in the form of a superparamagnetic iron oxide MR contrast agent to improve early tumor detection.

Finally, in the last part of my thesis, I have reviewed the current progress and state of art techniques for MRI based theranostic approaches. Other than liposomes and virus like particles (VLP),[57,58] polymer-based nanoparticles are receiving a lot of attention in the theranostic world. Among them, dendrimer[59–63] and copolymer-based[64–67] nanoparticles are commonly used and are a rapidly growing field of study. Hence, I have critically reviewed different aspects and promising directions of MR-guided cancer theranostic for polymer-like nanostructures such as dendrimer and copolymer core-shell nanovehicles.

References

(1) Janib, S. M.; Moses, A. S.; MacKay, J. A. Imaging and Drug Delivery Using Theranostic Nanoparticles. *Adv. Drug Deliv. Rev.* **2010**, *62* (11), 1052–1063. https://doi.org/10.1016/j.addr.2010.08.004.

(2) Sunderland, C. J.; Steiert, M.; Talmadge, J. E.; Derfus, A. M.; Barry, S. E. Targeted Nanoparticles for Detecting and Treating Cancer. *Drug Dev. Res.* **2006**, *67* (1), 70–93. https://doi.org/10.1002/ddr.20069.

(3) Kelkar, S. S.; Reineke, T. M. Theranostics: Combining Imaging and Therapy. *Bioconjug. Chem.* **2011**, *22* (10), 1879–1903. https://doi.org/10.1021/bc200151q.

(4) Key, J.; Leary, J. F. Nanoparticles for Multimodal in Vivo Imaging in Nanomedicine. *Int. J. Nanomedicine* **2014**, *9*, 711–726. https://doi.org/10.2147/IJN.S53717.

(5) Peer, D.; Karp, J. M.; Hong, S.; Farokhzad, O. C.; Margalit, R.; Langer, R. Nanocarriers as an Emerging Platform for Cancer Therapy. *Nat. Nanotechnol.* **2007**, *2* (12), 751–760. https://doi.org/10.1038/nnano.2007.387.

(6) Allen, T. M.; Cullis, P. R. Liposomal Drug Delivery Systems: From Concept to Clinical Applications. *Adv. Drug Deliv. Rev.* **2013**, *65* (1), 36–48. https://doi.org/10.1016/J.ADDR.2012.09.037.

(7) Zhu, J.; Shi, X. Dendrimer-Based Nanodevices for Targeted Drug Delivery Applications. *J. Mater. Chem. B* **2013**, *1* (34), 4199. https://doi.org/10.1039/c3tb20724b.

(8) Wang, Z.; Niu, G.; Chen, X. Polymeric Materials for Theranostic Applications. *Pharm. Res.* **2014**, *31* (6), 1358–1376. https://doi.org/10.1007/s11095-013-1103-7.

(9) Takeda, K.; Kobari, M.; Akaishi, S.; Matsuno, S. Targeting Pancreatic Chemotherapy Cancer Using Liposome against Antibody-Combined. *J. Exp. Med.* **1994**, *175*, 29–42.

(10) Matsumura, Y.; Maeda, H. A New Concept for Macromolecular Therapeutics in Cancer Chemotherapy: Mechanism of Tumoritropic Accumulation of Proteins and the Antitumor Agent Smancs. *Cancer Res.* **1986**, *46* (12 Pt 1), 6387–6392.

(11) Duncan, R. Tumour Targeting by Enhanced Permeability and Retention (EPR) Effect. *Ann. Oncol.* **1998**, *9* (2), 39.

(12) Nel, A.; Ruoslahti, E.; Meng, H. New Insights into "Permeability" as in the Enhanced Permeability and Retention Effect of Cancer Nanotherapeutics. *ACS Nano* **2017**, *11* (10), 9567–9569. https://doi.org/10.1021/acsnano.7b07214.

(13) Fang, J.; Nakamura, H.; Maeda, H. The EPR Effect: Unique Features of Tumor Blood Vessels for Drug Delivery, Factors Involved, and Limitations and Augmentation of the Effect. *Adv. Drug Deliv. Rev.* **2011**, *63* (3), 136–151. https://doi.org/10.1016/j.addr.2010.04.009.

(14) Wijagkanalan, W.; Kawakami, S.; Hashida, M. Designing Dendrimers for Drug Delivery and Imaging: Pharmacokinetic Considerations. *Pharm. Res.* **2011**, *28* (7), 1500–1519. https://doi.org/10.1007/s11095-010-0339-8.

(15) Liang, Z.-P.; Lauterbur, P. C.; IEEE Engineering in Medicine and Biology Society. *Principles of Magnetic Resonance Imaging : A Signal Processing Perspective*; SPIE Optical Engineering Press, 2000.

(16) Helm, L.; Merbach, A. E. A. A. E.; Tóth, E.; Toth, E.; Helm, L.; Merbach, A. E. A. A. E.; Tóth, E.; Toth, E.; Helm, L.; Merbach, A. E. A. A. E. *The Chemistry of Contrast Agents in Medical Magnetic Resonance Imaging*, 2nd ed.; Merbach, A., Helm, L., Tóth, É., Eds.; Wiley: Chichester, UK, 2013. https://doi.org/10.1002/9781118503652.

(17) Hosta-Rigau, L.; Schattling, P.; Teo, B. M.; Lynge, M. E.; Städler, B. Recent Progress of Liposomes in Nanomedicine. *J. Mater. Chem. B* **2014**, *2* (39), 6686–6691. https://doi.org/10.1039/C4TB00825A.

(18) Béalle, G.; Di Corato, R.; Kolosnjaj-Tabi, J.; Dupuis, V.; Clément, O.; Gazeau, F.; Wilhelm, C.; Ménager, C. Ultra Magnetic Liposomes for MR Imaging, Targeting, and Hyperthermia. *Langmuir* **2012**, *28* (32), 11834–11842. https://doi.org/10.1021/la3024716.

(19) Pradhan, P.; Giri, J.; Rieken, F.; Koch, C.; Mykhaylyk, O.; Döblinger, M.; Banerjee, R.; Bahadur, D.; Plank, C. Targeted Temperature Sensitive Magnetic Liposomes for Thermo-Chemotherapy. *J. Control. Release* **2010**, *142* (1), 108–121. https://doi.org/10.1016/j.jconrel.2009.10.002.

(20) Mikhaylov, G.; Mikac, U.; Magaeva, A. A.; Itin, V. I.; Naiden, E. P.; Psakhye, I.; Babes, L.; Reinheckel, T.; Peters, C.; Zeiser, R.; et al. Ferri-Liposomes as an MRI-Visible Drug-Delivery System for Targeting Tumours and Their Microenvironment. *Nat. Nanotechnol.* **2011**, *6* (9), 594–602. https://doi.org/10.1038/nnano.2011.112.

(21) Amstad, E.; Kohlbrecher, J.; Müller, E.; Schweizer, T.; Textor, M.; Reimhult, E. Triggered Release from Liposomes through Magnetic Actuation of Iron Oxide Nanoparticle Containing Membranes. *Nano Lett.* **2011**, *11* (4), 1664–1670. https://doi.org/10.1021/nl2001499.

(22) Langereis, S.; Hijnen, N.; Strijkers, G.; Nicolay, K.; Grüll, H. Research Spotlight: Multifunctional Liposomes for MRI and Image-Guided Drug Delivery. *Ther. Deliv.* **2014**,

5 (1), 21–24. https://doi.org/10.4155/tde.13.128.

(23) Tai, L. A.; Tsai, P. J.; Wang, Y. C.; Wang, Y. J.; Lo, L. W.; Yang, C. S. Thermosensitive Liposomes Entrapping Iron Oxide Nanoparticles for Controllable Drug Release. *Nanotechnology* **2009**, *20* (13). https://doi.org/10.1088/0957-4484/20/13/135101.

(24) Koning, G. A.; Eggermont, A. M. M.; Lindner, L. H.; Ten Hagen, T. L. M. Hyperthermia and Thermosensitive Liposomes for Improved Delivery of Chemotherapeutic Drugs to Solid Tumors. *Pharm. Res.* **2010**, *27* (8), 1750–1754. https://doi.org/10.1007/s11095-010-0154-2.

(25) Tagami, T.; Foltz, W. D.; Ernsting, M. J.; Lee, C. M.; Tannock, I. F.; May, J. P.; Li, S. D. MRI Monitoring of Intratumoral Drug Delivery and Prediction of the Therapeutic Effect with a Multifunctional Thermosensitive Liposome. *Biomaterials* **2011**, *32* (27), 6570–6578. https://doi.org/10.1016/j.biomaterials.2011.05.029.

(26) Alberts, D. S.; Muggia, F. M.; Carmichael, J.; Winer, E. P.; Jahanzeb, M.; Venook, A. P.; Skubitz, K. M.; Rivera, E.; Sparano, J. A.; Dibella, N. J.; et al. Efficacy and Safety of Liposomal Anthracyclines in Phase I/II Clinical Trials. *Semin. Oncol.* **2004**, *31*, 53–90. https://doi.org/10.1053/J.SEMINONCOL.2004.08.010.

(27) Northfelt, D. W.; Dezube, B. J.; Thommes, J. A.; Miller, B. J.; Fischl, M. A.; Friedman-Kien, A.; Kaplan, L. D.; Du Mond, C.; Mamelok, R. D.; Henry, D. H. Pegylated-Liposomal Doxorubicin versus Doxorubicin, Bleomycin, and Vincristine in the Treatment of AIDS-Related Kaposi's Sarcoma: Results of a Randomized Phase III Clinical Trial. *J. Clin. Oncol.* **1998**, *16* (7), 2445–2451. https://doi.org/10.1200/JCO.1998.16.7.2445.

(28) Hortobagyi, G. N.; Ueno, N. T.; Xia, W.; Zhang, S.; Wolf, J. K.; Putnam, J. B.; Weiden, P. L.; Willey, J. S.; Carey, M.; Branham, D. L.; et al. Cationic Liposome-Mediated E1A Gene Transfer to Human Breast and Ovarian Cancer Cells and Its Biologic Effects: A Phase I Clinical Trial. *J. Clin. Oncol.* **2001**, *19* (14), 3422–3433. https://doi.org/10.1200/JCO.2001.19.14.3422.

(29) Delanian, S.; Baillet, F.; Huart, J.; Lefaix, J.-L.; Maulard, C.; Housset, M. Successful Treatment of Radiation-Induced Fibrosis Using Liposomal CuZn Superoxide Dismutase: Clinical Trial. *Radiother. Oncol.* **1994**, *32* (1), 12–20. https://doi.org/10.1016/0167-8140(94)90444-8.

(30) Rahman, A.; Treat, J.; Roh, J. K.; Potkul, L. A.; Alvord, W. G.; Forst, D.; Woolley, P. V. A Phase I Clinical Trial and Pharmacokinetic Evaluation of Liposome-Encapsulated Doxorubicin. *J. Clin. Oncol.* **1990**, *8* (6), 1093–1100. https://doi.org/10.1200/JCO.1990.8.6.1093.

(31) Morris, P. E.; Papadakos, P.; Russell, J. A.; Wunderink, R.; Schuster, D. P.; Truwit, J. D.; Vincent, J.-L.; Bernard, G. R. A Double-Blind Placebo-Controlled Study to Evaluate the Safety and Efficacy of L-2-Oxothiazolidine-4-Carboxylic Acid in the Treatment of Patients with Acute Respiratory Distress Syndrome*. *Crit. Care Med.* **2008**, *36* (3), 782–788. https://doi.org/10.1097/CCM.0B013E318164E7E4.

(32) Meunier, F.; Prentice, H. G.; Ringden, O. Liposomal Amphotericin B (AmBisome): Safety Data from a Phase II/III Clinical Trial. *J. Antimicrob. Chemother.* **1991**, *28* (suppl B), 83–91. https://doi.org/10.1093/jac/28.suppl_B.83.

(33) Gilad, A. A.; Winnard Jr, P. T.; van Zijl, P. C. M.; Bulte, J. W. M. Developing MR Reporter Genes: Promises and Pitfalls. *NMR Biomed.* **2007**, *20*, 275–290. https://doi.org/10.1002/nbm.

(34) Westmeyer, G. G.; Jasanoff, A. Genetically Controlled MRI Contrast Mechanisms and Their Prospects in Systems Neuroscience Research. *Magn. Reson. Imaging* **2007**, *25* (6), 1004–1010. https://doi.org/10.1016/j.mri.2006.11.027.

(35) Lee, S. W.; Lee, S. H.; Biswal, S. Magnetic Resonance Reporter Gene Imaging. *Theranostics* **2012**, *2* (4), 403–412. https://doi.org/10.7150/thno.3634.

(36) Vandsburger, M. H.; Radoul, M.; Cohen, B.; Neeman, M. MRI Reporter Genes: Applications For Imaging Of Cell Survival, Proliferation, Migration and Differentiation. *NMR Biomed.* **2013**, *26* (7), 872–884. https://doi.org/10.1002/nbm.2869.

(37) Yang, C.; Tian, R.; Liu, T.; Liu, G. MRI Reporter Genes for Noninvasive Molecular Imaging. *Molecules* **2016**, *21* (5), 1–16. https://doi.org/10.3390/molecules21050580.

(38) Pawelczyk, E.; Arbab, A. S.; Pandit, S.; Hu, E.; Frank, J. A. Expression of Transferrin Receptor and Ferritin Following Ferumoxides-Protamine Sulfate Labeling of Cells: Implications for Cellular Magnetic Resonance Imaging. *NMR Biomed.* **2006**, *19* (5), 581–592. https://doi.org/10.1002/nbm.1038.

(39) Harmelin, A.; Meir, G.; Dafni, H.; Neeman, M.; Cohen, B. Ferritin as an Endogenous MRI Reporter for Noninvasive Imaging of Gene Expression in C6 Glioma Tumors. *Neoplasia* **2006**, *7* (2), 109–117. https://doi.org/10.1593/neo.04436.

(40) Zhang, X.; Yan, J.; Huang, Y.; Tang, Q.; Ming, P.; Xu, G.; Zhao, N.; Gong, Y.; Liu, L.; Gong, K. Reconstruction and Expression of the MRI-Contrast Protein, Ferritin, with Recombinant Rabies Vectors. *Biotechnol. Lett.* **2010**, *32* (6), 743–748. https://doi.org/10.1007/s10529-010-0229-5.

(41) Hasegawa, S.; Furukawa, T.; Saga, T. Molecular MR Imaging of Cancer Gene Therapy: Ferritin Transgene Reporter Takes the Stage. *Magn. Reson. Med. Sci.* **2010**, *9* (2), 37–47.

https://doi.org/10.2463/mrms.9.37.

(42) Genove, G.; DeMarco, U.; Xu, H.; Goins, W. F.; Ahrens, E. T. A New Transgene Reporter for in Vivo Magnetic Resonance Imaging. *Nat. Med.* **2005**, *11* (4), 450–454. https://doi.org/10.1038/nm1208.

(43) Iordanova, B.; Robison, C. S.; Ahrens, E. T. Design and Characterization of a Chimeric Ferritin with Enhanced Iron Loading and Transverse NMR Relaxation Rate. *J. Biol. Inorg. Chem.* **2010**, *15* (6), 957–965. https://doi.org/10.1007/s00775-010-0657-7.

(44) Deans, A. E.; Wadghiri, Y. Z.; Bernas, L. M.; Yu, X.; Rutt, B. K.; Turnbull, D. H. Cellular MRI Contrast via Coexpression of Transferrin Receptor and Ferritin. *Magn. Reson. Med.* **2006**, *56* (1), 51–59. https://doi.org/10.1002/mrm.20914.

(45) Gossuin, Y.; Muller, R. N.; Gillis, P. Relaxation Induced by Ferritin: A Better Understanding for an Improved MRI Iron Quantification. *NMR Biomed.* **2004**, *17* (7), 427–432. https://doi.org/10.1002/nbm.903.

(46) Cohen, B.; Ziv, K.; Plaks, V.; Harmelin, A.; Neeman, M. Ferritin Nanoparticles as Magnetic Resonance Reporter Gene. *Wiley Interdiscip. Rev. Nanomedicine Nanobiotechnology* **2009**, *1* (2), 181–188. https://doi.org/10.1002/wnan.11.

(47) Vande Velde, G.; Rangarajan, J. R.; Toelen, J.; Dresselaers, T.; Ibrahimi, A.; Krylychkina, O.; Vreys, R.; Van Der Linden, A.; Maes, F.; Debyser, Z.; et al. Evaluation of the Specificity and Sensitivity of Ferritin as an MRI Reporter Gene in the Mouse Brain Using Lentiviral and Adeno-Associated Viral Vectors. *Gene Ther.* **2011**, *18* (6), 594–605. https://doi.org/10.1038/gt.2011.2.

(48) Choi, S. H.; Cho, H. R.; Kim, H. S.; Kim, Y. H.; Kang, K. W.; Kim, H.; Moon, W. K. Imaging and Quantification of Metastatic Melanoma Cells in Lymph Nodes with a Ferritin MR Reporter in Living Mice. *NMR Biomed.* **2012**, *25* (5), 737–745. https://doi.org/10.1002/nbm.1788.

(49) Gossuin, Y.; Burtea, C.; Monseux, A.; Toubeau, G.; Roch, A.; Muller, R. N.; Gillis, P. Ferritin-Induced Relaxation in Tissues: An in Vitro Study. *J. Magn. Reson. Imaging* **2004**, *20* (4), 690–696. https://doi.org/10.1002/jmri.20152.

(50) Cohen, B.; Benjamin, L. E.; Harmelin, A.; Ziv, K.; Neeman, M.; Israely, T.; Kalchenko, V.; Plaks, V. MRI Detection of Transcriptional Regulation of Gene Expression in Transgenic Mice. *Nat. Med.* **2007**, *13* (4), 498–503. https://doi.org/10.1038/nm1497.

(51) Pereira, S. M.; Moss, D.; Williams, S. R.; Murray, P.; Taylor, A. Overexpression of the MRI Reporter Genes Ferritin and Transferrin Receptor Affect Iron Homeostasis and Produce Limited Contrast in Mesenchymal Stem Cells. *Int. J. Mol. Sci.* **2015**, *16* (7),

15481–15496. https://doi.org/10.3390/ijms160715481.

(52) Naumova, A. V.; Yarnykh, V. L.; Balu, N.; Reinecke, H.; Murry, C. E.; Yuan, C. Quantification of MRI Signal of Transgenic Grafts Overexpressing Ferritin in Murine Myocardial Infarcts. *NMR Biomed.* **2012**, *25* (10), 1187–1195. https://doi.org/10.1002/nbm.2788.

(53) Zhen, Z.; Tang, W.; Todd, T.; Xie, J. Ferritins as Nanoplatforms for Imaging and Drug Delivery. *Expert Opin. Drug Deliv.* **2014**, *11* (12), 1913–1922. https://doi.org/10.1517/17425247.2014.941354.

(54) Paul, D.; Bartenschlager, R. Architecture and Biogenesis of Plus-Strand RNA Virus Replication Factories. *World J. Virol.* **2013**, *2* (2), 32. https://doi.org/10.5501/wjv.v2.i2.32.

(55) Gitlin, L.; Hagai, T.; LaBarbera, A.; Solovey, M.; Andino, R. Rapid Evolution of Virus Sequences in Intrinsically Disordered Protein Regions. *PLoS Pathog.* **2014**, *10* (12). https://doi.org/10.1371/journal.ppat.1004529.

(56) Ahola, T.; Karlin, D. G. Sequence Analysis Reveals a Conserved Extension in the Capping Enzyme of the Alphavirus Supergroup, and a Homologous Domain in Nodaviruses. *Biol. Direct* **2015**, *10* (1), 16. https://doi.org/10.1186/s13062-015-0050-0.

(57) Cadena-Nava, R. D.; Comas-Garcia, M.; Garmann, R. F.; Rao, A. L. N.; Knobler, C. M.; Gelbart, W. M. Self-Assembly of Viral Capsid Protein and RNA Molecules of Different Sizes: Requirement for a Specific High Protein/RNA Mass Ratio. *J. Virol.* **2012**, *86* (6), 3318–3326. https://doi.org/10.1128/jvi.06566-11.

(58) Annamalai, P.; Rao, A. L. N. Dispensability of 3′ TRNA-like Sequence for Packaging Cowpea Chlorotic Mottle Virus Genomic RNAs. *Virology* **2005**, *332* (2), 650–658. https://doi.org/10.1016/j.virol.2004.12.009.

(59) Kesharwani, P.; Jain, K.; Jain, N. K. Dendrimer as Nanocarrier for Drug Delivery. *Progress in Polymer Science*. 2014, pp 268–307. https://doi.org/10.1016/j.progpolymsci.2013.07.005.

(60) Tomalia, D. A.; Reyna, L. A.; Svenson, S. Dendrimers as Multi-Purpose Nanodevices for Oncology Drug Delivery and Diagnostic Imaging. *Biochem. Soc. Trans.* **2007**, *35* (Pt 1), 61–67. https://doi.org/10.1042/BST0350061.

(61) Kannan, R. M.; Nance, E.; Kannan, S.; Tomalia, D. A. Emerging Concepts in Dendrimer-Based Nanomedicine: From Design Principles to Clinical Applications. *J. Intern. Med.* **2014**, *276* (6), 579–617. https://doi.org/10.1111/joim.12280.

(62) Cheng, Y.; Zhao, L.; Li, Y.; Xu, T. Design of Biocompatible Dendrimers for Cancer Diagnosis and Therapy: Current Status and Future Perspectives. *Chem. Soc. Rev.* **2011**, *40* (5), 2673. https://doi.org/10.1039/c0cs00097c.

(63) Svenson, S.; Tomalia, D. A. Dendrimers in Biomedical Applications—reflections on the Field. *Adv. Drug Deliv. Rev.* **2012**, *64*, 102–115. https://doi.org/10.1016/J.ADDR.2012.09.030.

(64) Li, Y.; Xiao, K.; Luo, J.; Lee, J.; Pan, S.; Lam, K. S. A Novel Size-Tunable Nanocarrier System for Targeted Anticancer Drug Delivery. *J. Control. Release* **2010**, *144* (3), 314–323. https://doi.org/10.1016/j.jconrel.2010.02.027.

(65) Filippousi, M.; Papadimitriou, S. A.; Bikiaris, D. N.; Pavlidou, E.; Angelakeris, M.; Zamboulis, D.; Tian, H.; Van Tendeloo, G. Novel Core-Shell Magnetic Nanoparticles for Taxol Encapsulation in Biodegradable and Biocompatible Block Copolymers: Preparation, Characterization and Release Properties. *Int. J. Pharm.* **2013**, *448* (1), 221–230. https://doi.org/10.1016/j.ijpharm.2013.03.025.

(66) Bakewell, S. J.; Carie, A.; Costich, T. L.; Sethuraman, J.; Semple, J. E.; Sullivan, B.; Martinez, G. V.; Dominguez-Viqueira, W.; Sill, K. N. Imaging the Delivery of Drug-Loaded, Iron-Stabilized Micelles. *Nanomedicine Nanotechnology, Biol. Med.* **2017**, *13* (4), 1353–1362. https://doi.org/10.1016/j.nano.2017.01.009.

(67) Schleich, N.; Sibret, P.; Danhier, P.; Ucakar, B.; Laurent, S.; Muller, R. N.; Jérôme, C.; Gallez, B.; Préat, V.; Danhier, F. Dual Anticancer Drug/Superparamagnetic Iron Oxide-Loaded PLGA-Based Nanoparticles for Cancer Therapy and Magnetic Resonance Imaging. *Int. J. Pharm.* **2013**, *447* (1–2), 94–101. https://doi.org/10.1016/j.ijpharm.2013.02.042.

Part I. Theranostic approach to cancer with liposomal nanoparticles

Chapter 2

Magnetic Heating Stimulated Cargo Release with Dose Control using Multifunctional MR and Thermosensitive Liposome

Abstract

Rationale: Magnetic resonance imaging (MRI) is one of the most widely used diagnostic tools in the clinic. In this setting, real-time monitoring of therapy and tumor site would give the clinicians a handle to observe therapeutic response and to quantify drug amount to optimize the treatment. In this work, we developed a liposome-based cargo (cancer drugs) delivery strategy that could simultaneously monitor the real-time alternating magnetic field-induced cargo release from the change in MRI relaxation parameter R_1 and the location and condition of liposomes from the change in R_2. The tumor site can then be monitored during the cargo release because liposomes are able to passively target the tumor site through the enhanced permeability and retention (EPR) effect. Physical insights from the experimental results and corresponding Monte Carlo spin dynamics simulations are also discussed.

Methods: Superparamagnetic iron oxide (SPIO) nanoparticles, diethylenetriaminepentaacetic acid gadolinium(III) (Gd(III)-DTPA), and a model cancer drug (fluorescein) were co-loaded in PEGylated thermosensitive liposomes. The liposomes were characterized by transmission electron cryo-microscopy (cryoTEM), dynamic light scattering (DLS), and inductively coupled plasma optical emission spectrometry (ICP-OES). An alternating magnetic field (AMF) was used to create

controlled mild hyperthermia (39-42°C) and facilitate controlled cargo (model cancer drug fluorescein) release from the thermosensitive liposomes. MRI relaxation parameters, R_1 and R_2, were measured at room temperature. The temporal variation in R_1 was used to obtain the temporal profile of cargo release. Due to their similar sizes, both the gadolinium and cargo would be released from the liposomes together as a result of heating. The temporal variation in R_2 was used to monitor SPIO nanoparticles to enhance the tumor contrast. Monte Carlo spin dynamics simulations were performed by solving the Bloch equations and modeling SPIO nanoparticles as magnetized impenetrable spheres.

Results: TEM images and DLS measurements showed the diameter of the liposome nanoparticles to be ~ 200 nm. AMF heating showed effective release of the model drug. It was found that R_1 increased linearly by about 70% and then saturated as the cargo release process was completed, while R_2 remained approximately constant with an initial 7%-drop and then recovered. The linear increase in R_1 is consistent with the expected linear cargo release with time upon AMF heating. Monte Carlo spin dynamics simulations suggest that the initial temporal fluctuation of R_2 is due to changes of SPIO aggregation and the slow non-recoverable degradation of liposomal membranes that increases water permeability with time by the heating process. The simulations show an order of magnitude increase in R_2 at higher water permeability.

Conclusion: We have performed a MR parameter study of the release of a cargo (model cancer drug, fluorescein) by magnetic heating from thermosensitive multifunctional liposomes loaded with dual contrast agents. The size of the liposome nanoparticles loaded with model cancer drug (fluorescein), gadolinium chelate, and SPIO nanoparticles was appropriate for a variety of cancer therapies. A careful and detailed analysis with theoretical explanation and simulation was carried

out to investigate the correlation between MRI relaxation parameters, R_1 and R_2, and different cargo release fractions. We have quantified the cargo release using R_1, which shows a linear relation between percentage release with changes in R_1. This result provides a strong basis for the dosage control of drug delivered. On the other hand, the fairly stable R_2 with an almost constant value suggests that it could be used to monitor the position and condition of the liposomal site, as SPIO nanoparticles mostly remained in the aqueous core of the liposome. Because our synthesized SPIO-encapsulated liposomes could be targeted to tumor sites passively by the EPR effect, or actively through magnetofection, this study provides a solid ground for developing MR cancer theranostics by a combination of this nanostructure and AMF heating strategy. Furthermore, our simulation results predict a sharp increase in R_2 during the AMF heating, which opens up the exciting possibility of high-resolution, high-contrast real-time imaging of the liposomal site during the drug release process, provided AMF heating can be incorporated into an MRI setup. Our use of the clinically approved materials, along with confirmation by theoretical simulations, make this technique a promising candidate for translational MR cancer theranostics.

2.1. Introduction

Cancer is the second highest leading cause of death worldwide, after cardiovascular diseases. Recently developed cancer theranostic approaches provide a promising direction to detect and treat cancer simultaneously.[1–6] This kind of molecular therapeutics, coupled with biomedical imaging, enhances the scope and efficacy of the treatment. For example, one of the major challenges to the treatment of cancer by chemotherapy is to deliver the required high dose at tumor sites while minimizing the toxic effects on benign tissues. Nanoparticle-mediated targeted and controlled drug delivery along with real-time imaging could achieve the desired result by reducing harmful effects on the benign tissues.

Nanovehicles of optimum size, functionality to target tumor cells, and capability to carry both the drug and contrast agent and deliver drugs at the tumor site under external signaling are required for such a theranostic procedure.[7–9] Various kinds of nanovehicles have been developed recently for the purpose of targeted delivery and controlled drug release.[7–15] Among them, promising candidates are liposomes[16–22] that have shown appealing features for drug delivery, biocompatibility, and clinical efficiency. Pharmacokinetic properties of the drug are significantly altered after encapsulation in the liposome and the toxicity of the drug is substantially reduced.[23] Furthermore, the drug is restricted from early activation during the circulation process. Different formulations of liposomes are now in clinical trial or already clinically approved.[23–31] They have been shown to be effective to decrease the off-target toxicity on other tissues. For example, liposomal anthracycline delivery reduces cardiotoxicity.[23] However, no significant increase in the therapeutic efficacy has so far been found in the clinical trials.[23]

To alleviate this problem, liposome extravasation and bioavailability could be increased with the use of mild hyperthermia (39-42°C) .[23,32–35] Moreover, by increasing the concentration of drug at the tumor site through the leaky vascular permeability, chemotherapy at a slightly higher temperature has shown improved efficacy of the drugs. It has been found that a series of drugs show improved efficiency by heat activation. The synergistic effect of hyperthermia and chemotherapy are far more effective than the monotherapies.[36–40] The enhanced efficiency of the drugs has been attributed to the higher level of tumor perfusion, resulting in increased sensitivity to the tumor area.[23] Recent studies also showed that under mild hyperthermia, heat-shock proteins released during cell necrosis acted as a trigger for antitumor immunity, thus regressing the tumor and reducing metastasis.[41] Hence, a combination of mild hyperthermia and significantly increased amount of drug delivery at the tumor site while reducing any interaction of the drugs with the healthy tissues along with simultaneous monitoring of the drug release and tumor site would be a vastly improved form of chemotherapy that could considerably improve the efficiency of the treatment.

Hyperthermia can be created by different methods such as a water bath,[34] high-intensity focused ultrasound (HIFU),[42–44] and alternating magnetic field (AMF) induced heat.[45–48] However, water baths could not provide spatially accurate treatment and HIFU is restricted in its ability for deep thermal therapy to a large area or penetrating bone and air. Here, the use of AMF to create mild hyperthermia has the advantages of achieving high accuracy in a specific area along with higher penetration capability, which is an alternative approach for disrupting the blood brain barrier.[49] Most importantly, as an ongoing project in our group, the AMF facility could be integrated into the existing MRI instrumentation and radio-frequency amplifiers for MR

theranostics to simultaneously treat the cancer by using AMF and monitor the cancer treating process.

To complete such a drug delivery scheme, it is essential to have an efficient real-time monitoring system to observe and control the drug release at the target site.[50–53] MRI is a powerful noninvasive imaging modality in this regard, which has no harmful radiation and has general clinical acceptance. Previous studies have utilized single-modal MRI-guided drug delivery systems.[34,43,54,55] However for an effective therapy, it is important to monitor simultaneously both the drug release and tumor site. Dual-modal imaging is recommended over single-modal, as the latter could provide more handle to the clinicians to optimize the personalized treatment for better point-of-care. Combination of other imaging modalities might increase the scope of such treatments.[56–58] However, it is often restricted by high-energy ionizing radiation or limited penetration through the body. Hence, dual-modality within the scope of MRI could eliminate such restrictions for a successful treatment.

In clinical settings, clinicians mainly rely on either positive contrast T_1-weighted imaging or negative contrast T_2-weighted imaging. However, a combination of both could provide insights on both the pathological phenomena and soft tissue anatomy to improve MR cancer imaging for stage detection, early diagnosis, and vascular imaging.[59] Therefore, many studies have turned to the design of encapsulating dual-modal MRI contrast agents in different formulations of liposomes and other nanocarriers.[44,60–68] For example, Bos and coworkers[44] have described the encapsulation of superparamagnetic iron oxide (SPIO) nanoparticles and Gd-chelate (ProHance) in liposomes for dual modal MRI. They have demonstrated *in vivo* HIFU treatment and discussed corresponding relaxation parameter changes. Other studies include different formulation of dual-modal MR

contrast agents, such as synthesis of gadolinium and iron oxide-conjugated nanoparticles,[61] surface functionalization of SPIO-encapsulated liposomes with gadolinium chelates,[64,67] size-controlled iron oxide nanoparticles[63] etc. Novel nanoparticle formulations with iron and manganese were developed for dual modal imaging and future theranostic purposes.[68]

In this work, we have encapsulated SPIO nanoparticles, diethylenetriaminepentaacetic acid gadolinium(III) dihydrogen salt hydrate (Gd(III)-DTPA, commercially known as Magnevist) molecules, and a commonly used small-molecule model cancer drug (a fluorophore tracer, fluorescein[48,69–71]) into thermosensitive liposome nanoparticles. We have demonstrated real-time AMF-controlled fluorescein release under mild hyperthemia and done a careful characterization of dual MRI parameters -- longitudinal relaxation rate (R_1) and transverse relaxation rate (R_2) with different amounts of cargo release, as shown schematically in **Figure 2.1**. Gd(III)-DTPA molecules are released simultaneously with the cargo (fluorescein), changing R_1 and making it sensitive to the percentage of cargo release. The R_2 parameter tracks SPIO nanoparticles. We have performed a detailed analysis and explained the correlation between the relaxation parameters and cargo release with mathematical modelling and Monte Carlo spin dynamics simulations. Synthesized liposomes could be efficiently targeted to specific tumor sites through magnetic force[72,73] or active targeting.[16,74] Hence, this work serves as a proof of concept for future MR theranostic approach, which could simultaneously fulfill all three important needs: 1) on-demand cargo release using AMF-controlled mild hyperthermia; 2) monitoring the position and condition of liposomal accumulation site (such as a tumor) throughout the measurement by monitoring R_2; 3) dosage control of the cargo release process by monitoring the R_1 parameter. Although we demonstrated our method using a model drug, existing *in vivo* and *in vitro* cancer drug release data

and the associated diffusion models[75,76] provide a strong basis for the validity of our results for real cancer drug release in animal body.

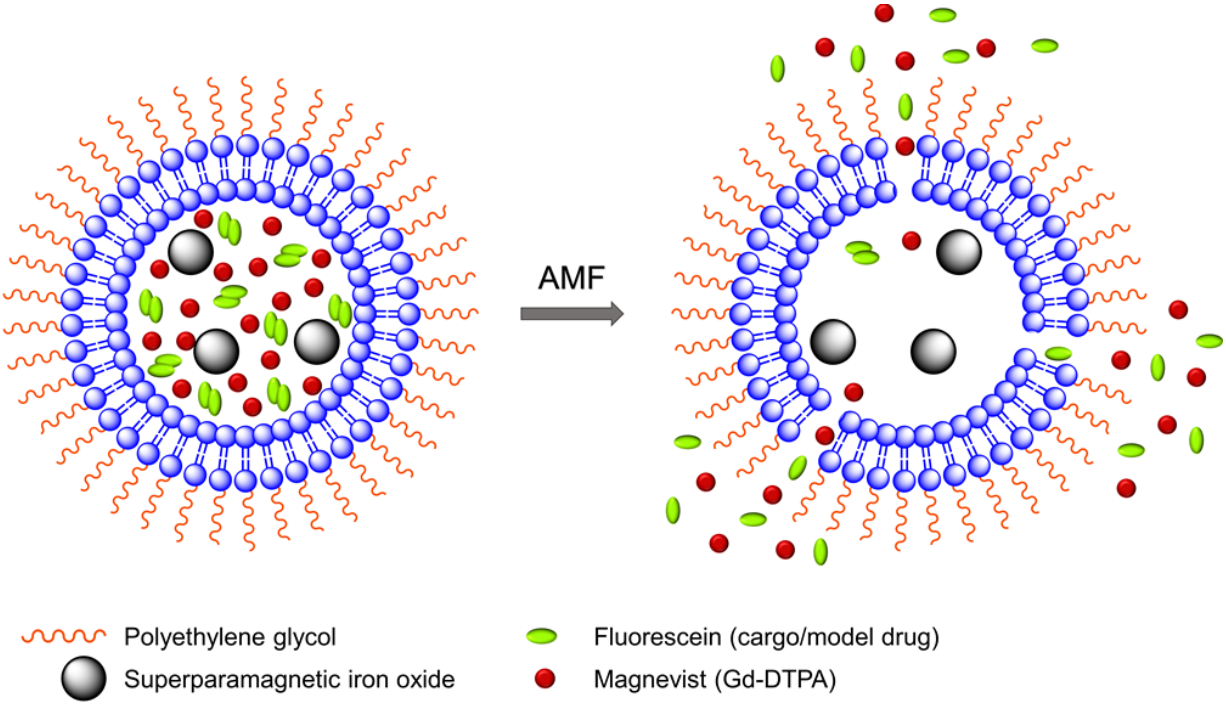

Figure 2.1. A schematic diagram of model drug/cargo (fluorescein) and contrast agents (magnetic nanoparticles and Gd(III)-DTPA) released from thermosentive PEGylated liposomes under mild hyperthemia with alternating magnetic field (AMF). It illustrates the liposomal membrane permeability change and release of Gd(III)-DTPA and fluorescein upon AMF-induced heating.

Here, we have used clinically approved formulations, so the procedure has the potential to be readily adapted with magnetofection or any existing targeting approach. Theoretical simulations were carried out to understand the dynamical process during the AMF heating and a qualitative confirmation has been reached. The expected sharp rise in R_2 with slightly increased water permeability of liposome, as seen from the simulations, indicates the possibility of high-resolution, high-contrast MR imaging of the liposomal site in *in situ* measurements.

2.2. Materials and methods

2.2.1. Preparation of hydrating solution

Dextran-coated iron oxide nanoparticles of diameter 5-10 nm with 10 mg/ml concentration were purchased from Ocean Nanotech, USA. 0.5 ml of iron oxide solution was added to 1.5 ml of phosphate buffer saline (PBS, 100 mM) (Sigma Aldrich) containing Gd (III)-DTPA (Sigma Aldrich) and fluorescein (Sigma Aldrich) to obtain 2 ml of hydrating solution with a final concentration of 200 mM Gd (III)-DTPA and 100 mM fluorescein at pH 7.4.

2.2.2. Synthesis of liposome nanoparticles

A total of 40 micromole of 1,2-dipalmitoyl-sn-glycero-3-phosphocholine (DPPC) (Avanti Polar Lipids, Inc.), 1,2-distearoyl-sn-glycero-3-phosphocholine (DSPC) (Corden Pharma), Cholesterol (Sigma Aldrich), and 1,2-distearoyl-sn-glycero-3-phosphoethanolamine-N-[amino(polyethylene-glycol)-2000] (DSPE-PEG(2000)) (Corden Pharma) at a molar ratio of 67:15:13:5 were dissolved in a chloroform/methanol (2:1) (Sigma Aldrich) mixture to yield a uniform solution of density between 10-20 mg/ml. The homogeneous solution was evaporated under high vacuum at 40°C and kept for 5 hours in a rotatory evaporator for complete removal of the organic solvent. The produced thin film was hydrated with hydrating solution containing iron oxide nanoparticles, Gd(III)-DTPA, and fluorescein at pH 7.4 for 1 hour in a rotatory evaporator at a constant speed at 65°C. The resulting solution was passed through 400-nm (31 times) and 100-nm (51 times) filters, respectively, during extrusion using a mini extruder (Avanti Polar Lipid, Inc.). Non-entrapped iron oxide nanoparticles, Gd(III)-DTPA, and fluorescein were removed by repeated washing using Sephadex G-25M PD-10 (Sigma Aldrich). The liposome solution was

further purified by repeated filtration through 0.1 μm Amicon low-binding Durapore PVDF membranes (Millipore Corporation, Bedford, MA) at a centrifuge speed of 2000 rpm.

2.2.3. Material characterization

The size and zeta potential analysis were performed by dynamic light scattering (DLS) using a Zetasizer Nano (Malvern Instruments Ltd., Worcestershire, U.K.). The sizes of the liposome nanoparticles were measured before and after heating in 100 mM PBS buffer. The zeta potential of the liposome solution was recorded in deionized water. The morphology, distribution, and size of liposome nanoparticles were determined by transmission electron cryomicroscopy (CryoTEM). Grids were made by taking 2.5 μl of the liposome sample on a glow-discharged Quantifoil holey-carbon grid (SPI Quantifoil R1.2/1.3).[77] The grids were subsequently blotted dry and a about 100-nm-thick residual film of suspended solution across the holes in the grids was obtained by using a manual plunger. This solution was then rapidly plunged frozen around -196 ^{o}C into a 2:1 mixture of liquid propane: liquid ethane to produce a vitrified glassy solution within the holes. This quick freezing produced an amorphous ice-containing sample in the holy carbon film. The grid was then loaded with Gatan cryo specimen holder into FEI Titan Krios (Electron Imaging Center for NanoMachines, California NanoSystems Institute) microscope for imaging. The images were acquired by operating the machine at 200 kV with a TIETZ F415MP 16 megapixel CCD camera.

The concentration of iron or Gadolinium were quantitatively determined by inductively coupled plasma optical emission spectrometry (ICP-OES) using a Shimadzu ICPE-9000 instrument. Different concentrations of liposome samples and supernatant solution were digested overnight with 10 mL of aqua regia at 95°C. Afterward, the solution was diluted with a 2% HNO_3

for quantitative measurement. The calibration curves for Fe or Gd were obtained from 0 ppm to 10 ppm and the results were fitted to obtain Fe and Gd amounts.

2.2.4. AMF-controlled cargo (model drug fluorescein) release

The set up was the same as described in the previous studies.[47,48] Superparamagnetic heating was executed using a Magnetic Hyperthermia System manufactured by MSI Automation Inc. A five-turn copper coil (both the height and diameter = 50 mm) was used for the experiment. The magnetic field oscillation frequency, amplitude, and induction power were 375 kHz, 20 kA/m, and 5 kW, respectively. Fluorescence spectra were acquired using an Acton Spectra Pro 2300i CCD cooled below -120°C with liquid nitrogen. CUBE 445-40C laser (Coherent Inc., Santa Clara, CA, USA) was used for excitation at a wavelength of 448 nm and a power of 4 mW. Scattered and stray light beams were blocked with a long pass filter.

The synthesized liposome solution was diluted 10 times with 100 mM PBS buffer. 1 ml of the solution was exposed to AMF for 105 minutes, and the fluorescence yield of fluorescein was measured after each 15 minutes of AMF cycle at room temperature. Bulk temperature was recorded using a thermometer after each cycle. Each time, 50 μL of the sample was added to 3.5 ml of PBS buffer (100 mM) in a standard 1-cm fluorescence cuvette. The intensity around the fluorescein emission maximum was integrated over the wavelength range from 510 – 520 nm for three scans. The process was repeated three times and averaged over three such integrated emission spectra. The errors were computed from the standard deviation of three measurements. The fluorescence spectra of PBS were recorded identically and used as the background for all the analyses.

In order to determine the percentage of cargo release as a result of AMF heating, the sample was completely lysed with a solution of 60 μL of 10% Triton X-100 and fluorescence spectra were acquired. The fluorescence spectra were acquired for 10% Triton added PBS buffer and a background spectrum for Triton was obtained without adding the sample to the Triton solution. The percentage of cargo release in each case was calculated according to the equation[45]:

$$\% \text{ Cargo release} = \left(\frac{\text{Flourescence of AMF treated sample-Fluorescence before AMF treatment}}{\text{Fluorescence after lysing with Triton -Fluorescence of Triton Background}}\right) \times 100\ \% \quad (2.1)$$

2.2.5. Tracking MRI parameters

The samples with different cargo release were collected and the relaxation rates were measured using a 600 MHz (AV600, Bruker) Nuclear Magnetic Resonance (NMR) spectrometer and micro-imaging setup. The relaxation rates of the sample after complete lysing by Triton X-100 were also measured. R_1 was measured using the saturation recovery pulse sequence and R_2 was measured by the CPMG (Carr-Purcell-Meiboom-Gill) pulse sequence. The relaxation delay time was varied from 5-15 s, depending on the samples and the number of scans was = 1. The saturation time was 300 ms and time of recovery was ranging from 5 ms to 10 s for saturation recovery pulse sequence. For CPMG pulse sequence, half of the interval between successive 180^o pulses (τ_{CP}) was = 500 μs and time of echo (TE) was ranging from 2 to 100 ms. Each measurement was repeated three times and the average value was taken. The errors were calculated from the standard deviation of the three measurements. All measurements were performed at room temperature.

The background relaxation rates were measured from the supernatant obtained after precipitating all the liposomes by centrifugation (20,000 g). The supernatant had been checked with TEM and DLS to ensure it was free from liposomes. The background correction was done on the relaxation rate and the corrected relaxation rates were determined for each sample. Percentage changes in the relaxation rates were calculated as follows:

$$\Delta R\ (\%) = \frac{(S\text{-}B)\text{-}(S_0\text{-}B)}{(S_0\text{-}B)} \tag{2.2}$$

Where, ΔR (%) is the percentage changes in relaxation rate, S is sample relaxation rate after heating, B is background relaxation rate, S_0 is the initial relaxation rate before heating. Longitudinal relaxivity (r_1) and transverse relaxivity (r_2) were deduced from the measurement of relaxation rates at different dilutions before and after completing magnetic heating and corrected by the background relaxation rate as follows:

$$\text{Corrected relaxation rate} = \text{Sample relaxation rate} - \text{Background relaxation rate} \tag{2.3}$$

Corrected Fe and Gd concentrations were obtained from ICP-OES measurements according to the **Equation 2.4**:

$$\text{Corrected concentration} = \text{Sample concentration} - \text{Background concentration} \tag{2.4}$$

The corrected relaxation rates were plotted with the corrected concentration and a linear fit was obtained. The relaxivity parameter was obtained from the slope of the fitted straight line.

2.2.6. Monte Carlo spin dynamics simulations

Monte Carlo spin dynamics simulations using a diffusion model were performed to calculate R_2 parameters for different inter-nanoparticle separation of SPIO aggregations and water permeability of liposome membrane. SPIO nanoparticles were modeled as magnetized impenetrable spheres of radius 5 nm. Based on cryoTEM images, we estimated that there were 7 SPIO nanoparticles inside each 100-nm radius liposome. Inter-nanoparticle distances were taken as 2, 6, and 10 times of SPIO nanoparticle radius to simulate different degree of aggregation. The root mean square (rms) angular frequency shift at the nanoparticle surface (compared to a point infinitely far away) was taken as $\Delta\omega_r = 1.7 \times 10^7$ rad/s. The diffusing water magnetizations were first positioned stochastically and the diffusion was modeled by random walks with periodic boundary conditions. The diffusion coefficient was taken as 2.3×10^{-9} m^2/s for water at 25ºC. In the simulation process, the effect of liposome membrane permeability was included as the probability of a diffusing water magnetization striking the liposome membrane to cross the barrier and enter into the liposome. After each random-walk step, each water magnetization experienced a new, combined, net magnetic field, which was calculated by adding the dipolar fields from all the magnetic nanoparticles present. The Z-component of the induced dipolar field, $B_{dip,Z}$, at position (d, θ) form the magnetic nanoparticle could be approximated by:

$$B_{dip,z}(d,\theta) = \sqrt{5/4}\,\frac{r^3 \Delta\omega_r}{\gamma d^3}(3\cos^2\theta - 1) \qquad (2.5)$$

where, γ is the gyromagnetic ratio of ^1H, r is the radius of the magnetic nanoparticle, $\Delta\omega_r$ is the rms angular frequency shift at the magnetic nanoparticle surface, d is the distance from the point

to the center of the magnetic nanoparticle, and θ is the angle between the Z-axis and the position vector of the point.

Following an initial 90^{o}_{+y} excitation pulse that flips all the equilibrium water magnetizations from +z to the +x direction, the time evolutions of 1000 diffusing water magnetizations were calculated by numerical integration of the Bloch equations[78] by Matlab (The MathWorks, Inc., Natick, MA, USA) using ordinary differential equation (ODE) solvers. As in the actual experiments, τ_{CP} in the CPMG pulse sequence was taken as 500 μs. The average net water magnetization was calculated by averaging all the individual water magnetizations. The CPMG T_2 relaxation rate (R_2) was obtained by a linear fitting of the negative natural logarithm of the normalized transverse average water magnetization as a function of time.

2.3. Results and discussions

2.3.1. Material characterization

The DLS results in PBS buffer provide an effective diameter of 231 nm for liposome nanoparticles with polydispersity index = 0.134. The intensity profile for size distribution has been shown in **Figure 2.2A.** It suggests that the nanoparticles are stable and well dispersed under biological conditions at pH 7.4. DLS measurements were repeated after AMF heating and a similar sizes (diameter = 223 nm +/- 1.6 nm) of liposome nanoparticles with polydispersity = 0.178 were obtained. The zeta potential of the liposome nanoparticles measured in water was found to be -12.63 mV. CryoTEM results are shown in the left and right panels of **Figure 2.2B** at different magnifications. They show homogeneous distribution and morphology of liposomes with

embedded SPIO nanoparticles. Electron-dense objects, such as SPIO, appear as darker regions in the image. Larger aggregates of SPIO were visible as dark spots at this resolution. The magnified one in inset of the right panel demonstrates the encapsulation of SPIO nanoparticles inside the inner aqueous core of the liposomes. The Gd and Fe concentrations in the liposome solution were determined by ICP-OES to be 1.37 mM and 22.2 mM with ~5% uncertainty, respectively. Considering the unencapsulated 0.00382 mM Gd and 6.50 mM SPIO in the supernatant, the effective iron and Gd concentrations in the liposome solution are 15.7 mM and 1.37 mM, respectively.

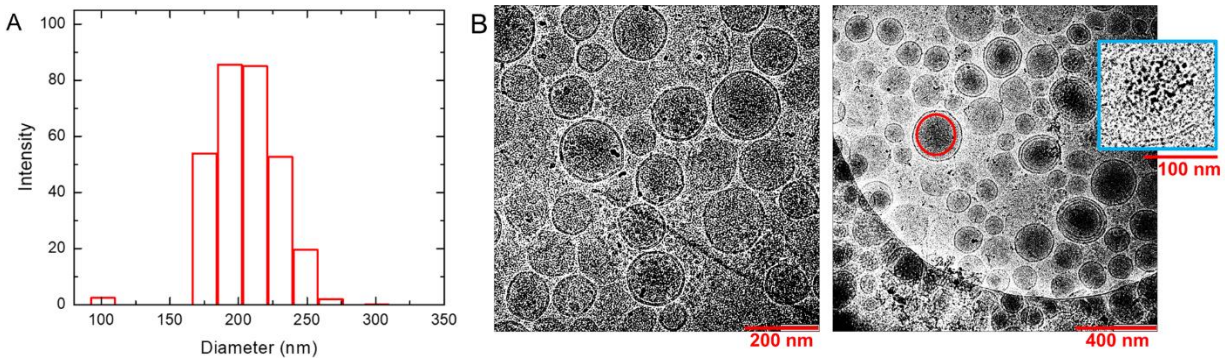

Figure 2.2. Characterization of liposomes. (A) Dynamic light scattering (DLS) of synthesized liposomes. It demonstrates the distribution of nanoparticles with an average diameter 231 nm and polydispersity 0.134. (B) CryoTEM images show the homogeneous distribution and morphology of liposomes at different magnifications. They show an average diameter around 200 nm and successful formation of bilayered spherical liposomes. The darker regions mark the presence of SPIO inside the liposome. A representative red circle is drawn to show such an SPIO concentrated region. The magnified liposome in the blue box of the right panel shows the SPIO encapsulation inside the aqueous liposome core. Larger aggregates of SPIO appear as darker spots.

The synthesized liposomes with a uniform size distribution (diameter ≈ 200 nm) and low polydispersity (< 0.2) indicate a homogeneous distribution in the solution. CryoTEM images demonstrate the successful encapsulation of SPIO nanoparticles inside the liposome nanoparticles. The optimal size of the encapsulating liposome nanoparticle plays a key role in this kind of

theranostic approach. A smaller size, < 5 nm, accelerates fast excretion through kidney filtration, while larger-size nanoparticles are easily recognized for uptake by the reticuloendothelial system (RES). A size comparable to the inter-endothelial cell gap of a few hundred nanometers is considered as a key factor for the determination of optimal size, and previous studies have shown that the preferred size range is about 50-200 nm[79,80] to reduce fast clearance and enhance passive tumor targeting by enhanced permeability and retention (EPR) effect.[81]

SPIO-encapsulated liposomes are ideal candidates for magnetic targeting to tumors and recent *in vivo* studies have shown the nanocarriers in the range of 200 nm could be efficiently targeted to the tumors by magnetofection.[17,72,73] In order to maximize the hyperthermia effect and magnetic targeting, a size of about 200 nm is generally preferred, as the magnetic force on the liposome would get enhanced in proportion to its size.[17] The association of polyethylene glycol (PEG) with the liposome nanoparticles is to increase the circulation time in blood for passive targeting by EPR. The unaltered size and polydispersity index before and after the AMF heating suggest that the liposome structure remained intact and the SPIO nanoparticles remained inside the liposome throughout the procedure. Additionally, the presence of SPIO nanoparticles inside the liposomes offers the nanovehicles active tumor targeting capability for superficial tumors by external magnetic force.[72,73] Consequently, SPIO-encapsulated liposomes are structurally suitable to make nanoparticles biocompatible and offer a clinically proven, versatile platform for the further enhancement of pharmacological efficacy and targeting efficiency.

2.3.2. AMF-controlled cargo (model drug fluorescein) release

The cargo release profile following AMF heating was monitored by using the self-quenching property of the fluorescein[69,71] that serves as a model for cancer drug, as it has a molecular size similar to that of the real cancer drug. The fluorescence yield is quenched depending on whether the fluorescein is inside the liposome with a high concentration or outside the liposome with a lower concentration. This property was used to quantify the percentage of fluorescein release from the liposome under AMF heating. All fluorescence measurements were performed after cooling the sample to room temperature following AMF heating and increasing the bulk temperature up to 39°C. In a controlled water bath experiment, we heated liposomes containing fluorescein up to 80°C and performed fluorescence experiments after cooling the sample to room temperature. No change in the spectral characteristics of fluorescein was seen in these studies.

The characteristic cargo release pattern measured by fluorescence yield is shown by the dotted red curve in **Figure 2.3A**. We find from the dotted red curve in **Figure 2.3A** that the percentage of cargo release was initially low, and after a threshold, it increased at a faster rate and finally reached the maximum, indicating complete cargo release. The CryoTEM images in **Figure 2.2B and Figure 2.2C** show that the number of SPIO nanoparticles in each liposome varies, leading to the conjecture that the higher loaded liposomes released cargo at the beginning, and later on, other liposomes with average loading started to release cargo. **Figure 2.3A** and **2.3B** show experimental points for cumulative AMF heating time and corresponding temperature of the bulk sample (before cooling). **Figure 2.3A** (dotted red curve) shows that the cargo release rate is fastest in the (30 – 45) minute time interval and levels off after an hour, indicating complete cargo release. However, the exact timing is sensitive to the experimental conditions and needs to be optimized,

based on the clinical settings. A control liposome sample was measured before and after the treatment procedure to ensure that there was no leakage otherwise.

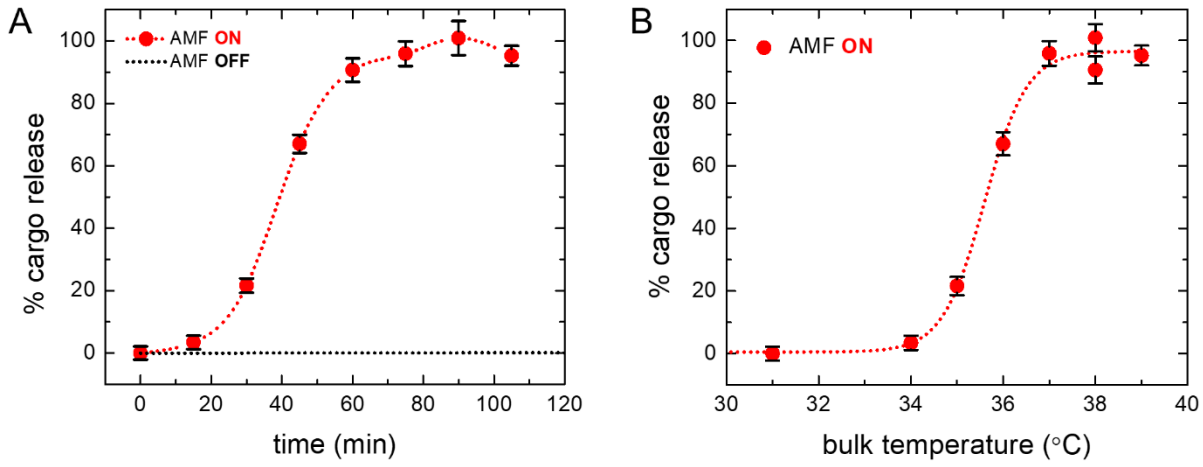

Figure 2.3. Cargo (fluorescein) release profile. (A) Cargo (fluorescein) release profile is shown as a function of the cumulative AMF heating time. Dotted red curve demonstrates the percentage of cargo release at different times. The characteristic pattern indicates an initial slow rate of release, then an increased rate of release between 30 to 45 minutes, and finally leveling off, indicating the complete release. The dotted black curve shows the spontaneous release of cargo from liposomes without AMF treatment and horizontal line depicts no leakage is observed otherwise. (B) Cargo (fluorescein) release profile is shown as a function of the bulk temperature (before cooling to room temperature). It demonstrates that the maximum change in the bulk temperature during the process from no cargo release to complete occurs over about 3°C. The dotted lines through the data points are included in each case as a guide to the eye.

The dotted black line in **Figure 2.3A** represents the spontaneous cargo release profile of liposomes, which clearly shows cargo did not leak without AMF heating. **Figure 2.3B** shows the profile of the corresponding bulk temperature change with cargo release. The saturation temperature for the drug release is 37°C and the dramatic increase in the rate of drug release occurred from 34-37°C resulting in almost 100% drug release**.** AMF heating experiments show that a significant percentage of drug release starts above 35°C and saturates at 37°C for this liposome. **Figure S2.1** in the supplementary materials shows a comparison of cargo release at

different temperatures under AMF heating (red bar) and bulk heating in a bath (black bar). We find a significantly higher percentage of drug release at around 36°C under AMF heating, compared to that under the bulk bath heating. The choice of liposome provides the flexibility to easily manipulate the transition temperature by changing the lipid composition according to the clinical requirement.[82]

Measuring local temperature inside the nanovehicle is challenging. However, there have been several methods to measure temperature inside the core of liposomes by optical spectroscopy or using polymers.[83–87] An ongoing effort in our labs is to develop theoretical methods to account for the aggregate formation and the size distribution of the magnetic nanoparticles inside the core of liposome to accurately estimate the specific loss power and heating efficiency for MR nanotheranostic hyperthermia in cancer therapy.[35] Based on those studies, generally speaking, higher the number of SPIO nanoparticles in the core of the liposome, more heat can be induced by the application of AMF.

2.3.3. Tracking MRI parameters

Figure 2.4A shows the percentage change of the MRI parameter R_1 with the percentage of cargo release (dotted red line). We find a linear increase in the percentage of R_1 with the percentage of cargo release, and a maximum increase of R_1 of 69.8 %, indicates 100% cargo release. The results have been given in a tabular form in **Table 2.1**. This change in the R_1 value is attributed to the simultaneous release of Gd(III)-DTPA along with the model drug molecule fluorescein (cargo) from the liposome nanoparticles, since the presence of Gd(III)-DTPA outside the liposome would significantly increase the R_1 value of the water protons due to the free interaction of Gd(III) with the water protons, compared to those in the encapsulated state.[34] This hypothesis has been further

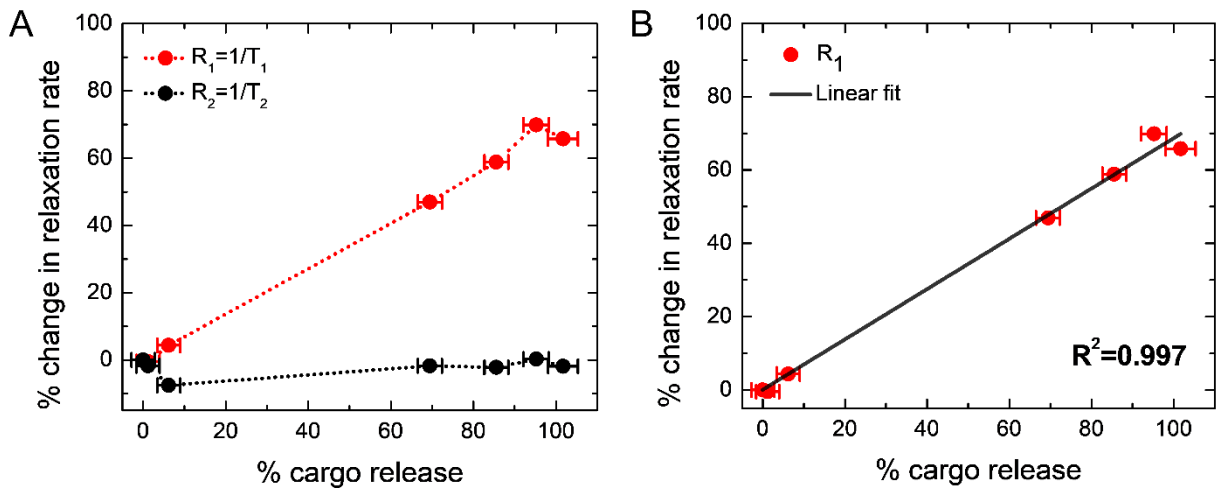

Figure 2.4. Correlation between changes in MR relaxation rates and cargo (fluorescein) release. (A) Red curve indicates the percentage change in R_1 and black curve indicates the percentage change in R_2. It demonstrates that R_1 increases linearly with cargo release, and reaches a maximum increase of about 70%, when cargo release was complete. R_2 remains nearly constant; however, it shows an initial 7%-drop (from the second to the third point, corresponding to the path of no cargo release to about 6% cargo release) and then a gradual increase to the initial value. Please see the text for the plausible explanation. The dotted lines through the data points are included in each case as a guide to the eye. (B) Fitted linear plot for percentage change in longitudinal relaxation rate (R_1) with percentage cargo release. The slope of the line is 0.686 with squared correlation coefficient $R^2 = 0.997$.

confirmed by measuring the R_1 value of the liposome solution after completely lysing with Triton X-100, which provides the exact same value as found from the maximum R_1 value after complete cargo release. It implies that the local heating increases the permeability of liposome membrane,[88,89] allowing leakage of both Gd(III)-DTPA and cargo, and R_1 increases linearly with the cargo release. In order to further investigate the linear nature of the plot, we have fitted percentage changes in R_1 against percentage cargo (fluorescein) release in **Figure 2.4B** and obtained a linear equation (**Equation 2.6**) with squared correlation coefficient $R^2 = 0.997$.

$$\%\ \text{Change in}\ R_1 = 0.686 \times \%\ \text{Change in cargo release} \tag{2.6}$$

Table 2.1. Data for percentage changes in MR relaxation rates with different percentage of cargo (fluorescein) release

% Cargo (fluorescein) release[a]	% R_1 change[b]	% R_2 change[b]
0	0	0
1.194	-0.482	-1.746
6.202	4.373	-7.548
69.449	46.935	-1.766
85.559	58.833	-2.195
95.228	69.904	0.272
101.739	65.780	-1.878

[a]Standard deviation is 3 %
[b]Standard deviation is 0.3 %

The black curve in **Figure 2.4A** shows the percentage change of R_2, which remains essentially constant, independent of cargo release (data are shown in **Table 2.1**). However, a closer look reveals that initially (along second to third point in the black curve in **Figure 2.4A**, corresponding to the path of no cargo release to about 6% cargo release or the 3rd point in **Table 2.1**) it dropped by about 7% and later increased to the initial value. DLS measurements did not show any significant change of the liposome size as a result of mild AMF heating. On the other hand, the R_2 parameter of the completely lysed sample (where all the SPIO nanoparticles should be outside the liposome encapsulation) was found to be reduced by about 20%, compared to that in the pretreated sample (data not shown). Hence, mild AMF heating is not causing any significant leakage of SPIO nanoparticles from the liposome encapsulation, as also concluded in earlier work.[44] Since SPIO particles remained inside the liposomes during AMF heating and the liposomes could be attached to the tumor site, the encapsulated SPIO particles could be used for online monitoring of the tumor site. Our theoretical simulations provide a qualitative explanation of the initial small drop and later slight increase of R_2 under mild AMF heating (**Figure 2.4A**), as discussed in the next section.

In order to further understand and quantify the changes of the relaxation rates, R_1 and R_2, relaxivities (r_1 and r_2) were determined by measuring the relaxation rates at different dilutions both

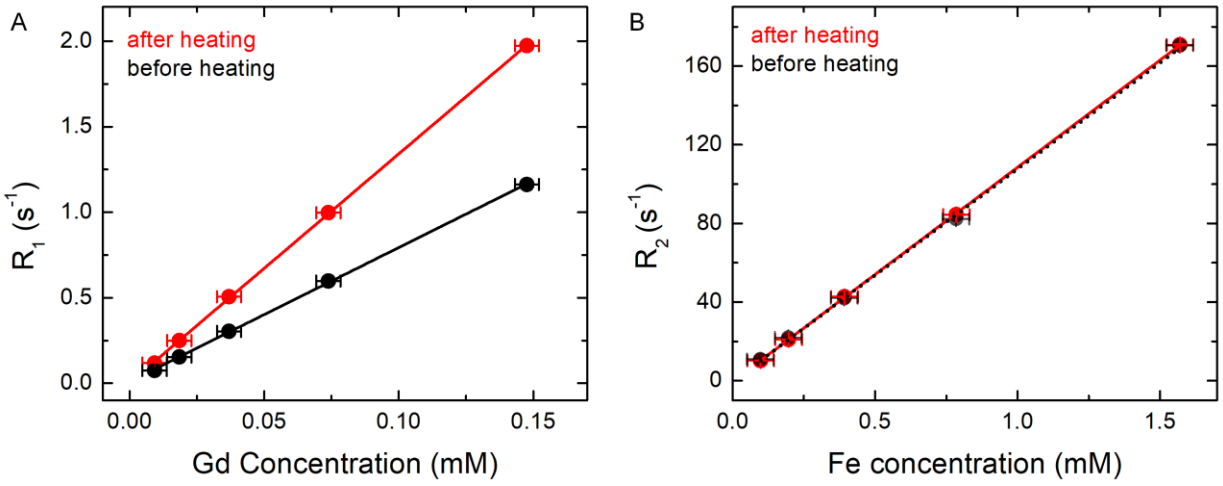

Figure 2.5. MR relaxation rates were measured at different dilutions before and after complete AMF heating. (A) R_1 versus Gd concentration before and after complete AMF heating. It shows the slope of the fitted linear plot before (black) r_1= 7.84 s^{-1} mM^{-1} (Gd) and after complete AMF heating (red) r_1 = 13.38 s^{-1} mM^{-1} (Gd). (B) R_2 versus Fe concentration before and after complete AMF heating. It shows the slope of the fitted linear plot before (black) r_2= 108.01 s^{-1} mM^{-1} (Fe) and after complete AMF heating (red) r_2=108.93 s^{-1} mM^{-1} (Fe). The uncertainties in R_1 and R_2 are < 1%, whereas the uncertainties in the concentration are ~ 5%.

before and after complete AMF heating. In **Figure 2.5A**, black and red lines show R_1 versus Gd concentration plots before and after complete AMF heating, respectively. The slope of the black line (before AMF heating) is r_1 =7.84 s^{-1} mM^{-1} , while the slope of the red line (after AMF heating) is r_1 = 13.38 s^{-1} mM^{-1}. In **Figure 2.5B**, we show the plots of R_2 versus Fe concentration both before (in black) and after (in red) complete AMF heating. It shows that the slopes of the red and black lines are r_2 = 108.93 s^{-1} mM^{-1} and 108.01 s^{-1} mM^{-1}, respectively, *i.e.* they are about equal. It is clear from the plots that AMF heating significantly affects the R_1 versus Gd concentration curve and increases r_1 of the AMF-treated sample by ≈ 70%, whereas the heating has almost no effect on the R_2 versus Fe concentration curve. Furthermore, the complete linear nature of the plots in **Figure 2.5** confirms that the changes in longitudinal relaxation rates, R_1, are mainly affected by Gd or

Gd(III)-DTPA concentration, and changes in transverse relaxation rates, R_2, are associated with Fe or SPIO concentration.

2.3.4. Monte Carlo spin dynamics simulations

Figure 2.6A shows the effect of liposome membrane permeability on R_2 for different inter-nanoparticle distances (D_{pp}) of the SPIO aggregates. Here, we define water permeability as the probability of a diffusing water magnetization striking the liposome membrane to cross the barrier

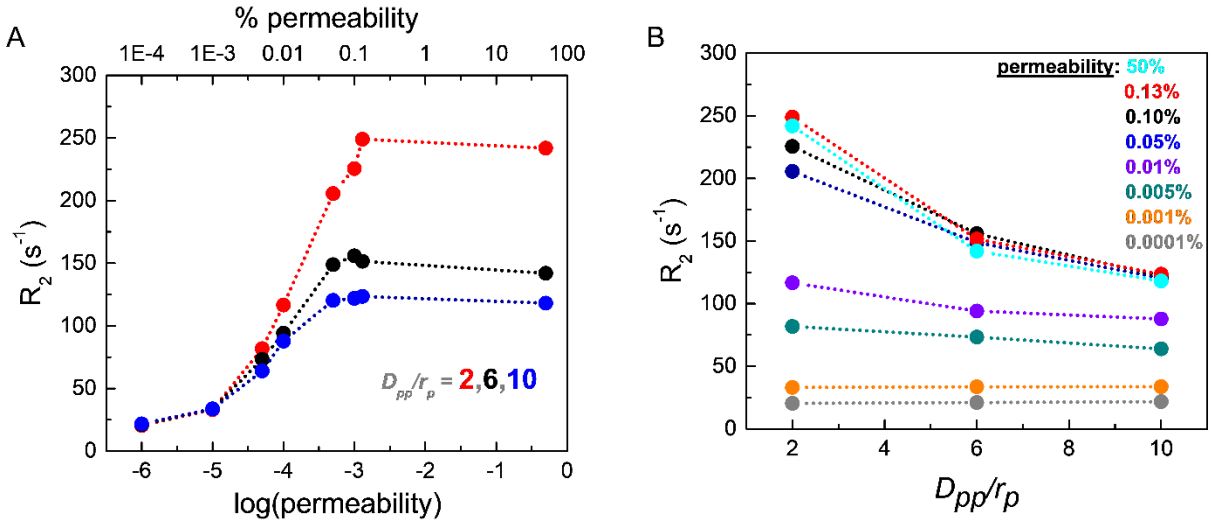

Figure 2.6. The effects of liposome membrane permeability and SPIO aggregation inside liposome on CPMG R_2 relaxation rates. (A) CPMG relaxation rates R_2 are plotted as a function of the liposome membrane permeability at three different aggregation states with D_{pp} (inter-SPIO nanoparticle distance) / r_p (single SPIO radius) = 2, 6, and 10, respectively. The radius of a single SPIO, r_p = 5 nm. (B) CPMG relaxation rates R_2 are plotted as a function of the degree of aggregation, Dpp/r_p, at different liposome membrane permeability conditions. The dotted lines through the points are included in each case as guides to the eye.

and enter inside the liposome. We have plotted membrane permeability versus R_2 for different values of D_{pp}/r_p (where r_p is the radius of a SPIO nanoparticle). Higher D_{pp} indicates weaker aggregation of SPIO and smaller D_{pp} implies stronger aggregation. We find from **Figure 2.6A** that the nature of variation of R_2 with permeability is qualitatively independent of D_{pp}/r_p. R_2 increases

sharply with permeability from 1×10^{-3} to 0.1% and saturates for permeability > 0.1%. Thus, even a small change in liposome membrane permeability in the range (1×10^{-3} to 0.1%) would result in a significant increase of R_2. As permeability increases, the water molecules are more likely to diffuse closer to the SPIO nanoparticles encapsulated inside the liposome and exchange faster with the "fresh" water magnetization outside the liposome, thus experiencing stronger fluctuating magnetic fields and resulting in a higher R_2 value, as seen in **Figure 2.6A**. **Figure 2.6B** shows the correlation between R_2 and D_{pp}/r_p for different liposome membrane permeabilities. We find that the liposome membrane with permeability higher than 1×10^{-3}% exhibits a significant drop in R_2 value with higher D_{pp}. However, the liposomes with membrane permeability less than 1×10^{-3}% do not show a noticeable change in R_2 for different degree of aggregation. The diffusing water magnetizations experience stronger dipolar magnetic fields when SPIO is in stronger aggregation state, compared to those in the weaker aggregation state where the resulting net SPIO dipolar field experienced by diffusing water magnetizations is partially cancelled by individual fields.[44,54]

We have estimated the chance of a diffusing water magnetization passing through the intact liposome membrane per collision would be between 0.001% and 0.01% under normal condition,[90,91] taking the thickness of liposome membrane ≈ 3 nm and the water permeability $10^{-1.95}$ cm/s. The liposome membrane undergoes reversible permeability change on heating,[88,89] and this change is significantly higher near the phospholipid phase transition temperature of ≈ 41°C.[44] In this experiment, we did the heating close to the transition temperature, leading to the possibility of significant permeability change of the synthesized thermosensitive liposome membrane. However, the R_2 measurements were done after cooling the sample to room temperature. Since the permeability change should be mostly reversible initially under mild heating, we do not expect any significant increase of the measured R_2 due to the change of membrane permeability at the initial

stage. On the other hand, during the process of AMF heating, as the membrane permeability increases, there should be higher access of water molecules inside the liposome, thus increasing D_{pp} and causing disaggregation of SPIO clusters. This change of the SPIO aggregation state inside the liposome should be retained when the solution is cooled to room temperature and cause a slight decrease of R_2 value initially. As the heating process is repeatedly continued, the change in the liposome membrane permeability might not be completely reversible upon cooling to room temperature, causing the R_2 value to rise. The interplay of these two opposing effects explains the observed initial small drop in R_2 and a subsequent slight increase, as seen in **Figure 2.4A** (black curve).

On the other hand, unencapsulated SPIO nanoparticles would be dispersed uniformly in the solution. Only a very small fraction can form aggregates under thermal equilibrium and the average value of D_{pp}/r_p is expected to be higher for such aggregates in the absence of any physical constraints like the liposome membrane to ensure that they remain close to one another. Hence, the R_2 value should decrease if all the SPIO nanoparticles are no longer enclosed by the liposome as a result of lysing with Triton X-100. Experimentally, we have observed ≈ 20% decrease in the R_2 value after lysing with Triton X-100 (data not shown) and this decrease is much higher than the initial 7%-drop in R_2 due to mild AMF heating. Since **Figure 2.4A** does not show any large drop (≈ 20%) in the R_2 value, we conclude that SPIO nanoparticles remain within the liposome enclosure during the mild AMF heating process.

We performed R_2 measurements at room temperature after cooling the sample, when the liposome membrane property should be largely restored. However, our simulation results (**Figure 2.6A**) predict a sharp increase in R_2 with small increase of the liposome membrane permeability.

Therefore, we expect to observe a significant increase in R_2 for *in situ* MRI measurements with AMF heating. Since liposomes could be efficiently functionalized to target the tumor site,[16,74] such *in situ* real-time MRI measurements with AMF heating opens up the possibility of high-resolution, high-contrast imaging of the tumor site during the MR theranostic process because of the large R_2 values.

In principle, the r_1 and r_2 relaxivities in spin systems with magnetic nanoparticles increase with temperature,[92] as both diffusion of the water ^1H spins and nanoparticle cluster size increase with temperature.[35] In our current study, however, such temperature-dependent effects may be ignored compared with the dominating permeability-dependent effect, due to the small temperature range used under mild hyperthermia condition and the fact that the magnetic nanoparticles are encapsulated inside the core of the liposome. On the other hand, the liposome membrane permeability changes significantly over the mild-hyperthermia temperature range, as the temperature above which the fluorescein drug release rate from this liposome increases rapidly is about 35°C (**Figure 2.3B**), although the phospholipid phase transition temperature for this liposome is 41°C.[44]

2.3.5. Future scope and application

While we have used liposomes with similar compositions to that used by Bos and coworkers,[44] we have incorporated a model cancer drug fluorescein to study controlled dose release at target site. Furthermore, we have used AMF controlled delivery, which safely allows deeper penetration inside human body compared to HIFU and increases the scope of treatment. Earlier studies[37,55] have shown that encapsulation of a cancer drug inside temperature-sensitive liposomes increases tumor drug concentrations and improves antitumor efficacy of the drugs. The

studies have shown 2-4 fold[40] and 2-16 fold[93] increase compared to non-heated condition, respectively. We have used a similar PEGylated temperature sensitive liposome and shown AMF controlled heating mechanism in relation to dosage delivery and carefully characterized MR relaxation parameters by encapsulating contrast agents at the same time. Hence, our study successfully extends previous studies to MR cancer theranostics. Moreover, at higher temperature, the permeability of liposome membrane increases. The simulations show that the R_2 parameter increases rapidly with the permeability of the liposome membrane, raising the possibility of getting high-quality MRI images, if MR measurements could be done during AMF heating at the elevated temperature.

In this study, we have used cargo fluorescein as a model cancer drug and established a detailed correlation between the magnetic heating stimulated cargo releases with MR relaxation parameters through experimental study and theoretical understanding. Previous extensive studies were done[75,76,94] to understand the rate of release of real cancer drugs at *in vitro* and *in vivo* conditions and the results have been well understood by different diffusion- and dissolution-based mathematical models (squared correlation coefficient near 1), such as the Reciprocal Powered Time (RPT) or Weibull (W) model.[75,76] Authors[76] found that *in vitro* and *in vivo* data could be best fitted in the RPT model, which is based on the general equation of dissolution and diffusion rate limited process $dw/dt = (D/h)\times S\times C_s$ under sink condition, where dw/dt is the rate of drug release, D is the drug molecule diffusion coefficient, S is the effective surface area of drug with release medium, C_s is solubility of the drug, and h is the length of diffusion path. Other studies found a good linear correlation between drug release in *in vitro* experiments with the drug absorption in *in vivo* experiments.[75] Hence, it is clear that the rate of real cancer drug release primarily depends on diffusion and solubility. The diffusion coefficient depends on the hydrodynamic size of the drug

molecule. It is well known that the hydrodynamic size of fluorescein is similar to many cancer drug molecules and therefore fluorescein was used as a model cancer drug in a large number of previous studies.[48,69–71]

Another important factor comes from the solubility of the drug, which depends on its particular nature, bonding, and hydrophobicity. For the poorly soluble cancer drugs, the rate of release would be slower and, accordingly, the AMF time could be adjusted depending on the exact clinical situation. However, the probability of encapsulation of a molecule in a liposome is also proportional to its solubility of the molecule in the medium, and hence correspondingly fewer cancer drug molecules would be encapsulated. As a result, the AMF driven percentage release of drug, *i.e.*, [(dw/dt)/w * 100], through diffusion of encapsulated molecules with different solubility would be similar. Hence, we expect qualitatively similar results for both model drug fluorescein and real cancer drug in *in vitro* or *in vivo* conditions, when the results are plotted as the percentage of drug release. Simultaneous release of Gd(III)-DTPA and fluorescein or the changes in aggregation status of SPIO are expected to remain unaltered for *in vivo* situation. Thus, the observed linear correlation between percentage drug release versus the percentage increase in R_1 can also be expected for real cancer drugs in clinical conditions, because the drug release process is essentially a diffusion process through a membrane. Similarly, the characteristic pattern of percentage changes in R_2 as a function of the percentage release of encapsulated drug would remain qualitatively the same for real cancer drugs in clinical condition. However, if the real drug would interact with the membrane of liposome or the process would not be diffusion, the results could be different. Nevertheless, for a large class of commonly used cancer drugs, the diffusion model holds and our results should remain valid for real cancer drugs in clinical conditions.

In this proof-of-concept study, we have focused on the effect of temperature on drug release. In a mild hyperthermia, blood perfusion and tumor oxygenation pattern change inhomogeneously and this change in local environment is very crucial for planning an effective treatment protocol. Various bioheat equations, tissue parameters, and temperature details should be taken into account to estimate tumor perfusion and changes in tumor local environment after employing mild heating. In this regard, many theoretical modeling and experiments were done[95–97] with real tumor. Future *in vivo* and clinical studies are required in this regard to implement the technique for clinical application.

2.4. Conclusions

Real-time visualization of nano-drug carrier biodistributions, drug release processes, and therapeutic responses could provide critical information to dynamically optimize treatment operations in precision medicine in real time. In this work, we have demonstrated a novel MR theranostic approach that could be combined with the established targeting capacity of liposomes to deliver and release cargo with spatial control by AMF heating and simultaneously monitor both the cargo release and condition of the liposomal sites. We have used appropriate sizes of liposome nanoparticles and shown that the cargo release from the liposomes by AMF-controlled mild hyperthermia could be quantified by measuring the longitudinal relaxation rate, R_1. We have confirmed that SPIO remained inside the liposome enclosure during AMF heating by observing that R_2 remained approximately constant during the heating process. Monte Carlo spin dynamics simulations provided qualitative explanations for the observed variations in R_2 during the AMF heating process and predicted a sharp increase in R_2 due to a small increase in the liposome

membrane permeability. The simulation results imply that real-time, *in-situ* MRI measurements with AMF heating could provide high-resolution, high-contrast image of the liposomal site during the heating process.

In conclusion, this work provides a proof of concept for monitoring cargo (cancer drugs) release with dosage control and liposomal site simultaneously by MRI technique. We have used clinically approved materials such as liposome, SPIO, and Gd(III)-DTPA in our experiments to accelerate the chance of getting readily accepted for pre-clinical or translational MR theranostics. Future work should be done *in vivo* with real drug molecules, with active targeting by magnetofection, and with real-time, *in-situ* MRI measurements and AMF heating.

Supplementary materials

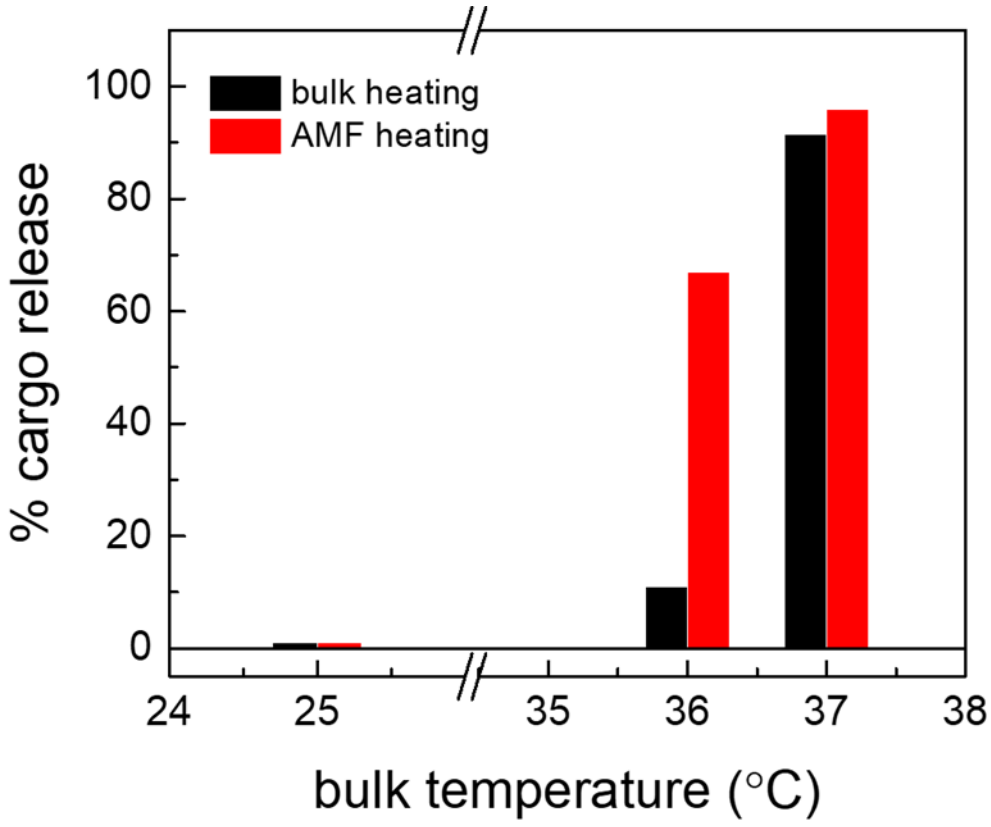

Figure S2.1. Comparison between AMF heating and thermal bath heating in the desired temperature range. Red bar indicates the percentage cargo release with AMF heating at different bulk temperatures, whereas the black bar indicates that for thermal bath heating. It shows there is no cargo release near room temperature from liposome, cargo release efficiency is significantly higher at 36°C, compared to bulk heating and finally both are saturating at 37°C.

Acknowledgements

This chapter is a reproduction of a manuscript submitted to the journal Nanotheranostics: Ray, S; Cheng, C-A; Chen, W; Li, Z; Zink, J; Lin, Y-Y. Magnetic Heating Stimulated Cargo Release with Dose Control using Multifunctional MR and Thermosensitive Liposome. I gratefully acknowledge my coauthors Ms. Chi-An Cheng, Mr. Wei Chen for helping in magnetic heating experiments, Dr. Zhao Li for help in experiments and performing computer simulations; Prof. Jeffrey Zink and Prof. Yung-Ya Lin for supervising this project. I would like to thank Mr. Ivo Atanasov, Dr. Peng Ge, Dr. Christian Beren for technical support and Prof. William Gelbart, Prof. Charles M. Knobler, Prof. Neil K. Garg, Prof. Andre Nel for lab facility. This work was supported by National Science Foundation (CHE-1112574, CHE-1416598), University of California Cancer Research Award (CRR-13-201412), and the Hirshberg Foundation for Pancreatic Cancer Research (YYL, ZL).

References

(1) Kelkar, S. S.; Reineke, T. M. Theranostics: Combining Imaging and Therapy. *Bioconjug. Chem.* **2011**, *22* (10), 1879–1903. https://doi.org/10.1021/bc200151q.

(2) Wang, H.; Li, X.; Tse, B. W.-C.; Yang, H.; Thorling, C. A.; Liu, Y.; Touraud, M.; Chouane, J. B.; Liu, X.; Roberts, M. S.; et al. Indocyanine Green-Incorporating Nanoparticles for Cancer Theranostics. *Theranostics* **2018**, *8* (5), 1227–1242. https://doi.org/10.7150/thno.22872.

(3) Janib, S. M.; Moses, A. S.; MacKay, J. A. Imaging and Drug Delivery Using Theranostic Nanoparticles. *Adv. Drug Deliv. Rev.* **2010**, *62* (11), 1052–1063. https://doi.org/10.1016/j.addr.2010.08.004.

(4) Wang, J.; Liu, L.; You, Q.; Song, Y.; Sun, Q.; Wang, Y.; Cheng, Y.; Tan, F.; Li, N. All-in-One Theranostic Nanoplatform Based on Hollow MoS_x for Photothermally-Maneuvered Oxygen Self-Enriched Photodynamic Therapy. *Theranostics* **2018**, *8* (4), 955–971. https://doi.org/10.7150/thno.22325.

(5) Sunderland, C. J.; Steiert, M.; Talmadge, J. E.; Derfus, A. M.; Barry, S. E. Targeted Nanoparticles for Detecting and Treating Cancer. *Drug Dev. Res.* **2006**, *67* (1), 70–93. https://doi.org/10.1002/ddr.20069.

(6) Tan, J.; Yang, N.; Zhong, L.; Tan, J.; Hu, Z.; Zhao, Q.; Gong, W.; Zhang, Z.; Zheng, R.; Lai, Z.; et al. A New Theranostic System Based on Endoglin Aptamer Conjugated Fluorescent Silica Nanoparticles. *Theranostics* **2017**, *7* (19), 4862–4876. https://doi.org/10.7150/thno.19101.

(7) Singh, R.; Lillard, J. W. Nanoparticle-Based Targeted Drug Delivery. *Exp. Mol. Pathol.* **2009**, *86* (3), 215–223. https://doi.org/10.1016/J.YEXMP.2008.12.004.

(8) Brannon-Peppas, L.; Blanchette, J. O. Nanoparticle and Targeted Systems for Cancer Therapy. *Adv. Drug Deliv. Rev.* **2012**, *64*, 206–212. https://doi.org/10.1016/J.ADDR.2012.09.033.

(9) Parekh, G.; Shi, Y.; Zheng, J.; Zhang, X.; Leporatti, S. Nano-Carriers for Targeted Delivery and Biomedical Imaging Enhancement. *Ther. Deliv.* **2018**, *9* (6), 451–468. https://doi.org/10.4155/tde-2018-0013.

(10) Hekman, M. C.; Rijpkema, M.; Muselaers, C. H.; Oosterwijk, E.; Hulsbergen-Van de Kaa, C. A.; Boerman, O. C.; Oyen, W. J.; Langenhuijsen, J. F.; Mulders, P. F. Tumor-Targeted Dual-Modality Imaging to Improve Intraoperative Visualization of Clear Cell Renal Cell Carcinoma: A First in Man Study. *Theranostics* **2018**, *8* (8), 2161–2170. https://doi.org/10.7150/thno.23335.

(11) Ashton, J. R.; Castle, K. D.; Qi, Y.; Kirsch, D. G.; West, J. L.; Badea, C. T. Dual-Energy

CT Imaging of Tumor Liposome Delivery After Gold Nanoparticle-Augmented Radiation Therapy. *Theranostics* **2018**, *8* (7), 1782–1797. https://doi.org/10.7150/thno.22621.

(12) Kong, X.; Dong, B.; Song, X.; Wang, C.; Zhang, N.; Lin, W. Dual Turn-on Fluorescence Signal-Based Controlled Release System for Real-Time Monitoring of Drug Release Dynamics in Living Cells and Tumor Tissues. *Theranostics* **2018**, *8* (3), 800–811. https://doi.org/10.7150/thno.21577.

(13) Slowing, I. I.; Vivero-Escoto, J. L.; Wu, C.-W.; Lin, V. S.-Y. Mesoporous Silica Nanoparticles as Controlled Release Drug Delivery and Gene Transfection Carriers. *Adv. Drug Deliv. Rev.* **2008**, *60* (11), 1278–1288. https://doi.org/10.1016/J.ADDR.2008.03.012.

(14) Kotb, S.; Detappe, A.; Lux, F.; Appaix, F.; Barbier, E. L.; Tran, V. L.; Plissonneau, M.; Gehan, H.; Lefranc, F.; Rodriguez-Lafrasse, C.; et al. Gadolinium-Based Nanoparticles and Radiation Therapy for Multiple Brain Melanoma Metastases: Proof of Concept before Phase I Trial. *Theranostics* **2016**, *6* (3), 418–427. https://doi.org/10.7150/thno.14018.

(15) Yen, S. K.; Padmanabhan, P.; Selvan, S. T. Multifunctional Iron Oxide Nanoparticles for Diagnostics, Therapy and Macromolecule Delivery. *Theranostics* **2013**, *3* (12), 986–1003. https://doi.org/10.7150/thno.4827.

(16) Hosta-Rigau, L.; Schattling, P.; Teo, B. M.; Lynge, M. E.; Städler, B. Recent Progress of Liposomes in Nanomedicine. *J. Mater. Chem. B* **2014**, *2* (39), 6686–6691. https://doi.org/10.1039/C4TB00825A.

(17) Béalle, G.; Di Corato, R.; Kolosnjaj-Tabi, J.; Dupuis, V.; Clément, O.; Gazeau, F.; Wilhelm, C.; Ménager, C. Ultra Magnetic Liposomes for MR Imaging, Targeting, and Hyperthermia. *Langmuir* **2012**, *28* (32), 11834–11842. https://doi.org/10.1021/la3024716.

(18) Pradhan, P.; Giri, J.; Rieken, F.; Koch, C.; Mykhaylyk, O.; Döblinger, M.; Banerjee, R.; Bahadur, D.; Plank, C. Targeted Temperature Sensitive Magnetic Liposomes for Thermo-Chemotherapy. *J. Control. Release* **2010**, *142* (1), 108–121. https://doi.org/10.1016/j.jconrel.2009.10.002.

(19) Mikhaylov, G.; Mikac, U.; Magaeva, A. A.; Itin, V. I.; Naiden, E. P.; Psakhye, I.; Babes, L.; Reinheckel, T.; Peters, C.; Zeiser, R.; et al. Ferri-Liposomes as an MRI-Visible Drug-Delivery System for Targeting Tumours and Their Microenvironment. *Nat. Nanotechnol.* **2011**, *6* (9), 594–602. https://doi.org/10.1038/nnano.2011.112.

(20) Amstad, E.; Kohlbrecher, J.; Müller, E.; Schweizer, T.; Textor, M.; Reimhult, E. Triggered Release from Liposomes through Magnetic Actuation of Iron Oxide Nanoparticle Containing Membranes. *Nano Lett.* **2011**, *11* (4), 1664–1670. https://doi.org/10.1021/nl2001499.

(21) Zhang, L.; Cui, H. HAase-Sensitive Dual-Targeting Irinotecan Liposomes Enhance the Therapeutic Efficacy of Lung Cancer in Animals. *Nanotheranostics* **2018**, *2* (3), 280–294.

https://doi.org/10.7150/ntno.25555.

(22) Knights-Mitchell, S. S.; Romanowski, M. Near-Infrared Activated Release of Doxorubicin from Plasmon Resonant Liposomes. *Nanotheranostics* **2018**, *2* (4), 295–305. https://doi.org/10.7150/ntno.22544.

(23) Koning, G. A.; Eggermont, A. M. M.; Lindner, L. H.; Ten Hagen, T. L. M. Hyperthermia and Thermosensitive Liposomes for Improved Delivery of Chemotherapeutic Drugs to Solid Tumors. *Pharm. Res.* **2010**, *27* (8), 1750–1754. https://doi.org/10.1007/s11095-010-0154-2.

(24) Allen, T. M.; Cullis, P. R. Liposomal Drug Delivery Systems: From Concept to Clinical Applications. *Adv. Drug Deliv. Rev.* **2013**, *65* (1), 36–48. https://doi.org/10.1016/J.ADDR.2012.09.037.

(25) Meunier, F.; Prentice, H. G.; Ringden, O. Liposomal Amphotericin B (AmBisome): Safety Data from a Phase II/III Clinical Trial. *J. Antimicrob. Chemother.* **1991**, *28* (suppl B), 83–91. https://doi.org/10.1093/jac/28.suppl_B.83.

(26) Morris, P. E.; Papadakos, P.; Russell, J. A.; Wunderink, R.; Schuster, D. P.; Truwit, J. D.; Vincent, J.-L.; Bernard, G. R. A Double-Blind Placebo-Controlled Study to Evaluate the Safety and Efficacy of L-2-Oxothiazolidine-4-Carboxylic Acid in the Treatment of Patients with Acute Respiratory Distress Syndrome*. *Crit. Care Med.* **2008**, *36* (3), 782–788. https://doi.org/10.1097/CCM.0B013E318164E7E4.

(27) Rahman, A.; Treat, J.; Roh, J. K.; Potkul, L. A.; Alvord, W. G.; Forst, D.; Woolley, P. V. A Phase I Clinical Trial and Pharmacokinetic Evaluation of Liposome-Encapsulated Doxorubicin. *J. Clin. Oncol.* **1990**, *8* (6), 1093–1100. https://doi.org/10.1200/JCO.1990.8.6.1093.

(28) Delanian, S.; Baillet, F.; Huart, J.; Lefaix, J.-L.; Maulard, C.; Housset, M. Successful Treatment of Radiation-Induced Fibrosis Using Liposomal CuZn Superoxide Dismutase: Clinical Trial. *Radiother. Oncol.* **1994**, *32* (1), 12–20. https://doi.org/10.1016/0167-8140(94)90444-8.

(29) Hortobagyi, G. N.; Ueno, N. T.; Xia, W.; Zhang, S.; Wolf, J. K.; Putnam, J. B.; Weiden, P. L.; Willey, J. S.; Carey, M.; Branham, D. L.; et al. Cationic Liposome-Mediated E1A Gene Transfer to Human Breast and Ovarian Cancer Cells and Its Biologic Effects: A Phase I Clinical Trial. *J. Clin. Oncol.* **2001**, *19* (14), 3422–3433. https://doi.org/10.1200/JCO.2001.19.14.3422.

(30) Northfelt, D. W.; Dezube, B. J.; Thommes, J. A.; Miller, B. J.; Fischl, M. A.; Friedman-Kien, A.; Kaplan, L. D.; Du Mond, C.; Mamelok, R. D.; Henry, D. H. Pegylated-Liposomal Doxorubicin versus Doxorubicin, Bleomycin, and Vincristine in the Treatment of AIDS-Related Kaposi's Sarcoma: Results of a Randomized Phase III Clinical Trial. *J. Clin. Oncol.* **1998**, *16* (7), 2445–2451. https://doi.org/10.1200/JCO.1998.16.7.2445.

(31) Alberts, D. S.; Muggia, F. M.; Carmichael, J.; Winer, E. P.; Jahanzeb, M.; Venook, A. P.; Skubitz, K. M.; Rivera, E.; Sparano, J. A.; Dibella, N. J.; et al. Efficacy and Safety of Liposomal Anthracyclines in Phase I/II Clinical Trials. *Semin. Oncol.* **2004**, *31*, 53–90. https://doi.org/10.1053/J.SEMINONCOL.2004.08.010.

(32) Field, S. B.; Bleehen, N. M. Hyperthermia in the Treatment of Cancer. *Cancer Treat. Rev.* **1979**, *6*, 63–94.

(33) Wust, P.; Hildebrandt, B.; Sreenivasa, G.; Rau, B.; Gellermann, J.; Riess, H.; Felix, R.; Schlag, P. Hyperthermia in Combined Treatment of Cancer. *Lancet Oncol.* **2002**, *3* (8), 487–497. https://doi.org/10.1016/S1470-2045(02)00818-5.

(34) Tagami, T.; Foltz, W. D.; Ernsting, M. J.; Lee, C. M.; Tannock, I. F.; May, J. P.; Li, S. D. MRI Monitoring of Intratumoral Drug Delivery and Prediction of the Therapeutic Effect with a Multifunctional Thermosensitive Liposome. *Biomaterials* **2011**, *32* (27), 6570–6578. https://doi.org/10.1016/j.biomaterials.2011.05.029.

(35) Wang, C.; Hsu, C. H.; Li, Z.; Hwang, L. P.; Lin, Y. C.; Chou, P. T.; Lin, Y. Y. Effective Heating of Magnetic Nanoparticle Aggregates for in Vivo Nano-Theranostic Hyperthermia. *Int. J. Nanomedicine* **2017**, *12*, 6273–6287. https://doi.org/10.2147/IJN.S141072.

(36) Clavel, C. M.; Nowak-Sliwinska, P.; Pəunescu, E.; Griffioen, A. W.; Dyson, P. J. In Vivo Evaluation of Small-Molecule Thermoresponsive Anticancer Drugs Potentiated by Hyperthermia. *Chem. Sci.* **2015**, *6* (5), 2795–2801. https://doi.org/10.1039/c5sc00613a.

(37) Ponce, A. M.; Vujaskovic, Z.; Yuan, F.; Needham, D.; Dewhirst, M. W. Hyperthermia Mediated Liposomal Drug Delivery. *Int. J. Hyperth.* **2006**, *22* (3), 205–213. https://doi.org/10.1080/02656730600582956.

(38) Unezaki, S.; Maruyama, K.; Takahashi, N.; Koyama, M.; Yuda, T.; Suginaka, A.; Iwatsuru, M. Enhanced Delivery and Antitumor Activity of Doxorubicin Using Long-Circulating Thermosensitive Liposomes Containing Amphipathic Polyethylene Glycol in Combination with Local Hyperthermia. *Pharm. Res.* **1994**, *11* (8), 1180–1185. https://doi.org/10.1023/A:1018949218380.

(39) Needham, D.; Anyarambhatla, G.; Kong, G.; Dewhirst, M. W. A New Temperature-Sensitive Liposome for Use with Mild Hyperthermia: Characterization and Testing in a Human Tumor Xenograft Model. *Cancer Res.* **2000**, *60* (5), 1197–1201.

(40) Kong, G.; Braun, R. D. R. D.; Dewhirst, M. M. W.; Braun, R. D. R. D.; Colvin, O. M.; Needham, D.; Dewhirst, M. M. W. Hyperthermia Enables Tumor-Specific Nanoparticle Delivery: Effect of Particle Size. *Cancer Res.* **2000**, *60* (16), 4440–4445.

(41) Lin, F.; Hsu, C.-H.; Lin, Y. Nano-Therapeutic Cancer Immunotherapy Using Hyperthermia-Induced Heat Shock Proteins: Insights from Mathematical Modeling. *Int. J. Nanomedicine* **2018**, *13* (June), 1–11.

(42) Boissenot, T.; Bordat, A.; Fattal, E.; Nicolas, T. Ultrasound-Triggered Drug Delivery for Cancer Treatment Using Drug Delivery Systems: From Theoretical Considerations to Practical Applications. *J. Control. Release* **2016**, *241*, 144–163.

(43) Ranjan, A.; Jacobs, G. C.; Woods, D. L.; Negussie, A. H.; Partanen, A.; Yarmolenko, P. S.; Gacchina, C. E.; Sharma, K. V.; Frenkel, V.; Wood, B. J.; et al. Image-Guided Drug Delivery with Magnetic Resonance Guided High Intensity Focused Ultrasound and Temperature Sensitive Liposomes in a Rabbit Vx2 Tumor Model. *J. Control. Release* **2012**, *158* (3), 487–494. https://doi.org/10.1016/j.jconrel.2011.12.011.

(44) Lorenzato, C.; Oerlemans, C.; van Elk, M.; Geerts, W. J. C.; Denis de Senneville, B.; Moonen, C.; Bos, C. MRI Monitoring of Nanocarrier Accumulation and Release Using Gadolinium-SPIO Co-Labelled Thermosensitive Liposomes. *Contrast Media Mol. Imaging* **2016**, *11* (3), 184–194. https://doi.org/10.1002/cmmi.1679.

(45) Tai, L. A.; Tsai, P. J.; Wang, Y. C.; Wang, Y. J.; Lo, L. W.; Yang, C. S. Thermosensitive Liposomes Entrapping Iron Oxide Nanoparticles for Controllable Drug Release. *Nanotechnology* **2009**, *20* (13). https://doi.org/10.1088/0957-4484/20/13/135101.

(46) Thomas, C. R.; Ferris, D. P.; Lee, J.; Choi, E.; Cho, M. H.; Kim, E. S.; Stoddart, J. F.; Shin, J.; Cheon, J.; Zink, J. I. Noninvasive Remote Controlled Release of Drug Molecules in Vitro Using Magnetic Actuation of Mechanised Nanoparticles. *J. Am. Chem. Soc.* **2010**, *132*, 10623–10625.

(47) Saint-Cricq, P.; Deshayes, S.; Zink, J. I.; Kasko, A. M. Magnetic Field Activated Drug Delivery Using Thermodegradable Azo-Functionalised PEG-Coated Core-Shell Mesoporous Silica Nanoparticles. *Nanoscale* **2015**, *7* (31), 13168–13172. https://doi.org/10.1039/c5nr03777h.

(48) Rühle, B.; Datz, S.; Argyo, C.; Bein, T.; Zink, J. I. A Molecular Nanocap Activated by Superparamagnetic Heating for Externally Stimulated Cargo Release. *Chem. Commun.* **2016**, *52* (9), 1843–1846. https://doi.org/10.1039/C5CC08636A.

(49) Banks, W. A.; Gray, A. M.; Erickson, M. A.; Salameh, T. S.; Damodarasamy, M.; Sheibani, N.; Meabon, J. S.; Wing, E. E.; Morofuji, Y.; Cook, D. G.; et al. Alternating Magnetic Field-Induced Hyperthermia Increases Iron Oxide Nanoparticle Cell Association/Uptake and Flux in Blood– Brain Barrier Models. *Pharm. Res.* **2015**, *32* (5), 1615–1625. https://doi.org/10.1007/978-1-4614-5915-6.

(50) Song, X.; Han, X.; Yu, F.; Zhang, X.; Chen, L.; Lv, C. Polyamine-Targeting Gefitinib Prodrug and Its Near-Infrared Fluorescent Theranostic Derivative for Monitoring Drug Delivery and Lung Cancer Therapy. *Theranostics* **2018**, *8* (8), 2217–2228. https://doi.org/10.7150/thno.24041.

(51) Li, X.; Schumann, C.; Albarqi, H. A.; Lee, C. J.; Alani, A. W. G.; Bracha, S.; Milovancev, M.; Taratula, O.; Taratula, O. A Tumor-Activatable Theranostic Nanomedicine Platform

for NIR Fluorescence-Guided Surgery and Combinatorial Phototherapy. *Theranostics* **2018**, *8* (3), 767–784. https://doi.org/10.7150/thno.21209.

(52) Langereis, S.; Hijnen, N.; Strijkers, G.; Nicolay, K.; Grüll, H. Research Spotlight: Multifunctional Liposomes for MRI and Image-Guided Drug Delivery. *Ther. Deliv.* **2014**, *5* (1), 21–24. https://doi.org/10.4155/tde.13.128.

(53) Ho, L. C.; Hsu, C. H.; Ou, C. M.; Wang, C. W.; Liu, T. P.; Hwang, L. P.; Lin, Y. Y.; Chang, H. T. Unibody Core-Shell Smart Polymer as a Theranostic Nanoparticle for Drug Delivery and MR Imaging. *Biomaterials* **2015**, *37*, 436–446. https://doi.org/10.1016/j.biomaterials.2014.10.006.

(54) Lorenzato, C.; Cernicanu, A.; Meyre, M. E.; Germain, M.; Pottier, A.; Levy, L.; de Senneville, B. D.; Bos, C.; Moonen, C.; Smirnov, P. MRI Contrast Variation of Thermosensitive Magnetoliposomes Triggered by Focused Ultrasound: A Tool for Image-Guided Local Drug Delivery. *Contrast Media Mol. Imaging* **2013**, *8* (2), 185–192. https://doi.org/10.1002/cmmi.1515.

(55) Ponce, A. M.; Viglianti, B. L.; Yu, D.; Yarmolenko, P. S.; Michelich, C. R.; Woo, J.; Bally, M. B.; Dewhirst, M. W. Magnetic Resonance Imaging of Temperature-Sensitive Liposome Release: Drug Dose Painting and Antitumor Effects. *JNCI J. Natl. Cancer Inst.* **2007**, *99* (1), 53–63. https://doi.org/10.1093/jnci/djk005.

(56) Talanov, V. S.; Regino, C. A. S.; Kobayashi, H.; Bernardo, M.; Choyke, P. L.; Brechbiel, M. W. Dendrimer-Based Nanoprobe for Dual Modality Magnetic Resonance and Fluorescence Imaging. *Nano Lett.* **2006**, *6* (7), 1459–1463. https://doi.org/10.1021/nl060765q.

(57) Wen, S.; Li, K.; Cai, H.; Chen, Q.; Shen, M.; Huang, Y.; Peng, C.; Hou, W.; Zhu, M.; Zhang, G.; et al. Multifunctional Dendrimer-Entrapped Gold Nanoparticles for Dual Mode CT/MR Imaging Applications. *Biomaterials* **2013**, *34* (5), 1570–1580. https://doi.org/10.1016/j.biomaterials.2012.11.010.

(58) Luo, Y.; Zhao, L.; Li, X.; Yang, J.; Guo, L.; Zhang, G.; Shen, M.; Zhao, J.; Shi, X. The Design of a Multifunctional Dendrimer-Based Nanoplatform for Targeted Dual Mode SPECT/MR Imaging of Tumors. *J. Mater. Chem. B* **2016**, *4* (45), 7220–7225. https://doi.org/10.1039/c6tb02190e.

(59) Haribabu, V.; Farook, A. S.; Goswami, N.; Murugesan, R.; Girigoswami, A. Optimized Mn-Doped Iron Oxide Nanoparticles Entrapped in Dendrimer for Dual Contrasting Role in MRI. *J. Biomed. Mater. Res. - Part B Appl. Biomater.* **2016**, *104* (4), 817–824. https://doi.org/10.1002/jbm.b.33550.

(60) Szpak, A.; Fiejdasz, S.; Prendota, W.; Strączek, T.; Kapusta, C.; Szmyd, J.; Nowakowska, M.; Zapotoczny, S. T1-T2 Dual-Modal MRI Contrast Agents Based on Superparamagnetic Iron Oxide Nanoparticles with Surface Attached Gadolinium

Complexes. *J. Nanoparticle Res.* **2014**, *16* (11), 1–11. https://doi.org/10.1007/s11051-014-2678-6.

(61) Zhou, Z.; Huang, D.; Bao, J.; Chen, Q.; Liu, G.; Chen, Z.; Chen, X.; Gao, J. A Synergistically Enhanced T_1 - T_2 Dual-Modal Contrast Agent. *Adv. Mater.* **2012**, *24* (46), 6223–6228. https://doi.org/10.1002/adma.201203169.

(62) Hu, F.; Zhao, Y. S. Inorganic Nanoparticle-Based T1 and T1/T2 Magnetic Resonance Contrast Probes. *Nanoscale* **2012**, *4* (20), 6235. https://doi.org/10.1039/c2nr31865b.

(63) Jung, H.; Park, B.; Lee, C.; Cho, J.; Suh, J.; Park, J. Y.; Kim, Y. R.; Kim, J.; Cho, G.; Cho, H. J. Dual MRI T1and T2(*)Contrast with Size-Controlled Iron Oxide Nanoparticles. *Nanomedicine Nanotechnology, Biol. Med.* **2014**, *10* (8), 1679–1689. https://doi.org/10.1016/j.nano.2014.05.003.

(64) Soenen, S. J. H.; Desender, L.; De Cuyper, M. Complexation of Gadolinium(III) Ions on Top of Nanometre-Sized Magnetoliposomes. *Int. J. Environ. Anal. Chem.* **2007**, *87* (10–11), 783–796. https://doi.org/10.1080/03067310701336320.

(65) Shin, T.; Choi, J.; Yun, S.; Kim, I.; Song, H.; Kim, Y. T 1 and T 2 Dual-Mode MRI Contrast Agent for Enhancing Accuracy by Engineered Nanomaterials. *ACS Nano* **2014**, *8* (4), 3393–3401. https://doi.org/10.1021/nn405977t.

(66) Estelrich, J.; Sánchez-Martín, M. J.; Busquets, M. A. Nanoparticles in Magnetic Resonance Imaging: From Simple to Dual Contrast Agents. *Int. J. Nanomedicine* **2015**, *10*, 1727–1741. https://doi.org/10.2147/IJN.S76501.

(67) De Cuyper, M.; Soenen, S. J. H.; Coenegrachts, K.; Beek, L. Ter. Surface Functionalization of Magnetoliposomes in View of Improving Iron Oxide-Based Magnetic Resonance Imaging Contrast Agents: Anchoring of Gadolinium Ions to a Lipophilic Chelate. *Anal. Biochem.* **2007**, *367* (2), 266–273. https://doi.org/10.1016/j.ab.2007.05.006.

(68) Chen, J.; Zhang, W. J.; Guo, Z.; Wang, H. B.; Wang, D. D.; Zhou, J. J.; Chen, Q. W. PH-Responsive Iron Manganese Silicate Nanoparticles as T1- T2∗ Dual-Modal Imaging Probes for Tumor Diagnosis. *ACS Appl. Mater. Interfaces* **2015**, *7* (9), 5373–5383. https://doi.org/10.1021/acsami.5b00727.

(69) Huang, H. L.; Lu, P. H.; Yang, H. C.; Lee, G. Da; Li, H. R.; Liao, K. C. Fiber-Optic Triggered Release of Liposome in Vivo: Implication of Personalized Chemotherapy. *Int. J. Nanomedicine* **2015**, *10* (May), 5171–5185. https://doi.org/10.2147/IJN.S85915.

(70) Paris, J. L.; Cabañas, M. V.; Manzano, M.; Vallet-Regí, M. Polymer-Grafted Mesoporous Silica Nanoparticles as Ultrasound-Responsive Drug Carriers. *ACS Nano* **2015**, *9* (11), 11023–11033. https://doi.org/10.1021/acsnano.5b04378.

(71) Niesman, M. R.; Khoobehi, B.; Peyman, G. A. Encapsulation of Sodium Fluorescein for

Dye Release Studies. *Investig. Ophthalmol. Vis. Sci.* **1992**, *33* (7), 2113–2119.

(72) Al-Jamal, K. T.; Bai, J.; Wang, J. T.-W.; Protti, A.; Southern, P.; Bogart, L.; Heidari, H.; Li, X.; Cakebread, A.; Asker, D.; et al. Magnetic Drug Targeting: Preclinical in Vivo Studies, Mathematical Modeling, and Extrapolation to Humans. *Nano Lett.* **2016**, *16* (9), 5652–5660. https://doi.org/10.1021/acs.nanolett.6b02261.

(73) T-w, J.; Bai, J.; T-W Wang, J.; Rubio, N.; Protti, A.; Heidari, H.; Elgogary, R.; Southern, P.; Al-Jamal, T.; Sosabowski, J.; et al. Triple-Modal Imaging of Magnetically-Targeted Nanocapsules in Solid Tumours In Vivo. *Theranostics* **2016**, *6*, 3. https://doi.org/10.7150/thno.11918.

(74) Takeda, K.; Kobari, M.; Akaishi, S.; Matsuno, S. Targeting Pancreatic Chemotherapy Cancer Using Liposome against Antibody-Combined. *J. Exp. Med.* **1994**, *175*, 29–42.

(75) D'Souza, S. A Review of In Vitro Drug Release Test Methods for Nano-Sized Dosage Forms. *Adv. Pharm.* **2014**, *2014*, 1–12. https://doi.org/10.1155/2014/304757.

(76) Barzegar-Jalali, M.; Adibkia, K.; Valizadeh, H.; Shadbad, M. R. S.; Nokhodchi, A.; Omidi, Y.; Mohammadi, G.; Nezhadi, S. H.; Hasan, M.; Reza, M.; et al. Kinetic Analysis of Drug Release from Nanoparticles. *J. Pharm. Pharm. Sci.* **2008**, *11* (1), 167–177.

(77) Beren, C. E. *ABSTRACT OF DISSERTATION Effect of Secondary Structure on the Size, Configurational Statistics, and Packaging of Long-RNA by Viral Capsid Protein*; 2017.

(78) Liang, Z.-P.; Lauterbur, P. C.; IEEE Engineering in Medicine and Biology Society. *Principles of Magnetic Resonance Imaging : A Signal Processing Perspective*; SPIE Optical Engineering Press, 2000.

(79) Nel, A.; Ruoslahti, E.; Meng, H. New Insights into "Permeability" as in the Enhanced Permeability and Retention Effect of Cancer Nanotherapeutics. *ACS Nano* **2017**, *11* (10), 9567–9569. https://doi.org/10.1021/acsnano.7b07214.

(80) Fang, J.; Nakamura, H.; Maeda, H. The EPR Effect: Unique Features of Tumor Blood Vessels for Drug Delivery, Factors Involved, and Limitations and Augmentation of the Effect. *Adv. Drug Deliv. Rev.* **2011**, *63* (3), 136–151. https://doi.org/10.1016/j.addr.2010.04.009.

(81) Merbach, A. E.; Helm, L.; Tóth, E. *The Chemistry of Contrast Agents in Medical Magnetic Resonance Imaging*, 2nd ed.; Wiley: Chichester, UK, 2013. https://doi.org/10.1002/9781118503652.

(82) Yang, C.; City, T. (19) United States (12) Patent Application Publication (10) Pub . No .: US 2009 / 0004258 A1 I05. **2009**, *1* (19).

(83) Dong, J.; Zink, J. I. Taking the Temperature of the Interiors of Magnetically Heated Nanoparticles. *ACS Nano* **2014**, *8* (5), 5199–5207. https://doi.org/10.1021/nn501250e.

(84) Vetrone, F.; Naccache, R.; Zamarrón, A.; Juarranz de la Fuente, A.; Sanz-Rodríguez, F.;

Martinez Maestro, L.; Martín Rodriguez, E.; Jaque, D.; García Solé, J.; Capobianco, J. A. Temperature Sensing Using Fluorescent Nanothermometers. *ACS Nano* **2010**, *4* (6), 3254–3258. https://doi.org/10.1021/nn100244a.

(85) Ye, F.; Wu, C.; Jin, Y.; Chan, Y.-H.; Zhang, X.; Chiu, D. T. Ratiometric Temperature Sensing with Semiconducting Polymer Dots. *J. Am. Chem. Soc.* **2011**, *133* (21), 8146–8149. https://doi.org/10.1021/ja202945g.

(86) Freddi, S.; Sironi, L.; D'Antuono, R.; Morone, D.; Donà, A.; Cabrini, E.; D'Alfonso, L.; Collini, M.; Pallavicini, P.; Baldi, G.; et al. A Molecular Thermometer for Nanoparticles for Optical Hyperthermia. *Nano Lett.* **2013**, *13* (5), 2004–2010. https://doi.org/10.1021/nl400129v.

(87) Polo-Corrales, L.; Rinaldi, C. Monitoring Iron Oxide Nanoparticle Surface Temperature in an Alternating Magnetic Field Using Thermoresponsive Fluorescent Polymers. *J. Appl. Phys.* **2012**, *111* (7), 07B334. https://doi.org/10.1063/1.3680532.

(88) Eze, M. O. Phase Transitions in Phospholipid Bilayers: Lateral Phase Separations Play Vital Roles in Biomembranes. *Biochem. Educ.* **1991**, *19* (4), 204–208.

(89) Forbes, N.; Pallaoro, A.; Reich, N. O.; Zasadzinski, J. A. Rapid, Reversible Release from Thermosensitive Liposomes Triggered by Near-Infra-Red Light. *Part. Part. Syst. Charact.* **2014**, *31* (11), 1158–1167. https://doi.org/10.1016/j.semcancer.2015.04.010.Targeting.

(90) Paula, S.; Volkov, A. G.; Van Hoek, A. N.; Haines, T. H.; Deamer, D. W. *Permeation of Protons, Potassium Ions, and Small Polar Molecules Through Phospholipid Bilayers as a Function of Membrane Thickness*; 1996; Vol. 70.

(91) Huster, D.; Jin, A. J.; Arnold, K.; Gawrisch, K. *Water Permeability of Polyunsaturated Lipid Membranes Measured by 170 NMR*; 1997; Vol. 73. https://doi.org/10.1016/S0006-3495(97)78118-9.

(92) Issa, B.; Obaidat, I. M.; Hejasee, R. H.; Qadri, S.; Haik, Y. NMR Relaxation in Systems with Magnetic Nanoparticles: A Temperature Study. *J. Magn. Reson. Imaging* **2014**, *39* (3), 648–655. https://doi.org/10.1002/jmri.24197.

(93) Matteucci, M.; Anyarambhatla, G.; Rosner, G.; Azuma, C. Hyperthermia Increases Accumulation of Technetium-99m-Labeled Liposomes in Feline Sarcomas. *Clin Cancer Res* **2000**, *6*, 3748–3755.

(94) Park, K.; Lee, G. Y.; Kim, Y. S.; Yu, M.; Park, R. W.; Kim, I. S.; Kim, S. Y.; Byun, Y. Heparin-Deoxycholic Acid Chemical Conjugate as an Anticancer Drug Carrier and Its Antitumor Activity. *J. Control. Release* **2006**, *114* (3), 300–306. https://doi.org/10.1016/j.jconrel.2006.05.017.

(95) Oleson, J. R.; Dewhirst, M. W.; Harrelson, J. M.; Leopold, K. A.; Samulski, T. V; Tso, C. Y. Tumor Temperature Distributions Predict Hyperthermia Effect. *Int. J. Radiat. Oncol.*

Biol. Phys. **1989**, *16* (3), 559–570. https://doi.org/10.1016/0360-3016(89)90472-0.

(96) Cho, C. H.; Sreenivasa, G.; Plotkin, M.; Pietsch, H.; Wust, P.; Ldemann, L. Tumour Perfusion Assessment during Regional Hyperthermia Treatment: Comparison of Temperature Probe Measurement with H215O-PET Perfusion. *Int. J. Hyperth.* **2010**, *26* (4), 404–411. https://doi.org/10.3109/02656731003605662.

(97) Sun, X.; Xing, L.; Clifton Ling, C.; Li, G. C. The Effect of Mild Temperature Hyperthermia on Tumour Hypoxia and Blood Perfusion: Relevance for Radiotherapy, Vascular Targeting and Imaging. *Int. J. Hyperth.* **2010**, *26* (3), 224–231. https://doi.org/10.3109/02656730903479855.

Chapter 3

High-contrast Background-free Magnetic Resonance Molecular Imaging

Abstract

One of the holy grails in cancer detection and therapy is to simultaneously image and deliver drugs to the tumor site using a safe nanoparticle. Liposomes are well-known safe and stable nanoparticles that can be loaded with a drug and suitable contrast agent for magnetic resonance imaging (MRI). However, the loading of a contrast agent such as gadolinium in liposomes generally results in poor contrast and various artifacts in *in vivo* experiments, compared to free gadolinium chelate experiments. Current work demonstrates the effective filtering of artifacts and contrast enhancement to obtain high quality images of the tumor sites in mouse models using a paramagnetic liposome, a novel pulse sequence in active-feedback MRI, and robust data analysis. Our results show a significant improvement in eliminating artifacts and increasing contrast compared to the standard MRI techniques, and a close correlation with histopathology and inductively coupled mass spectrometry results. This newly developed protocol could be used for any paramagnetic nanoparticle to improve detection sensitivity. We expect this methodology to produce similar improvements in human imaging, having the potential to significantly improve early tumor detection in clinical practice.

3.1. Introduction

Magnetic resonance imaging (MRI) is a non-invasive tool to obtain high-resolution anatomical images of a tumor site. Recent advances[1–4] in targeting a tumor site by nanoparticles such as liposomes[5–7] carrying both drug and an MRI contrast agent have added a new dimension in cancer therapy. The possibility of online monitoring of the tumor site during the drug release process, as well as the detection of early tumors, would significantly improve the prognosis of cancer patients. However, MR imaging suffers from poor contrast and the problem of artifacts that originate from calcification, fat, hemorrhage, blood clots etc., mimicking MRI signals from the contrast agent.[8] The problem is further aggravated when the imaging is performed by loading the contrast agent in a nanoparticle such as a liposome for theranostic applications.

Biocompatibility, size controllability, and functional versatility make liposomes ideal nanovehicles for carrying and delivering cargo inside the human body. Such self-assembled spherical lipid bilayer are already clinically approved[5,6,9–12] and are capable of carrying both hydrophilic and hydrophobic drugs in their aqueous core and in lipid membrane respectively. Liposomal nanoparticles can be modified into *in vivo* long-circulating nanovehicles by engineering them with a conjugating moiety and polyethylene glycol (PEG) for active and passive targeting, respectively. Gd^{3+} chelates have been extensively studied in the past and a couple of them have been approved as MRI contrast agents for clinical use. However, for theranostic use, Gd^{3+} chelates have to be encapsulated in a nanoparticle such as a liposome that can simultaneously carry drug molecules and target the tumor site. Moreover, the toxicity of Gd^{3+} for renal patients could be somewhat alleviated by its encapsulation in liposomes. On the other hand, the encapsulation of Gd^{3+} restricts the relaxivity of the contrast agent compared to the free chelate due to limited water

flux between the aqueous core and the outside bulk water,[13–16] resulting in limited contrast and the problem of artifacts in the conventional T_1-weighted images. There have been many efforts to solve these problems in previous studies,[13,16–18] such as optimizing the size of the liposomes, increasing the load of Gd^{3+}- chelates, etc., however the problem still exists.

Contrast in conventional MRI techniques largely depends on the differing molecular dynamics of different tissues, resulting in variations of the relaxation times of the signal.[19] These imaging techniques have limited efficiency to differentiate between tissues or materials with only a slight difference in the relaxation parameters. The online monitoring of the tumor or the detection of the early tumors is associated with a slight shift in magnetic susceptibility and conventional MR imaging techniques often fail to identify such small changes. This meager shift in the local field is independent of molecular dynamics and is thus essentially invisible to the conventional relaxation-based imaging mechanisms such as T_1, T_2 or T_2^*.[19,20] Another related methodology, susceptibility-weighted imaging (SWI)[21] is a post-processing technique where further enhancement of the contrast is achieved by applying phase mapping to the T_2* images. However, SWI struggles in cases where T_2^* decays limit the amount of phase shift, or where the resonance offset change across the imaging plane is inadequate. Hence, a highly sensitive and safer MRI approach capable of theranostic application is highly desirable for the online monitoring of the tumor during the drug release process at the tumor site and also for detecting early tumors.

It was demonstrated previously that the use of the radiation damping feedback field, a nonlinear approach that relied on Lenz's law, could enhance the contrast by amplifying a small magnetic difference of the system.[22–26] In general, radiation damping effects are more pronounced in a high-field condition, but an active-feedback circuit can produce the same effect in a low

magnetic field. A small change in the magnetization is collected and fed back into the sample in a loop during the evolution of the magnetization. Such nonlinear dynamics are highly sensitive to the initial magnetization conditions, and in some cases produce chaotic dynamics.[23] The selective nature of this active-feedback field has been found to magnify the contrast between tissues with only a slight variation in magnetic properties.[24–28] However, the reactionary nature of the previously used active-feedback[27,29–36] pulse sequence efficiently return the sample magnetization back to its equilibrium orientation on a short time scale and limits the extent of the contrast by restricting its nonlinear evolution.

In this work, we have designed a new pulse sequence by introducing a continuous-wave (CW) radio-frequency field in the presence of an active-feedback field to extend the nonlinear evolution of magnetization over time. This improved pulse sequence having a CW component can stabilize and preserve the contrast against decay, and can ameliorate the sensitivity of the active-feedback method. We find from theoretical simulations of the active-feedback process that the new pulse sequence produces a characteristic biexponential temporal variation of the longitudinal magnetization in the difference images between the proton spins with and without Gd-liposomes. We have used the difference imaging technique with and without Gd-liposome (paramagnetic liposome) to locate a tumor site and have taken anatomical MR images of paramagnetic liposomes attached to the tumor site. Removal of artifacts and enhancement of contrast have been demonstrated by exploiting the biexponential temporal characteristic of MRI signal coupled with difference imaging. This new technique results in significantly superior imaging contrast of the positions of Gd-liposomes, compared to conventional MRI methods in subcutaneous glioblastoma multiform (GBM) mice models. These findings are verified by inductively coupled plasma mass spectrometry (ICP-MS) results.

3.2. Results and discussion

3.2.1. Material characterization

The liposomes were prepared by the thin layer evaporation method and Gd was incorporated into the bilayer. PEG lipids were incorporated into the surface of the liposome for longer circulation time in the blood in order to increase the chances of targeting cancer cells through the enhanced permeability retention (EPR) effect. Liposomes were characterized by negative stain transmission electron microscopy (TEM) and dynamic light spectroscopy (DLS). DLS study (data not shown) has shown that the nanoparticles have a mean diameter of 168.0 nm with standard deviation of 76.6 nm consistent with **Figure 3.1** demonstrating the representative TEM images for the synthesized nanoparticles, indicating a uniform distribution and successful formation of bilayered liposomes.

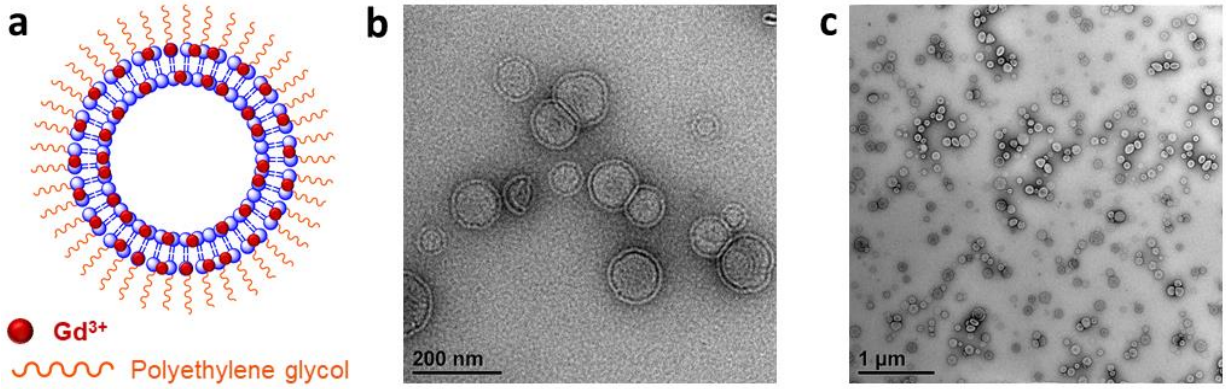

Figure 3.1. Schematic diagram with material characterization a) Schematic diagram of paramagnetic liposomes (Gd-liposomes), where red dots show the presence of Gd on the bilayer and the orange lines representing polyethylene glycol (PEG) for EPR effect b) TEM images show successful formation of bilayered liposome c) Demonstrates homogeneous distribution and morphology of nanoparticles under TEM.

3.2.2. Relaxation measurements

Different relaxation parameters like longitudinal and transverse relaxation decay rates (T_1 and T_2) at different concentrations were probed for the Gd-liposome solution in a 300MHz Varian microimaging setup and plotted to obtain the longitudinal and transverse relaxivity values, r_1 and r_2, respectively . Further, those were compared with the standard contrast agents, such as Gadavist and Magnevist. As shown in **Figure 3.2**, the nanoparticle solution exhibited an r_1 value of 1.68 s^{-1} mM^{-1}, whereas Gadavist and Magnevist showed r_1 values of 4.70 and 4.32 s^{-1} mM^{-1} respectively. In contrast, the nanoparticles demonstrated a higher r_2 value of 8.93 s^{-1} mM^{-1} compared to for Gadavist and 5.34 s^{-1} mM^{-1} for Magnevist. Hence, the prepared Gd-liposomes are much weaker T_1 contrast agents, compared to the standard, clinically used Gd compounds, whereas they are much stronger T_2 contrast agents compared to others. This feature of Gd-nanoparticles could be attributed to their particular structure, where the amphiphilic Gd-DTPA-BSA molecules were incorporated into the hydrophobic bilayer of the liposome through the hydrophobic interaction. The hydrophilic head with Gd^{3+} should orient itself towards either the inner aqueous core of the liposome or the outer water sphere. If the Gd^{3+} ions are in contact with the continuous water flow of the bulk water, then nanoparticles should behave like strong T_1 agents. However, our results are not consistent with such a conclusion. Therefore, we have hypothesized that Gd^{3+} ions might be preferentially located at the side of the inner aqueous core rather than the outer surface, restricting their access to the bulk water. Moreover, the high concentration of the Gd^{3+} in the small bilayer of 2-5 nm would act as a source of strong magnetic dipolar field, making the nanoparticles a good T_2 agent. In the following sections, we have compared MR images taken by standard T_2 and T_1 pulse sequences versus those with the active-feedback MR images obtained by employing a continuous wave pulse sequence.

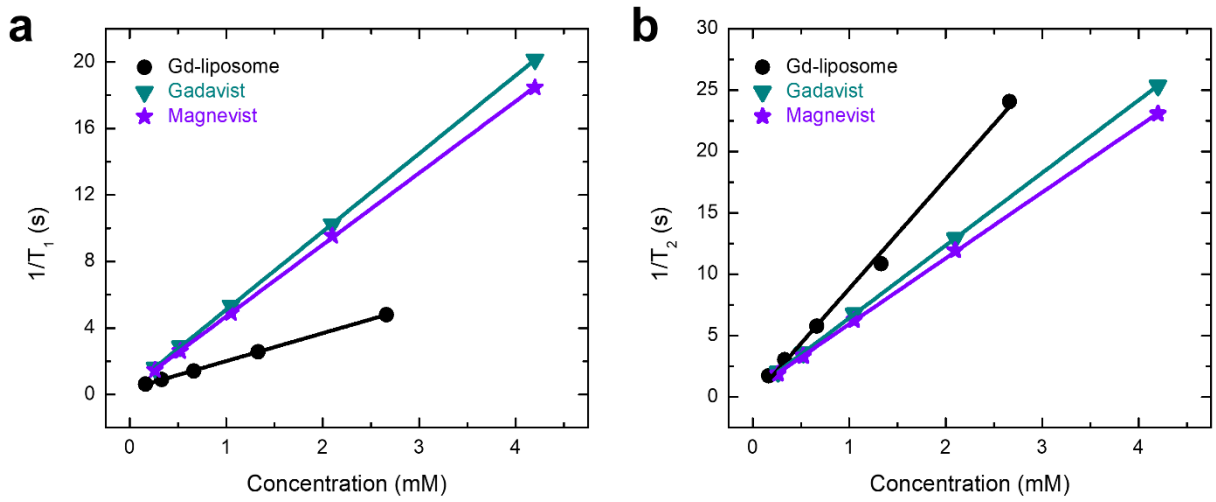

Figure 3.2. Relaxation rate measurement of paramagnetic liposomes (Gd-liposomes) and comparison with commercial contrast agents a) Longitudinal relaxation rate ($1/T_1$) measurement at different concentrations. Relaxivity (r_1) is calculated from the slopes of the fitted line; black represents paramagnetic liposome (Gd-liposome) with $r_1 = 1.68\ mM^{-1}s^{-1}$, green represents Gadavist with $r_1 = 4.70\ mM^{-1}s^{-1}$, purple represents Magnevist with $r_1 = 4.32\ mM^{-1}s^{-1}$ b) Transverse relaxation rate ($1/T_2$) measurement at different concentration. Relaxivity (r_2) is calculated from the slopes of the fitted line; black represents paramagnetic liposome (Gd-liposome) with $r_2 = 8.93\ s^{-1}\ mM^{-1}$, green represents Gadavist with $r_2 = 5.92\ s^{-1}\ mM^{-1}$, purple represents Magnevist with $r_2 = 5.34\ s^{-1}\ mM^{-1}$ (Uncertainty in all the results are 10%)

3.2.3. Continuous wave active-feedback (cwaf) pulse sequence and theoretical simulation

An electronic feedback (active-feedback) device was used to mimic the non-linear nature of the radiation damping to prevent instabilities in the time evolution of magnetization.[30,31] Radio-frequency continuous wave (CW) was incorporated in a new pulse sequence design (**Figure 3.3a**) to extend the non-linear evolution of the magnetization by preventing the system from reaching equilibrium. As a result, the return of the magnetization to the equilibrium orientation was delayed by stabilizing the proton spins of the sample with a different alignment called a fixed point. Additionally, phase alteration of the electronic feedback was done to enhance the natural radiation damping effect for contrast enhancement purposes under specific conditions, leading to potentially chaotic dynamics for simple-spin systems.[29]

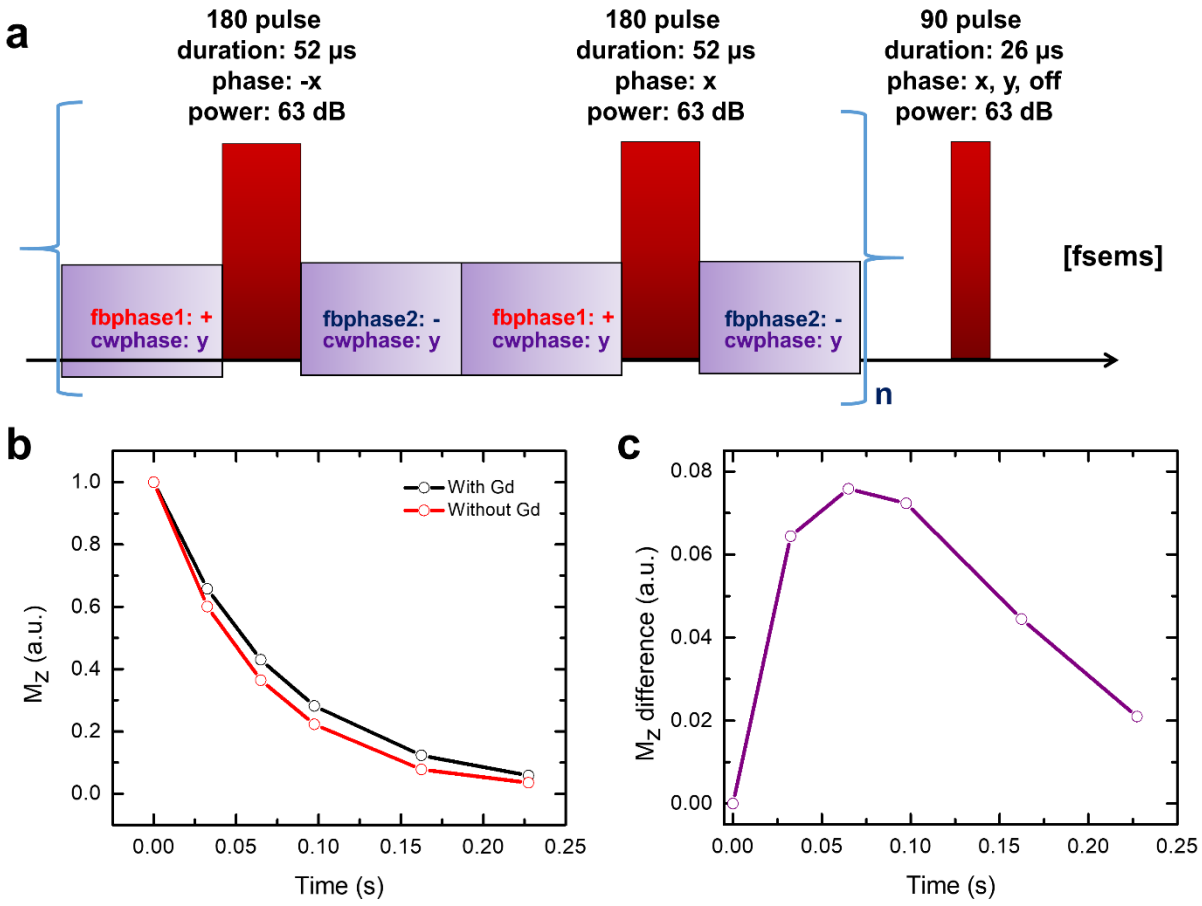

Figure 3.3. Pulse sequence and simulation result a) Pulse sequence for active-feedback (fb) imaging with continuous wave (cw) and feedback phase; lastly acquisition with fast spin echo image sequence (fsems). b) Simulation result for the decay of longitudinal magnetization with (black) and without (red) Gd respectively. c) The temporal variation of longitudinal magnetization of Gd-liposome.

Let **m(r)** = **M(r)**/Meq be the normalized magnetization vector, where **M(r)** is magnetization vector and Meq is the equilibrium magnetization. The time evolution of **m(r)** is governed by the classical Bloch equations[37,38] and depends: on the local magnetic field **B(r**,t) defined in the rotating frame; the longitudinal (T_1) and transverse (T_2) relaxation times, and the self-diffusion coefficient (D). Information concerning the CW and active-feedback is contained in **B**(**r**,t). In an appropriate frame of reference, we can write the local magnetic field **B**(**r**,t)=$\mathbf{B_z}$+$\mathbf{B_{cw}}$

+ $\mathbf{B}_{+,af}$, where $\mathbf{B}_z$, $\mathbf{B}_{cw}$, $\mathbf{B}_{+af}$ are the longitudinal component of the magnetic field, the contribution from CW and the contribution from active-feedback field, respectively. The active-feedback field can be modeled as a time-dependent magnetic field,[39,40] given by

$$\gamma B_{+,af}(t) = \frac{ie^{-i\varphi}}{\tau_r V}\iiint m_+(r,t)d^3r \qquad (3.1)$$

Here, the active-feedback time constant $\tau_r = (2\pi\eta M_0 Q\gamma)^{-1}$,[22] η and Q being the filling and quality factors of the coil, ϕ, usually assumed to be zero, depends on the tuning efficiency of the probe,[40] γ is gyromagnetic ratio, $\mathbf{m}_+$ is the transverse magnetization; and V is the total volume. The time evolution of the system will minimize $\int m_+(r)\, d^3r$**,** and fixed points correspond to $\frac{\partial m}{\partial t} = 0$.

The time evolution of the system finally proceeds to the creation of stable fixed points **(Figure S3.1)**. However, the effect of relaxation impedes the long-term stability of the fixed points, as the signal *in vivo* is not expected to last for more than a few hundreds of milliseconds. In fact, we would expect the *in vivo* signal to saturate completely long before the magnetization would be able to arrive at the stable fixed points. Despite the nature of the signal to eventually saturate, the simulations show that the evolution of the magnetization proceeds towards the fixed points. Considering a realistic system and modeling Gd-liposomes as sources of strong dipolar magnetic fields, the simulations results with the pulse sequence (**Figure 3.3a**) for the decay of the longitudinal magnetization (M_Z) with and without Gd-liposomes-are shown in **Figure 3.3b**. The figure shows that there is an *en route* difference of longitudinal decay between decays with and without Gd-liposome. Assuming Gd-liposomes are targeted to the tumor site, this variation represents the difference between healthy and tumor tissue. Since, we are mostly interested in this change, point-to-point differences were calculated and **Figure 3.3c** shows the corresponding

predicted temporal variation of M_Z for Gd-liposomes. The predicted temporal variation exhibits biexponential behavior and provides a strong handle for discriminating between artifacts and spurious points.

3.2.4. *In vivo* mice experiments

In this experiment, the PEGylated nanoparticles were injected through the tail vein of a mouse at a concentration about 30 μg/g, and we relied on passive targeting through the EPR effect. The *in vivo* mice experiments were done in a 7T Varian microimaging instrument. The MR images were taken before and after a few hours of injecting the Gd-liposomes in an otherwise identical experimental setup, where the position of the animal was kept fixed. Thus, any changes in the images taken before and after injecting Gd-liposome could be assigned to the presence of Gd-liposomes in the mouse body. In order to image Gd-liposomes, we have acquired the direct differences of the intensity images taken before and after injecting Gd-liposome; these images will be referred to as difference images. The temporal evolution of the difference images has been obtained by taking such images at different time points. **Figure 3.4** shows such a difference image taken with active-feedback technique (employing CW pulse sequence as shown in **Figure 3.3a** for a part of the right hind leg of a mouse, where a tumor was grown. However, the difference image in **Figure 3.4** lights up quite a few places in the image because of various artifacts making it difficult to accurately identify the position of the Gd-liposomes attached to the tumor. We have exploited an important characteristic feature of the active-feedback image with CW pulse sequence to eliminate artifacts and false imaging and compared with the images obtained by various conventional MR imaging protocols.

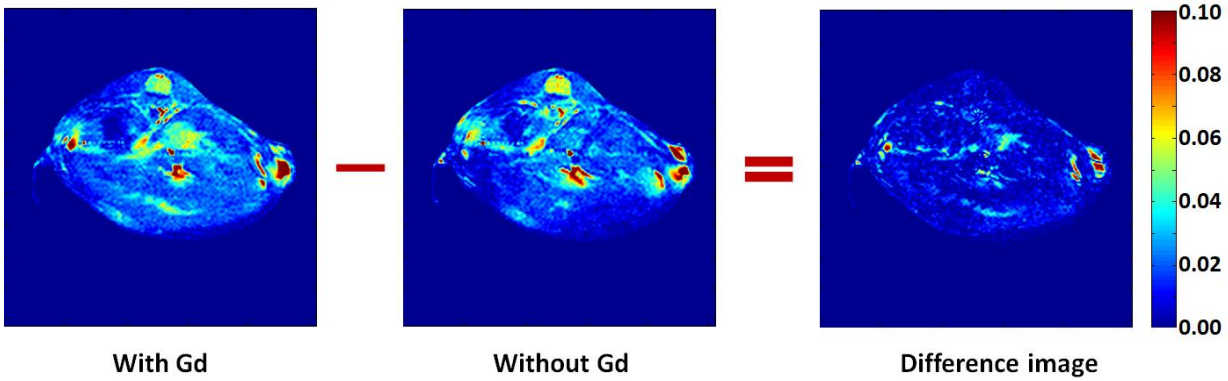

Figure 3.4. Difference imaging: The absolute intensity difference between two images taken before and after injecting paramagnetic liposome (Gd-liposome), acquired by active-feedback pulse sequence for the same slice under identical experimental conditions.

After injecting Gd-liposomes, the images were acquired under different preparation times of 33, 66, 99, 165 and 231 ms with our specially designed CW active-feedback pulse sequence. The difference images obtained at different preparation times are shown in **Figure 3.5a**. The longitudinal intensity differences correspond to the differences in longitudinal (z) magnetization and its temporal variation should be biexponential (**Figure 3.3c**)

$$\text{Intensity Difference} = A \times \left(e^{-\frac{t}{T_{AF1}}} - e^{-\frac{t}{T_{AF2}}}\right) \tag{3.2}$$

where, T_{AF2} and T_{AF1} are rise-time and decay-time constants respectively. A typical temporal variation of the difference images obtained from the experiment is shown in **Figure 3.5b** along with a biexponential fit. The characteristic pattern of the plot in **Figure 3.5b** is in good accordance with the predicted temporal variation in **Figure 3.3c**. The intensity points whose temporal variation of longitudinal intensity difference cannot be fitted by a biexponential curve with the goodness of fit (R^2) >0.7 were removed as artifacts or false imaging. The threshold R^2 value has been chosen

based on pixel-wise R^2 mapping. In **Figure 3.5c**, we show the values of the parameter T_{AF1} extracted from such fits at different points after eliminating artifacts.

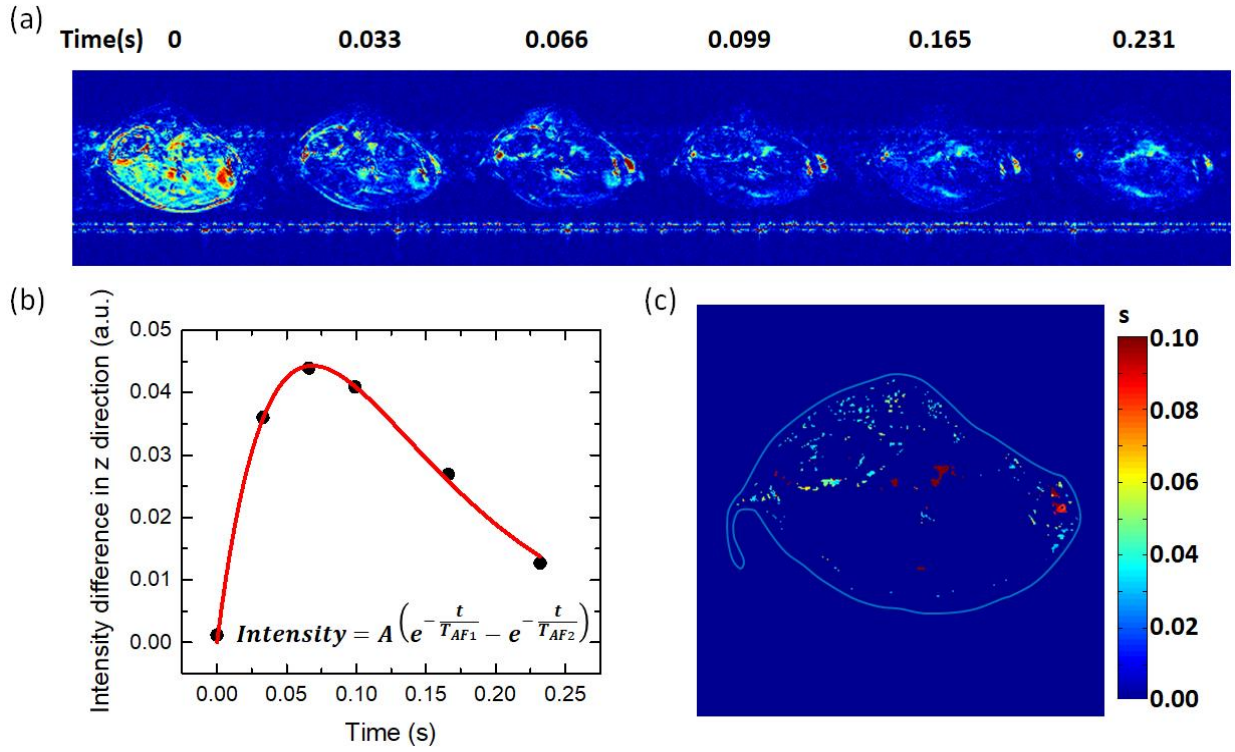

Figure 3.5. Time evolution of difference imaging a) The difference imaging is shown for different preparation times of 33, 66, 99, 165 and 231 ms for a particular slice. b) The temporal variation of the difference images fitted with a bi-exponential equation. c) Shows the parameter (T_{AF1}) at different points where goodness of fit>0.7, poorly fitted points have been removed as artifacts. The position of the tumor site is most intense and unambiguous.

In left panel of **Figure 3.6**, we show the difference images for the two mice and in the middle panel the same image for the points that follow the characteristic biexponential temporal variation with the goodness of fit >0.7 and eliminate the points that do not show this characteristic feature. The middle panel shows the results for tumors in two mice (mouse-1 and mouse-2) with excellent contrast and without artifacts. Based on the observations and theoretical justifications, we claim that the images only contain the points where Gd-liposomes actually exist. The relative intensities are indicating the concentrations of the Gd-liposomes in this image. The right column

of **Figure 3.6** shows an overlay of the parameter-corrected difference images with a conventional MR image of the mouse to understand the anatomy. The yellow circle indicates the tumor position and the darker regions are parts of the liver. The images obtained by our new technique show clearly the positions of Gd-liposomes as white and grey dots with an excellent contrast, thus clearly displaying the location of the tumor.

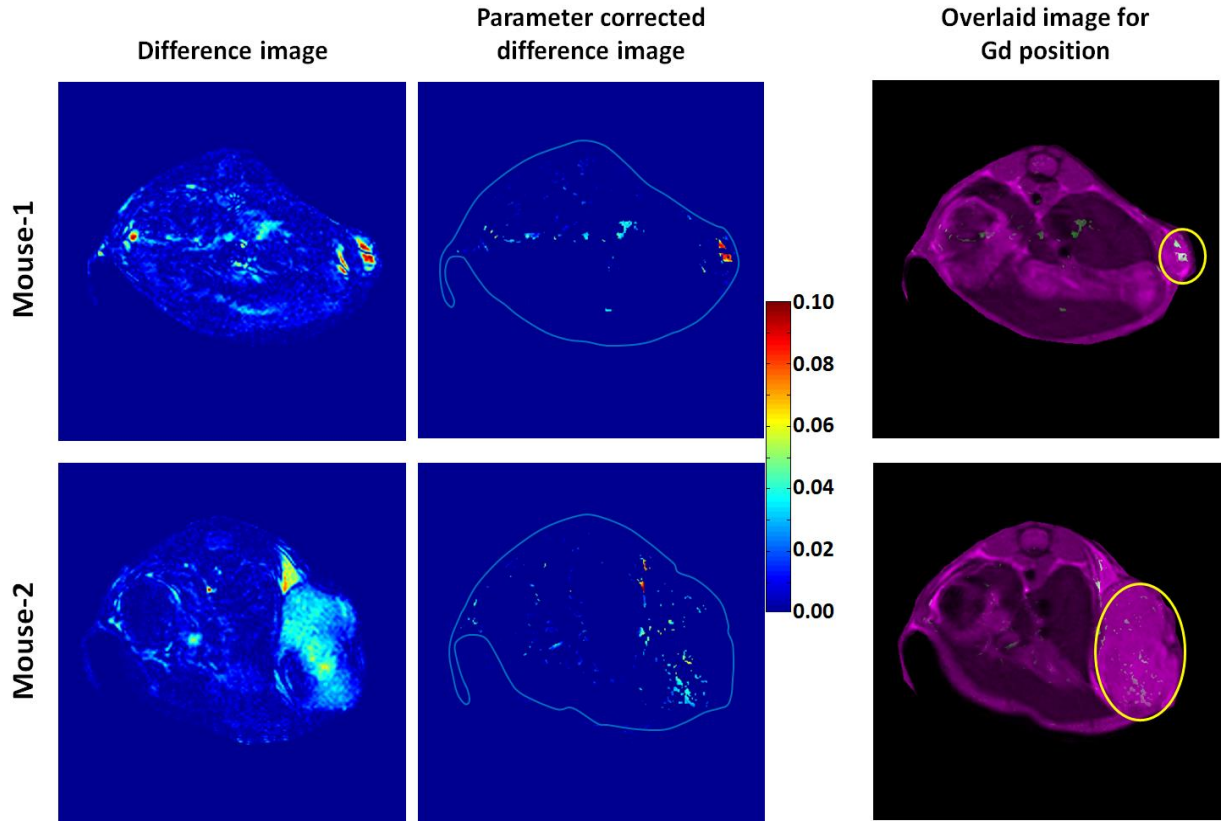

Figure 3.6. Parameter corrected difference image: Left column is showing the difference images for two mice. Middle column is demonstrating the same difference image for points that show the expected temporal behavior with the goodness of fit>0.7. The highest concentrations of paramagnetic liposomes (Gd-liposomes) are clearly seen at the tumor site. Right column is showing an overlay of this parameter corrected difference image with a standard MR image. See text for the details.

This method was compared with conventional techniques such as inversion recovery T_1, spin echo multi slice T_2 (SEMS T_2), gradient echo multi slice (GEMS T_2) and T_2-weighted

techniques. We followed identical procedures of acquiring images before and after injecting the Gd-liposomes and obtained the parameter-fitted difference images for the conventional MR techniques to compare with our specially designed active feedback technique. In **Figure 3.7**, we show MRI images obtained by various conventional techniques versus our new technique for the two mice, clearly demonstrating that our new technique shows the best contrast to locate the Gd-liposomes very efficiently without any background noise, artifacts or false imaging.

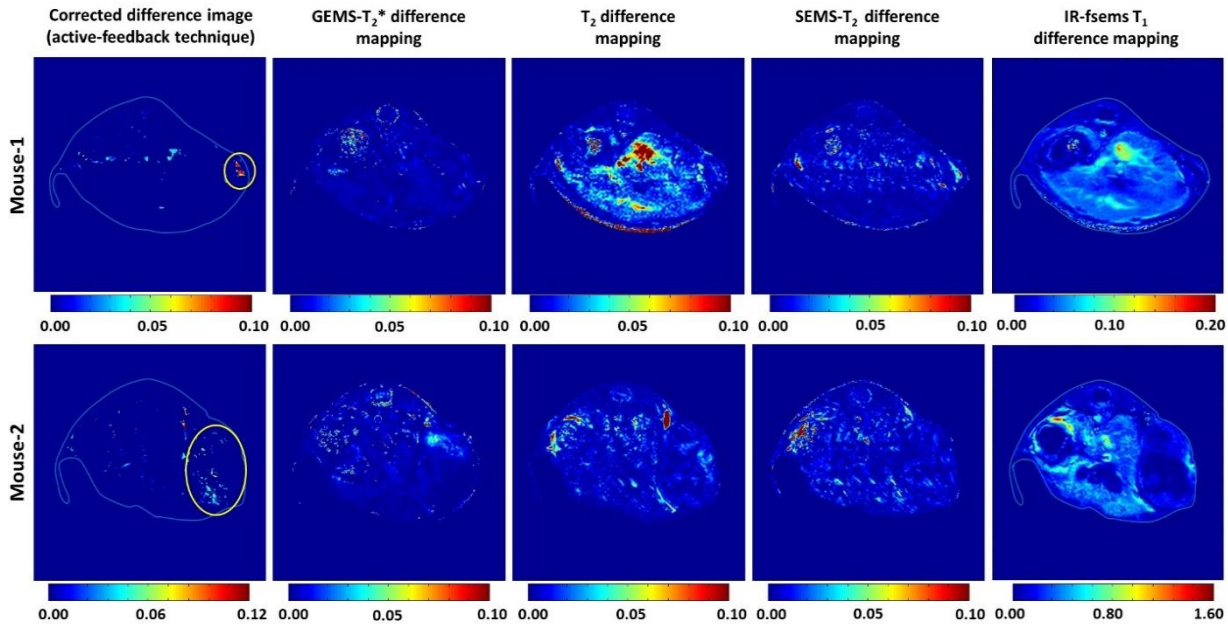

Figure 3.7. Comparison with conventional techniques: The comparison among different MR images taken using conventional techniques and our parameter-corrected difference imaging technique with active-feedback continuous-wave pulse sequence. Results are shown for mouse-1 and mouse-2. The yellow circles show the positions of the tumor. See text for the details.

3.2.5. Histopathology and targeting efficiency

The mice were sacrificed after the experiment and histological sections were made to locate the position of the tumor shown in **Figure 3.6** with yellow circles. Inductively coupled mass

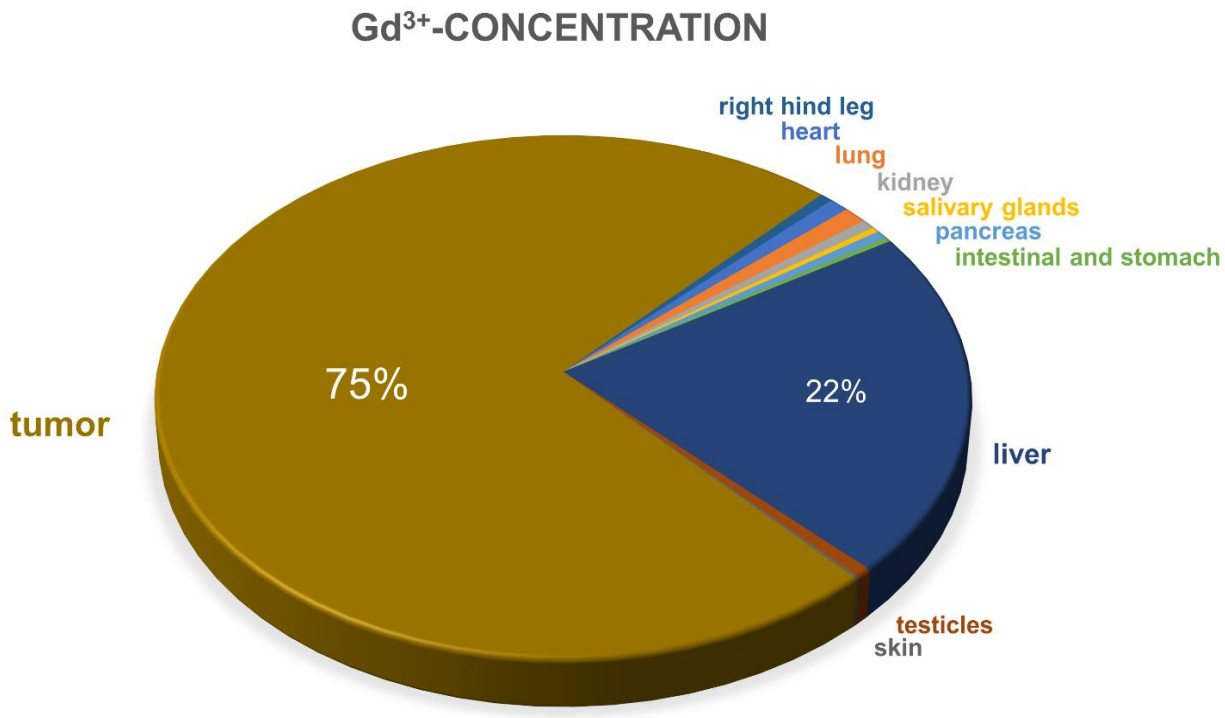

Figure 3.8. Inductively coupled mass spectrometry (ICP-MS) result: It demonstrates the concentration of Gd is 74.80 µg/g at tumor, 21.80 µg/g in the parts of the liver and 0.13 - 1.05 µg/g in other parts of the body. Uncertainties in the results are 10%.

spectrometry (ICP-MS) results for Gd are displayed in **Figure 3.8**, showing the highest concentration of the Gd at the tumor site (74.80 µg/g) followed by a concentration of 21.8 µg/g at the parts of liver. Notably, the kidney has only 0.6 µg/g Gd, while other body parts have 0.13-1.05 µg/g Gd. In this context, it is worthwhile to mention that the clinical dosage for humans is usually 15 µg/g in regular use, however a 3 times higher dose of Magnevist and a 15 times higher dose for

Gadavist were found to be well tolerated for healthy human.[41,42] **Figure 3.8** shows the percentages of Gd concentration in different parts of the mouse indicating 75% concentration at the tumor site, even for passive targeting. The use of active targeting[6,43] could enhance this efficiency very significantly and better images could be obtained. Moreover, the incorporation of Gd-chelate into the bilayer of liposome should reduce the chances of leakage.

3.3. Conclusions

The ability to obtain artifact-free high-contrast images of the tumor site by encapsulating both the contrast agent and drug molecules in a nanoparticle plays a key role for the success of cancer theranostics. However, generally the encapsulation of the contrast agent reduces its ability to generate high-contrast images. In this work, we have demonstrated how high-contrast, artifact-free images could be obtained by employing a specially designed active feedback technique compared to available conventional MR imaging techniques. This newly developed MRI pulse sequence is based on an active-feedback technique employing a CW radio-frequency field in the transverse plane to extend the nonlinear evolution of the proton spins by preventing them from reaching equilibrium. The technique stabilizes and preserves the generated contrast in the context of fixed-point dynamics. We have developed a novel analytical procedure to obtain high-contrast background-free and artifact-free images by exploiting the characteristic biexponential temporal variation of the intensity points of the difference images. The technique successfully lights up the positions of the nanoparticles accurately with a close correlation with histopathology and inductively-coupled mass-spectrometry results, where other conventional techniques give ambiguous images full of various artifacts.

Under clinical conditions, the field strength, filling and quality factors of the coil are usually not enough to produce an observable radiation damping field. We have shown how to overcome this problem with the implementation of an active feedback circuit, designed to read the free induction decay (FID), amplify and then retransmit the signal back onto the sample, thus emulating the effect of the radiation damping feedback field.[28] While the process is not the true radiation damping feedback field, the system exhibits the same non-linear response for the total magnetization and can thus be used in settings where radiation damping is negligible, i.e. at clinical setting using a low magnetic strength MRI.

The liposomal nanoparticles used in this work have been well studied for drug delivery and imaging purposes, however the sensitivity is poor because of insufficient interaction of Gd^{3+} with bulk water.[13,16] This work shows a superior contrast mechanism to solve this long-standing problem. Here we have shown the nanoparticle accumulation at the tumor site through passive targeting. The dosage is within the clinical limit and could be reduced significantly by active targeting. This nanostructure provides high stability, limits the chances of releasing free Gd in the body, ensures better targeting to cancer cells and has the capability to be a potent theranostic for early cancer with high sensitivity without compromising contrast.

This protocol employing a characteristic temporal biexponential feature of the difference image under the new pulse sequence could be used as a powerful analytical tool for the robust detection of other paramagnetic nanostructures that generally suffer from limited contrast. Hence, our technique is an important step to achieve success in cancer theranostics using paramagnetic nanoparticles and it has the capability to generate high quality PET-like MR images.

3.4. Materials and methods

3.4.1. Preparation of Gd-liposomes

A total of 112.5 micromole of 1,2-distearoyl-*sn*-glycero-3-phosphocholine(DSPC) (Corden pharma),1,2-distearoyl-*sn*-glycero-3-phosphoethanolamine-N-[amino(polyethylene-glycol)2000] (DSPE-PEG2000) (Corden pharma), DTPA-bis(stearylamide) (Gadolinium salt) (Gd-DTPA-BSA)) (Avanti Polar Lipids, Inc), Cholestrol (Sigma Aldrich), (in a molar ratio of 1.10:0.15:0.75:1) were dissolved in chloroform/methanol (2:1) (Sigma Aldrich) mixture to yield a uniform solution of density typically between 10-20 mg/ml.[44,45] The homogeneous solution was evaporated under high vacuum at 40 ºC and kept for 8 hours in a rotatory evaporator for the complete evaporation of organic solvent. The produced thin film was hydrated with phosphate buffer saline (10 mM PBS) (Sigma Aldrich) at pH 7.4 for 1 hour above its transition temperature (65 ºC) in a rotatory evaporator at a constant speed of about 60 rpm with occasional vertexing and sonication . The resulting solution was passed through a 400 and 100 nm filters with 61 times each during extrusion using a mini extruder from Avanti Polar Lipid.

3.4.2. Characterization of Gd-liposomes

The size and morphology of the nanoparticles were verified with negatively stained transmission electron microscopy (TEM). The Gd-liposome solution was diluted 75-100 times and 6μL was taken on carbon coated copper grid, stained with 2% uranyl acetate solution, and dried. The grid was loaded with a Gatan specimen holder into T12 cryo-electron microscope (Electron Imaging Center for NanoMachines, California NanoSystems Institute) microscope for imaging. The images were acquired by operating the machine at 120 kV with a Gatan 2k×2k CCD camera.

The hydrodynamic diameter was measured with dynamic light scattering (DLS) after diluting by 300 times in 10 mM PBS buffer using a Coulter Beckman Dynamic Light Scattering Analyzer – N4 Plus (UCLA Molecular Instrumentation Center).

3.4.3. MRI measurements

All MR images and relaxation measurements were performed in a 300 MHz, 7T Varian INOVA microimaging system with 5 mm bore.

In order to obtain relaxation parameters, the nanoparticle solution was diluted to different concentrations and Gadavist (Radiologysolutions.Bayer) and Magnevist (Radiologysolutions.Bayer**)** were brought for comparison. Number of scans was taken as 1 and relaxation delay time was 3 s for each. T_1 was measured using inversion recovery pulse sequence with inversion time (TI) ranging from 1 ms to 3 s. T_2 was obtained with CPMG (Carr-Purcell-Meiboom-Gill) pulse sequence and the half of the interval between successive 180^o pulses in the CPMG pulse sequence (τ_{CP}) was = 1 ms. Time of echo (TE) was ranging from 4 to 300 ms. The relaxation rates were plotted with the concentration of Gd to obtain a linear fit. The longitudinal and transverse relaxivity parameters (r_1 and r_2) were calculated from the slope of the fitted straight line.

All MR images in this work were acquired after preparation stage by fast spin echo image sequence with repetition time (TR) = 7.5 s, echo spacing time = 10 ms, number of echos = 8, number of scans = 1, on transverse plane (axial), the field of view (FOV) = 3.2. cm × 3.2 cm, thickness = 1 mm, matrix size = 128 × 128, zero padding = 512 × 512. The T_2*-weighted images were acquired by GEMS with flip angle 30^o, TR= 0.15 s, TE is 5, 5.1, 6, 10, and 15 ms respectively.

The T_2-weighted images were acquired by SEMS sequence with TR= 7.5 s and time of echo (TE or τ) 10, 30, 50 and 70 ms respectively. T_1-weighted images were obtained by inversion recovery (IR) pulse sequence with TR= 7.5 s and TI = 97 ms , 197 ms, 297 ms, 597 ms, 1.297 s and 3.097s. Active-feedback pulse sequence with CW was used, as shown in **Figure 3.3a)** with different preparation times of 33 ms, 66 ms, 99 ms, 165 ms and 231 ms. Details of hardware design of the active-feedback instrument could be found elsewhere.[28,46]

3.4.4. Cell culture

The U87-MG cell lines were purchased from Bioresource Collection and Research Center (BCRC, Taiwan), derived from American Type Culture Collection (ATCC). It is cultured in minimum essential medium Eagle (MEM, Sigma-Aldrich) supplemented with 10% fetal bovine serum (FBS) (Gibco) and 100 U/mL penicillin-streptomycin antibiotics (Sigma-Aldrich). The cells were plated in T-75 flasks and maintained in a 5% CO_2 humidified incubator at 37 ^{o}C. About four flasks of cells were collected after washing with PBS three times and treatment with trypsin (Biowest) treatment. The suspended cells were centrifuged at 967.5 g for 5 minutes and concentrated to 1×10^5 cell/μL before implantation.

3.4.5. Animal surgery

All animal experiments were done in accordance with the regulations approved by the Institution Animal Care and Utilization Committee at National Taiwan University, Taiwan. The male NOD CB17-*Prkd*^{scid}/IcrCr1B1tw (NOD/SCID) mice were obtained from BioLASCO, Taiwan. *In vivo* subcutaneous glioblastoma multiform (GBM) mouse models were prepared by injecting the U87-MG cells on the right hind legs of the mice. After injecting the mouse with the

GBM cells, we waited for 8 days. Then, about 200 microliters of the nanoparticle solution with 2% heparin to prevent coagulation was injected (Hamilton 30 gauge syringe, equipped with pump to push the drug) through the tail of the mouse. During the measurement, mouse was anesthetized with about 1.5% isoflurane and its position was held fixed inside the instrument. The heart rate and respiratory signs of the mice were carefully monitored. The measurements were taken once just before injecting the Gd-liposomes nanoparticle solution and again a few hours after injecting the mouse with Gd-liposome solution. The mouse position was kept undisturbed between these two measurements.

3.4.6. Histopathology

After the experiment, the mouse-1 was sacrificed, and its different tissues were dissected. Then all the dissected tissues were digested separately in concentrated nitric acid. Concentrated hydrofluoric acid was added as required to dissolve any undigested material. The solution was evaporated just to dryness and taken up in 2 washes of 5% nitric acid for inductively coupled mass spectrometry (ICP-MS) analysis for elemental Gd at the Agilent 7500c quadrupole ICP-MS with hydrogen/helium octopole collision cell.

3.4.7. Computer simulations for theorical calculations

Spin dynamics code was run using MATLAB (The Mathworks, Inc., South Natick, MA, USA). The Gd-nanoparticle was modeled as an impenetrable sphere of 168 nm diameter. The nanoparticle was placed at the center of a cubic box with volume fraction 0.000005 and the root mean square (rms) angular frequency shift at the particle surface $\Delta\omega_r = 50 \times 10^7$ rad/s. 50000 average voxels of magnetic moment with diffusing proton spins were simulated randomly.

Constant background relaxation and inhomogeneity were modeled by taking a magnetic dipolar field at healthy tissue with $\Delta\omega_r = 40 \times 10^7$ rad/s. The diffusion process was modeled as a random walk in a cubic lattice with each diffusion step of size $\sqrt{6 \times D \times t}$, where D is the diffusion coefficient of water ($D = 2.5\times10^{-5}$ cm^2/s) and t is the diffusion time step.[47,48] After each step, different magnetization offset and phase shift along the z-direction in the rotating frame experienced by the spins were calculated according to the following **Equation 3.3** for each voxel,

$$B_z(d,\theta) = \sqrt{\left(\frac{5}{4}\right)} r^3 \Delta\omega_r (3\cos^2\theta - 1)/\gamma d^3 \qquad (3.3)$$

Here, γ is the gyromagnetic ratio of proton, r is the particle radius, d is the distance from the particle center and θ is the angle between the z-axis and the position where B_z (magnetic field along z direction) is evaluated. Another set of 50000 average voxels of proton spins was taken to take care of healthy tissues, where no Gd-nanoparticle should be present, considering a perfect targeting case.

At every step the resonance offset at the rotating frame was evaluated according to the formula $\Delta\omega_{offset} = \gamma B_z$ for each spin. The average transverse magnetizations experienced by both sets of spins were numerically integrated taking care of CW pulse and accordingly substituted for $\mathbf{B}(\mathbf{r},t)$ (where, $\mathbf{B}(\mathbf{r},t)=\mathbf{B_z} + \mathbf{B_{cw}} + \mathbf{B_{+,af,}}$; $\mathbf{B_{+,af,}}$ calculated from **Equation 3.1** to solve Bloch equation for every voxel.

Supplementary materials

Figure S3.1 shows a simple two-component case with a resonance offset difference of only $\Delta\omega$ = 10 Hz, and tumor component occupy 20 % of the total volume, whereas the rest 80 % was occupied by the healthy tissues. Accordingly, the weighted contribution was calculated from **Equation 3.1**. Continuous wave (CW) pulse was applied along x-axis along with active-feedback. The explicit dependence of **Equation 3.1** on the magnetization renders Bloch equation nonlinear ($\frac{\partial \mathrm{m}}{\partial \mathrm{t}} \propto \mathrm{m} \times \mathrm{i} \int \mathrm{m}_{+}(\mathrm{r}) \mathrm{d}^{3}\mathrm{r}$), thus complicating any analytical considerations. However, the effect of strong radiation damping can be visualized by numerically integrating **Equation 3.1** into Bloch equation in the absence of relaxation terms, as depicted in **Figure S3.1**. The two components of the magnetization (proton spins in healthy and tumor tissues) can be seen to effectively repel each other as they spiral towards opposite poles of the Bloch sphere (**Figure S3.1a**). The development of the contrast can be tracked along the m_x direction (**Figure S3.1b**). It is seen that the contrast between the two components continues to grow until the components reach their stable fixed points.

The origin of the fixed points is a direct consequence of the active-feedback field's tendency to minimize itself in presence of CW. In the absence of CW pulse, the radiation damping field will naturally bring the total magnetization back towards the more stable +z orientation, (direction of strong external static magnetic field) where $\gamma B_{af,+} = 0$. However, the constant perturbation of the CW requires that the total magnetization would evolve in such a way as to minimize the total Zeeman energy and hence will not stabilize along +z direction. Since the magnetization is forced to remain in the transverse plane, the most stable orientation is to have

both components (heathy and tumor proton spins) align antiparallel to each other. This configuration reduces the total magnetization from the entire sample, which reduces the overall

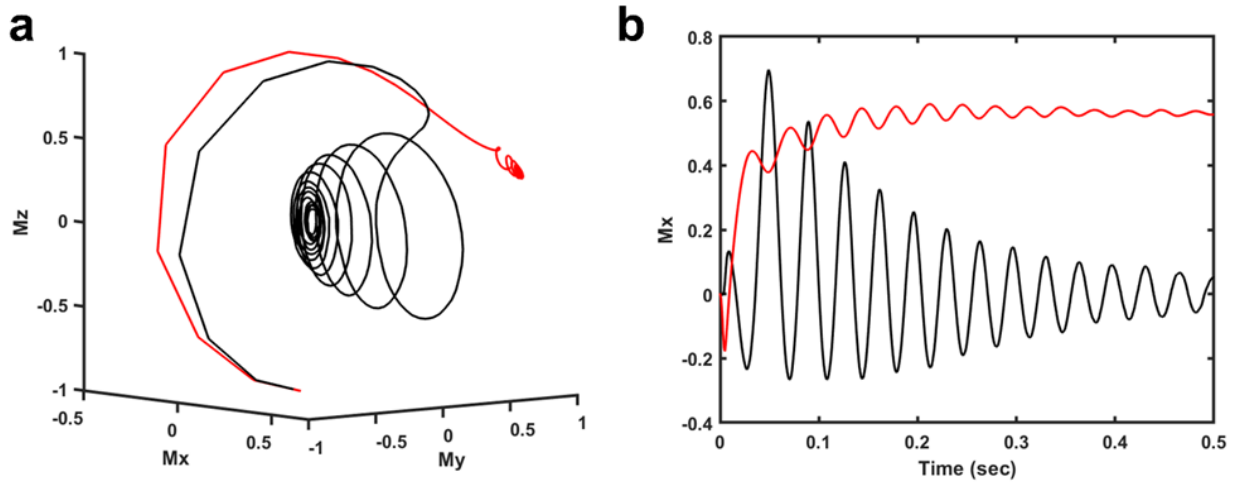

Figure S3.1. Formation of fixed point with 4000 voxels and an impenetrable sphere of 130 nm diameter and a root mean square (rms) angular frequency shift at the particle surface equal to 1.5×10^6 rad/s. **a)** Black and red curve depicts the formation of fixed point for tumor tissue and healthy tissue respectively **b)** Time evolution of magnetization of voxels with healthy (red) and tumor (black) tissue proton spins along x axis. It demonstrates the bifurcation of magnetization along x-axis due to the presence of continuous wave (CW) pulse along x direction.

active-feedback field. In the case of equal volumes, the magnetization is perfectly cancelled in the anti-parallel orientation resulting in $\gamma B_{af,+} = 0$. Consequently, the natural tendency of the magnetization under CW and a strong active-feedback field is to significantly reorient the components anti-parallel to each other. However, in realistic situations, the tumor tissues would generally be a small percentage of the healthy tissues and hence the two components would not have equal and opposite contributions to **Equation 3.1**. We have performed simulations assuming 80 % contribution from the healthy tissues and 20 % contribution from the tumor tissues to **Equation 3.1**, resulting in a non-zero active-feedback term. Thus, the smaller component from the tumor tissues experiences the radiation damping of the stronger component from the healthy tissues. As can be seen in **Figure S3.1**, the smaller component (black) from the tumor tissues takes significantly longer to stabilize, as it is evolving under the radiation damping of the more dominant

component (red) from the healthy tissues. Despite the different time evolutions, fixed points appear for both the weak and strong components and the total active-feedback field is minimized at the fixed points.

Acknowledgements

This chapter is a version of 'Ray, S; Hsu, C.-H.; Lin F-C; Lin, Y-Y. High-contrast Background-free Magnetic Resonance Molecular Imaging. *In preparation*'. I gratefully acknowledge my coauthors Dr. Chao-Hsiung Hsu for performing in vivo experiments, Dr. Zhao Li for helping in material characterization, Ms. Fang-Chu Lin for helping in experiments and Prof. Yung-Ya Lin for his guidance and supervision in this project. I want to thank Prof. Ying-Chih Lin, Prof. William Gelbart, Prof. Charles M. Knobler, Prof. Neil K. Garg for lab facilities, Dr. Shane Quee Hee (ICP-MS facility at School of Public Health, UCLA) for ICP-MS measurements, National Taiwan University for in vivo facility and NSF-EAPSI for travel expenses to commute Taiwan. This work was supported by NSF grant CHE-1112574 and CHE-1416598, University of California Cancer Research Award (CRR-13-201412), and the Hirshberg Foundation for Pancreatic Cancer Research.

References

(1) Singh, R.; Lillard, J. W. Nanoparticle-Based Targeted Drug Delivery. *Exp. Mol. Pathol.* **2009**, *86* (3), 215–223. https://doi.org/10.1016/J.YEXMP.2008.12.004.

(2) Sunderland, C. J.; Steiert, M.; Talmadge, J. E.; Derfus, A. M.; Barry, S. E. Targeted Nanoparticles for Detecting and Treating Cancer. *Drug Dev. Res.* **2006**, *67* (1), 70–93. https://doi.org/10.1002/ddr.20069.

(3) Kelkar, S. S.; Reineke, T. M. Theranostics: Combining Imaging and Therapy. *Bioconjug. Chem.* **2011**, *22* (10), 1879–1903. https://doi.org/10.1021/bc200151q.

(4) Janib, S. M.; Moses, A. S.; MacKay, J. A. Imaging and Drug Delivery Using Theranostic Nanoparticles. *Adv. Drug Deliv. Rev.* **2010**, *62* (11), 1052–1063. https://doi.org/10.1016/j.addr.2010.08.004.

(5) Allen, T. M.; Cullis, P. R. Liposomal Drug Delivery Systems: From Concept to Clinical Applications. *Adv. Drug Deliv. Rev.* **2013**, *65* (1), 36–48. https://doi.org/10.1016/J.ADDR.2012.09.037.

(6) Hosta-Rigau, L.; Schattling, P.; Teo, B. M.; Lynge, M. E.; Städler, B. Recent Progress of Liposomes in Nanomedicine. *J. Mater. Chem. B* **2014**, *2* (39), 6686–6691. https://doi.org/10.1039/C4TB00825A.

(7) Mikhaylov, G.; Mikac, U.; Magaeva, A. A.; Itin, V. I.; Naiden, E. P.; Psakhye, I.; Babes, L.; Reinheckel, T.; Peters, C.; Zeiser, R.; et al. Ferri-Liposomes as an MRI-Visible Drug-Delivery System for Targeting Tumours and Their Microenvironment. *Nat. Nanotechnol.* **2011**, *6* (9), 594–602. https://doi.org/10.1038/nnano.2011.112.

(8) Shin, T.; Choi, J.; Yun, S.; Kim, I.; Song, H.; Kim, Y. T 1 and T 2 Dual-Mode MRI Contrast Agent for Enhancing Accuracy by Engineered Nanomaterials. *ACS Nano* **2014**, *8* (4), 3393–3401. https://doi.org/10.1021/nn405977t.

(9) Delanian, S.; Baillet, F.; Huart, J.; Lefaix, J.-L.; Maulard, C.; Housset, M. Successful Treatment of Radiation-Induced Fibrosis Using Liposomal CuZn Superoxide Dismutase: Clinical Trial. *Radiother. Oncol.* **1994**, *32* (1), 12–20. https://doi.org/10.1016/0167-8140(94)90444-8.

(10) Unezaki, S.; Maruyama, K.; Takahashi, N.; Koyama, M.; Yuda, T.; Suginaka, A.; Iwatsuru, M. Enhanced Delivery and Antitumor Activity of Doxorubicin Using Long-Circulating Thermosensitive Liposomes Containing Amphipathic Polyethylene Glycol in Combination with Local Hyperthermia. *Pharm. Res.* **1994**, *11* (8), 1180–1185.

https://doi.org/10.1023/A:1018949218380.

(11) Northfelt, D. W.; Dezube, B. J.; Thommes, J. A.; Miller, B. J.; Fischl, M. A.; Friedman-Kien, A.; Kaplan, L. D.; Du Mond, C.; Mamelok, R. D.; Henry, D. H. Pegylated-Liposomal Doxorubicin versus Doxorubicin, Bleomycin, and Vincristine in the Treatment of AIDS-Related Kaposi's Sarcoma: Results of a Randomized Phase III Clinical Trial. *J. Clin. Oncol.* **1998**, *16* (7), 2445–2451. https://doi.org/10.1200/JCO.1998.16.7.2445.

(12) Alberts, D. S.; Muggia, F. M.; Carmichael, J.; Winer, E. P.; Jahanzeb, M.; Venook, A. P.; Skubitz, K. M.; Rivera, E.; Sparano, J. A.; Dibella, N. J.; et al. Efficacy and Safety of Liposomal Anthracyclines in Phase I/II Clinical Trials. *Semin. Oncol.* **2004**, *31*, 53–90. https://doi.org/10.1053/J.SEMINONCOL.2004.08.010.

(13) Kamaly, N.; Miller, A. D. Paramagnetic Liposome Nanoparticles for Cellular and Tumour Imaging. *Int. J. Mol. Sci.* **2010**, *11* (4), 1759–1776. https://doi.org/10.3390/ijms11041759.

(14) Strijkers, G. J.; Mulder, W. J. M.; Van Heeswijk, R. B.; Frederik, P. M.; Bomans, P.; Magusin, P. C. M. M.; Nicolay, K. Relaxivity of Liposomal Paramagnetic MRI Contrast Agents. *Magn. Reson. Mater. Physics, Biol. Med.* **2005**, *18* (4), 186–192. https://doi.org/10.1007/s10334-005-0111-y.

(15) Unger, E.; Shen, D. K.; Wu, G.; Fritz, T. Liposomes as MR Contrast Agents: Pros and Cons. *Magn. Reson. Med.* **1991**, *22* (2), 304–308. https://doi.org/10.1002/mrm.1910220229.

(16) Tilcock, C.; Unger, E.; Cullis, P.; Macdougall, P. Liposomal Gd-DTPA: Preparation and Characterization of Relxavity. *Radiology* **1989**, *171*, 77–80.

(17) Hak, S.; Sanders, H. M. H. F.; Agrawal, P.; Langereis, S.; Grüll, H.; Keizer, H. M.; Arena, F.; Terreno, E.; Strijkers, G. J.; Nicolay, K. A High Relaxivity Gd(III)DOTA-DSPE-Based Liposomal Contrast Agent for Magnetic Resonance Imaging. *Eur. J. Pharm. Biopharm.* **2009**, *72* (2), 397–404. https://doi.org/10.1016/j.ejpb.2008.09.017.

(18) Laurent, S.; Vander Elst, L.; Thirifays, C.; Muller, R. N. Relaxivities of Paramagnetic Liposomes: On the Importance of the Chain Type and the Length of the Amphiphilic Complex. *Eur. Biophys. J.* **2008**, *37* (6), 1007–1014. https://doi.org/10.1007/s00249-008-0331-y.

(19) Liang, Z.-P.; Lauterbur, P. C.; IEEE Engineering in Medicine and Biology Society. *Principles of Magnetic Resonance Imaging : A Signal Processing Perspective*; SPIE Optical Engineering Press, 2000.

(20) Zimmerman, R. A.; Gibby, W. A.; Carmody, R. F. *Neuroimaging : Clinical and Physical Principles*; Springer New York, 2000.

(21) Haacke, E. M.; Xu, Y.; Cheng, Y.-C. N.; Reichenbach, J. R. Susceptibility Weighted Imaging (SWI). *Magn. Reson. Med.* **2004**, *52* (3), 612–618. https://doi.org/10.1002/mrm.20198.

(22) Bloembergen, N.; Pound, R. V. Radiation Damping in Magnetic Resonance Experiments. *Phys. Rev.* **1954**, *95* (1), 8–12. https://doi.org/10.1103/PhysRev.95.8.

(23) Lin, Y. Y.; Lisitza, N.; Ahn, S.; Warren, W. S. Resurrection of Crushed Magnetization and Chaotic Dynamics in Solution NMR Spectroscopy. *Science* **2000**, *290* (5489), 118–122.

(24) Datta, S.; Huang, S. Y.; Lin, Y. Y. Contrast Enhancement by Feedback Fields in Magnetic Resonance Imaging. *J. Phys. Chem. B* **2006**, *110* (44), 22071–22078. https://doi.org/10.1021/jp060658k.

(25) Huang, S. Y.; Furuyama, J. K.; Lin, Y.-Y. Designing Feedback-Based Contrast Enhancement for in Vivo Imaging. *Magn. Reson. Mater. Physics, Biol. Med.* **2007**, *19* (6), 333–346. https://doi.org/10.1007/s10334-006-0061-z.

(26) Huang, S. Y.; Wolahan, S. M.; Mathern, G. W.; Chute, D. J.; Akhtari, M.; Nguyen, S. T.; Huynh, M. N.; Salamon, N.; Lin, Y.-Y. Improving MRI Differentiation of Gray and White Matter in Epileptogenic Lesions Based on Nonlinear Feedback. *Magn. Reson. Med.* **2006**, *56* (4), 776–786. https://doi.org/10.1002/mrm.20987.

(27) Li, Z.; Hsu, C.-H.; Dimitrov, N.; Hwang, D. W.; Chang, H.-W.; Hwang, L.-P.; Lin, Y.-Y. Sensitive Imaging of Magnetic Nanoparticles for Cancer Detection by Active Feedback MR. *Magn. Reson. Med.* **2015**, *74* (1), 33–41. https://doi.org/10.1002/mrm.25632.

(28) Chen, Y.-W.; Hsu, C.-H.; Hwang, D. W. Novel MRI Contrast Development by Lock-in Suppression. *Magn. Reson. Med.* **2014**, *71* (5), 1676–1681. https://doi.org/10.1002/mrm.25162.

(29) Abergel, D. Chaotic Solutions of the Feedback Driven Bloch Equations. *Phys. Lett. A* **2002**, *302* (1), 17–22. https://doi.org/10.1016/S0375-9601(02)01079-4.

(30) Louis-Joseph, A.; Abergel, D.; Lallemand, J.-Y. Neutralization of Radiation Damping by Selective Feedback on a 400 MHz NMR Spectrometer. *J. Biomol. NMR* **1995**, *5* (2), 212–216. https://doi.org/10.1007/BF00208813.

(31) Broekaert, P.; Jeener, J. Suppression of Radiation Damping in NMR in Liquids by Active

Electronic Feedback. *J. Magn. Reson. Ser. A* **1995**, *113* (1), 60–64. https://doi.org/10.1006/JMRA.1995.1056.

(32) Abergel, D.; Louis-Joseph, A.; Lallemand, J. Y. Amplification of Radiation Damping in a 600-MHz NMR Spectrometer: Application to the Study of Water-Protein Interactions. *J. Biomol. NMR* **1996**, *8* (1), 15–22. https://doi.org/10.1007/BF00198136.

(33) Abergel, D.; Carlotti, C.; Louis-Joseph, A.; Lallemand, J. Improvements in Radiation-Damping Control in High-Resolution NMR. *J. Magn Reson Ser B* **1995**, *109*, 218–222.

(34) Abergel, D.; Louis-Joseph, A.; Lallemand, J.-Y. Self-Sustained Maser Oscillations of a Large Magnetization Driven by a Radiation Damping-Based Electronic Feedback. *J. Chem. Phys.* **2002**, *116* (16), 7073–7080. https://doi.org/10.1063/1.1462583.

(35) Hobson, R. F.; Kaiser, R. Some Effects of Radiation Feedback in High Resolution NMR. *J. Magn. Reson.* **1975**, *20* (3), 458–474. https://doi.org/10.1016/0022-2364(75)90003-7.

(36) Louis-Joseph, A.; Abergel, D.; Lebars, I.; Lallemand, J. Y. Enhancement of Water Suppression by Radiation Damping-Based Manipulation of Residual Water in Jump and Return NMR Experiments. *Chem. Phys. Lett.* **2001**, *337* (1–3), 92–96. https://doi.org/10.1016/S0009-2614(01)00174-9.

(37) Bloch, F. Nuclear Induction. *Phys. Rev.* **1946**, *70* (7–8), 460–474. https://doi.org/10.1103/PhysRev.70.460.

(38) Abragam, A. *The Principles of Nuclear Magnetism*; Clarendon Press, 1983.

(39) Vlassenbroek, A.; Jeener, J.; Broekaert, P. Radiation Damping in High Resolution Liquid NMR: A Simulation Study. *J. Chem. Phys.* **1995**, *103* (14), 5886–5897. https://doi.org/10.1063/1.470468.

(40) Huang, S. Y.; Anklin, C.; Walls, J. D.; Lin, Y. Y. Sizable Concentration-Dependent Frequency Shifts in Solution NMR Using Sensitive Probes. *J. Am. Chem. Soc.* **2004**, *126* (49), 15936–15937. https://doi.org/10.1021/ja046208s.

(41) Bayer in Radiology | Gadavist® (gadobutrol) injection 1 mmol/mL https://www.radiologysolutions.bayer.com/products/mr/contrast/gadavist/ (accessed Nov 18, 2018).

(42) Bayer in Radiology | Magnevist® (gadopentetate dimeglumine) injection 0.5 mmol/mL https://www.radiologysolutions.bayer.com/products/mr/contrast/magnevist/ (accessed Nov 18, 2018).

(43) Takeda, K.; Kobari, M.; Akaishi, S.; Matsuno, S. Targeting Pancreatic Chemotherapy Cancer Using Liposome against Antibody-Combined. *J. Exp. Med.* **1994**, *175*, 29–42.

(44) Mulder, W. J. M.; Strijkers, G. J.; Griffioen, A. W.; Bloois, L. van; Molema, G.; Storm, G.; Koning, G. A.; Nicolay, K. A Liposomal System for Contrast-Enhanced Magnetic Resonance Imaging of Molecular Targets. *Bioconjugate Chem.* **2004**, *15*, 799–806. https://doi.org/10.1021/bc049949r.

(45) Van Tilborg, G. A. F.; Mulder, W. J. M.; Deckers, N.; Storm, G.; Reutelingsperger, C. P. M.; Strijkers, G. J.; Nicolay, K. Annexin A5-Functionalized Bimodal Lipid-Based Contrast Agents for the Detection of Apoptosis. *Bioconjug. Chem.* **2006**, *17* (3), 741–749. https://doi.org/10.1021/bc0600259.

(46) Hsu, C.-H. Early Cancer Detection by Active Feedback Magnetic Resonance Molecular Imaging, National Tsing-Hua University, 2014.

(47) Gillis, P.; Moiny, F.; Brooks, R. A. OnT2-Shortening by Strongly Magnetized Spheres: A Partial Refocusing Model. *Magn. Reson. Med.* **2002**, *47* (2), 257–263. https://doi.org/10.1002/mrm.10059.

(48) Matsumoto, Y.; Jasanoff, A. T2 Relaxation Induced by Clusters of Superparamagnetic Nanoparticles: Monte Carlo Simulations. *Magn. Reson. Imaging* **2008**, *26* (7), 994–998. https://doi.org/10.1016/J.MRI.2008.01.039.

Part II. Use of Natural Iron Content in the Body for MR Contrast Enhancement for Early Theranostics

Chapter 4

Contrast and Sensitivity Enhancement for Early Tumor Detection Using a Ferritin Replicon

Abstract

The improvement in MRI contrast and sensitivity would greatly help in the detection of early tumors. However, the toxicity of contrast agents often creates various complications. In this context, recent studies have shown promising directions to develop nontoxic contrast agents by utilizing MR reporter genes, such as the iron-binding protein ferritin. Ferritin could be overexpressed in cells, forming ferritin cages that conserve iron in the superparamagnetic form capable of improving MRI contrast. Here this protein is expressed by a self-replicating viral-RNA molecule derived from Nodamura, a ssRNA insect virus, which has a very compact genome, split between two co-packaged RNA molecules. Among them, RNA1 (replicon) molecule encodes the virus's own RNA-dependent RNA polymerase (RdRp) which acts both on RNA1 and RNA2 allowing them to self-replicate autonomously without the need for any other viral protein. Specifically, we seek to utilize this self-replicating RNA to express and amplify ferritin, leading to increased iron storage in the form of ferrihydrite. These superparamagnetic iron oxide crystals could enhance contrast in MR images. We have assessed the effect on MRI relaxivity for the construct RNA1 Noda-ferritin transfected cells both in *in vitro* and *in vivo* experiments and compared the results with Noda-luciferase construct used as a control. We have shown the effect

of these constructs with and without the presence of tumor cells and presented statistical data for mice models.

4.1. Introduction

The detection of early tumors in clinical practice could significantly improve the prognosis of cancer and potentially save ~30% of the patients, based on various assumptions. Magnetic resonance imaging (MRI)[1] has advantages for its nonionizing radiation and is preferred over other ionizing techniques for early detection purposes. However, it suffers from poor contrast and low sensitivity and fails to detect small tumors. Since, tumor morphology is quite similar to that of healthy tissue, it becomes very difficult to distinguish the former from latter by the MRI method. One of the common ways to improve the contrast is by using MR contrast agents[2] that attach to the tumor and improve its observability. The most common contrast materials are metal compounds[2] such as gadolinium (Gd) chelates, iron oxide (IO) nanoparticles, manganese (Mn) chelates etc. However, these are foreign materials to the human body and generally have some toxic effects. Further, those exogenous contrast agents are often limited in terms of extent of penetration and delivery. Therefore, there is an urgent need to develop risk-free MR contrast for early detection of tumors.

In this context, endogenous MR reporter genes[3–7] could be particularly useful to assess microenvironment, monitor gene therapy, transgene expression, understanding metabolic processes etc. They could improve the signals from cells for MR imaging and the MR signal would not be diluted even after cell division. However, the development of MR reporter genes is still in its infancy and as contrast agents, they often suffer from poor sensitivity, low resolution and sometimes pharmacokinetics issues.[7] Commonly used MR reporter genes include enzyme-based moieties, various receptors on cells and metalloproteins. Metalloproteins could help to improve the MR contrast by binding and increasing the concentration of metal inside the cell. One of the

ideal candidates is Ferritin,[8–22] that binds to iron in human cells and stores it in a form of superparamagnetic iron oxide (SPIO), which is a well-known MR contrast agent.

Ferritin is an iron storage protein in almost all species. Ferritin cages (shown in **Figure 4.1**)[23] preserve iron, and are composed of 24 subunits with a mix of heavy (21kDa) and light chains (19kDa). The light chain is responsible for maintaining stability of the ferritin cage and heavy chain transforms Fe (II) to Fe (III) and helps in cage construction etc.[24] The internal and external diameters of a ferritin cage are about 8 and 12 nm, respectively.[24] The ferritin cages store iron as superparamagnetic ferrihydrite crystals and act as T_2 contrast agents in MRI.[25] Recent studies have shown that ferritin has impressive potential[8,12,15,16,18,22] to act as a nontoxic contrast agent to accumulate iron oxide in the cells to monitor tumor locations; it is a noninvasive marker to probe therapeutic outcome and it can be delivered using viral vectors.[9,11,25,26] Further, it is able to cross blood-brain-barrier, which is hard for exogenous contrast agents.[8] However, its low sensitivity and resolution are still significant problems in MR detection.

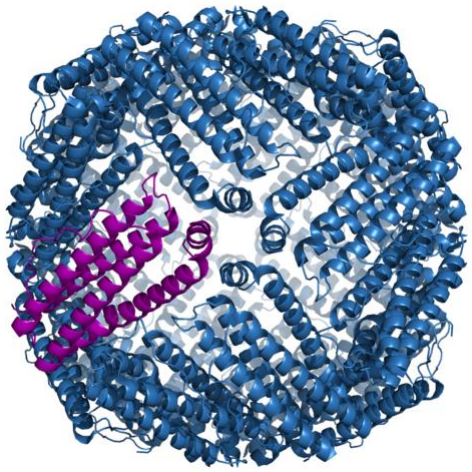

Figure 4.1. Schematic diagram of ferritin: It illustrates the ferritin cage structure. This is a murine ferritin complex. Image is taken from https://en.wikipedia.org/wiki/Ferritin.[23]

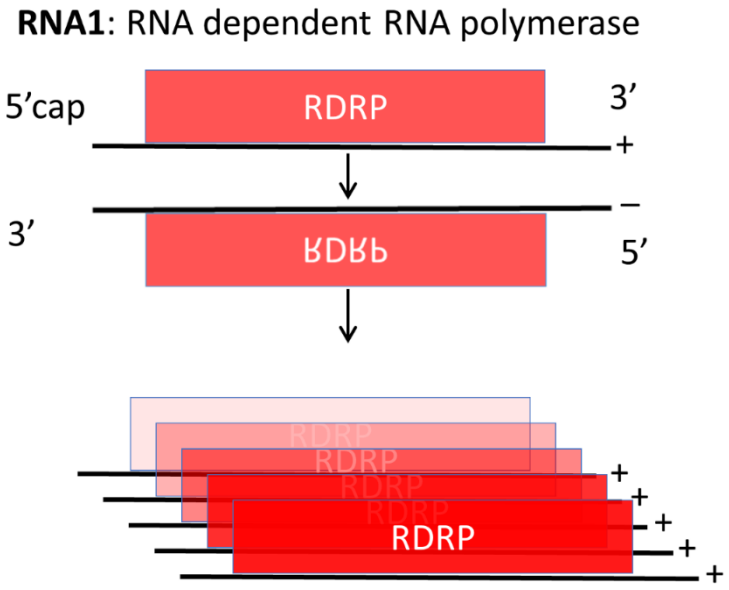

Figure 4.2. Self-replication of RNA1: It illustrates self-replicating feature of RNA1. RNA1 encodes its own RNA dependent RNA polymerase (RdRp) and replicates numerous copies of positive strand from a single one.

Therefore, to improve contrast, we have used a new method to amplify ferritin protein without requiring cell division. We have proposed and shown that the amplification of ferritin expression could be achieved by utilizing a replicon, a self-replicating RNA. The replicon is the RNA dependent RNA polymerase (RdRp) of Nodamura.[27–29] **Figure 4.2** illustrates the self-replication of RNA1, which codes virus's own RdRp and this autonomous replication minimizes the demands on host. RNA 1 is able to express foreign genes and could be packaged inside Cowpea Chlorotic Mottle Virus (CCMV)[30–32] for *in vivo* or *in vitro* delivery. So altogether, replicon is an ideal platform to engineer our gene of interest (GOI). **Figure 4.3** shows examples of such engineered constructs of different GOI with replicon.

Figure 4.3. Replicon constructs: RNA1 could amplify any gene of interest. Ferritin gene is fused with RdRp of RNA1 by T2A self-cleaving peptide to amplify ferritin protein. This construct is termed replicon-ferritin and its expression will lead to an increase in iron storage and MR signal amplification. The replicon-control is the RdRp bound to the luciferase gene that supposed not to show any MR signal enhancement, as luciferase cannot bind to iron.

In this work, we have utilized the replicon to express and amplify ferritin protein in the cells. This amplification in ferritin will lead to increased binding and storage of iron oxide inside the ferritin cage in a form of SPIO, and subsequently lead to increased T_2 ($1/R_2$) contrast in MRI. This scheme has been illustrated in **Figure 4.4**. We have performed both *in vivo* and *in vitro* experiments, analyzed and compared our data in different environments, such as in the presence and absence of tumor cells. We have seen significant contrast enhancement in both *in vivo* and *in vitro* experiments and discussed the feasibility of its use as a contrast agent.

4.2. Results and discussion

In this work, we have taken advantage of the self-replication process of replicon to amplify the naturally occurring iron binding protein, ferritin. For this purpose, we have fused Ferritin gene as our gene of interest (GOI) with RdRp. In a parallel experiment, we have taken our GOI as luciferase, which has no interaction with iron concentration in the cells. Therefore, the construct replicon-luciferase could act as a control to compare the effect of the iron concentration change in

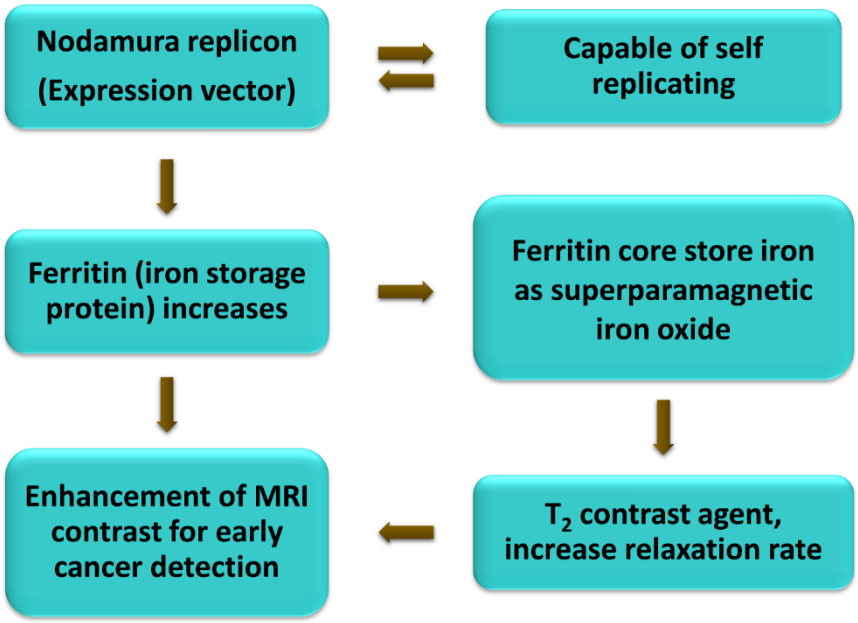

Figure 4.4. Strategy of contrast amplification: This figure shows the full scheme of the project, where self-replicating RNA1 is exploited to amplify iron-binding ferritin protein that would lead to an increased storage of superparamagnetic iron oxide (SPIO) inside the cell. The amplified quantity of T_2 ($1/R_2$) contrast agent SPIO in cell will lead to improved R_2 contrast in the area of interest.

the cells and subsequent effects on MR contrast. We have investigated these two constructs—replicon-ferritin and replicon-control for further *in vivo* and *in vitro* studies to confirm our hypothesis regarding the MR contrast enhancement due to the increased concentration of iron oxide in the cells. The respective constructs of replicon-ferritin and replicon-control are shown in **Figure 4.3**.

4.2.1. *In vivo* study

Glioblastoma multiform (GBM) mice models were created using U87-MG cell line for *in vivo* studies. The GBM cells were transfected with different replicon constructs using lipofectamine. For this purpose, 2.5 - 5 µg of replicon-constructs was added to 250 µL of Opti-

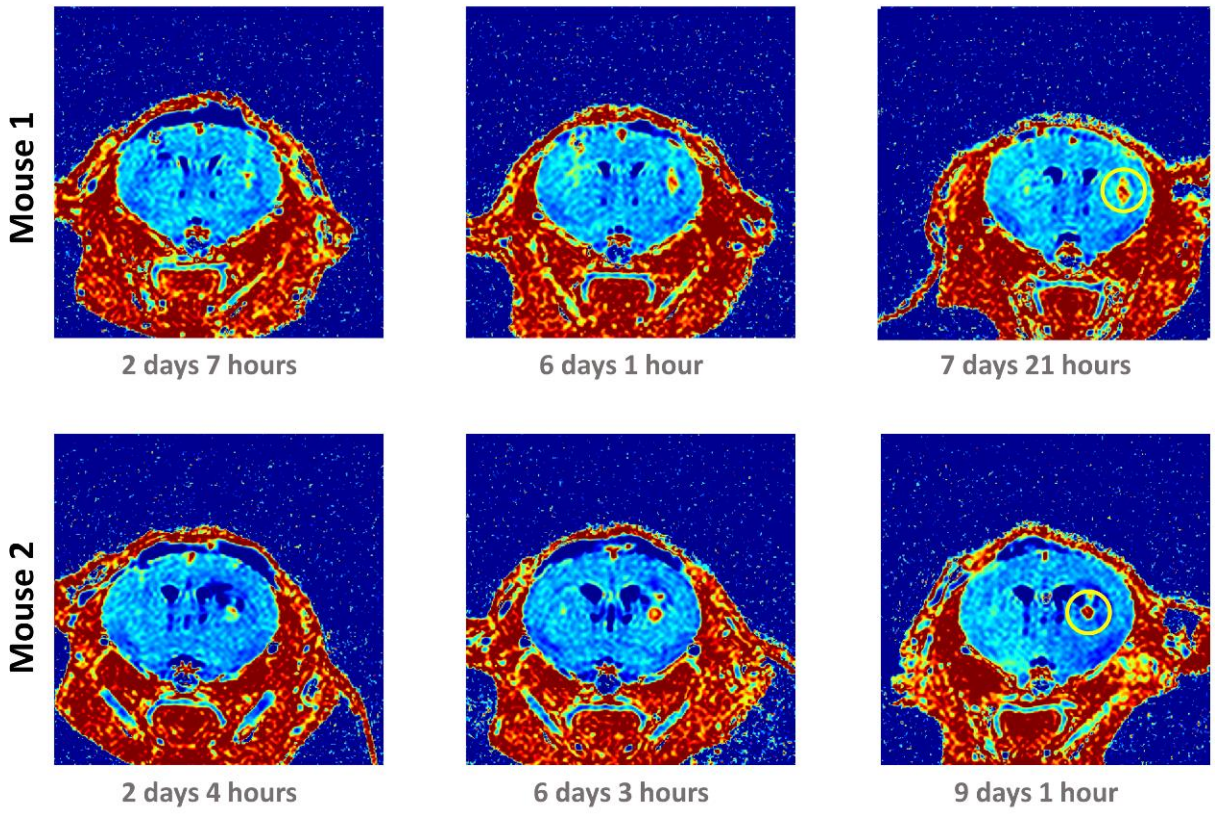

Figure 4.5. Representative *in vivo* images for GBM mouse models at early stages: This figure demonstrates R_2 parameter mapping images. The contrast amplification is seen in right side (side of replicon-ferritin) of the mouse brain for early (~2-9 days after injection of tumor cells) tumor. Both Mouse 1 and Mouse 2 show a region (circled in yellow) in right side with higher contrast, compared to the surroundings and this contrast increases with time. Besides, left side (side of replicon-control) does not show any such area with high contrast. The color scale corresponds to R_2 values.

MEM (Reduced Serum Media), and 15 µL of lipofectamine was added to 250 µL of Opti-MEM. After ~ 5 minutes these two solutions were mixed together to prepare ~500 µL replicon mixture. After about 25 minutes, the prepared replicon mixture was added to $2\times10^{\wedge6}$ cells (U-87 MG) contained in 1.5 ml Opti-MEM with 2% fetal bovine serum (FBS). 2 ml Dulbecco's phosphate-buffered saline (DPBS) was added to the cells and cells were kept for 12-15 hours. Then the cell medium was washed away, and fresh cell culture medium was added to grow cells for another 8-

12 hours and finally cells were harvested with trypsin, washed 3 times with phosphate-buffered saline (PBS) and centrifuged at 967.5 g for 5 minutes. 5 μl of the transfected cells (number of cells ~$1.5\times10^{\wedge5}$ - $5\times10^{\wedge5}$) with replicon-ferritin were injected to the right sides of the brain of a mouse and the replicon-control with cells were infected (5 μl) into the left sides respectively for evaluating the effects of the experiment and control simultaneously. During the experiment, the mouse was anesthetized with Ketalar (40 mg/kg) and Rompun (15 mg/kg). The animal MRI was acquired with a 7 T Varian microimaging system and all MR images have FOV = 3 cm × 3 cm, thickness = 0.8 mm, matrix size = 128 × 128, and zero padding = 512 × 512. The T_2-weighted images were acquired by spin echo multi slice (SEMS) with repetition time (TR) 7.5 s and varying echo time (TE) like 10, 30, 50, 70, 90 ms etc.

Twelve mice were evaluated and R_2 ($1/T_2$) parameters were plotted for the right and left sides of the mouse's brain. **Figure 4.5** shows R_2 mapping MR images of two representative mice in early days (~1-9 days) after injecting the transfected GBM cells. The presence of intense red-yellow coloration in the right panel of the mouse's brain clearly indicates the contrast enhancement in the right side compared to the left side of the brain. We have calculated the relative contrast as

$$\frac{R_{2,av}(\text{right})-R_{2,av}(\text{left})}{R_{2,av}(\text{left})} \qquad 4.1$$

Where, $R_{2,av}$ (right) is the average R_2 value of intense (high R_2) part in the right side of the brain and $R_{2,av}$ (left) is the average R_2 value of intense (high R_2) part in the left side of the brain (if high R_2 region exists). We have identified and included the voxels with higher R_2, compared to normal brain tissue to calculate the average R_2. Sometimes, we have observed a lower R_2 value in the tumor region, compared to the normal brain tissue, which might be due to the presence of the

injection fluid. The average increase in relative positive contrast has been observed to be about 7 % for initial 1-4 days and ~12 % for 7-10 days after the injection. In the case of a particular mouse, we have seen a maximum relative contrast enhancement of ~32 % in 7-10 days. Lower contrast values obtained during the initial 1-4 days might reflect the fact that the tumor did not grow sufficiently during this period. In general, we have observed inhomogeneous tumor growth and a mix of higher and lower R_2 regions inside the tumor. Sometimes hotspots are only concentrated in a small region of the tumor, rather than covering the entire tumor area. We have found that the R_2 value averaged over the entire tumor area was higher compared to that in the normal brain tissues. The averaging procedure often results in a poor contrast, compared to the expected contrast in the hotspot areas only. However, it is difficult to choose our region of interest without any bias. Moreover, we have noticed such higher R_2 regions in the hotspot regions of the left side (control side) of the mouse brain also. So, it might be due to the blood clots that could be formed during the injection procedure. Another possibility is the different growth-rate and morphology of the tumors in the two sides of the brain. We have shown all the data and statistical analyses in **Table S4.1** for the initial days (~1-4 days) and after ~7-10 days. Since, we are discussing the detection of early tumors, the data for later days have not been included here. We find that the hotspot regions in the left side having higher R_2 values give negative contrast. Considering both the positive and negative contrasts, only 4 % increase for initial days and ~9 % for later days have been observed. The fluctuations in data might come from the presence of injection fluid, differences of tumor growth and morphology, and choice of the region of interest. Since, a lot of uncertainties are coming from the inherent inhomogeneity of the orthotopic brain tumor models, a localized subcutaneous model might be used in future for the sake of simplicity.

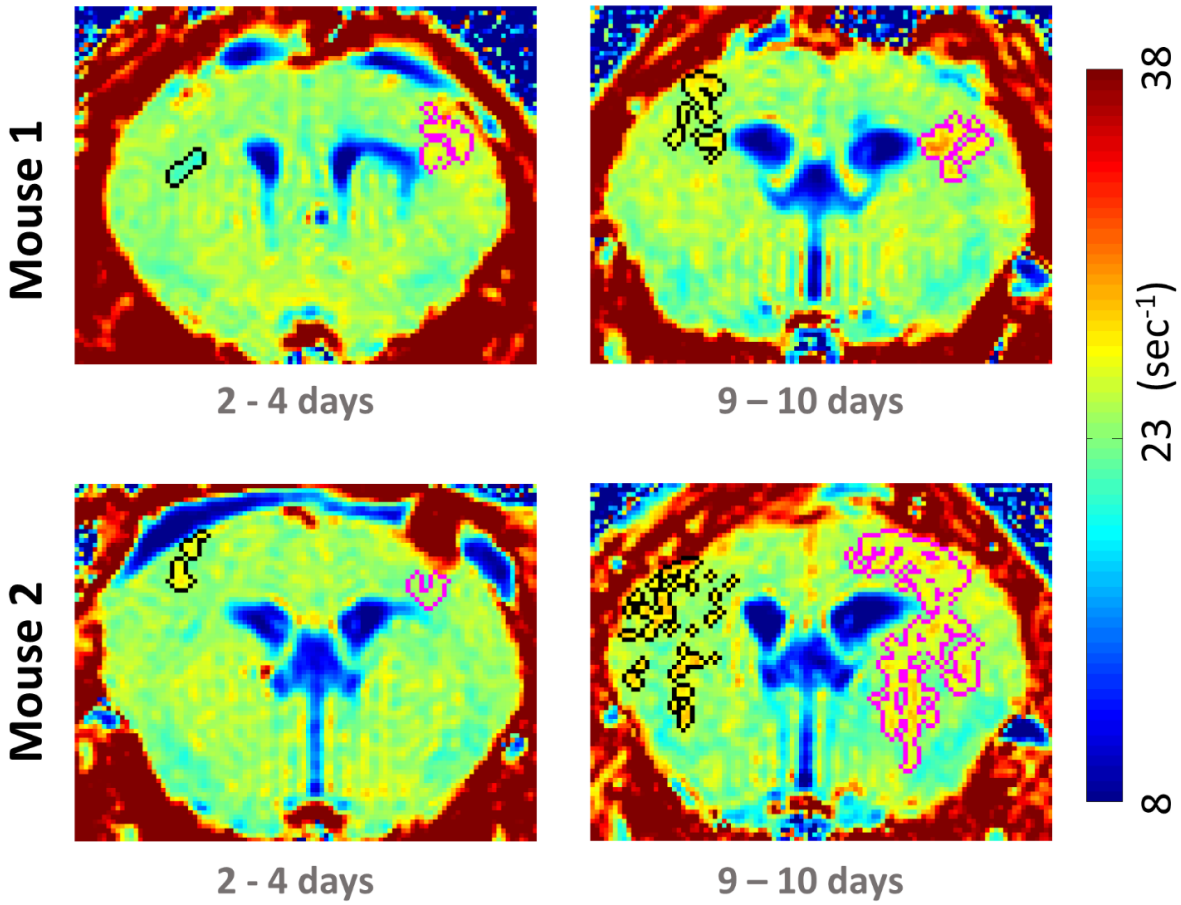

Figure 4.6. Representative *in vivo* images for mouse models without tumor at early stages: This figure demonstrates representative mouse images, after the injection of only replicon constructs without tumor cells. It shows both right (circled in pink) and left (circled in black) have shown higher R_2 compared to the surroundings. However, still we can see comparatively higher contrast in the right area (side of replicon-ferritin) than left area (side of replicon-control). The contrast in right side is particularly better after 9-10 days of injection. All images are R_2 mapping images and R_2 values are shown in the color scale.

We have carried out another set of control *in vivo* experiments by injecting only the construct (with invivofectamine instead of lipofectamine) - replicon-ferritin and replicon-control to the right and left sides of the mouse's brain respectively to eliminate the complications arising due to the tumor model. **Figure 4.6** shows the R_2 parameter mapping images for a representative mouse. We can see that a part in the right side has greater contrast compared to the left side, which

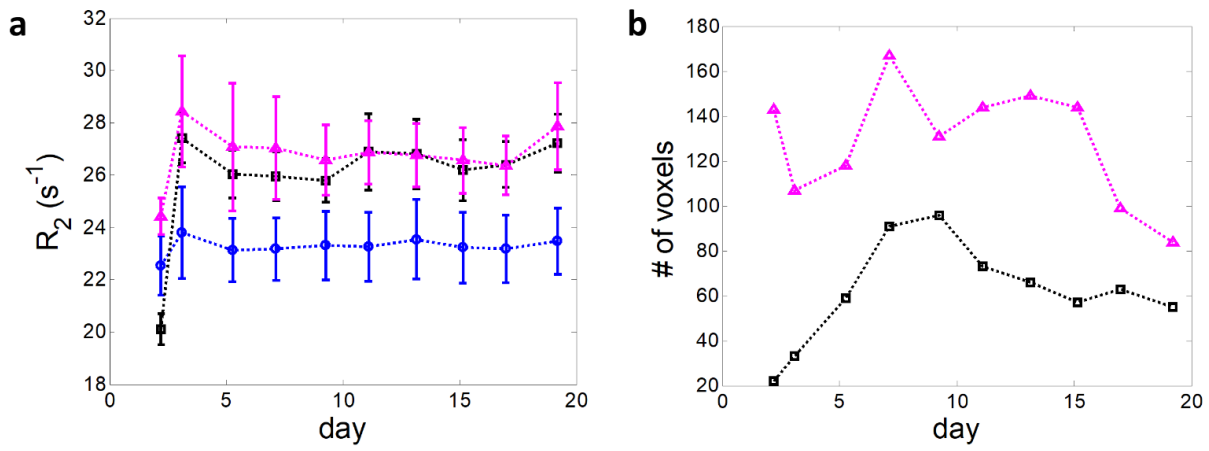

Figure 4.7. a) Variation of R_2 parameter for different region: Representative mouse data shown in different days after injecting the replicon-ferritin and replicon-control solutions. The pink color indicates a higher R_2 region in the right side (side of replicon-ferritin), black is indicating the same for left side (side of replicon-control) and blue represents the average R_2 of regular brain tissue. Definite increase of R_2 has been observed for affected regions compared to regular brain tissue. b) Voxel size of different regions: Number of voxels with higher R2 compared to regular brain tissue are plotted. Pink color represents the right side of the brain, where black is showing for left region of the brain. It shows, the example of one mouse, where we found number of voxels in right side is larger, compared to left side.

could be attributed to the contrast enhancement due to the ferritin amplification. It is worthwhile to mention that, whether or not we would be able to observe the difference in contrast between the right and left sides of the mouse brain, we have always observed positive contrast between the injected areas and normal brain tissues (**Figure 4.7a**). The detailed statistical data for the contrast between the right and left sides of the mouse's brain is presented in **Table S4.2**, where we can see an average positive contrast. However, large fluctuations in contrast exist. We think our choice of voxels might be partly responsible for the fluctuations in the contrast. Often, larger number of voxels in the right side (ferritin side) compared to the left side (control) have shown positive contrast. **Figure 4.7b** illustrates such an example. This feature might result in a lower than expected average R_2 in the ferritin side. However, it is hard to choose a region of interest for calculating contrast, without any kind of prior preferences. In addition, fluctuations might also

come from the somewhat uncontrolled amount of fluid injected to the mouse in different experiments. Blood clots or hemorrhage might be responsible for the negative contrasts as well. Therefore, to understand the *in vivo* results and detailed mechanism, we have mimicked the experiment in an *in vitro* setup.

4.2.2. *In vitro* study

To carry out *in vitro* experiments, a source of iron supplementation was required during the cell culture unlike *in vivo* experiments, where the animal body has its own iron source. For this purpose, previous experiments[9,11,15,20] have employed ferric ammonium citrate (FAC),[11,15] and holotransferrin.[9,20] Here, we have used 2 mg/ml of holotransferrin and 1mM FAC in our optimized protocol, as they more closely mimicked the natural biological process. 5 μg of replicon-construct was used for each 10 cm cell plate and the cells were transfected with lipofectamine 2000. We have carried out all of our *in vitro* experimental assays with and without iron supplementation in this form. Replicon constructs were introduced to Baby Hamster Kidney (BHK) cells in addition to GBM (U-87 MG). Since many research works were previously performed with Nodamura replicons using BHK cells,[27,33] we have included BHK as a reference.

All *in vitro* experiments were done in a 600 MHz (AV600, Bruker) Nuclear Magnetic Resonance (NMR) spectrometer and micro-imaging setup. Usually, horizontal MR machines are used for cell experiments, however we have used a vertical one. Therefore, an inhomogeneous gradient is formed along the capillaries due to the gravity effect, showing large fluctuations in sampling because of the presence of unequal numbers of cells. This inherent deviation in sampling was larger than differences between different samples. Thus, we have carried out a couple of experiments for optimization. The cells are packed into capillaries and centrifuged at a speed of

500 g for 2 minutes. Extra liquid is taken out from the top with a Hamilton syringe. We have assumed that the cells in different capillaries should form a uniform vertical gradient under centrifugal force. Hence, we have detected the homogeneous region in regular MR image and compared signals from the slices with thicknesses of about 0.8-1.2 mm at the same height. However, still we have seen fluctuations, because the amount of cells present in a slice of thickness ~ 1 mm may not be enough to reach a statistically significant conclusion. Usually, a full cell plate is used in horizontal MRI to avoid these kinds of uncertainties. To overcome this problem, we have packed cells from each 10 cm cell plate into two to three capillaries, centrifuged at a speed of 500 g for 2 minutes and taken out extra liquid from the top, as described previously. In this way, we got 2-3 capillaries of one sample from each cell plate. We have put each set of capillaries inside 5 mm capped glass tube separately. Then MR parameter R_2 was measured using NMR spectroscopy with spin echo pulse sequence. We have acquired combined signal from all the capillaries containing the same sample from the whole cell plate. Each such sample was measured separately, in an identical spectrometer condition. Thus, we have compared the signals from the whole cell plates, similar to other studies done in horizontal MRI, assuming each cell plate of equal dimension would carry near equal number of cells.

Finally, we have transfected both cell lines (U-87 MG and BHK-21) with replicon-ferritin and replicon-control in parallel. Control experiments were done before transfecting the cells with or without iron supplements. R_2 was measured using spin echo pulse sequence with relaxation delay time (D1) 15 sec, number of scans = 1. TE (time of echo) were 500 us, 2 ms, 4 ms, 6 ms, 8 ms, 10 ms, 15 ms, 20 ms, 25 ms, 30 ms, 35 ms, 40 ms, 50 ms, 70 ms,100 ms, 150 ms and 200 ms. Each MR measurement was repeated three times and the average value and standard deviation were calculated.

Table 4.1. Comparison of *in vitro* R_2 in different conditions: a) Variation of R_2 parameter for different constructs: It illustrates the R_2 measurement in two different cell lines (BHK and GBM) for replicon-ferritin and replicon-control. b) R_2 parameter study in control *in vitro* experiments: Demonstrates the differences of R_2 values with or without iron supplements (same amount as used during transfection) for different cell lines (BHK and GBM).

a)

Type of cell	R_2 (s^{-1})	
	Replicon-Luciferase	Replicon-Ferritin
BHK	48.03 ± 0.03	51.83 ± 0.04
GBM	37.89 ± 0.03	42.75 ± 0.07

b)

Type of cell	R_2 (s^{-1})	
	Before transfection w/Fe	Before transfection w/o Fe
BHK	40.85 +/-0.01	39.62 +/- 0.01
GBM	33.75 +/-0.08	24.24 +/- 0.02

Table 4.1a shows the R_2 values of different cell lines, when transfected with replicon-ferritin or replicon-control (24-36 hours after transfection), indicating that there is a 7.9 % relative contrast enhancement in R_2 for BHK cells, compared to the control, whereas, 12.8 % relative

increase was seen for the GBM cells compared to the control. Standard deviations range from ~3-7 %, which are significantly smaller than the change. Therefore, we conclude that observation of a positive contrast enhancement for replicon-ferritin could be attributed to the higher SPIO content in the cell. We have repeated this study for other time points, such as 3 days or 5 days after transfection. However, we could not confirm any specific trend, and obtained highest contrast during the initial 24-36 hours so far. The optimization of the frequency of the iron supplement, might help to determine the pattern of time dependence of the amplification. We have also done experiments with varying amounts of replicon-construct and iron supplements; however, we have not seen any further improvement in contrast. Thus, we have kept the concentrations same as previously described (2 mg/ml of holotransferrin ,1mM FAC and 5 μg replicon-construct/ 10 cm cell-plate) and cells were collected 24-36 hours after trasfection for rest of the experiments.

To understand the details of *in vivo* experiments, we have done a couple of control experiments to understand the effect of iron supplement. We have recorded the R_2 of cells before transfection and then with equal amount of iron supplement. The results are shown in **Table 4.1b** showing the increase of R_2 after the addition of supplemental iron in both the cell lines as expected. However, a closer look reveals that the increase (~39%) of R_2 in the GBM cells is much higher compared to that (~3%) in the BHK cells, before and after the addition of iron supplements. Since we have recorded the signal after washing away excess iron in the medium, it indicates that the GBM cells are more prone to uptake iron compared to the nonmalignant BHK cells. This might explain the *in vivo* result showing better contrast for the GBM mice models versus the healthy models. It is noteworthy that, the transfected cells show higher R_2, compared to the native cells in both the cases. We have also seen a similar trend in the *in vivo* results. In spite of the difference between the right and left sides of the mouse brain, we have always observed a change in contrast

between normal brain tissue and the replicon-ferritin/replicon-control part. So, at the qualitative level, *in vivo* and *in vitro* experiments give similar results. However, there seems to be some disagreement between the *in vivo* and *in vitro* experiments at the quantitative level. It is possible that these differences are coming from different iron sources and local environments.

4.3. Conclusions

In this work, we have shown the possibility of using a novel contrast agent that is naturally present in human body to develop a risk free technique for early tumor detection. We have presented a proof of principle study for enhancing iron concentration inside the cell by the use of a self-replicating RNA molecule, replicon. Replicon-luciferase has been used as a control and both *in vivo* and *in vitro* studies have been performed. Both studies have shown a positive contrast in the side of mouse's brain where replicon-ferritin was injected compared to the control side in early time points. Further, both the studies have shown an improved contrast for the malignant tumor compared to the normal tissue. In particular, *in vivo* results have shown ~12.4 % positive contrast enhancement in the GBM mice models compared to the replicon-ferritin model. However, large fluctuations in contrast were seen requiring *in vitro* studies that showed 12.8 % increase in relative contrast with respect to the control. Future studies are required to optimize the protocol and obtain more statistical data. Future experiments on optimization and time point calibration could give more insights of the process and help to achieve contrast enhancement in early tumor detection in clinical practice.

Supplementary materials

Table S4.1. Statistical data for tumor bearing mice: Illustrates the average R_2 data for all mice in both sides of the brain in ~1-4 days and ~7-10 days after injection of replicon constructs with tumor cells. Calculation of relative contrast is shown.

Mouse ID	R_2 (sec^{-1})				Relative contrast **(%)**	
	Replicon-ferritin side		Replicon-control side			
	1 - 4 (days)	7 - 10 (days)	1 - 4 (days)	7 - 10 (days)	1 - 4 (days)	7 - 10 (days)
1	27.7	29.1	24.4	24.5	13.5	18.8
2	28.8	27.7	24.8	23.8	16.1	16.4
3	26.1	28.8	25.9	27.5	0.8	4.7
4	26.2	28.5	26.1	27.8	0.4	2.5
5	26.7	27.7	26	27.5	2.7	0.7
6	28.2	36	28.9	32.2	-2.4	11.8
7	27.3	32.9	23.7	29.3	15.2	12.3
8	25.4	30.7	25.3	31.1	0.4	-1.3
9	26	33.9	24.2	25.7	7.4	31.9
10	26	33.4	27.3	29.7	-4.8	12.5
11	23.8	29.9	26.7	32.3	-10.9	-7.4
12	26.9	26.7	24.7	26.8	8.9	-0.4
Overall average					3.9 ± 8.4	8.5 ± 10.8
Positive average					7.3 ± 6.5	12.4 ± 9.5

Table S4.2. Statistical data for mice without tumors: Demonstrates the average R_2 data for all mice in both sides of the brain in ~1-4 days and ~7-10 days after injection of replicon constructs without tumor cells. Calculation of relative contrast is shown.

Mouse ID	R_2 (sec^{-1})				Relative contrast **(%)**	
	Replicon-ferritin side		Replicon-control side			
	1 - 4 (days)	7 - 10 (days)	1 - 4 (days)	7 - 10 (days)	1 - 4 (days)	7 - 10 (days)
1	23.9	30	26	31.7	-8.1	-5.4
2	24.3	26.9	20.1	26.1	20.9	3.1
3	24.2	25.3	24.9	28.8	-2.8	-12.1
4	25	25.6	25.2	26.4	-0.8	-3.0
5	18	28.9	20.9	27.2	-13.9	6.2
6	16.2	28.5	14	27.7	15.7	2.9
Overall average					1.8 ± 13.6	-1.4 ± 6.8
Positive average					18.3 ± 3.7	4.1 ± 1.9

Acknowledgements

I gratefully acknowledge Mr. Jerrell Tisnado for performing all the biological work, Dr. Chao-Hsiung Hsu for carring out *in vivo* experiments. I thank Dr. Zhao Li and Ms. Huimin Yang for helping during *in vivo* experiments. I want to specially thank Prof. Yung-Ya Lin, Prof. Charles Knobler and Prof. William Gelbart for their guidance and supervison.

References

(1) Liang, Z.-P.; Lauterbur, P. C.; IEEE Engineering in Medicine and Biology Society. *Principles of Magnetic Resonance Imaging : A Signal Processing Perspective*; SPIE Optical Engineering Press, 2000.

(2) Merbach, A. E.; Helm, L.; Tóth, E. *The Chemistry of Contrast Agents in Medical Magnetic Resonance Imaging*, 2nd ed.; Wiley: Chichester, UK, 2013. https://doi.org/10.1002/9781118503652.

(3) Yang, C.; Tian, R.; Liu, T.; Liu, G. MRI Reporter Genes for Noninvasive Molecular Imaging. *Molecules* **2016**, *21* (5), 1–16. https://doi.org/10.3390/molecules21050580.

(4) Vandsburger, M. H.; Radoul, M.; Cohen, B.; Neeman, M. MRI Reporter Genes: Applications For Imaging Of Cell Survival, Proliferation, Migration and Differentiation. *NMR Biomed.* **2013**, *26* (7), 872–884. https://doi.org/10.1002/nbm.2869.

(5) Lee, S. W.; Lee, S. H.; Biswal, S. Magnetic Resonance Reporter Gene Imaging. *Theranostics* **2012**, *2* (4), 403–412. https://doi.org/10.7150/thno.3634.

(6) Westmeyer, G. G.; Jasanoff, A. Genetically Controlled MRI Contrast Mechanisms and Their Prospects in Systems Neuroscience Research. *Magn. Reson. Imaging* **2007**, *25* (6), 1004–1010. https://doi.org/10.1016/j.mri.2006.11.027.

(7) Gilad, A. A.; Winnard Jr, P. T.; van Zijl, P. C. M.; Bulte, J. W. M. Developing MR Reporter Genes: Promises and Pitfalls. *NMR Biomed.* **2007**, *20*, 275–290. https://doi.org/10.1002/nbm.

(8) Deans, A. E.; Wadghiri, Y. Z.; Bernas, L. M.; Yu, X.; Rutt, B. K.; Turnbull, D. H. Cellular MRI Contrast via Coexpression of Transferrin Receptor and Ferritin. *Magn. Reson. Med.* **2006**, *56* (1), 51–59. https://doi.org/10.1002/mrm.20914.

(9) Iordanova, B.; Robison, C. S.; Ahrens, E. T. Design and Characterization of a Chimeric Ferritin with Enhanced Iron Loading and Transverse NMR Relaxation Rate. *J. Biol. Inorg. Chem.* **2010**, *15* (6), 957–965. https://doi.org/10.1007/s00775-010-0657-7.

(10) Choi, S. H.; Cho, H. R.; Kim, H. S.; Kim, Y. H.; Kang, K. W.; Kim, H.; Moon, W. K. Imaging and Quantification of Metastatic Melanoma Cells in Lymph Nodes with a Ferritin MR Reporter in Living Mice. *NMR Biomed.* **2012**, *25* (5), 737–745. https://doi.org/10.1002/nbm.1788.

(11) Vande Velde, G.; Rangarajan, J. R.; Toelen, J.; Dresselaers, T.; Ibrahimi, A.; Krylychkina, O.; Vreys, R.; Van Der Linden, A.; Maes, F.; Debyser, Z.; et al. Evaluation of the

Specificity and Sensitivity of Ferritin as an MRI Reporter Gene in the Mouse Brain Using Lentiviral and Adeno-Associated Viral Vectors. *Gene Ther.* **2011**, *18* (6), 594–605. https://doi.org/10.1038/gt.2011.2.

(12) Cohen, B.; Ziv, K.; Plaks, V.; Harmelin, A.; Neeman, M. Ferritin Nanoparticles as Magnetic Resonance Reporter Gene. *Wiley Interdiscip. Rev. Nanomedicine Nanobiotechnology* **2009**, *1* (2), 181–188. https://doi.org/10.1002/wnan.11.

(13) Pawelczyk, E.; Arbab, A. S.; Pandit, S.; Hu, E.; Frank, J. A. Expression of Transferrin Receptor and Ferritin Following Ferumoxides-Protamine Sulfate Labeling of Cells: Implications for Cellular Magnetic Resonance Imaging. *NMR Biomed.* **2006**, *19* (5), 581–592. https://doi.org/10.1002/nbm.1038.

(14) Harmelin, A.; Meir, G.; Dafni, H.; Neeman, M.; Cohen, B. Ferritin as an Endogenous MRI Reporter for Noninvasive Imaging of Gene Expression in C6 Glioma Tumors. *Neoplasia* **2006**, *7* (2), 109–117. https://doi.org/10.1593/neo.04436.

(15) Genove, G.; DeMarco, U.; Xu, H.; Goins, W. F.; Ahrens, E. T. A New Transgene Reporter for in Vivo Magnetic Resonance Imaging. *Nat. Med.* **2005**, *11* (4), 450–454. https://doi.org/10.1038/nm1208.

(16) HASEGAWA, S.; FURUKAWA, T.; SAGA, T. Molecular MR Imaging of Cancer Gene Therapy: Ferritin Transgene Reporter Takes the Stage. *Magn. Reson. Med. Sci.* **2010**, *9* (2), 37–47. https://doi.org/10.2463/mrms.9.37.

(17) Zhang, X.; Yan, J.; Huang, Y.; Tang, Q.; Ming, P.; Xu, G.; Zhao, N.; Gong, Y.; Liu, L.; Gong, K. Reconstruction and Expression of the MRI-Contrast Protein, Ferritin, with Recombinant Rabies Vectors. *Biotechnol. Lett.* **2010**, *32* (6), 743–748. https://doi.org/10.1007/s10529-010-0229-5.

(18) Zhen, Z.; Tang, W.; Todd, T.; Xie, J. Ferritins as Nanoplatforms for Imaging and Drug Delivery. *Expert Opin. Drug Deliv.* **2014**, *11* (12), 1913–1922. https://doi.org/10.1517/17425247.2014.941354.

(19) Naumova, A. V.; Yarnykh, V. L.; Balu, N.; Reinecke, H.; Murry, C. E.; Yuan, C. Quantification of MRI Signal of Transgenic Grafts Overexpressing Ferritin in Murine Myocardial Infarcts. *NMR Biomed.* **2012**, *25* (10), 1187–1195. https://doi.org/10.1002/nbm.2788.

(20) Pereira, S. M.; Moss, D.; Williams, S. R.; Murray, P.; Taylor, A. Overexpression of the MRI Reporter Genes Ferritin and Transferrin Receptor Affect Iron Homeostasis and Produce Limited Contrast in Mesenchymal Stem Cells. *Int. J. Mol. Sci.* **2015**, *16* (7), 15481–15496. https://doi.org/10.3390/ijms160715481.

(21) Cohen, B.; Benjamin, L. E.; Harmelin, A.; Ziv, K.; Neeman, M.; Israely, T.; Kalchenko, V.; Plaks, V. MRI Detection of Transcriptional Regulation of Gene Expression in Transgenic Mice. *Nat. Med.* **2007**, *13* (4), 498–503. https://doi.org/10.1038/nm1497.

(22) Gossuin, Y.; Burtea, C.; Monseux, A.; Toubeau, G.; Roch, A.; Muller, R. N.; Gillis, P. Ferritin-Induced Relaxation in Tissues: An in Vitro Study. *J. Magn. Reson. Imaging* **2004**, *20* (4), 690–696. https://doi.org/10.1002/jmri.20152.

(23) Granier, T.; D'Estaintot, L. B.; Gallois, B.; Chevalier, J.-M. M.; Précigoux, G.; Santambrogio, P.; Arosio, P.; Langlois d'Estaintot, B.; Gallois, B.; Chevalier, J.-M. M.; et al. Structural Description of the Active Sites of Mouse L-Chain Ferritin at 1.2 Å Resolution. *J. Biol. Inorg. Chem.* **2003**, *8* (1–2), 105–111. https://doi.org/10.1007/s00775-002-0389-4.

(24) Gossuin, Y.; Muller, R. N.; Gillis, P. Relaxation Induced by Ferritin: A Better Understanding for an Improved MRI Iron Quantification. *NMR Biomed.* **2004**, *17* (7), 427–432. https://doi.org/10.1002/nbm.903.

(25) Ahrens, E. T.; Bulte, J. W. M. Tracking Immune Cells in Vivo Using Magnetic Resonance Imaging. *Nat. Rev. Immunol.* **2013**, *13* (10), 755–763. https://doi.org/10.1038/nri3531.

(26) Iordanova, B.; Goins, W. F.; Clawson, D. S.; Hitchens, T. K.; Ahrens, E. T. Quantification of HSV-1-Mediated Expression of the Ferritin MRI Reporter in the Mouse Brain. *Gene Ther.* **2013**, *20* (6), 589–596. https://doi.org/10.1038/gt.2012.70.

(27) Gitlin, L.; Hagai, T.; LaBarbera, A.; Solovey, M.; Andino, R. Rapid Evolution of Virus Sequences in Intrinsically Disordered Protein Regions. *PLoS Pathog.* **2014**, *10* (12). https://doi.org/10.1371/journal.ppat.1004529.

(28) Paul, D.; Bartenschlager, R. Architecture and Biogenesis of Plus-Strand RNA Virus Replication Factories. *World J. Virol.* **2013**, *2* (2), 32. https://doi.org/10.5501/wjv.v2.i2.32.

(29) Ahola, T.; Karlin, D. G. Sequence Analysis Reveals a Conserved Extension in the Capping Enzyme of the Alphavirus Supergroup, and a Homologous Domain in Nodaviruses. *Biol. Direct* **2015**, *10* (1), 16. https://doi.org/10.1186/s13062-015-0050-0.

(30) Cadena-Nava, R. D.; Comas-Garcia, M.; Garmann, R. F.; Rao, A. L. N.; Knobler, C. M.; Gelbart, W. M. Self-Assembly of Viral Capsid Protein and RNA Molecules of Different Sizes: Requirement for a Specific High Protein/RNA Mass Ratio. *J. Virol.* **2012**, *86* (6), 3318–3326. https://doi.org/10.1128/jvi.06566-11.

(31) Annamalai, P.; Rao, A. L. N. Dispensability of 3′ TRNA-like Sequence for Packaging Cowpea Chlorotic Mottle Virus Genomic RNAs. *Virology* **2005**, *332* (2), 650–658.

https://doi.org/10.1016/j.virol.2004.12.009.

(32) Comas-Garcia, M.; Cadena-Nava, R. D.; Rao, A. L. N.; Knobler, C. M.; Gelbart, W. M. In Vitro Quantification of the Relative Packaging Efficiencies of Single-Stranded RNA Molecules by Viral Capsid Protein. *J. Virol.* **2012**, *86* (22), 12271–12282. https://doi.org/10.1128/JVI.01695-12.

(33) Ball, L. A.; Amann, J. M.; Garrett, B. K. Replication of Nodamura Virus after Transfection of Viral RNA into Mammalian Cells in Culture. *J Virol* **1992**, *66* (4), 2326–34.

Part III. Review on Current Trends of Magnetic Resonance Cancer Theranostics with Different Nanoparticles

Chapter 5

Dendrimer- and Copolymer-based Nanoparticles for Magnetic Resonance Cancer Theranostics

Abstract

Cancer theranostics is one of the most important approaches for detecting and treating patients at an early stage. To develop such a technique, accurate detection, specific targeting, and controlled delivery are the key components. Various kinds of nanoparticles have been proposed and demonstrated as potential nanovehicles for cancer theranostics. Among them, polymer-like dendrimers and copolymer-based core-shell nanoparticles could potentially be the best possible choices. At present, magnetic resonance imaging (MRI) is widely used for clinical purposes and is generally considered the most convenient and noninvasive imaging modality. Superparamagnetic iron oxide (SPIO) and gadolinium (Gd)-based dendrimers are the major nanostructures that are currently being investigated as nanovehicles for cancer theranostics using MRI. These structures are capable of specific targeting of tumors as well as controlled drug or gene delivery to tumor sites using pH, temperature, or alternating magnetic field (AMF)-controlled mechanisms. Recently, Gd-based pseudo-porous polymer-dendrimer supramolecular nanoparticles have shown 4-fold higher T_1 relaxivity along with highly efficient AMF-guided drug release properties. Core-shell copolymer-based nanovehicles are an equally attractive alternative for designing contrast agents and for delivering anti-cancer drugs. Various copolymer materials could be used as core and shell components to provide biostability, modifiable surface properties, and even adjustable imaging contrast enhancement. Recent advances and challenges in MRI cancer

theranostics using dendrimer- and copolymer-based nanovehicles have been summarized in this review article, along with new unpublished research results from our laboratories.

5.1. Magnetic resonance cancer theranostics

Theranostics refers to the development of molecular diagnostics and targeted therapeutics in an interdependent, collaborative manner. Nano-theranostics takes advantage of the high capacity of nano-platforms to ferry cargo and load onto them both imaging and therapeutic functions. The resulting nanosystems, which are capable of diagnosis, drug delivery, and monitoring of therapeutic response, are expected to play a significant role in the dawning era of personalized medicine, and much research effort has been devoted toward that goal. For example, magnetic resonance (MR) nano-theranostics uses magnetic nanoparticles for cancer detection by MR molecular imaging and for cancer therapy by MR nanomedicine. Through active and passive targeting mechanisms, the magnetic nanoparticles can serve as "molecular beacons" to enhance the MR image contrast for early lesion detection. Moreover, through interacting with external alternating magnetic fields produced by the MR hardware, these magnetic nanoparticles accumulated at the lesions can generate heat to serve as "molecular bullets" to kill cancer cells directly through hyperthermia or indirectly through thermal activation and controlled release of drugs.

Cancer theranostic approaches include three major components: (i) detection, (ii) targeting, (iii) controlled delivery and release [1–7]. For detection, several methods including positron emission tomography (PET), computed tomography (CT), single-photon emission computed tomography (SPECT), fluorescence, near-infrared (NIR) radiation spectroscopy, and magnetic resonance imaging (MRI) have been used [4]. Among these techniques, MRI serves as a powerful, noninvasive tool for cancer detection and is commonly used worldwide. However, MRI suffers a major drawback—limited contrast between the healthy and malignant tissues in the early stages of cancers. Hence, much effort has been invested to enhance the tumor contrast in MRI by using

different types of contrast agents. At present, gadolinium (Gd) and superparamagnetic iron oxide (SPIO) are the most widely used contrast agents in the clinical setups [8–12].

While a considerable amount of work has been invested in improving Gd and SPIO-based MRI contrast agents, accurate targeting of cancer cells remains a fundamental challenge for cancer theranostics. Conventional chemotherapy cannot distinguish between the healthy cells and diseased cells, and consequently results in the death of a large number of healthy cells. To alleviate this problem, a safer approach of targeted drug delivery is highly desirable. Effective targeting using nanovehicles would allow for a lower administered dosage of therapeutics, thus minimizing the adverse side effects that are major problems for either active or passive targeting.

A common challenge for all types of cancer therapies is the unwanted damage to healthy cells while treating the malignant tumor. Hence, a primary goal of any type of cancer therapy (chemotherapy, gene therapy, immunotherapy, induced hyperthermia, radiotherapy, *etc.*) is to deliver the required drug or gene to the malignant tumor site only and to reduce the damage to healthy cells. For this purpose, a suitable biocompatible and preferably biodegradable nanovehicle is required to deliver the therapeutics to the tumor site, while minimizing any unwanted side effects. The drug release from the nanovehicle is commonly controlled by heat, temperature, or pH values. For example, magnetic hyperthermia could be induced and exploited by coupling the magnetic dipoles of SPIO nanoparticles to an external alternating magnetic field [13], producing heat to kill the drug-resistant cancer cells. Alternatively, the heat generated could be used to manipulate thermosensitive drug carriers for controlled drug release [14]. Particularly, a nanovehicle carrying the drug via an acid cleavable bond could be used for drug delivery by releasing the drug upon approaching the more acidic tumor microenvironment [15]. An effective drug targeting and delivery method would require a suitable and biocompatible nanovehicle to carry the drug and to serve as

a contrast-enhancing agent that could be conjugated to different targeting moieties for efficient detection.

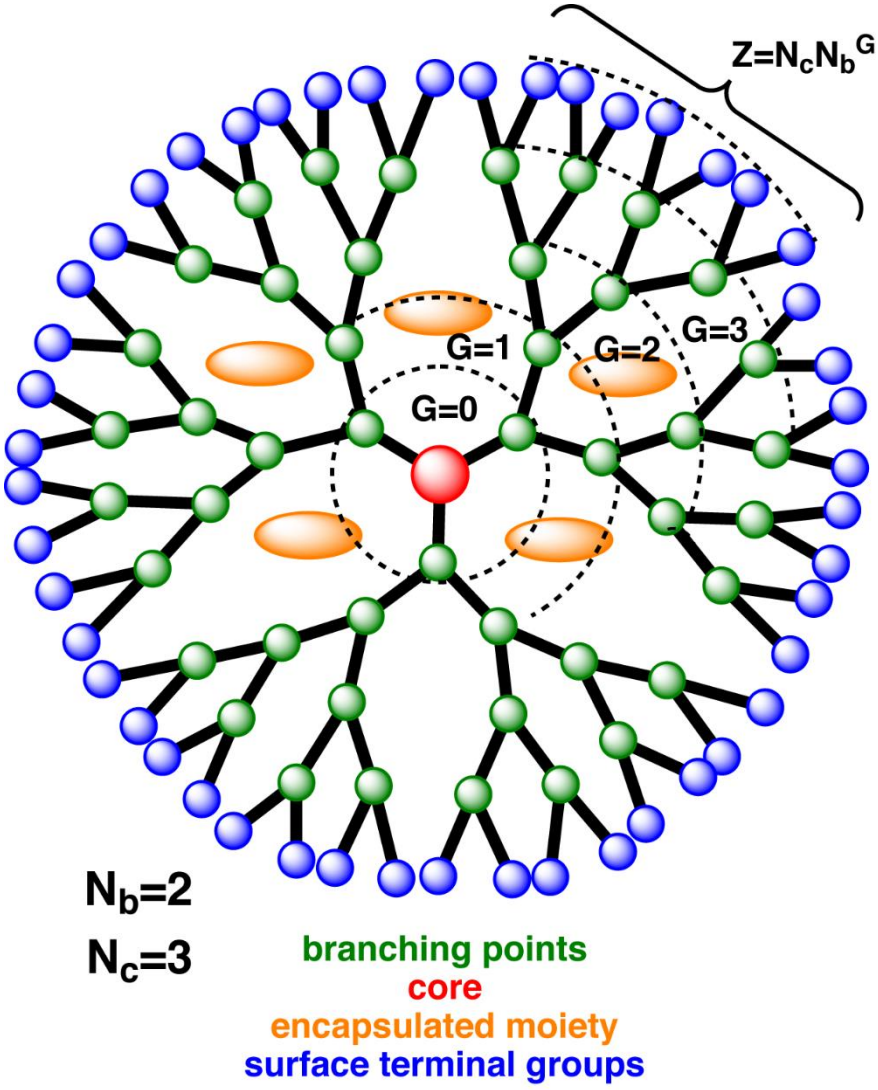

Figure 5.1. Schematic diagram of dendrimer, illustrating core (red), branching points (green), surface terminal groups (blue), and position of encapsulated moiety (orange) that can be contrast agent or drug. The dotted spherical boundaries dictate the generation (G). G = 0 for the core, G = 1 for the next concentric shell, and so on. N_c represents the number of branches in the core, whereas N_b is the branch cell multiplicity. In this figure, $N_c = 3$ and $N_b = 2$, which gives the total number of surface terminal groups, $Z = N_c N_b^G = 48$.

In this review, we summarize various approaches to cancer theranostics within the scope of magnetic resonance with simultaneous diagnosis and treatment. At present, a worldwide effort

is going on in search of suitable nanovehicles for this purpose [16]. In this context, polymer-based nanoparticles are considered more attractive and feasible because of their controllable size and biocompatibility [17]. The scope of this review article is to discuss the current status of research regarding the use of polymer-like dendrimer (**Figure 5.1**) and core-shell copolymer-based (**Figure 5.2**) nanoparticles as nanovehicles for use in cancer therapy in conjunction with MRI-guided detection, diagnosis and treatment. The development of novel nano-biomaterials for contrast agents, targeting, and drug delivery is beyond the scope of this review and can be found in these references [1–4,8,14]. We aim to summarize the most recent advances and directions of dendrimer and core-shell copolymer-based, MRI-guided, theranostic approaches to cancer treatment, including published and unpublished work from our laboratories.

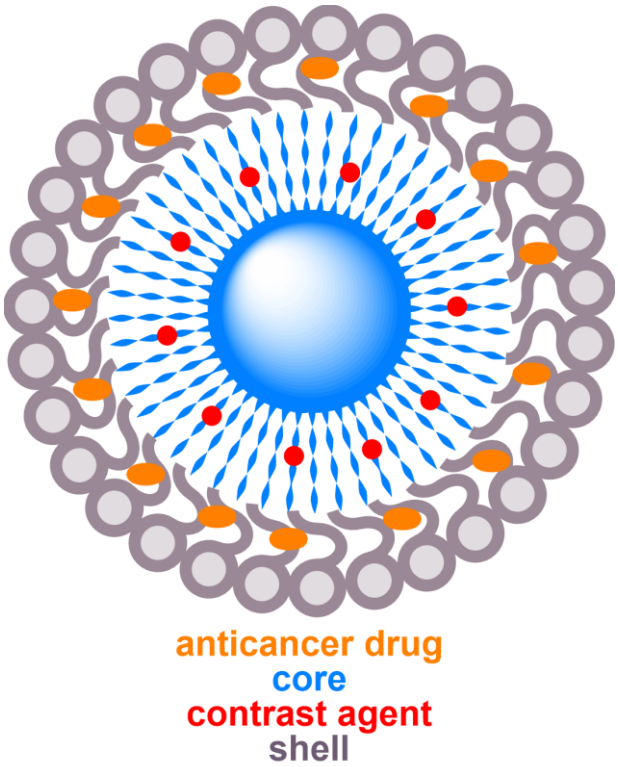

Figure 5.2. Schematic diagram of a typical core-shell structure formed by copolymers, illustrating core (blue), shell (grey), MRI contrast agent (red), and anticancer drug (orange).

5.2. Dendrimer-based nanoparticles for MR cancer theranostics

The dendrimer molecule has polymer-like repetitive structures with a symmetric, almost spherical shape. Most of the polymers are not water-soluble. However, the dendrimers can be made water-soluble if needed. A schematic diagram of the dendrimer is shown in **Figure 5.1**. The dendrimer is used as a versatile drug delivery nanovehicle in nanomedicine. Its flexible structure allows for a wide variety of molecules to be conjugated to the exterior while it is still capable of carrying different kinds of drugs by forming covalent or non-covalent bonds within the core [18]. Dendrimers can modify hydrophobic quantum dots to water-soluble hydrophilic dots and such properties have recently attracted a lot of attention due to the presence of more functional groups at a higher density compared to other linear ligands. For example, the presence of dense ligand layer and the strong inter-ligand interaction in polyamidoamine (PAMAM) dendrimer makes it thermally, chemically and photochemically more stable in comparison to the other hydrophilic ligands with thinner layer. The presence of various anchoring groups increases its versatility for interacting with different ligands for targeting, drug loading and encapsulating contrast agents. Furthermore, the terminal groups can be modified to attach to other biomolecules and reduce their toxicity to benign tissues. These special features make them excellent coating agents as well as nanovehicles [19].

Nanoparticle biodistribution and targeting depend on the size, shape, and heterogeneity of the nanoparticles. The controllable size of the dendrimer is one of its important advantages for cancer therapy applications. Although the dendrimer is highly branched, it has a symmetrical structure as well as a low polydispersity index, reflecting the homogeneous size distribution of the particles. These properties allow the dendrimer to be used for targeting and treating cancer cells [20–22]. Larger particles could be easily identified as foreign objects and eliminated from the body by

the mononuclear phagocyte system (MPS), whereas particles smaller than 5–6 nm could be removed via renal filtration [8]. To increase the circulation time within the body for adequate drug delivery, the optimal size of the nanoparticles should be in the range of 10 nm to 100 nm approximately. The size of the dendritic nanovehicle can be optimized to prolong the circulation time within the body. Moreover, the unique topology of the dendrimer helps it circulate in the bloodstream much longer than a linear polymer.

The dendrimer composition may include a wide variety of substances depending on its applications [18,21,23]. For example, the PAMAM dendrimer is one of the most commonly used classes of dendrimers due to its highly symmetric, multi-branched, spherically ordered structure, and biocompatibility [23,24]. While a large variety of dendrimer compositions have become available in recent years, different generations (G) of dendrimers have also been explored simultaneously in different studies. Generation is a parameter used to classify dendrimers into categories based on their size and branching properties, as depicted in **Figure 5.1**. The terminal surface group (Z) of the dendrimer is related to the core multiplicity (N_c) and branch cell multiplicity (N_b) with generation (G), such that $Z = N_c N_b^G$ [20]. Different generations of dendrimers have distinct spacing and branching features. Void space between the branches and the concentration of exterior branches determines the dendrimer's capability of entrapping and releasing drug molecules, and optimal ratios for conjugation of targeting moieties. Additionally, the dendrimers show generation-dependent cytotoxicity, pharmacokinetics, and biodistribution behaviors [25]. Therefore, a proper choice of generation is crucial in order for the dendrimer to serve as an efficient delivery nanovehicle. Recent therapeutic applications revolve around the use of generation 2.5–5 dendritic nanovehicles [26], as they possess lower cytotoxicity from non-specific drug release at healthy tissue sites in comparison to other conventionally used cationic polymers.

In the following, we will summarize various approaches to functionalize dendrimers for targeting, detection, and drug delivery with minimal side effects under the guidance of MRI techniques. In **Table S5.1** (see supplementary materials), we present a short overview of different possible dendrimer-related therapeutic advances of this field in recent years, with the key details of imaging, targeting approaches, drugs, delivery mechanisms, and types of cancers.

5.2.1. T_2-mode SPIO-based dendrimer nanoparticles

Dendrimer-coated SPIO nanoparticles are one type of ideal candidate for theranostic applications. These complexes are particularly useful for their adjustable size, biocompatibility and low toxicity [27,28]. In recent years, SPIOs have been studied extensively as an important T_2 contrast agent that could exhibit high transverse relaxivity in MRI. This higher relaxivity produces a negative contrast in MRI T_2-weighted imaging. The exact position of the tumor can be determined by this negative contrast, as the MR signal decreases at the malignant tumor site at a faster rate in comparison to that at healthy tissue.

Magnetic nanoparticles can serve as "molecular beacons" to enhance the MR image contrast for early lesion detection through active (e.g., antibody–antigen) and passive (e.g., enhanced permeability and retention effect, EPR) targeting mechanisms. An effective form of active targeting involves exploitation of the magnetic properties of the nanoparticles under a magnetic field gradient known as magnetofection [29,30]. If an external magnet is placed near the tumor, the magnetic nanoparticles experience a driving force under the inhomogeneous magnetic field, resulting in accumulation of particles at the tumor site. This active targeting is superior to passive targeting where the latter relies on EPR. In passive targeting, nanoparticles and macromolecular drugs of specific sizes tend to accumulate in tumor tissue much more than they do in normal tissues

[31,32], which is known as the EPR effect. Such phenomenon could be explained by the stimulated production of blood vessels from proximal fast-growing malignant tumor cells. These newly formed vessels at the tumor site are usually abnormal in form and architecture, which leads to abnormal molecular and fluid transport dynamics. The EPR effect helps deliver and distribute the nanoparticles inside the cancer tissue, resulting in passive targeting. However, surface-functionalized SPIO showed better EPR effects in blood, enhanced stability, and had less potential of becoming agglomerated [27]. Following this logic, surface functionalization of SPIO with dendrimer enhances not only its stability and targeting capability, but also its capacity for encapsulating drugs or other specific conjugate ligands. These integrated structures possess multiple therapeutic potentials for killing cancer cells via induced magnetic hyperthermia using AMF, controlled drug delivery using pH and temperature, or gene therapy through gene delivery. Altogether, the dendrimer-SPIO complex could serve as a powerful therapeutic platform for simultaneously detecting and treating malignant tumors. The following two sections (section 5.2.1.1 "Chemotherapy" and 5.2.1.2 "Gene therapy") are devoted to the advancement and importance of these structures, and their relevant theranostic uses for eliminating the common problems of conventional therapies.

5.2.1.1. Chemotherapy

A major drawback encountered in traditional chemotherapy is the development of high resistance to the free drug in cancer cells. Often, a very high dose of medicine is required to target and significantly degrade the cancer cells, as traditional chemotherapy relies predominantly on passive targeting and does not show significant EPR effect. The non-specific administration of such a high dose naturally affects healthy cells adversely. For example, breast cancer cells can develop resistance to the commonly used cancer drug doxorubicin (DOX) via Pgp-mediated efflux

proteins that prevent drug uptake. As a free drug, DOX often exhibits cardiotoxic side effects [33]. Khodadust *et al.* [34] have shown that polyinosinic:polycytidylic acid (poly I:C)-modified G4 dendrimer-coated SPIO nanoparticles (PIC-G4DcMNP-DOX) could overcome this resistance and deliver DOX inside cancer cells to induce high cytotoxic effects. These authors performed a comparative study of DOX loading, release, and biocompatibility profiles on different generations of PAMAM dendrimer-coated SPIO structures, and found that G4 dendrimers were the most effective for both delivering DOX at a lower pH and overcoming the DOX resistance mechanism in breast cancer cells [35]. Here, poly l:C served as a moderator to reduce the toxic effects of the surface terminal amine group of the PAMAM dendrimer on healthy cells, while triggering apoptosis in human melanoma, breast cancer, and hepatoma cells [36,37]. So, a higher concentration of the modified nanovehicles could be administered without causing more damage to the healthy cells. However, this poly I:C is bound to the surface of the dendrimer by a phosphoramide bond, which is cleaved by the overexpressed phosphoramidase enzyme in the tumor cells, resulting in release of poly I:C and catalyzing the release of DOX to induce maximum toxicity inside the tumor cells [34]. The DOX-integrated nanovehicle, PIC-G4DcMNP-DOX, showed a lower half maximal inhibitory concentration, indicating higher cytotoxicity compared to free drug [34]. The IC_{50} for poly I:C was 7 μg mL^{-1} and the IC_{50} for DOX was 12 μg mL^{-1} in this integrated complex PIC-G4DcMNP-DOX, whereas free DOX and free poly I:C showed IC_{50} of 170 μg mL^{-1} and 450 μg mL^{-1}, respectively, when tested at 1 μM in DOX-resistant MCF-7 cells. Therefore, a lower dose of DOX could be administered to induce an equal amount of cytotoxic effect to the malignant cells. The nanoparticle also showed pH-controlled drug delivery functionality and the drug was released more efficiently at a lower pH. The presence of SPIO within the complex PIC-G4DcMNP-DOX could further be used to target specific cancer cells by magnetofection, as described before.

Undoubtedly, the poly I:C-modified and drug-loaded G4 PAMAM dendrimer would be preferable over free drug treatment for effective targeting and induction of cytotoxic effects in MCF-7 breast cancer cells, while minimizing adverse effects to healthy cells. However, there is a chance that the phosphoramide bonds may break in tissues other than at the tumor site, as earlier works found a small amount of phosphoramidase enzyme in most healthy tissues. So, a detailed further study is required to understand this mechanism to improve the drug delivery and targeting efficiency.

Pancreatic stellate cells (PSC) activate fibrotic stroma, which strongly resists drug molecules from entering the cancerous cells. As one can imagine, this high resistance places pancreatic cancers as the third leading cause of cancer-related deaths in 2016, as reported by pancreatic cancer action network. A high dose of free gemcitabine could still kill these cancer cells; however, drug administration has to be restricted for its toxic consequences on healthy cells. This problem was addressed by Yalcin *et al*. [38] using an effective dendrimer-based nanovehicle for an active targeting approach. The authors have shown that gemcitabine could be delivered to pancreatic cancer cells using an all-*trans* retinoic acid (ATRA)-conjugated dendrimer-coated SPIO as a nanovehicle. PSC activation of fibrotic stroma is associated with loss of retinol-containing droplets in the cytoplasm [39]. ATRA could be a potential drug to deactivate PSC and overcome the resistance of fibrotic stroma. This dendrimer-based nanovehicle could potentially not only overcome the resistance of fibrotic stroma, but also deliver the required lower dose of gemcitabine to the cancer site, thus minimizing the unwanted side effects. Here, the authors have taken the advantages of the dual mechanisms of (i) gemcitabine as an anti-cancer drug, and (ii) ATRA to deactivate PSC. However, a previous study using a combination of free retinoic acid and gemcitabine did not show any appreciable improvement in response rate, although these combinations were well tolerated by the patients [40]. On the positive side, this study demonstrated an effective drug-loaded delivery system

using an optimized *in vitro* protocol [38]. They have shown that a dendrimer-SPIO nanoparticle, loaded with 10 μM of both gemcitabine and ATRA in PBS buffer at pH = 4.2 released 72% of the drug and 81% of the ATRA within the first 10 h. This released combination was found to be capable of destroying various types of pancreatic cancer cells, including SU86.86, T3M4, and Panc-1 effectively. Although this experiment was performed *in vitro*, it is expected that the therapeutic efficiency would increase considerably when using a delivery nanovehicle as opposed to administering the combination of free drugs.

A major challenge for the successful use of theranostic particles is active targeting, while magnetofection and passive targeting have their own limitations. The advantage of dendrimer over other materials is its ability to bind to a wide variety of specific targeting ligands. Human carcinoma cells in the breast, ovary, endometrium, kidney, lung, head, neck, and brain are known to express folic acid (FA) receptors [41,42]. Chang *et al.* [43,44] have shown that SPIO coated with FA and polyethylene glycol (PEG)-conjugated PAMAM dendrimers could be used to selectively target those cancer cells that express FA receptors as well as to enhance the circulation time in the blood for better passive targeting. DOX could be loaded into the dendrimer segment using a hydrazone bond. This bond is sensitive to acidic environments, and has been shown to be capable of 75% drug delivery at pH = 5.03, but has less than 8% delivery at pH = 7.38 [43]. This controlled delivery approach would use a minimum amount of drug, thus reducing the undesirable side effects on nearby healthy cells.

Many anti-cancer drugs have poor solubility in water and are difficult to administer to patients. These anti-cancer drugs could be loaded inside dendrimer-based nanovehicles and administered to achieve much better targeting to the tumor site and efficient drug delivery. For example, 3,4-difluorobenzylidene curcumin (CDF) was reported to have high anti-cancer activities for ovarian,

pancreatic, cervical and lung cancers, but suffers from poor solubility [45–47]. Recently, Luong *et al.* [48] showed an effective approach to deliver the hydrophobic anti-cancer drug CDF using FA-PAMAM dendrimer with a SPIO core. Additionally, this approach of loading CDF in FA-PAMAM dendrimer provided higher targeting efficacy, anti-cancer activity, and superior MRI contrast-enhancing ability. Thus, it opens up the possibility of loading other hydrophobic drugs to achieve better targeting and effective therapy of folate receptor-expressing cancers. Paclitaxel (PTX) is another effective drug used for treating breast cancer, advanced ovarian carcinoma, lung cancer, head, neck, and acute leukemia, but suffers from poor water solubility [49,50]. In order to effectively administer such drugs, a similar packaging technique could be used. The anti-cancer drug PTX was put inside SPIO-coated dendrimer conjugated to FA, PEG, and cyanine 5.5 (Cy5.5) and then administered [51]. This dendrimer construct is water-soluble and showed high cellular uptake. Since the drug is bound by a cleavable ester bond, the acidic pH environment within tumor cells caused release of the drug, resulting in enhanced cytotoxic effects of PTX. Compared to the non-targeted conjugates, the uptake of the construct was verified using *in vitro* cell fluorescence analysis of a transfected human breast cancer cell line MCF-7. Davayani *et al*. have used a poly(amino ester)-coated SPIO-encapsulated G1 and G2 dendrimer for pH-sensitive drug delivery for prostate cancer [52]. This structure can carry hydrophobic drugs. The authors completed a comprehensive comparison of different functional groups on the dendrimer surface like OH and NH_2. *In vitro* studies using a human prostrate carcinoma cell line revealed that the drug release rate at 37 °C is significantly higher at pH = 5.8 compared to that at pH = 7.4 in standard physiological condition. This change is attributed to a conformational change due to the presence of amino groups in the backbone. Surface-conjugated amino dendrimers showed higher drug encapsulation but slower drug release behavior compared to hydroxyl-conjugated ones. A

cytotoxicity assay showed the biocompatible nature of the nanostructures. The efficacy and drug encapsulation could be increased by using a higher generation dendrimer.

Dendritic linear block copolymer modified with SPIO was used recently as an integrated theranostic structure [53,54]. These structures could be made by combining "grafting onto" [55] and "grafting from" [56] techniques that make SPIO water-soluble, biocompatible, and monodisperse to prevent their aggregation[53,54]. The polyamidoamine-*b*-poly(2-(dimethylamino)-ethyl methacrylate)-*b*-poly(poly(ethylene glycol) methyl ether methacrylate) (PAMAM-*b*-PDMAEMA-*b*-PPEGMA)-grafted SPIO dendrimer is capable of carrying and delivering drugs by fine-tuning the hydrogen-bonding interactions between PDMAEMA and DOX [56,57], making it a pH-sensitive controlled drug delivery system [53]. Studies on these materials showed that the cumulative drug release was maximum within 48 h at pH = 4.7 (83.1%), compared to that at pH = 7.4 (64.7%), and pH = 11.0 (8.3%) at 37 °C [53]. A similar structure was made using the two-step atom transfer radical polymerization (ATRP) procedure with a SPIO core and a dendritic linear-block copolymer with a focal point polyamidoamine-type dendron-*b*-poly(2-dimethylaminoethyl methacrylate)-*b*-poly(N-isopropylacrylamide) (PAMAM-*b*-PDMAEMA-*b*-PNIPAM) shell [54]. This structure showed different amounts of drug release at 25 °C and 37 °C, indicating thermosensitive control of drug release that was attributed to a conformational change of PNIPAM block chains [58]. Another interesting approach along this line is the synthesis of amphiphilic linear-dendritic-linear block copolymers made of a poly ε- caprolactone linear block, poly(amino-ester) dendritic block, and an m-PEG linear block. Oleic acid-coated SPIO was conjugated with G1, G2 and G3 dendrons via a ligand exchange method and *in vitro* pH-guided drug delivery was demonstrated [59].

Most of these dendritic structures were made of PAMAM dendrimer that suffers from the issue of toxicity from its degradation products, which inhibits its clinical use from a safety perspective. Recently, Nigam *et al.* [60] have shown the use of a peptide dendrimer whose core was made of ethylene diamine, and cationic amino acid was taken as the branching monomer. This class of dendrimer is called peptide dendrimer due to the resemblance of the amide linkage between amino acids with the peptide bonds between proteins. Here, the cells utilize amino acids as a nutrient in their metabolism and reduce the toxicity effect after degradation. This could be a potent candidate to solve the long-standing biocompatibility and safety challenges of dendrimer nanoparticles. This peptide dendrimer was loaded with SPIO for MRI detection and co-loaded with anti-cancer drug DOX for therapy similar to other approaches discussed before [60]. Moreover, a combination of DOX and magnetic hyperthermia effect with AMF has been shown to be effective for treating cervical cancers with this nanovehicle [60].

5.2.1.2. Gene therapy

Gene therapy could be one of the most effective therapies to treat cancers. However, traditional gene therapy suffers from non-specific delivery that produces adverse side effects on healthy tissues [61]. It involves transfer of a particular gene to the targeted site to replace or silence the malfunctioning one, which is responsible for the diseases. It is a very novel way to treat the disease from the origin itself and a very potent technique. However, certain issues like immunological side effects, insertional mutagenesis, *etc.*, limit the scope of this valuable approach. Recent studies show delivery of nonviral particles could be a safer approach to gene therapy with less side effects [62]. Still, it is quite challenging to find an appropriate carrier to encapsulate the genetic particle, limit its exposure to healthy cells, and pass through the cellular obstructions to deliver genes to the cell nucleus. Moreover, for effective gene therapy, the presence of contrast

agent in the carrier is necessary to visualize the process noninvasively. One common way for this is to unify two kinds of genes in the same probe: therapeutic genes and imaging reporter genes (*e.g.*, transferrin receptor gene [63] for MRI). The imaging reporter genes express contrast agents in the target site that could be imaged for efficient tracking of genetic material. However, these imaging reporter genes suffer from immune response, non-favorable kinetics, and lack of stability and biocompatible nature, thus limiting their uses. Here, nanoparticles offer a promising approach to bypass these problems by encapsulating both the therapeutic genes and the imaging reporter genes, thus opening up the possibility of gene therapy along with real-time monitoring of the tumor site. Nanoparticles like dendrimers provide additional means to conjugate bio-moieties for perfect targeting and to minimize the possibility of interaction of the genes with the outside environment and healthy cells. For example, the electrostatic interaction between positively charged PAMAM dendrimer with negatively charged phosphate backbone of DNA forms a complex that protects DNA from degradation [61]. Higher generations of dendrimers show better transfection efficiency due to weaker electrostatic interactions compared to lower generation ones. In an overall sense, dendrimer offers a composite approach to image and deliver genes simultaneously, minimizing the adverse effects of gene therapy.

Shili *et al*. have reported a nanohybrid system by combining plasmid DNA (pDNA) with SPIO for an effective nucleic acid therapy [64]. The authors functionalized different generations of dendrimers with pDNA and poly(styrene) sulfonate-coated SPIO to provide an integrated structure. They characterized and successfully transfected NIH 3T3 cells. Among the generations 2, 4, and 6, they found the optimal one to be G6.

Antisense therapy is an effective strategy for cancer therapy, where antisense oligonucleotides prevent target RNA translation to protein to inhibit cellular growth [65]. However, it suffers from poor diffusion across cell membranes and undergoes rapid degradation in the absence of a rational delivery mechanism [66]. These problems could be overcome by using a dendrimer-modified SPIO complexed with antisense survivin oligodeoxynucleotides (asODN) [67,68], since SPIO-coated dendrimer nanoparticles could protect asODN from degradation enzymes by changing the *in vivo* microenvironment inside the cell for a while [69]. Hence, the asODN-dendrimer-SPIO construct could efficiently deliver the gene and successfully inhibit the growth of cancer cells [68]. Among the different generations of dendrimers, G5 is the most effective one for enhancing gene delivery efficiency and downregulating growth of the malignant cells. The exact metabolism pathway is still under study.

Short interfering RNA (siRNA) is another potent candidate for cancer treatment due to its exceptional specificity and ability to silence expressed genes [70,71]. However, the low permeability of naked siRNA and unavailability of a nontoxic stable nanovehicle for delivery limit its potential applicability [71–73]. Recently, Taratula *et al.* [74] have shown that a poly(propylene imine) (PPI) G5 dendrimer-modified SPIO could solve this problem. They used Luteinizing Hormone-Releasing Hormone (LHRH), whose receptor is overexpressed in many cancer cells, as a specific targeting agent [75]. LHRH-conjugated SPIO-PPI G5-siRNA enhanced the stability and successfully delivered siRNA to the malignant cells. Furthermore, the use of LHRH in the construct enhanced the efficacy of anti-cancer drugs such as cisplatin by suppressing the negative effects on healthy cells [76]. Similar approaches to treat cancers with siRNA have been attempted with G4 PAMAM dendrimer-coated aminosilane-modified SPIO [77]. This kind of structure could overcome the resistance against DOX by breast cancer cells. Another report [78] studied a dendrimer-conjugated fluorophore-labeled

magnetic core to internalize siRNA by activating endosomal escape siRNA. The authors successfully showed that different doses of siRNA could be delivered into the cells using the dendrimer-conjugated magnetic nanoparticle, "dendriworms". The dendriworms were delivered *in vivo* to the transgenic glioblastoma mouse model via convection-assisted delivery. This approach offers a route to penetrate the cell cytoplasm freely, resulting in efficient delivery of intact functional siRNA to cells. Furthermore, the use of magnetic nanoparticles and fluorophores opens up the potential of multimodal tracking of siRNA to achieve maximum efficacy of such treatment. While this work focuses on the theranostic applications of the MRI-guided dendrimer-based nanovehicles, the readers can find well-written review articles that comprehensively address the development of gene therapy [61,79–81].

5.2.2. Other T_2-mode dendrimer nanoparticles

SPIO holds great promises for futuristic nanomedicine. However, in biological fluids or during exposure to magnetic fields, they sometimes suffer from aggregation and decreased dissolution rates [82]. Commonly used SPIO contrast agents require nonspecific uptake by mononuclear phagocytes to improve the local contrast, and at a hydrodynamic size of over 50 nm, these particles have very limited extravasation ability and are subject to easy uptake by the MPS, which severely undermines their targeting specificity [83]. Hence, the synthesis of biocompatible ultrasmall iron oxide nanoparticles capable of targeting tumor sites could alleviate such concerns, although the preparation of ultrasmall nanoparticles with sizes less than 10 nm is challenging. Recent progresses in this area include efforts [9,83–85] to prepare the nanoparticles, such as cyclic arginine–glycine–aspartic (RGD) peptides-coated stable iron oxides with 8.4 nm diameter [83]. The RGD coating provides targeting capability to various tumor cells with overexpressed $\alpha_V\beta_3$ integrin [86,87]. Yang *et al.* [84] incorporated ultrasmall iron oxide nanoparticles inside RGD-coated dendrimers

to target brain tumor (C6 glioma cell line) in mice. They showed specific targeting of C6 cells are possible using this nanoparticles. The dendrimer coating imparts extra stability and biocompatibility to the ultrasmall iron oxide nanoparticles and dendrimers provide means for drug delivery and targeted therapy. Future comprehensive studies for drug delivery and other kinds of therapies with dendrimers hold great promise for cancer theranostics.

5.2.3. T_1-mode dendrimer nanoparticles

Gd-based dendrimers are another class of potential candidates for theranostic uses in association with MRI techniques. Gd(III) is an effective contrast agent [8] that dramatically increases the longitudinal relaxation rate to exhibit positive contrast between malignant and healthy tissues. Similar to the approaches discussed in Section 5.2.2 for SPIO, theranostic nanovehicles have been designed with Gd(III) as a T_1 contrast agent, instead of SPIO as a T_2 contrast agent. For example, generation 5 amine-terminated PAMAM dendrimer was modified with a Gd-chelate complex (DOTA(Gd)) and targeting ligand FA with PEG to target cancers overexpressing FA receptors [88]. Later, terminal amines were acetylated and the anti-cancer drug DOX was loaded successfully to treat cancer cells simultaneously with this construct G5. NHAc-DOTA(Gd)-PEG-FA/DOX. Other specific approaches include the use of self-assembled particle dendrimersomes [89], which have been tested *in vivo* for the first time for theranostic uses very recently [90] with the anti-cancer drug prednisolone phosphate (PLP) on murine melanoma mouse models. This work demonstrated an inexpensive and easy alternative to liposome for theranostic purposes [91]. Also, Gd(III)-based dendritic nanoparticles were developed recently for specific targeting in gene therapy under MRI guidance [92], as targeting efficiency has remained a problem in gene delivery systems, as discussed in the previous section. We will summarize two novel directions of Gd(III) nanoparticles in the following Sections 5.2.3.1 and 5.2.3.2.

5.2.3.1. Supramolecular nanoparticle assembly for contrast enhancement and therapy

Gd (III)-incorporated dendrimers could increase contrast in MRI. However, the poor water accessibility to the buried Gd (III) core decreases its relaxation rate, resulting in an overall decreased MRI contrast [93]. To overcome this problem, a porous structure could be used to balance these two opposing effects to make a better contrast agent [94,95]. Chen *et al.* [96] designed a supramolecular nanoparticle assembly (SNP) of three molecular building blocks consisting of adamantane (Ad)-grafted PAMAM, β-cyclodextrin (CD)-grafted branched polyethylenimine (PEI), and Ad-grafted PEG, which is capable to chelate with a high concentration of Gd(III).DOTA . This structure would provide a pseudo-porous, polymer-dendrimer hydrogel network with good water accessibility. This nanostructure Gd(III).DOTA⊂SNP could be designed to fine-tune the two opposing contrast effects by the systematic variation of SNP size and degree of crosslinking between the materials. Our group and collaborators have shown that the highest relaxivity could be found when Ad-PAMAM and DOTA-CD-PEI exist at a ratio of 1:2, with a Gd(III) concentration of 3.9 mM in the Gd(III).DOTA⊂SNP assembly. Compared to the clinical Gd(III).DTPA complex, which exhibits an r_1 relaxivity of about 4.0 mM^{-1} s^{-1} at 600 MHz, Gd(III).DOTA⊂SNP has shown a remarkable 4-fold increase in r_1 relaxivity of 17.3 mM^{-1} s^{-1} at 600 MHz [96].

This enhanced contrast could be applied for dynamic monitoring of lymphatic drainage, which should be a very useful diagnostic tool for tracking cancer metastasis. Imaging of axillary lymph nodes to observe the lymphatic drainage system could be used as an important diagnostic protocol for breast cancer, as most of the lymphatic fluid from the breast depletes there [97]. It has been shown using *in vivo* mice model experiments that the use of Gd(III).DOTA⊂SNP increases imaging clarity dramatically, in comparison to the conventionally used Gd(III).DTPA [96].

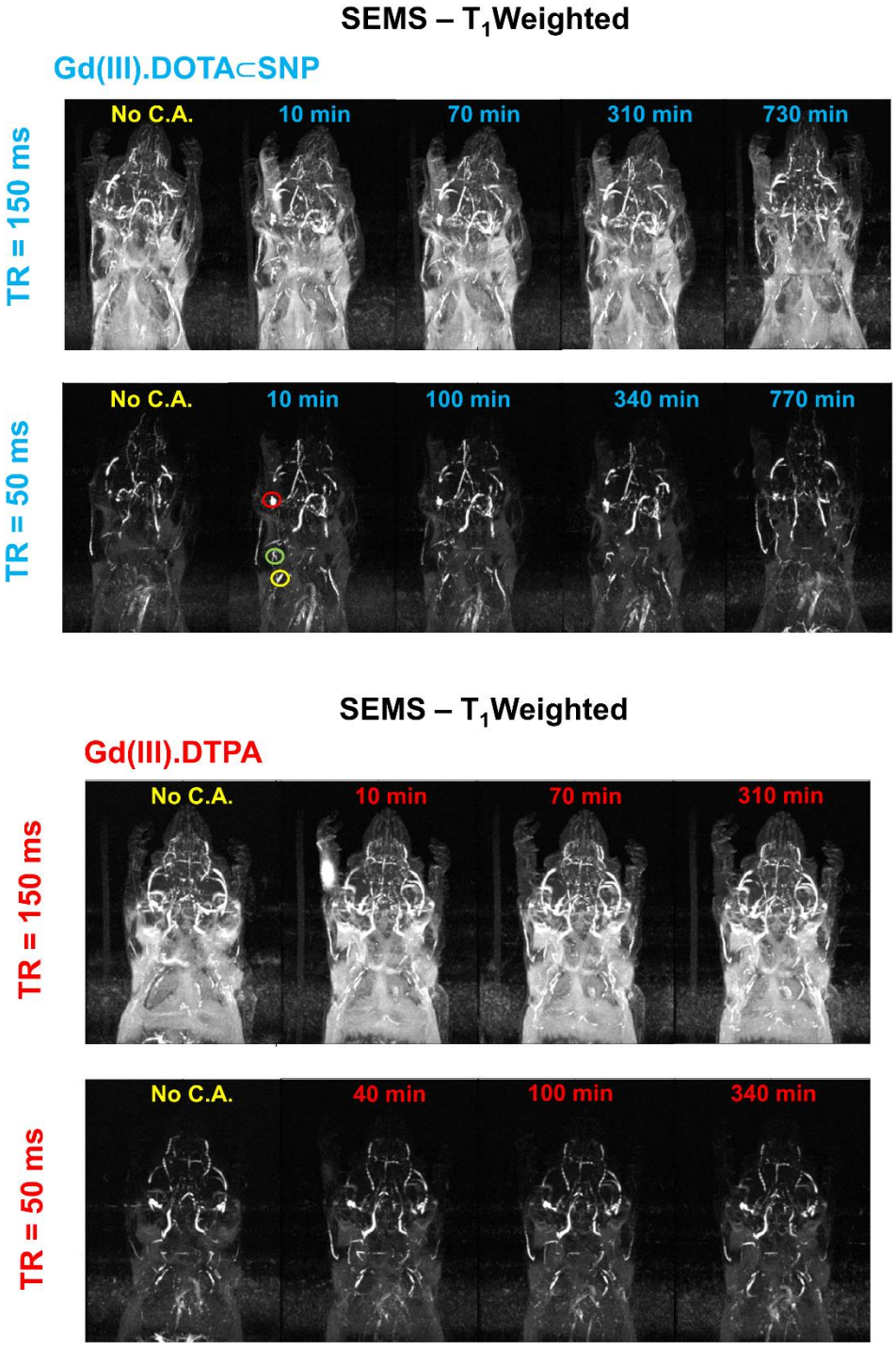

Figure 5.3. Comparison of MR images of lymph nodes in mice. **(A)** MR images of lymph nodes after injection of Gd(III).DOTA⊂SNPs at different time points under time of retention (TR) 150 ms and 50 ms and time of echo (TE) 10 ms. Red, green, and yellow circles represent the brachial, axillary and superficial lymph nodes, respectively. **(B)** MR imaging of the lymph nodes after injection of Gd(III).DTPA at different time points with time of retention 150 ms and 50 ms, where (A) shows superior contrast at TR = 50 ms.

Figure 5.3 shows the advantages of using Gd(III).DOTA⊂SNP over Gd(III).DTPA for imaging different lymph nodes with various parameters to obtain the best contrast in MRI. The plot of the average intensity versus time (**Figure 5.4**) shows the highest clarity for seeing axillary and superficial nodes 80 min after injection of Gd(III).DOTA⊂SNP. Altogether, an effective protocol for early tumor detection comprised the following parameters: time of retention, 150 ms and 50 ms; time of echo, 10 ms; and time after injection, 80 min. Imaging of Gd(III).DTPA in the mouse hand (**Figure 5.3B**) shows an initial high concentration of Gd(III).DTPA at the injection site 10 min after administering the injection, which dissipates after a short time, suggesting quick clearance of this conventional complex from the body. In contrast, the longer-lasting uniform distribution seen after Gd(III).DOTA⊂SNP injection (**Figure 5.3A**) implies that this nanovehicle is capable of circulating in the body for a longer period of time. This difference in clearance might be attributed to the difference in the sizes of the nanoparticles.

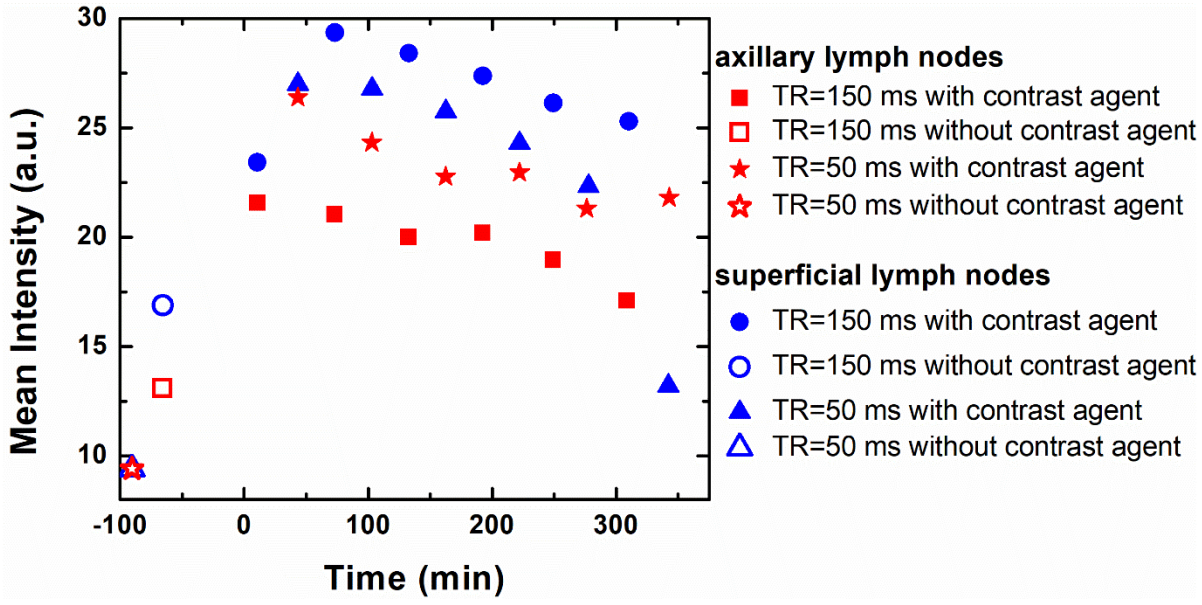

Figure 5.4. Plot of intensity vs. time after injection of SNP, which shows that the mean intensities of axillary and superficial nodes are highest 80 min after injecting Gd(III).DOTA⊂SNPs.

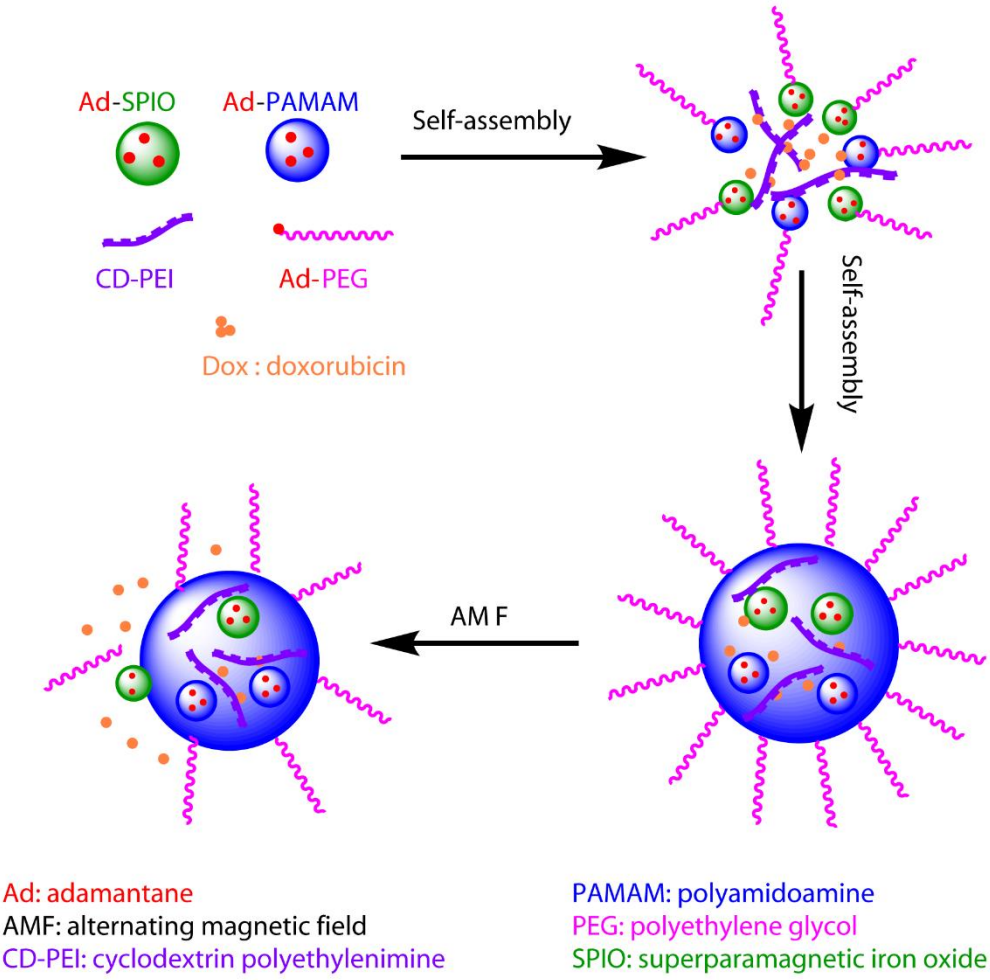

Figure 5.5. Schematic diagram of the theranostic application of a supramolecular nanoparticle assembly for induced hyperthermic treatment. The diagram shows that drugs (represented by small red balls) can be loaded during assembly of supramolecular nanoparticles, delivered to the tumor site, and released under AMF, which is controlled externally.

This structure could be used not only for improving imaging quality, but also for a variety of treatments. For example, gene delivery [98,99], photothermal treatment [100], and induced hyperthermia [101] could all be achieved using this new complex, classifying it as a potent candidate for theranostic applications. Recently, similar structures with SPIO have been synthesized as AMF-controlled drug delivery nanovehicles for optimized *in vivo* treatment protocols [101]. The study showed that

the DOX-loaded nanovehicles have increased cytotoxic effects under AMF, enhancing the antitumor efficacy in comparison to the treatment without AMF [101]. A schematic representation of this procedure is shown in **Figure 5.5**. The use of this complex allows for the current dosage of DOX to be reduced by a factor of at least 1000, dramatically reducing potential side effects in comparison to traditional protocols

5.2.3.2. Image-guided surgery

Real-time detection and monitoring of the tumor during surgery could be an effective alternative to chemotherapy or other types of therapy, by minimizing the possibility of unwanted side effects on nearby healthy tissue. Tan *et al.* [102] performed such image-guided surgery with the help of a dual-modal imaging probe (MRI and cyanine 5 (Cy5) fluorescence imaging) using G2 dendrimer conjugated with CLT1 peptide and loaded with Gd(III)-DOTA monoamide. This technique could be very effective for detecting and removing prostate cancer, because CLT1 is a cyclic peptide that preferentially binds to fibronectin, which is overexpressed in malignant prostate tissues compared to benign tissues [103–105]. This novel structure exhibited a signal-to-noise ratio 2-fold higher than that of the control agent in MRI, allowing for more accurate detection [102]. Cy5 provides additional bright fluorescence to help determine the precise position of the tumor. Targeting with a small molecular CLT1 peptide, instead of an exogenous monoclonal antibody, reduces the overall dose of the therapeutic and minimizes the potential of inducing a negative immune reaction. This size of the probe allows easy removal of the nanoparticles from the body via renal filtration, making it safe for biological applications. However, the nanostructure suffers from non-specific accumulation in the lung due possibly to either the relatively large size of the agent or the presence of free peptide [102]. Similar nanostructures with lower molecular weight might

help overcome this problem. Further study is required to optimize the nanostructure to reduce non-specific tissue accumulation.

5.2.4. Other T_1-mode dendrimer nanoparticles

Gd(III)-based dendrimers show promise as T_1 theranostic agents in MR. However, Gd has serious side effects called nephrogenic systemic fibrosis [106], especially for patients with renal problems. Although encapsulation of Gd should reduce adverse side effects, other alternatives have been explored. As an alternative, contrast agents based on Mn(II) have been developed [107–112], which could provide reasonable contrast in MRI and are expected to be much safer for patients with renal disease. For example, Zhu *et al*. synthesized a dendrimer-based contrast agent with $[Mn(EDTA)(H_2O)]^{2-}$ [113]. It was characterized and high relaxivity was observed. Its pharmacokinetic properties were evaluated and compared with $[Gd(DTPA)(H_2O)]^{2-}$ in mice. Its blood clearance was observed to be fast and excretion occurred through both the renal and hepatobiliary routes. Hence, it offers an alternative route for imaging patients with impaired renal function. Other recent promising approaches in this direction include the stacking of Mn(II) on negatively charged PEGlyted G2 dendrimer [114]. This nanoconstruct offers high specificity, sensitivity, and capacity to target cancer cells. The authors demonstrated *in vitro* application to the breast tumor cell line MCF-7. As an alternative to Gd-DOTA, Mn(II)-DOTA chelates were synthesized and conjugated with different generations of lysine dendrimer [106,115]. These Mn-DOTA dendrimers were targeted with CLT1 peptide and studies were performed on breast tumor mouse models. Further studies are required on these kinds of Mn(II)-based dendrimer nanoconstructs to evaluate their applications for therapy, drug delivery, and imaging. They could turn out to be safer and useful theranostic agents for patients with renal disease. Interesting studies

on Mn(II)-based dendrimers have been performed in T_1/T_2 and multimodal imaging, as will be discussed below.

5.2.5. Multimodal dendrimer nanoparticles

We have discussed the development of dendrimer nanoparticles for simultaneous detection and treatment of cancer using MRI in this review. However, multimodal imaging could provide better accuracy and more efficient detection of small tumors compared to single-modal techniques [116,117]. A lot of research has been done on dual-mode T_1- T_2 imaging using MRI. Such dual-modal imaging [118] would enable us to study both the soft tissue anatomy and pathological phenomenon simultaneously, leading to potential differentiation between normal and tumor tissues, early tumor detection, and prediction of cancer stages [119]. Very recently, Haribabu *et al*. have shown [119] an effective dual-modal approach by encapsulating manganese ferrite nanoparticles [120,121] in dendrimer and targeting it to tumor by FA. Here, iron served as a T_2 contrast agent and manganese as a T_1 contrast agent. The authors characterized different ratios of Fe-Mn conjugates and found the molar ratio of 0.5 worked best, giving $r_2/r_1 = 4.6$ at a magnetic field of 1.5 T. These kinds of structures could serve as potent theranostics for cancer treatment. However, drug delivery and other pharmacokinetic parameters should be evaluated in future studies.

Other approaches include combinations of different imaging techniques like CT, PET, and fluorescence imaging with MRI. Each imaging modality has its own advantages and disadvantages. For example, MRI enjoys the ability of deep penetration, superior resolution, and non-invasive detection. However, MRI suffers from poor contrast and sensitivity, which could be compensated by PET or SPECT, which have excellent contrast and sensitivity but low resolution. Similarly, CT provides better spatial resolution and optical imaging, such as fluorescence imaging,

gives high sensitivity. Hence, combinations with other imaging modalities could potentially overcome the shortcomings of MRI techniques. Examples of such promising directions include the use of entrapped gold (Au) nanoparticles with Gd(III) chelate inside dendrimer for CT and MRI dual-modal detection and targeted therapy [122–125]. This kind of approach was further modified with a SPIO and Au nanoparticle composite for simultaneous CT and MRI detections [126]. Recently, Luo *et al*. [127] have shown a nanocomposite FA-conjugated dendrimer with Mn(II) and Technetium-99m (^{99m}Tc) for targeted therapy and detection with MRI and SPECT. In this method, MRI provided the high spatial resolution, whereas SPECT gave information regarding the physiological condition of the tumor. Furthermore, the use of Mn(II), instead of Gd(III), made it potentially less toxic. A combination of MRI with fluorescence imaging technique to overcome the low sensitivity of MRI could be another useful theranostic approach [45,78,102,128,129]. As dual modality is better than single modality, tri-modal imaging could work even better compared to dual-modal imaging. Recently, Chen *et al*. [130] have shown that dendrimer functionalized with a nanocomposite of Au nanoparticle, Gd (III), and cyanine dye (Cy5.5) could serve as a tri-modal imaging agent for CT (Au nanoparticle), MRI (Gd(III)), and fluorescence imaging (Cy5.5) to provide better spatial and density resolutions with high sensitivity. Such integrated multimodal theranostic approaches undoubtedly hold great promise for futuristic nanomedicines.

5.2.6. Heteronuclear dendrimer nanoparticles

In magnetic resonance, "heteronuclear" generally refers to spins other than ^{1}H. For example, the fluorine isotope ^{19}F is a naturally abundant element, and could be used for MR imaging in the place of ^{1}H MR. However, due to its smaller longitudinal relaxation rate (r_1), the imaging quality and sensitivity are limited. A highly dense grouping of ^{19}F is required to produce a strong MRI signal. Typically, the dendrimers are directly synthesized. However, the synthesis of

increasingly complex and larger dendrimers demands more challenging approaches, where self-assembly provides an inexpensive alternative [131–133]. Criscione *et al.* [134] have shown a creative approach by self-assembling a ^{19}F probe using a partially fluorinated PAMAM dendrimer. This probe exhibited a fluorophobic effect where fluorinated molecules became separated and assembled into hydrophobic and lipophobic fluorous phases, followed by self-assembly via forming non-covalent bonds [131,132,135]. By incorporating a densely packed ^{19}F complex, the self-assembled structure was able to produce a strong MRI signal *in vivo* [134]. Chemical shift imaging along with ^{1}H MRI showed successful site-specific accumulation of the fluorinated particulates [136,137], and T_1 relaxation rate showed pH dependence in an *in vivo* setting [134]. These self-assembled fluorinated particulates were further modified with PEG for effective passive targeting by enhancing the circulation time in the blood [134]. The partially fluorinated dendrimer structure exhibited pH-dependent disassembly that was assumed to be induced by the presence of the dispersed amines on the surface. These structural characteristics might enable us to develop an efficient pH-guided drug delivery system in the future.

5.3. Copolymer-based nanoparticles for MR cancer theranostics

A core-shell nano-platform can be composed of a variety of materials. Although the core is surrounded by a hydrophilic shell, the overall structure is stabilized by either covalent or ionic bonds between the core and shell (**Figure 5.2**). The physiological stability, surface modification simplicity, drug releasing ability [138], and core and shell component flexibility of core-shell nano-platforms show great promise for theranostic purposes. Here, we aim to present the most recent

developments of core-shell nano-platforms formed by copolymers that consist of both hydrophobic and hydrophilic blocks.

The hydrophilic block of the copolymer (*e.g.*, PEG) often serves as the outer shell to provide good water solubility and biocompatibility, ultimately reducing the premature clearance of core-shell nanoparticles, therefore prolonging the circulation time in the blood. Alternatively, the hydrophobic block of the copolymer provides sufficient interactions with the typically hydrophobic anti-cancer drugs to increase the drug or contrast agent loading efficiency. The flexibility of the structure of copolymers enables them to encapsulate, bind, and/or conjugate to therapeutic and/or imaging agents with simple modification procedures, and adapt to various *in vivo* environments. Thus, they are excellent candidates as theranostic nano-platforms as well as coating materials.

5.3.1. T_2-mode copolymer nanoparticles

5.3.1.1. Targeting strategy

Most core-shell copolymer nanovehicles take advantage of the above-mentioned EPR effect to passively target and accumulate at the tumor site. Filippousi *et al.* [139] synthesized amphiphilic triblock copolymers of hydrophobic poly(propylene succinate) (PPSu) and hydrophilic PEG. The core-shell magnetic nanoparticles were formed by encapsulating magnetite (Fe_3O_4) and the anti-cancer drug paclitaxel (PTX) into the hydrophobic core. Furthermore, three copolymer samples were prepared with similar lengths of PEG blocks, but with different lengths of PPSu blocks, allowing for further investigation of the effect of the hydrophobic (PPSu) to hydrophilic (PEG) ratio of the polymeric matrix. All three samples exhibited satisfactory nanoparticle yield (ranging from 70.57% to 78.21%) and drug entrapment efficiency (ranging from

53% to 65%). However, the differences in the hydrophobic block among the three samples produced varying drug-release profile patterns in an *in vitro* environment. The copolymer sample of 5800 g mol^{-1} PPSu released approximately 100% PTX loaded within 25 h, while the sample with 18900 g mol^{-1} PPSu had a maximal release of 80% even after 240 h. A recent study published by Bakewell *et al.* [140] depicts the synthesis of a triblock copolymer mPEG-block-poly[(D-glutamic acid-gamma-hydroxamate)-co-(L-glutamic acid-γ-hydroxamate)]-block-poly[(L-tyrosine)-co-(D-phenylalanine)]-acetamide and its application as a drug-loaded, iron-stabilized platform. Anti-cancer drugs were loaded in the hydrophobic core, while iron chelates with hydroxamic acid moieties formed dative bonds among polymer stands and stabilized the micelle. In their study, six active pharmaceutical ingredients (API) were loaded individually, resulting in different loading efficiencies (ranging from 65% to 91%) and average diameters of the micelles (ranging from 58 nm to 120 nm). *In vivo* study in subcutaneous xenograft mouse models showed enhanced MRI contrast after injection of the micelles, and increased anti-tumor efficacy compared to free drug.

Schleich *et al.* [141] synthesized PTX/SPIO-loaded PLGA-based nanoparticles by mixing poly(lactide-co-glycolide) (PLGA), poly(ε-caprolactone-b-ethylene glycol) (PCL-b-PEG), (PLGA-PEG), oleic acid-coated SPIO, and PTX through emulsion-diffusion-evaporation. The resulting nanoparticles were composed of a hydrophobic core containing the SPIO and PTX, and a PEG block hydrophilic shell. Such PTX/SPIO-loaded nanoparticles possessed a high r_2/r_1 ratio of 33.4 at 20 MHz, which is higher than that of the conventionally available magnetic nanoparticle Resovist, presenting promising applications as a T_2 contrast agent. Both *in vitro* cytotoxicity studies of CT26 colon carcinoma cells and *in vivo* anti-tumor studies of CT26-tumor-bearing mice showed PTX/SPIO-loaded nanoparticles inhibited the growth of CT26 cells. Based on Kaplan-Meier survival rate analysis, the PTX-load and PTX/SPIO-loaded nanoparticles exhibited superior

survival rates, with median survival rates of 13 and 15 days respectively, than the PBS-administered control group with a median survival rate of 9 days.

Even with the same copolymer composition, different conjugated structures will affect drug release characteristics. Wang *et al.* [142] synthesized two similar core-shell nanoparticles using Fe_3O_4-SiO_2: poly(benzyl L-aspartate) (PBLA) and methoxy poly(ethylene glycol) (mPEG). The first core-shell nanoparticle, FeSi@PBLA@mPEG, was synthesized by first conjugating PBLA with Fe_3O_4-SiO_2, then conjugating the methoxy poly(ethylene glycol) benzaldehyde(mPEG-CHO) onto the resulting nanoparticle through benzoic-imine bonds. The second core-shell nanoparticle, FeSi@PBLA-mPEG, was produced in a one-step conjugation of Fe_3O_4-SiO_2 to the diblock copolymer of mPEG-PBLA, where mPEG and PBLA were copolymerized through peptide bonds. Both core-shell nanoparticles were loaded with the anti-cancer drug DOX to form the complexes FeSi@PBLA@mPEG@DOX and FeSi@PBLA-mPEG@DOX, respectively. *In vitro* drug release studies showed that in a PBS buffer solution of pH = 7.4, the drug release profile patterns of the two DOX-loaded core-shell nanoparticles were very similar, both being less than 25% after 50 h. When the buffer was adjusted to an acidic environment of pH = 5.8, the release of DOX from FeSi@PBLA@mPEG@DOX was accelerated and reached 45% after 50 h. In contrast, FeSi@PBLA-mPEG@DOX did not show much difference between the acidic and neutral conditions. This difference in drug release behavior between the two core-shell nanoparticles is mainly attributed to the pH-sensitive benzoic-imine bonds between mPEG and PBLA in FeSi@PBLA@mPEG@DOX.

Active targeting and delivery can be achieved by conjugating active tumor-targeting ligands onto the copolymer shell. A generally used targeting ligand is FA, as it is able to enhance the targeting efficiency of the nano-platform to cancer cells through folate receptor-mediated

endocytosis. Yang *et al.* [143] designed a wormlike polymer vesicle using amphiphilic triblock copolymers PEG_{114}-PLA_x-PEG_{46}-acrylate (PLA: poly(D,L-lactide). The short PEG segments of the wormlike vesicles bearing acrylate groups encapsulated clusters of SPIO nanoparticles into the vesicles, while the long PEG segments were bound to FA, offering the vesicles active tumor-targeting ability. The hydrophobic layer PLA was used to load the hydrophobic anti-cancer drug DOX. Folate receptor-mediated endocytosis led to a higher cellular uptake of FA-conjugated wormlike vesicles in the HeLa cell line than FA-free ones, resulting in higher cytotoxicity and increased MRI sensitivity. Patra *et al.* [144] manufactured core-shell nanoparticles of SPION@PS-b-PAA-DOX/FA with an SPIO core containing a contrast agent encompassed by a poly(styrene)-b-poly(acrylic acid) (PS-b-PAA) shell not only containing DOX for therapy, but also containing FA peripherally conjugated to the outer shell for recognition of the cancer site. Both the drug release profile and magnetization of such core-shell nanoparticles improved dramatically upon altering the neutral physiological pH of 7.4 to an acid pH of 5.3. At pH = 5.3, the nanoparticle revealed an initial burst of drug release from 0% to 37%, reaching a final 92% after 160 h. At pH = 7.4, however, the nanoparticle only had an initial release from 0% to 12%, reaching a final release of 32%. Additionally, the r_2 relaxivity of the nanoparticle at pH = 5.3 was found to be more than 5 times that at pH = 7.4. This result was expected, as DOX is conjugated to the core-shell nanoparticle through a pH-sensitive hydrazine linkage. Further *in vitro* cell viability assays on human breast cancer SkBr3 cells and colon cancer HCT116 cells demonstrated that SPION@PS-b-PAA-DOX/FA had a higher efficacy in killing cancer cells compared to free DOX, mainly because the conjugated drug could be internalized at a higher rate and had longer retention time in the intracellular environment. Wang *et al.* [145] co-encapsulated both SPIO nanocrystals and DOX into PLGA/polymeric liposome core-shell nanocarriers. The core-shell nanocarrier was self-

assembled from a hydrophobic PLGA core and a hydrophilic FA-coated PEGylated lipid shell. The MRI signal intensity of Hela cells incubated with the FA-targeting magnetic core-shell nanoparticles decreased in T_2-weighted imaging when the Fe concentration in the cells increased, and such trend was more obvious compared to magnetic PLGA sphere or magnetic core-shell nanocarrier without FA coating. The FA-targeting magnetic core-shell nanoparticles also showed greater cell uptake than non-targeting ones *in vitro*.

Ji *et al.* [146] synthesized a hollow, porous Fe_3O_4 ($HPFe_3O_4$) nanoparticle that was loaded with DOX in the cavity, then self-assembled with polymers of [7-(didodecylamino)coumarin-4-yl] methyl methacrylate (DDACMM) and PEG. The complex was then conjugated with FA for selective cancer targeting and was found to be NIR light responsive. The resulting $HPFe_3O_4$@DDACMM-PEG-FA nanoparticles showed continuous drug release under femtosecond pulse NIR laser exposure, with a final release amount of 70% at pH = 5.0, and 50% at pH = 7.4 after 24 h. When placed in the dark, however, less than 10% DOX was released during the 24-h period, regardless of the pH environment. An *in vitro* MTT assay on folate receptor protein-positive human KB FR(+) cells further verified this selective release under NIR exposure. The $HPFe_3O_4$@DDACMM-PEG-FA nanoparticles also possessed a high r_2 relaxation rate of 139.1 Fe mM^{-1} s^{-1}.

Alternatively, cRGD ligand can also serve as a targeting moiety, since it can target $\alpha_v\beta_3$ integrins on tumor endothelial cells. Nasongkla *et al.* [147] synthesized polymeric micelles using amphiphilic block copolymers of maleimide-terminated PEG-block-PLA (MAL-PEG-PLA) and methoxy-terminated PEG-block-PLA (mPEG-PLA). SPIO nanoparticles and DOX were loaded in the hydrophobic core, while cRGD was attached to the surface of the hydrophilic shell. *In vitro* MRI and cytotoxicity studies confirmed the enhanced MRI relaxivity and $\alpha_v\beta_3$-specific cytotoxic

response of the cRGD-conjugated polymeric micelles, due to the induced receptor-mediated endocytosis for cell uptake.

Cancer cell antigens are specific structural substances on the surface of cancer cells that can serve as a target for adaptive immuno-targeting. These antigens can be recognized and specifically bound by the corresponding antibody. Through the high selectivity and binding affinity between antibody and antigen, the nano-platform conjugated with antibody on the surface can be used to target corresponding cancer cells with high efficiency and specificity. This has been verified by both *in vitro* and *in vivo* studies of drug-loaded magnetic core-shell nanoparticles conducted by Gao *et al.* [148]. In their study, a core composed of PLGA, the anti-cancer drug DOX, and hydrophobic SPIONs, was first created using a single emulsion evaporation method, then subsequently conjugated with poly(allylamine hydrochloride) (PAH), and two differently sized poly(ethylene glycol) (PEG) molecules through a layer-by-layer strategy. The outer shell PEG molecules were conjugated with prostate stem cell antibody (scAb), for a more specific targeting capability to prostate stem cell antigen-positive PC3M cells. This specific binding was confirmed by an *in vitro* cytotoxicity study of scAb-PLGA-SPIO/DTX (nano-platform conjugated with scAb; DTX: docetaxel) and PLGA-SPIO/DTX (without scAb) on PC3M cells and HT29 cells. For PC3M cells, the IC_{50} of scAb-PLGA-SPIO/DOX was found to be significantly lower than that of PLGA-SPIO/DOX. In contrast, the prostate stem cell antigen-negative HT29 cells revealed IC_{50} values both with or without scAb that were very similar. *In vivo* MRI and antitumor efficacy studies also confirmed the effective targeting of scAb-PLGA-SPIO/DOX to the tumor site. *In vivo* MRI showed significant contrast between tumor and muscle after injection of either scAb-PLGA-SPIO/DOX or PLGA-SPIO/DOX, due to SPIO accumulation at the tumor site via the EPR effect. However, scAb-PLGA-SPIO/DOX showed further contrast enhancement due to the additional

antigen-antibody targeting interaction. Furthermore, scAb-PLGA-SPIO/DOX induced long-term tumor inhibition in PC3M tumor-bearing mice and possessed the smallest mean tumor volume of 156.4 ± 12.6 mm^3 (at 75 days) in comparison to the other conditions. Specifically, without the antibody scAb conjugated to PLGA-SPIO/DOX, the tumor volume was found to be 269.9 ± 225.4 mm^3 (at 72 days), free DOX-treated tumor had a volume of about 500 mm^3 (at 57 days), and PBS-treated tumor had a volume of about 750 mm^3 (at 33 days). As described, the copolymer sections in the core-shell nanoparticles provide a variety of functional groups that can bind different targeting moieties for extended applications to other cancer types for specific contrast enhancement and targeted therapy through antigen-antibody interactions.

Another promising active targeting strategy is magnetic targeting (MT). Magnetic targeting enhances accumulation and retention of drug-loaded magnetic nanoparticles in tumors by applying an extra, external magnetic field [149]. Yang *et al.* [150] produced a highly magnetic nanocarrier (HMNC) composed of a Fe_3O_4 core and an aqueous-stable, self-doped poly[N-(1-one-butyric acid)]aniline (SPAnH) shell. The surface of the HMNC was conjugated with the anti-cancer drug 1,3-bis(2-chloroethyl)-1-nitrosourea (BCNU). To achieve a high BCNU drug loading capacity and a long circulation time *in vivo*, the HMNC was further modified by grafting *o*-(2-aminoethyl)polyethylene glycol (EPEG) to form a self-protecting magnetic nanomedicine (SPMNM). Contrast enhancement and drug delivery efficiency via MT treatment were evaluated using a subcutaneous mouse tumor model. R_2 constant mappings showed an increased R_2 value at the tumor site, reaching the highest R_2 value with a 24-hour exposure of external magnetic field. The R_2 value at the tumor site significantly decreased after 48 h of MT, which the authors attributed to metabolization of SPMNM. The mice the received SPMNM with 24 h of MT treatment also showed a much higher survival rate compared to mice treated with free BCNU or SPMNM alone,

with a median survival of 63 days for SPMNM/MT vs. 50 days for free BCNU and 48 days for SPMNM alone. Recent studies by Liao *et al.* [151] and Zhu *et al.* [152] also took advantage of magnetic targeting by applying an extra magnetic field to mediate active targeting of theranostic platforms to the tumor site. In both studies, the strong fluorescence signals of the dual-modal probes confirmed the enhanced targeting under the extra magnetic field.

5.3.1.2. Triggered release mechanisms

To enhance controlled release of loaded drug, nanocarriers with a triggered release mechanism have attracted great attention in recent years. Core-shell structures that can release drugs in response to specific stimuli such as temperature, pH, and redox conditions have been developed to achieve superior anti-cancer efficacy and minimize drug resistance and side effects. Among these specific stimuli, pH-responsive drug delivery systems have received great attention for their potential applications in selective and controllable drug release at tumor sites. For example, Asadi *et al.* [153] developed a core-shell structure with SPIO core and copolymer shell that is composed of pendant-activated ester moieties, *i.e.*, pentafluorophenyl acrylate (PFPA) and polyethylene glycol monomethyl ether methacrylate (PEGMA). DOX was then loaded onto the copolymer shell. Drug release kinetic study found that the maximum DOX release at pH = 7.4 was about 14 wt%, which increased to 45 wt% at pH = 5.4, and remained higher than 35 wt% within 50 h. Biswas *et al.* [154] synthesized an amphiphilic block copolymer PEG-*b*-P(*t*BMA-co-MAA) (*t*BMA: *t*-butyl methacrylate; MAA: methacrylic acid) consisting of a hydrophilic PEG block and a hydrophobic methacrylate block containing pendant carboxylic acids. The copolymer micelle then encapsulated SPIO nanoparticles into its hydrophobic core, and loaded DOX. In acidic environments, more carboxylic acid groups in the copolymer exist as their neutral forms (COOHs) and therefore exhibit a weaker electrostatic interaction with the amine groups of DOX molecules,

resulting in higher DOX release in aqueous solution at pH = 5 compared with pH = 7.4. Feng *et al.* [155] synthesized triblock copolymers of PEG, poly(N-(N',N'-diisopropylaminoethyl) aspartamide) (P(Asp-DIP)), and poly (lysine-cholic acid) (P(Lys-Ca)) (PEG-P(Asp-DIP)-P(Lys-Ca). The copolymer encapsulated SPIO and PTX inside its core in aqueous solution at neutral pH, and disassembled in acidic lysosomal compartments for rapid drug release.

The design of a redox-responsive drug delivery system can be achieved by including disulfide bonds in the copolymer, which can be cleaved via a thiol-disulfide exchange reaction with the reducing agent glutathione tripeptide (GSH). The GSH concentration is relatively low in plasma (2–20 μM), but tumor tissue is highly reductive and shows much higher GSH concentration (~10 mM) [156]. Therefore, the disulfide bonds cannot be cleaved in plasma and disulfide bond-containing copolymers remain stable in blood circulation, while the disulfide bonds are expected to be broken in tumor tissue due to the local high GSH level. As a result, part of the nanocarrier will be detached and the cellular uptake of the nanocarrier will be enhanced in tumor tissue. For example, Yu *et al.* [157] synthesized the graft copolymer mPEG-SS-NH-graft-PAsp-DA, and loaded Fe_3O_4 and DOX to form drug-loaded magnetic nanomicelles. Detachment of the PEG shell in tumor tissue resulting from cleavage of disulfide bonds accelerated release of DOX and enhanced cellular uptake. Ding *et al.* [158] developed a degradable micellar system assembled from multiblock polyurethanes-bearing disulfide bonds throughout the backbone. The copolymers were also bound to gemini quaternary ammonium (QA) pendent groups in the side chain to increase permeability of the micelles across the cell membrane for higher delivery efficiency. SPIO nanoparticles and anti-cancer drug triptolide were loaded into the core of the structure. The micelles exhibited enhanced release of drug within tumor cells, probably because the disulfide bonds embedded in

the backbone were cleaved by the high GSH level in the tumor, resulting in destabilization of the micelles.

5.3.1.3. Gene therapy

Gene therapy uses transgenes to treat diseases and is a promising therapeutic approach for cancer treatment. Effective delivery of gene vectors into the target site is essential in gene therapy. Zhang *et al.* [159,160] synthesized nanovectors with an iron oxide nanoparticle core coated with a copolymer of chitosan, PEG, and PEI. Green fluorescent protein-encoding DNA was bonded to the nanovectors to test the gene delivery efficiency. *In vivo* studies on xenograft tumors of C6 glioma confirmed accumulation of the magnetic nanoparticles to the tumor, resulting in an increase of R_2 constant and gene expression, which could be further enhanced if the nanovectors were labeled by chlorotoxin. In their recent work [161], catechol was grafted onto the chitosan backbone of the copolymer shell to increase its affinity to the iron oxide core, and therefore enhanced MR relaxivity and enabled the possibility to fine-tune its physiochemical properties. In cell transfection experiments on the human GBM cell line SF767, the copolymer nanovectors showed high transfection efficiency with minimal cell toxicity. Wang *et al.* [162] synthesized core-shell micelles using a block copolymer of PLA and mPEG. SPIO nanoparticles were loaded into the cores of the micelles. To effectively load and protect the nucleic acids, the micelles were surface-coated with cationic polymers like chitosan and PEI. A plasmid DNA was loaded onto the core-shell micelles and efficiently transfected various cell lines. Lee *et al.* [163] synthesized magnetic micelles with a SPIO aggregates core and PHEA-g-PEG-bPEI copolymer shell, which was prepared by grafting PEG and PEI blocks onto the poly(2-hydroxyethyl aspartamide) (PHEA) backbone. pDNA was then loaded into the magnetic micelles, and gene transfection was confirmed *in vitro* using the CT-26 colon cancer cell line. Wan *et al.* [164] developed a magnetic theranostic gene delivery system

with a SPIO core and a biodegradable stearic acid-modified low molecular weight polyethyleneimine (Stearic-LWPEI) shell. This delivery system showed high minicircle DNA (mcDNA) binding capability, and was able to protect mcDNA from enzymatic degradation and controllably release mcDNA in the presence of polyanionic heparin. Lee *et al.* [165] conjugated human vascular endothelial growth factor (VEGF) siRNA to PEG-PCL copolymer, then prepared micelles by mixing PDMA-b-PCL diblock copolymer with PEG-PCL copolymer. Ultra-small SPIO (USPIO) nanoparticles and the anti-cancer drug 7-ethyl-10-hydroxycamptothecin (SN-38) were then loaded into the hydrophobic core of the PCL block of the micelle. In *in vivo* experiments on mice bearing LS174T human colon adenocarcinoma tumors with high VEGF expression, the SN-38/USPIO-loaded micelles significantly inhibited the growth of tumor, resulting from the synergistic effect of chemotherapy and gene silencing.

5.3.1.4. Hyperthermia and photothermal therapy

Magnetic nanoparticles can also be used for treatment of cancer through hyperthermia, which is the heating of cells in the range of 41–47 °C [166]. Hyperthermia effect also increases the drug release efficiency at the tumor site. Xie *et al.* [167] synthesized nanoparticles with a Mn-Zn ferrite nanocrystal core and a PEG-phospholipid (1,2-distearoyl-*sn*-glycero-3-phosphoethanolamine-*N*-[methoxy(polyethylene glycol)] copolymers, DSPE-PEG2000) shell. The core-shell structure displayed excellent magnetic and thermal performance (r_2 = 338 mM^{-1} s^{-1}, specific absorption rate SAR = 324 W g^{-1} Fe). When exposed to AMF of 12 A at 390 kHz, the Mn-Zn ferrite nanocrystal core induced heating of the tumor surface to approximately 43 °C 30 min after i.v. injection. To study tumor growth behavior, tumor-bearing mice were treated with four core-shell nanoparticle injections and eight AMF exposures in 12 days. Tumor growth was

significantly attenuated compared to that of the control group who received AMF exposure but without injection of core-shell nanoparticles.

It has been noticed that gold nanoparticles with specific shapes display strong surface plasmon resonance absorption intensity in the NIR region, making them potential candidates for photothermal therapy of cancer or other lesions [168]. The past decade has seen an increasing interest in combining Fe_3O_4 and Au nanoparticles for their theranostic potential in MRI contrast enhancement and photothermal therapy. Li *et al.* [169] encapsulated a Fe_3O_4 core with a star-shaped Au shell, and then conjugated PEI and hyaluronic acid on the surface for an outer shell. Photothermal images of tumor-bearing mice injected with the nanoparticles followed by irradiation with a 915 nm laser confirmed a rapid temperature increase at the tumor site from 32.8 °C to 58.9 °C after 90 s laser irradiation, and the local high temperature (above 50 °C) remained for 205 s. Dong *et al.* [170] developed a nanocomposite with a superparamagnetic Fe_3O_4 core, a middle shell of the amphiphilic block copolymer PS-b-PAA, and an outer layer of gold shell. Thermal images showed that during irradiation with an 808 nm laser, the temperature of the tumor region injected with the nanocomposite increased from approximately 35 °C to 60 °C. Chen *et al.* [171] designed a theranostic nanoparticle with an iron oxide core surrounded by a polysiloxane layer and grafted with poly(ethylene oxide). NIR-resonant gold sulfide nanoparticles (Au_2SNPs) were loaded in the shell. Under exposure to an 885 nm laser, the Au_2SNPs nanoparticles generated a significant temperature rise from room temperature to 54 °C, with no degradation of the photothermal capability observed during repeated laser on/off cycles.

5.3.1.5. Other T_2-mode copolymer nanoparticles

In addition to iron oxide, MnFe and FePt alloys can also serve as effective T_2 contrast agents. Yang *et al.* [172] synthesized amphiphilic block copolymers, loaded $MnFe_2O_4$ nanocrystals

and DOX in the hydrophobic PCL core, and attached the anti-HER antibody (HER, Herceptin) on the surface of the shell. *In vivo* experiments on mice bearing breast cancer showed that the core-shell nanoparticles were able to show superior R_2 enhancement at the tumor site than the passive control using the EPR effect without antibody targeting, and excellent effects for the inhibition of tumor growth. Liu *et al.* [173] encapsulated FePt alloy nanoparticle into Fe_2O_3, and then coated the structure with amphiphilic PEG graft poly(maleic anhydride-alt-1-octadecene) (C_{18}PMH-PEG) polymer. DOX was then loaded into the hydrophobic block of the polymer shell, while FA was conjugated to the hydrophilic part for folate targeting.

5.3.1.6. Multimodal imaging and combined therapy

Multimodal imaging is the integration of two or more imaging modalities, utilizing the strengths of individual modalities while overcoming their limitations. Fluorescence dyes and MRI contrast agents are loaded/encapsulated in the copolymer carriers/platforms to achieve bimodal imaging of fluorescence and MR. Liao *et al.* [151] encapsulated SPIO, cyanine dye (IR820), and PTX with poly(ε-caprolactone-co-lactide)-b-poly(ethylene glycol)-b-poly(ε-caprolactone-co-lactide) (PCLA-PEG-PCLA) copolymer. NIR fluorescence imaging and MR images of 4T1 tumor-bearing BALB/c mice showed accumulation of the SPIO/IR820-loaded copolymers at the tumor site 8 h after injection. When exposed to an extra magnetic field, the tumor regions were found to have a higher fluorescence intensity and lower MR signal compared to images acquired without the extra magnetic field, which also confirmed the efficiency of magnetic targeting.

Zhou *et al.* [174] combined ultrasound with T2-MRI for dual imaging. They designed a nano-platform with perfluorohexane (PFH) microbubbles as the core and PLGA as the shell. Fe_3O_4 nanoparticles were loaded in the shell, DOX was encapsulated in the inner surface of the shell, while FA was conjugated to the outer surface of the shell, and the resulting nano-platform had the

structure PFH/DOX@PLGA/Fe_3O_4-FA. The temperature-responsive PFH core enhanced ultrasound imaging contrast and high-intensity focused ultrasound (HIFU) therapeutic efficiency. Compared to the non-targeted group (no FA conjugation on the outer surface of the shell), the designed nano-platform showed superior contrast in T_2-weighted MR images and real-time ultrasound images.

Combined therapy of multiple treatments shows great promise due to synergistic therapeutic effects. Purushotham *et al.* prepared composite nanoparticles of 43 nm γ-Fe_2O_3 nanoparticles coated with PNIPAM [175]. The thermoresponsive polymer shell was then loaded with DOX. *In vivo* magnetic targeting to the tumor with DOX-loaded PNIPAM-iron oxide nanoparticles was studied in a rat model implanted with hepatocellular carcinoma (HCC). MRI and histology showed that the injected nanoparticles were localized in the HCC, which demonstrated the targeting efficiency of the core-shell nanoparticles. The *in vitro* DOX release under magnetic hyperthermia conditions (variable strength of alternating magnetic fields ranges from 0.1–4 kA m^{-1} and a starting temperature of 37 °C) reached 14.7% after a total of 47 min, within which there was 30 min of exposure to hyperthermia temperature (41–48 °C) and 17 min above body temperature (37 °C). Further adjustment on the lower critical solution temperature of PNIPAM can be reached by using appropriate copolymers to achieve better synergistic therapeutic effect. *In vivo* study of the above-mentioned nanostructure PFH/DOX@PLGA/Fe_3O_4-FA [174] also showed that, when combined with HIFU, the inhibition efficiency for tumor growth was notably stronger than that of all control groups (non-targeted, chemotherapy only, HIFU only, free DOX, and saline).

5.3.2. T_1-mode copolymer nanoparticles

Gd-based and manganese-based [176] contrast agents are commonly used T_1 contrast agents for MRI, and they produce efficient positive contrast enhancement in T_1-weighted imaging. For example, Tong *et al.* [177] designed and synthesized a core-shell nano-carrier using 1,4,7,10-tetraazacyclododecane-1,4,7,10-tetraacetic acid-poly(ethyleneglycol)-block-poly(acrylamide-co-acrylonitrile) (DOTA-PEG-b-poly(AAm-co-AN)). Gd^{3+} ions and DOX were loaded into the hydrophobic core and chelated on the shell during the self-assembly process. *In vitro* experiments showed an elevated r_1 relaxivity of 25.88 mM^{-1} s^{-1}. Moreover, the chelated structure enhanced the cellular uptake efficiency of DOX to 2.12 times that of free DOX.

5.3.2.1. pH-responsive copolymer nanoparticles

Polyelectrolyte multilayers are promising candidates as a material for the shell of core-shell nanoparticles due to their pH-responsive drug encapsulation and release. Huang *et al.* [178] first synthesized Gd_2O_3:Yb^{3+}:Er^{3+}, a functionalized mesoporous silica nanoparticle core, which was then coated by multiple layers of polyelectrolyte poly(allylamine hydrochloride) and poly(sodium 4-styrenesulfonate) using a layer-by-layer technique. DOX was then loaded onto the polyelectrolyte shell in a strong acidic condition of pH = 2.0. The resulting DOX-loaded core-shell nanoparticles had an r_1 rate of 7.35 mM^{-1} s^{-1}. While less than 10% DOX was released over a 72 h period in a PBS buffer of pH = 7.4, more than 60% DOX was released within 72 h at pH = 5.2. *In vitro* cytotoxicity studies on MCF-7 breast cancer cells showed that both DOX-loaded nanoparticles and free DOX exhibited high cytotoxicity, although the former exhibited higher cytotoxicity than the latter. However, this enhanced cytotoxicity in the DOX-loaded nanoparticles should not be attributed to the platform itself, as the core-shell nanoparticles without DOX had

negligible cytotoxic effects on MCF-7 cells. The authors attributed this enhanced performance to the acidic microenvironment of endosomes and lysosomes, and the weakly acidic extracellular environment at the tumor site, which in turn, likely lead to a more effective release of DOX inside tumor cells. Tian *et al.* [179] synthesized an azide-terminated diblock copolymer from oligo(ethylene glycol)methyl ether methacrylate (OEGMA), 2-(diisopropylamino)ethyl methacrylate (DPA), and glycidyl methacrylate (GMA) via consecutive ATRP. The resulting copolymer was then functionalized with DOTA(Gd) and 4-(prop-2-ynyloxy)benzaldehyde and the resulting copolymers were further co-assembled into mixed micellar nanoparticles. The presence of GMA moieties inside the cores enabled encapsulation of tetrakis[4-(2-mercaptoethoxy)phenyl]ethylene (TPE-4SH), and thus the resulting nanoparticles were capable of MR and fluorescence dual imaging. To achieve selective targeting toward tumor tissues and *in situ* drug release, the nanoparticles were surface-conjugated with pH low insertion peptide (pHLIP), which actuated the accumulation of micellar nanoparticles in tumor tissues, confirmed by *in vivo* MR images of tumor-bearing BALB/c nude mice. *In vitro* cytotoxicity study showed that pHLIP also enhanced the release of the loaded cancer drug camptothecin at the tissue site.

Our group and collaborators have recently studied a unibody core-shell (UCS) nanoparticle [180,181]. These UCS nanoparticles were synthesized using a polymer platform formed by resorcinol and 1,3-phenylenediamine monomers. In the two-step synthesis process, Gd^{3+} was first conjugated to the polymer backbone to form the Gd-core, then DOX was encapsulated within the shell surrounding the Gd-core. Resorcinol was chosen as one of the components in the core for its stabilizing hydroxyl groups at the physiological pH ranges of interest. 1,3-phenylenediamine was chosen as the shell unit for its capability for pH-controllable release via its amino groups, as demonstrated in **Figure 5.2** and **Figure 5.6**. In addition, hydrophobic patches in 1,3-

phenylenediamine provide tight packing of DOX molecules, resulting in a superior drug loading efficiency of 97.5%. The design of such UCS-Gd-DOX takes advantage of the acidic pH values of some malignant tumor tissues, ranging around 6.5 [182].

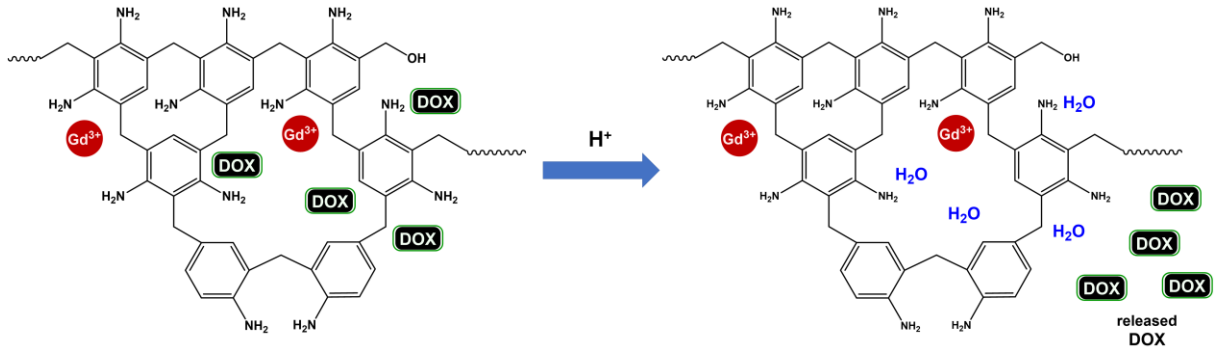

Figure 5.6. pH-controllable drug delivery and contrast-enhanced MR imaging based on core-shell smart polymer nanoparticles. At low pH, protonation of the amino groups on the shell leads to release of DOX molecules into the bulk solution. Upon release, the empty shell scaffolds take up water molecules, which interact with the inner-layer Gd, enhancing MRI contrast.

In vitro and *in vivo* studies of UCS-Gd-DOX as an innovative theranostic nanoparticle showed that: (1) DOX in the shell is effectively and selectively released in acidic environments (pH = 5.5) compared to weakly basic (pH = 7.4) physiological environments such as in the blood; (2) the signal-to-noise ratio (SNR) of the "region of interest" (ROI) after injection is increased by 10–30% (n = 3 mice). *In vitro* drug release studies showed that at pH = 8.0, 7.0, 6.0, 5.0, and 4.0, the release of DOX after 2 h was found to be <5%, 10%, 55%, 75%, and 80%, respectively. The increased release of DOX in acidic environments can be attributed to protonation of the polymer backbone. The notable increase in drug release from pH = 7.0 to pH = 6.0 verified the potential of UCS-Gd-DOX for targeted therapy towards malignant tumor tissues. In addition, based on data acquired from *in vitro* T_1-weighted MR images, the r_1 relaxivity of UCS-Gd-DOX at pH = 5.5 was found to be 14.5 mM^{-1} s^{-1}, which was significantly higher than that of UCS-Gd-DOX at pH = 7.4

($0.9\ mM^{-1}\ s^{-1}$), overall reflecting the pH-switchable MR contrast capability of UCS-Gd-DOX. We hypothesize this pH-switchability is a result of replacing the water molecules associated to the shell of the nanovehicle with DOX in an acidic condition.

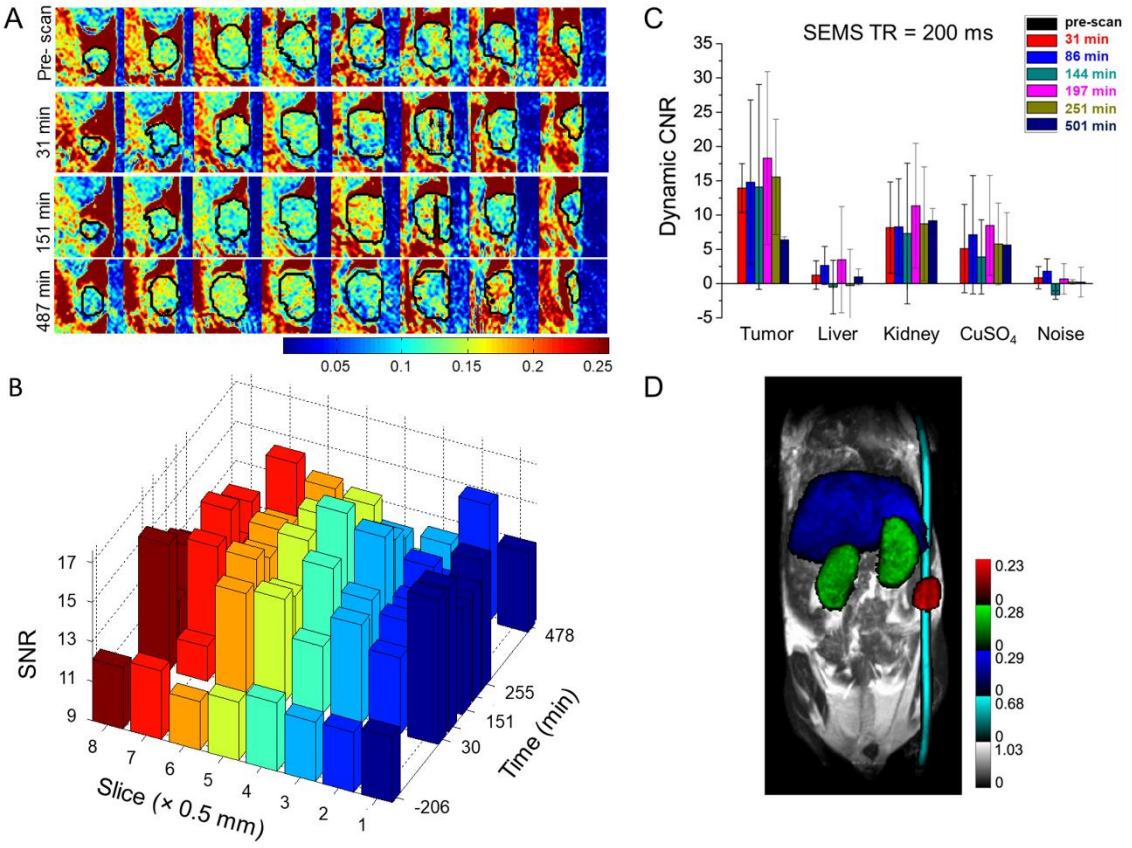

Figure 5.7. MR analysis of human cervical tumor-bearing mice using UCS-Gd-DOX. **(A)** 2D-slice images of tumor (black circles), where the color bar indicates the MR signal intensity. Only the image pixels with intensity values between ±2 standard deviations (STD) of the ROI signal were kept to avoid image artifacts. **(B)** SNR for each slice in (A) at time points: pre-scan (-206 min), 30 min, 82 min, 151 min, 203 min, 255 min, and 487 min. **(C)** Contrast-to-noise ratio (CNR) of tumor, liver, kidney, $CuSO_4$, and noise area before and after injection. Here CNR % = $(SNR_{postinjection} - SNR_{preinjection}) / SNR_{preinjection} \times 100\%$. Error bars represent mean ± standard deviation (n = 3 mice). **(D)** T1-weighted MR images acquired by "spin-echo multiple slices" (SEMS) and then processed by "maximum intensity projection". Repetition time (TR) = 200 ms, echo time (TE) = 10 ms, field of view (FOV) = 64×32 mm^2, matrix size = 256×128, slice thickness = 0.5 mm. The ROIs of tumor, liver, kidney, and $CuSO_4$ reference are indicated by red, blue, green, and cyan shades, respectively.

In vivo multiple-slice MR data of 3 mice is shown in **Figure 5.7**, where T_1-weighted images of NOD/SCID mice with heterotopic, subcutaneous human cervical cancers were acquired and processed with "maximum intensity projection". The contrast of the tumor area increases with time up to 251 min after the injection of UCS-Gd-DOX. This longer contrast enhancement period compared to free Gd-DPTA may be attributed to the longer circulation time of nanoparticles in the blood.

The pH-responsive design of the unibody core-shell nanoparticle not only improved the MRI contrast at the tumor site with respect to other tissue/organs, but also successfully suppressed growth of subcutaneous human cervical cancer in mouse xenograft models. As theranostic nanoparticles with Gd-conjugation and DOX-doping can be synthesized in a straightforward approach, we anticipate further expansive applications of UCS-Gd-DOX in the field of cancer treatment.

5.3.2.2. Combined therapy

Recent studies also combined chemotherapy with other treatments to achieve a synergistic therapeutic effect. For example, in recent work by Li *et al.* [183], CuS nanoparticles served as the core and were encapsulated by a copolymer shell formed by one-pot emulsifier-free emulsion polymerization of styrene, N-isopropylacrylamide, methacrylic acid, and polymerizable complex $Gd(AA)_3phen$. DOX was then loaded to the copolymer microsphere with a high loading capacity (15.3 wt%). This core-shell nano-platform can be used for photothermal therapy, since the photosensitive CuS cores effectively absorb NIR light and convert NIR light to heat. In addition, the local temperature rise during NIR irradiation shrinks the thermo-sensitive copolymer shell, promoting DOX release at the tumor site. *In vivo* therapeutic study on 4T1 tumor-bearing mice showed that tumor growth was significantly inhibited in the CuS@copolymer/DOX + NIR laser

group, compared to other groups (control group, free DOX group, and CuS@copolymer + NIR laser group), which demonstrated the promise of multiple treatment modalities. Gold nanostar (AuNS) can also serve as the core and enable plasmonic photothermal effects [184]. *In vivo* experiments on 4T1 breast tumor-bearing mice showed that AuNS@CP, which was formed by an AuNS core surrounded by a coordination polymers shell composed of the anti-cancer drug gemcitabine-5'-monophosphate (GMP) and Gd(III), significantly suppressed the growth of tumor under laser irradiation (median tumor volume of 138 mm^3 on day 15, n = 5) compared to all 6 control groups (median tumor volume ranged from 447 mm^3 to 1145 mm^3 on day 15).

5.3.2.3. Other T_1-mode copolymer nanoparticles

In recent years, manganese oxide (MnO_2)—a T_1 contrast agent—has attracted great interest in cancer theranostics because of its additional catalyzing function to decompose endogenous H_2O_2 inside tumors, subsequently contributing to synergistic cancer therapies. For example, Hu *et al.* [185] combined chemotherapy and photodynamic therapy (PDT), which is a recent, minimally-invasive modality that kills cancer cells by the cytotoxic singlet oxygen ($^1O_2$) generated from light-activated photosensitizers. To optimize the efficacy of the combination therapy, they fabricated a multifunctional polymeric nanoparticle system using amphiphilic block copolymer PCLA-PEG-PCLA. MnO_2 and hydrophilic DOX were then loaded in the water phase core, while the photosensitizer chlorin e6 (Ce6) was loaded in the hydrophobic layer. At the tumor location, encapsulated MnO_2 reacted with H_2O_2, a massive tumor metabolite, and generated O_2 for PDT and Mn^{2+} for MRI contrast enhancement. *In vivo* rat experiments showed that the MnO_2-, DOX-, and Ce6-loaded copolymer nanoparticle inhibited tumor growth effectively with an inhibition ratio of 92.35% (calculated by tumor weight), statistically (n =5 for each group) much higher than all 7 control groups. Wang *et al.* [186] used PLGA to load gold nanorods (AuNRs) and DTX to form a

PLGA/AuNR/DTX core, then coated it with MnO_2 ultrathin nanofilms. The higher GSH level in the tumor microenvironment caused the degradation of MnO_2 into Mn^{2+}, enabling T_1-MRI as well as controlled release of DTX at the tumor site. The combination of Mn^{2+} and AuNRs enabled T_1-MRI/CT dual imaging, which was confirmed by *in vivo* MRI/CT of mice bearing S-180 sarcoma tumors.

The Liu group have demonstrated the application of MnO_2 or its complex in core-shell nano-platforms for T_1-weighted MRI and therapy. In one study [187], they designed a nano-platform composed of MnO_2 core and nanoscale coordination polymer shell that is responsive to pH or H_2O_2 concentration. *In vivo* mouse experiments showed that the MR signal intensity in the tumor achieved approximately 2-fold positive enhancement at 12 h post injection. It was further found in the *in vivo* combination therapy that when combined with X-ray irradiation treatment, the nano-platform showed the most effective tumor growth inhibition effect. On Day 14, the tumor volume was approximately 1/6 that of the control group, and 1/4 that of the X-ray radiation alone group. In another study [188], they formed a core-shell structure consisting of Ce6-premodified human serum albumin (HSA-Ce6) core and RGD-premodified HSA (HSA-RGD) shell. Ce6 in the core served as a chelating agent for Mn^{2+} for T_1-weighted MRI and as a photosensitizer for fluorescence imaging, and enabled photodynamic therapy for cancer at the same time. *In vivo* experiments on mice bearing U87MG tumors showed enhancement in both r_1 relaxivity and T_1-weighted MR signal intensity and confirmed the targeting efficiency of RGD. As a result of the combined photodynamic/chemotherapy, the PTX-bound core-shell structure significantly inhibited tumor growth.

In a very recent work [189], Sun *et al.* designed and fabricated a nano-platform for T_1-weighted MR/fluorescence dual-modal imaging and imaging-guided cancer chemotherapy. They

first synthesized a PEI-driven self-assembled Gd-/Eu-doped CaF_2 nanocluster (GECN) as the core, loaded the anti-cancer drug cisplatin (CDDP), and then coated the core by PEG-coupled FA. It has been found that inorganic fluorides doped with lanthanides such as Gd and Eu possess excellent fluorescence properties as well as paramagnetic properties [190]. The r_1 rate constant of the nano-platform was measured to be 4.91 mM^{-1} s^{-1}, higher than that of Gd-DTPA (3.34 mM^{-1} s^{-1}). The nano-platform also displayed better contrast in *in vivo* images of mice bearing HeLa cells compare to Gd-DTPA, resulting from the active FA targeting.

5.3.3. Heteronuclear copolymer nanoparticles

Similar to fluorinated dendrimers, fluorinated core-shell copolymers have also been used as theranostic agents because of their good biocompatibility and low *in vivo* background signal compared to iron oxide, Gd^{3+}, and Mn oxides. Porsch *et al.* [191] synthesized fluorinated nanoparticles by self-assembly of star-shaped amphiphilic block copolymers. The hydrophilic segment of the copolymer was formed by the polymerization of monomers OEGMA and trifluoroethyl methacrylate (TFEMA) via ATRP. TFEMA was chosen for its chemically equivalent fluorine atoms that are able to produce optimal MRI signal, and OEGMA was chosen for its hydrophilic and highly dynamic structure, which was hypothesized by the authors to facilitate the mobility of the fluorine atoms of TFEMA. The authors studied five star-shaped copolymers with different numbers of arms (4 or 16 arms) and different molecular weights ranging from 10k to 52k, and noticed that larger hydrophobic cores increased the loading capacity of DOX while larger hydrophilic shells decreased it. *In vitro* studies showed that the designed nanoparticles can be taken up by breast cancer cells and deliver DOX into the cell nuclei with controllable drug release kinetics.

Perfluorooctyl bromide (PFOB) has attracted great attention in more recent work on fluorinated copolymer contrast agents, since it is approved by the FDA due to its safety. For example, Boissenot *et al.* [192] encapsulated PTX in core-shell nanocapsules made of a PFOB core and PLGA-PEG shell. ^{19}F MRI confirmed the passive accumulation of the core-shell nanoparticles to the tumor site, which led to a statistically (n = 9) significant 2-fold reduction in tumor growth of the mice at 10–12 days after CT-26 cells induction compared to the negative control or the generic PTX groups. Quang *et al.* [193] formed nanoparticles consisting of a PFOB core and a shell of PLGA followed by a coat of polystyrene sulfonate (PSS), which can facilitate entry of the nanoparticles into cells via caveolae-mediated endocytosis. *In vivo* study in normal BALB/c mice and immune-compromised NOD/SCID mice showed that one week after transplantation of human cells, 40% of the ^{19}F MRI signal was lost in normal mice, while only 10% was lost in immune-compromised mice, proving the potential use of this PSS-coated core-shell nanoparticle as a prognostic indicator for immune rejection in stem cell therapy.

5.4. Major challenges and safety aspects for clinical uses

Specific theranostic approaches for drug delivery could be very promising directions for detecting and eliminating cancer lesions at early stages, providing new hope to cancer patients worldwide. Unfortunately, this area of treatment still suffers from several safety issues and challenges. Firstly, the use of a high dose of Gd(III) is toxic to the kidney, thus the FDA does not approve administering Gd(III)-based drugs to patients with any serious renal problems. Although the alternative SPIO is a safer and biodegradable material, T_2-weighted MR imaging shows a negative contrast in comparison to T_1-weighted positive contrast, making it less efficient for

differentiating tumor tissues from healthy tissues. Pharmacokinetic considerations and biodistribution studies of specific nanoconstructs are very important for successful *in vivo* applications and clinical translation [194]. Major concerns for the use of either the dendrimer or the core-shell copolymer are material toxicity, rapid clearance from the body, imperfect biodistribution, and incomplete biodegradability [1]. However, PEGylation and other surface modifications could decrease the toxicity of the dendrimer to healthy tissues [25]. A potential solution for the dendrimer nanovehicle would be to use a peptide-like dendrimer having similar properties to those of protein and thus be biodegradable. Recently, lysine polypeptides or amino acid-based dendrimers have been developed [60] as biodegradable alternatives for delivery nanovehicles, and show future promise for clinical use [195]. A comprehensive discussion on the biodegradability of different kinds of dendrimers can be found in a recent review by Leiro *et al.* [196]. Core-shell copolymers could also be modified using polyesters such as PLGA, PLA, or poly(glycolide) as the polymer backbone to enhance biocompatibility and biodegradability [197–199].

Some of the approaches discussed in this review rely on pH-controlled delivery that is not very specific towards early tumors, as the pH values of early tumors are generally not very different from those of normal tissues. Therefore, more investigations are required in this line for controlled drug delivery. Similarly, passive targeting has its limitations.[200] Unlike passive targeting active targeting relies on cell specific recognition via target specific ligand binding and internalization happens through receptor-mediated endocytosis. Hence, nanoparticles are potent to be accumulated in tumor site in a higher concentration via active targeting, compared to passive targeting. Therefore, as discussed, future advancements should aim to upgrade all the theranostic structures to include active targeting moieties to specifically target cancer cells and minimize adverse side effects to healthy cells. Further clinical trials and experiments are required to optimize

the safety, viability, and applicability of different nanovehicles before they could be used for clinical purposes.

5.5. Conclusions

We have discussed the current status of research on MR-guided theranostic uses of polymer-like nanostructures such as dendrimer and copolymer core-shell-based nanoparticles. Polymer-like structures provide a means to target the tumor site and deliver the required amount of drug there while minimizing adverse side effects to surrounding healthy tissues. Several types of cancers such as pancreatic cancer cannot be treated by conventional chemotherapy, because the medicine cannot reach the tumor site due to the resistance offered by the surrounding stroma. However, ATRA-conjugated dendrimer-coated SPIO have the potential to overcome this resistance and deliver medicine to the tumor site [38] as described in section 5.2.1.1. Moreover, this type of theranostic could reduce the need for surgery, or increase the efficiency of surgical removal of the tumor to make the treatment as noninvasive as possible. However, the safety issues have not yet been fully resolved and FDA approval is still pending for the use of these types of nanovehicles for cancer therapy. This platform is still very young but developing rapidly. Regardless of the many hurdles and difficulties, the uses of dendrimer and copolymer core-shell nanovehicles provide a very promising direction for future nanomedicine and cancer therapy.

Supplementary materials

Table S5.1. Theranostic approaches using functionalized dendrimer.

Imaging probe	Dendrimer	Drug	Targeting approach	Delivery mechanism	Cancer	Ref.
SPIO (T_2 MRI)	G4 PAMAM modified with poly I:C	DOX	N/A [a]	pH-responsive	*In vitro*: breast cancer (MCF-7)	34
SPIO (T_2 MRI)	G4 PAMAM	DOX	N/A [a]	pH-responsive	*In vitro*: breast cancer (MCF-7)	35
SPIO (T_2 MRI)	G0 PAMAM	Gemcitabine	ATRA [a]	pH-responsive	*In* vitro: pancreatic cancer (SU86.86, T3M4, PANC-1)	38
SPIO (T_2 MRI)	G3.5 PAMAM	DOX	FA [a]	pH-responsive (hydrazone bond)	*In vivo*: melanoma (B16-F0 s.c.)	43
SPIO (T_2 MRI)	G2.5 PAMAM	DOX	FA [a]	pH-responsive (hydrazone bond)	*In vivo*: melanoma (B16-F0 s.c.)	44
SPIO (T_2 MRI)	G4 PAMAM	CDF	FA [a]	None	*In vitro*: cervical cancer (HeLa), ovarian cancer (SKOV3)	48
SPIO (T_2 MRI) with Cy5.5 for fluorescence	G3.5 PAMAM	PTX	FA [a]	pH-responsive (ester bond)	*In vitro*: breast cancer (MCF-7), hepatocarcinoma (H22) *In vivo*: hepatocarcinoma (H22 s.c.)	51
SPIO (T_2 MRI)	G1/G2	Quercetin	N/A [a]	pH-responsive	*In vitro*: prostate carcinoma (DU145)	52
SPIO (T_2 MRI)	G2.0 Dendritic linear triblock copolymer (PAMAM-*b*-PDMAEMA-*b*-PPEGMA)	DOX	N/A [a]	pH-responsive	*In vitro*: cervical cancer (HeLa)	53
SPIO (T_2 MRI)	G2.0 Dendritic linear triblock copolymer (PAMAM-*b*-PDMAEMA-*b*-PNIPAM)	DOX	N/A [a]	Temperature-responsive	*In vitro*: cervical cancer (HeLa)	54

SPIO (T_2 MRI)	G1/G2/G3 Dendritic linear block copolymer (linear poly(ε-caprolatone), dendritic polyamino-ester and linear PEG)	Quercetin	N/A [a]	pH-responsive		59
SPIO (T_2 MRI)	Peptide dendrimer	DOX and AMF	N/A [a]	None	*In vitro*: cervical cancer (HeLa), HeLa contaminant (KB), breast cancer (MCF-7), prostate cancer (PC-3)	60
SPIO (T_2 MRI)	G2/4/6 dendriplex	Gene therapy (plasmid DNA)	N/A [a]	None	*In vitro*: fibroblasts (NIH 3T3)	64
SPIO (T_2 MRI)	G5 PAMAM dendrimer	Gene therapy (antisense strategy using oligonucleotide)	*Survivin* gene [a]	None	*In vitro*: breast cancer (MCF-7, MDA-MB-435), liver cancer (HepG2), prostate cancer (LNCaP), promyelocytic leukemia (HL-60)	68
SPIO (T_2 MRI)	PPI G5 dendrimer	Gene therapy (siRNA) and cisplatin	LHRH peptide [a]	None	*In vitro*: lung carcinoma (A549; LHRH positive), ovarian cancer (SKOV-3; LHRH negative) *In vivo*: lung cancer (A549 s.c.)	74
SPIO (T_2 MRI)	G4 PAMAM dendrimer	Gene herapy (siRNA)	N/A [a]	None	*In vitro*: breast cancer (MCF-7)	77
SPIO (T_2 MRI) and fluorescence tracking of (EGFR) expression	G4	Gene therapy (siRNA)	Passive [a]	Convection-assisted delivery	*In vitro*: cervical cancer (HeLa) *In vivo*: glioblastoma (GBM-6, transgenic model)	78
Gd(III) (T_1 MRI)	G5 PAMAM dendrimer	DOX	FA	None	*In vitro*: HeLa contaminant (KB)	88
Gd(III) (T_1 MRI)	Dendrimersomes	PLP	Passive	None	*In vitro*: melanoma (B16.F10) *In vivo*: melanoma (B16.F10 s.c.)	90
Gd(III) (T_1 MRI)	G3 dendrigraft poly-L-lysines	Gene therapy	N/A	None	*In vitro*: pancreatic ductal	92

					adenocarcinoma (PaCa-2) *In vivo*: pancreatic ductal adenocarcinoma (PaCa-2 orthotopic)	
Gd(III) (T_1 MRI)	Supramolecular assembly of Ad-PAMAM, Ad-PEG,CD-PEI	DOX	Passive	AMF	*In vitro*: colorectal adenocarcinoma (DLD-1) *In vivo*: colorectal adenocarcinoma (DLD-1 s.c.)	96, 101
Gd(III) (T_1 MRI) with Cy 5 fluorescence probe	G2 polylysine dendrimer with a silsesquioxane core	Surgery	CGLIIQK NEC, CLTI (peptides)	None	*In vivo*: prostate cancer (PC3-GFP orthotopic)	102
^{19}F MRI	Fluorinated G3 and G6 PAMAM	Rhodamine B as model drug	Passive	pH-responsive	*In vitro*: Chinese hamster ovarian cancer (CHO; phantom) *In vivo*: female B6 mouse	134

[a] SPIO structures are also potent for magnetofection targeting approaches.

EGFR: epidermal growth factor receptor; **s.c**.: subcutaneous

Acknowledgments

This chapter is a reproduction of the publication: Ray, S.; Li, Z.; Hsu, C.-H.; Hwang, L.-P.; Lin, Y.-C.; Chou, P.-T.; Lin, Y.-Y. Dendrimer- and Copolymer-Based Nanoparticles for Magnetic Resonance Cancer Theranostics. Theranostics 2018, 8 (22), 6322–6349. https://doi.org/10.7150/thno.27828. I gratefully acknowledge Dr. Zhao Li for writing copolymer-based part, Dr. Chao-Hsiung Hsu for helping in data reproduction for figures and Prof. Yung-Ya Lin for supervising this project. I want to thank Prof. L.-P Hwang, Prof. Y.-C Lin and Prof. P.-T. Chou for helping to improve this manuscript and lab facilities. This work was supported by the National Science Foundation (CHE-1112574 and CHE-1416598), University of California Cancer Research Award (CRR-13-201412), Hirshberg Foundation for Pancreatic Cancer Research, and Taiwan Ministry of Science and Technology (NSC 100-2113-M-002-008, NSC 101-2113-M-002-018, and MOST 103-2923-M-002-006). Thanks to Dr. Sheba Plamthottam for graphics assistance.

References

(1) Janib, S. M.; Moses, A. S.; MacKay, J. A. Imaging and Drug Delivery Using Theranostic Nanoparticles. *Adv. Drug Deliv. Rev.* **2010**, *62* (11), 1052–1063. https://doi.org/10.1016/j.addr.2010.08.004.

(2) Sunderland, C. J.; Steiert, M.; Talmadge, J. E.; Derfus, A. M.; Barry, S. E. Targeted Nanoparticles for Detecting and Treating Cancer. *Drug Dev. Res.* **2006**, *67* (1), 70–93. https://doi.org/10.1002/ddr.20069.

(3) Kelkar, S. S.; Reineke, T. M. Theranostics: Combining Imaging and Therapy. *Bioconjug. Chem.* **2011**, *22* (10), 1879–1903. https://doi.org/10.1021/bc200151q.

(4) Key, J.; Leary, J. F. Nanoparticles for Multimodal in Vivo Imaging in Nanomedicine. *Int. J. Nanomedicine* **2014**, *9*, 711–726. https://doi.org/10.2147/IJN.S53717.

(5) Huang, G.; Chen, H.; Dong, Y.; Luo, X.; Yu, H.; Moore, Z.; Bey, E. A.; Boothman, D. A.; Gao, J. Superparamagnetic Iron Oxide Nanoparticles: Amplifying Ros Stress to Improve Anticancer Drug Efficacy. *Theranostics* **2013**, *3* (2), 116–126. https://doi.org/10.7150/thno.5411.

(6) Yen, S. K.; Padmanabhan, P.; Selvan, S. T. Multifunctional Iron Oxide Nanoparticles for Diagnostics, Therapy and Macromolecule Delivery. *Theranostics* **2013**, *3* (12), 986–1003. https://doi.org/10.7150/thno.4827.

(7) Kotb, S.; Detappe, A.; Lux, F.; Appaix, F.; Barbier, E. L.; Tran, V. L.; Plissonneau, M.; Gehan, H.; Lefranc, F.; Rodriguez-Lafrasse, C.; et al. Gadolinium-Based Nanoparticles and Radiation Therapy for Multiple Brain Melanoma Metastases: Proof of Concept before Phase I Trial. *Theranostics* **2016**, *6* (3), 418–427. https://doi.org/10.7150/thno.14018.

(8) Merbach, A. E.; Helm, L.; Tóth, E. *The Chemistry of Contrast Agents in Medical Magnetic Resonance Imaging*, 2nd ed.; Wiley: Chichester, UK, 2013. https://doi.org/10.1002/9781118503652.

(9) Li, M.; Kim, H. S.; Tian, L.; Yu, M. K.; Jon, S.; Moon, W. K. Comparison of Two Ultrasmall Superparamagnetic Iron Oxides on Cyto-Toxicity and MR Imaging of Tumors. *Theranostics* **2012**, *2* (1), 76–85. https://doi.org/10.7150/thno.3462.

(10) Ho, D. N.; Kohler, N.; Sigdel, A.; Kalluri, R.; Morgan, J. R.; Xu, C.; Sun, S. Penetration of Endothelial Cell Coated Multicellular Tumor Spheroids by Iron Oxide Nanoparticles. *Theranostics* **2012**, *2* (1), 66–75. https://doi.org/10.7150/thno.3568.

(11) Li, L.; Jiang, W.; Luo, K.; Song, H.; Lan, F.; Wu, Y.; Gu, Z. Superparamagnetic Iron Oxide Nanoparticles as MRI Contrast Agents for Non-Invasive Stem Cell Labeling and Tracking. *Theranostics* **2013**, *3* (8), 595–615. https://doi.org/10.7150/thno.5366.

(12) Li, Z.; Hsu, C.-H.; Dimitrov, N.; Hwang, D. W.; Chang, H.-W.; Hwang, L.-P.; Lin, Y.-Y. Sensitive Imaging of Magnetic Nanoparticles for Cancer Detection by Active Feedback MR. *Magn. Reson. Med.* **2015**, *74* (1), 33–41. https://doi.org/10.1002/mrm.25632.

(13) van der Zee, J. Heating the Patient: A Promising Approach? *Ann. Oncol.* **2002**, *13* (8), 1173–1184. https://doi.org/10.1093/annonc/mdf280.

(14) Chilkoti, A.; Dreher, M. R.; Meyer, D. E.; Raucher, D. Targeted Drug Delivery by Thermally Responsive Polymers. *Adv Drug Deliv Rev* **2002**, *54* (5), 613–630. https://doi.org/http://www.ncbi.nlm.nih.gov/entrez/query.fcgi?cmd=Retrieve&db=PubMed&dopt=Citation&list_uids=12204595.

(15) Wu, W.; Luo, L.; Wang, Y.; Wu, Q.; Dai, H.; Li, J.; Durkan, C.; Wang, N. Endogenous PH-Responsive Nanoparticles with Programmable Size Changes for Targeted Tumor Therapy and Imaging Applications. *Theranostics* **2018**, *8* (11), 3038. https://doi.org/10.7150/thno.23459.

(16) Peer, D.; Karp, J. M.; Hong, S.; Farokhzad, O. C.; Margalit, R.; Langer, R. Nanocarriers as an Emerging Platform for Cancer Therapy. *Nat. Nanotechnol.* **2007**, *2* (12), 751–760. https://doi.org/10.1038/nnano.2007.387.

(17) Wang, Z.; Niu, G.; Chen, X. Polymeric Materials for Theranostic Applications. *Pharm. Res.* **2014**, *31* (6), 1358–1376. https://doi.org/10.1007/s11095-013-1103-7.

(18) Kesharwani, P.; Jain, K.; Jain, N. K. Dendrimer as Nanocarrier for Drug Delivery. *Progress in Polymer Science*. 2014, pp 268–307. https://doi.org/10.1016/j.progpolymsci.2013.07.005.

(19) Zhao, Y.; Liu, S.; Li, Y.; Jiang, W.; Chang, Y.; Pan, S.; Fang, X.; Wang, Y. A.; Wang, J. Synthesis and Grafting of Folate–PEG–PAMAM Conjugates onto Quantum Dots for Selective Targeting of Folate-Receptor-Positive Tumor Cells. *J. Colloid Interface Sci.* **2010**, *350* (1), 44–50. https://doi.org/10.1016/J.JCIS.2010.05.035.

(20) Tomalia, D. A.; Reyna, L. A.; Svenson, S. Dendrimers as Multi-Purpose Nanodevices for Oncology Drug Delivery and Diagnostic Imaging. *Biochem. Soc. Trans.* **2007**, *35* (Pt 1), 61–67. https://doi.org/10.1042/BST0350061.

(21) Cheng, Y.; Zhao, L.; Li, Y.; Xu, T. Design of Biocompatible Dendrimers for Cancer Diagnosis and Therapy: Current Status and Future Perspectives. *Chem. Soc. Rev.* **2011**, *40* (5), 2673. https://doi.org/10.1039/c0cs00097c.

(22) Ma, Y.; Mou, Q.; Wang, D.; Zhu, X.; Yan, D. Dendritic Polymers for Theranostics. *Theranostics* **2016**, *6* (7), 930–947. https://doi.org/10.7150/thno.14855.

(23) Svenson, S.; Tomalia, D. A. Dendrimers in Biomedical Applications—reflections on the Field. *Adv. Drug Deliv. Rev.* **2012**, *64*, 102–115. https://doi.org/10.1016/J.ADDR.2012.09.030.

(24) Tomalia, D. A.; Baker, H.; Dewald, J.; Hall, M.; Kallos, G.; Martin, S.; Roeck, J.; Ryder, J.; Smith, P. A New Class of Polymers: Starburst-Dendritic Macromolecules. *Polym. J.* **1985**, *17* (1), 117–132. https://doi.org/10.1295/polymj.17.117.

(25) Lo, S.-T.; Kumar, A.; Hsieh, J.-T.; Sun, X. Dendrimer Nanoscaffolds for Potential Theranostics of Prostate Cancer with a Focus on Radiochemistry. *Mol. Pharm.* **2013**, *10* (3), 793–812. https://doi.org/10.1021/mp3005325.

(26) Fréchet, J. M. J.; Tomalia, D. A. *Dendrimers and Other Dendritic Polymers*; Fréchet, J. M. J., Tomalia, D. A., Eds.; Wiley: Chichester, UK, 2001.

(27) Colombo, M.; Carregal-Romero, S.; Casula, M. F.; Gutiérrez, L.; Morales, M. P.; Böhm, I. B.; Heverhagen, J. T.; Prosperi, D.; Parak, W. J. Biological Applications of Magnetic Nanoparticles. *Chem. Soc. Rev.* **2012**, *41* (11), 4306. https://doi.org/10.1039/c2cs15337h.

(28) Sun, W.; Mignani, S.; Shen, M.; Shi, X. Dendrimer-Based Magnetic Iron Oxide Nanoparticles: Their Synthesis and Biomedical Applications. *Drug Discov. Today* **2016**, *21* (12), 1873–1885. https://doi.org/10.1016/j.drudis.2016.06.028.

(29) Scherer, F.; Anton, M.; Schillinger, U.; Henke, J.; Bergemann, C.; Krüger, A.; Gänsbacher, B.; Plank, C. Magnetofection: Enhancing and Targeting Gene Delivery by Magnetic Force in Vitro and in Vivo. *Gene Ther.* **2002**, *9* (2), 102–109. https://doi.org/10.1038/sj.gt.3301624.

(30) Liu, W.-M.; Xue, Y.-N.; Peng, N.; He, W.-T.; Zhuo, R.-X.; Huang, S.-W. Dendrimer Modified Magnetic Iron Oxide Nanoparticle/DNA/PEI Ternary Magnetoplexes: A Novel Strategy for Magnetofection. *J. Mater. Chem.* **2011**, *21* (35), 13306. https://doi.org/10.1039/c1jm11460c.

(31) Matsumura, Y.; Maeda, H. A New Concept for Macromolecular Therapeutics in Cancer Chemotherapy: Mechanism of Tumoritropic Accumulation of Proteins and the Antitumor Agent Smancs. *Cancer Res.* **1986**, *46* (12 Pt 1), 6387–6392.

(32) Duncan, R. Tumour Targeting by Enhanced Permeability and Retention (EPR) Effect. *Ann. Oncol.* **1998**, *9* (2), 39.

(33) Singal, P.; Li, T.; Kumar, D.; Danelisen, I.; Iliskovic, N. Adriamycin-Induced Heart Failure: Mechanisms and Modulation. *Mol. Cell. Biochem.* **2000**, *207* (1/2), 77–86. https://doi.org/10.1023/A:1007094214460.

(34) Khodadust, R.; Unsoy, G.; Gunduz, U. Development of Poly (I:C) Modified Doxorubicin Loaded Magnetic Dendrimer Nanoparticles for Targeted Combination Therapy. *Biomed. Pharmacother.* **2014**, *68* (8), 979–987. https://doi.org/10.1016/J.BIOPHA.2014.10.009.

(35) Rouhollah, K.; Pelin, M.; Serap, Y.; Gozde, U.; Ufuk, G. Doxorubicin Loading, Release, and Stability of Polyamidoamine Dendrimer-Coated Magnetic Nanoparticles. *J. Pharm. Sci.* **2013**, *102* (6), 1825–1835. https://doi.org/10.1002/jps.23524.

(36) Weber, A.; Kirejczyk, Z.; Besch, R.; Potthoff, S.; Leverkus, M.; Häcker, G. Proapoptotic Signalling through Toll-like Receptor-3 Involves TRIF-Dependent Activation of Caspase-8 and Is under the Control of Inhibitor of Apoptosis Proteins in Melanoma Cells. *Cell Death Differ.* **2010**, *17* (6), 942–951. https://doi.org/10.1038/cdd.2009.190.

(37) Salvador, A.; Igartua, M.; Hernández, R. M.; Pedraz, J. L. Combination of Immune Stimulating Adjuvants with Poly(Lactide-Co-Glycolide) Microspheres Enhances the Immune Response of Vaccines. *Vaccine* **2012**, *30* (3), 589–596. https://doi.org/10.1016/J.VACCINE.2011.11.057.

(38) Yalçın, S.; Erkan, M.; Ünsoy, G.; Parsian, M.; Kleeff, J.; Gündüz, U. Effect of Gemcitabine and Retinoic Acid Loaded PAMAM Dendrimer-Coated Magnetic Nanoparticles on Pancreatic Cancer and Stellate Cell Lines. *Biomed. Pharmacother.* **2014**, *68* (6), 737–743. https://doi.org/10.1016/J.BIOPHA.2014.07.003.

(39) Apte, M. V; Haber, P. S.; Applegate, T. L.; Norton, I. D.; McCaughan, G. W.; Korsten, M. A.; Pirola, R. C.; Wilson, J. S. Periacinar Stellate Shaped Cells in Rat Pancreas: Identification, Isolation, and Culture. *Gut* **1998**, *43* (1), 128–133. https://doi.org/10.1136/GUT.43.1.128.

(40) Michael, A.; Hill, M.; Maraveyas, A.; Dalgleish, A.; Lofts, F. 13-Cis-Retinoic Acid in Combination with Gemcitabine in the Treatment of Locally Advanced and Metastatic Pancreatic Cancer — Report of a Pilot Phase II Study. *Clin. Oncol.* **2007**, *19* (2), 150–153. https://doi.org/10.1016/j.clon.2006.11.008.

(41) Weitman, S. D.; Lark, R. H.; Coney, L. R.; Fort, D. W.; Frasca, V.; Zurawski, V. R.; Kamen, B. A. Distribution of the Folate Receptor GP38 in Normal and Malignant Cell Lines and Tissues. *Cancer Res.* **1992**, *52* (12), 3396–3401.

(42) Shi, X.; Wang, S. H.; Swanson, S. D.; Ge, S.; Cao, Z.; Van Antwerp, M. E.; Landmark, K. J.; Baker, J. R. Dendrimer-Functionalized Shell-Crosslinked Iron Oxide Nanoparticles for In-Vivo Magnetic Resonance Imaging of Tumors. *Adv. Mater.* **2008**, *20* (9), 1671–1678. https://doi.org/10.1002/adma.200702770.

(43) Chang, Y.; Liu, N.; Chen, L.; Meng, X.; Liu, Y.; Li, Y.; Wang, J. Synthesis and Characterization of DOX-Conjugated Dendrimer-Modified Magnetic Iron Oxide Conjugates for Magnetic Resonance Imaging, Targeting, and Drug Delivery. *J. Mater. Chem.* **2012**, *22* (19), 9594. https://doi.org/10.1039/c2jm16792a.

(44) Chang, Y.; Meng, X.; Zhao, Y.; Li, K.; Zhao, B.; Zhu, M.; Li, Y.; Chen, X.; Wang, J. Novel Water-Soluble and PH-Responsive Anticancer Drug Nanocarriers: Doxorubicin–PAMAM Dendrimer Conjugates Attached to Superparamagnetic Iron Oxide Nanoparticles (IONPs). *J. Colloid Interface Sci.* **2011**, *363* (1), 403–409. https://doi.org/10.1016/J.JCIS.2011.06.086.

(45) Kesharwani, P.; Banerjee, S.; Padhye, S.; Sarkar, F. H.; Iyer, A. K. Parenterally

Administrable Nano-Micelles of 3,4-Difluorobenzylidene Curcumin for Treating Pancreatic Cancer. *Colloids Surfaces B Biointerfaces* **2015**, *132*, 138–145. https://doi.org/10.1016/J.COLSURFB.2015.05.007.

(46) Padhye, S.; Banerjee, S.; Chavan, D.; Pandye, S.; Swamy, K. V.; Ali, S.; Li, J.; Dou, Q. P.; Sarkar, F. H. Fluorocurcumins as Cyclooxygenase-2 Inhibitor: Molecular Docking, Pharmacokinetics and Tissue Distribution in Mice. *Pharm. Res.* **2009**, *26* (11), 2438–2445. https://doi.org/10.1007/s11095-009-9955-6.

(47) Luong, D.; Kesharwani, P.; Killinger, B. A.; Moszczynska, A.; Sarkar, F. H.; Padhye, S.; Rishi, A. K.; Iyer, A. K. Solubility Enhancement and Targeted Delivery of a Potent Anticancer Flavonoid Analogue to Cancer Cells Using Ligand Decorated Dendrimer Nano-Architectures. *J. Colloid Interface Sci.* **2016**, *484*, 33–43. https://doi.org/10.1016/J.JCIS.2016.08.061.

(48) Luong, D.; Sau, S.; Kesharwani, P.; Iyer, A. K. Polyvalent Folate-Dendrimer-Coated Iron Oxide Theranostic Nanoparticles for Simultaneous Magnetic Resonance Imaging and Precise Cancer Cell Targeting. *Biomacromolecules* **2017**, *18* (4), 1197–1209. https://doi.org/10.1021/acs.biomac.6b01885.

(49) Kerbel, R. S.; Kamen, B. A. The Anti-Angiogenic Basis of Metronomic Chemotherapy. *Nat. Rev. Cancer* **2004**, *4* (6), 423–436. https://doi.org/10.1038/nrc1369.

(50) Lin, X.; Deng, L.; Xu, Y.; Dong, A. Thermosensitive in Situ Hydrogel of Paclitaxel Conjugated Poly(ε-Caprolactone)-Poly(Ethylene Glycol)-Poly(ε-Caprolactone). *Soft Matter* **2012**, *8* (12), 3470. https://doi.org/10.1039/c2sm07172j.

(51) Chang, Y.; Li, Y.; Meng, X.; Liu, N.; Sun, D.; Liu, H.; Wang, J. Dendrimer Functionalized Water Soluble Magnetic Iron Oxide Conjugates as Dual Imaging Probe for Tumor Targeting and Drug Delivery. *Polym. Chem.* **2013**, *4* (3), 789–794. https://doi.org/10.1039/C2PY20740K.

(52) Dayyani, N.; Khoee, S.; Ramazani, A. Design and Synthesis of PH-Sensitive Polyamino-Ester Magneto-Dendrimers: Surface Functional Groups Effect on Viability of Human Prostate Carcinoma Cell Lines DU145. *Eur. J. Med. Chem.* **2015**, *98*, 190–202. https://doi.org/10.1016/j.ejmech.2015.05.028.

(53) He, X.; Wu, X.; Cai, X.; Lin, S.; Xie, M.; Zhu, X.; Yan, D. Functionalization of Magnetic Nanoparticles with Dendritic–Linear–Brush-Like Triblock Copolymers and Their Drug Release Properties. *Langmuir* **2012**, *28* (32), 11929–11938. https://doi.org/10.1021/la302546m.

(54) Wu, X.; He, X.; Zhong, L.; Lin, S.; Wang, D.; Zhu, X.; Yan, D. Water-Soluble Dendritic-Linear Triblock Copolymer-Modified Magnetic Nanoparticles: Preparation, Characterization and Drug Release Properties. *J. Mater. Chem.* **2011**, *21* (35), 13611. https://doi.org/10.1039/c1jm11613d.

(55) Park, J.; Yu, M. K.; Jeong, Y. Y.; Kim, J. W.; Lee, K.; Phan, V. N.; Jon, S. Antibiofouling Amphiphilic Polymer-Coated Superparamagnetic Iron Oxide Nanoparticles: Synthesis, Characterization, and Use in Cancer Imaging in Vivo. *J. Mater. Chem.* **2009**, *19* (35), 6412. https://doi.org/10.1039/b902445j.

(56) Lattuada, M.; Hatton, T. A. Functionalization of Monodisperse Magnetic Nanoparticles. *Langmuir* **2007**, *23* (4), 2158–2168. https://doi.org/10.1021/LA062092X.

(57) Chandra, S.; Dietrich, S.; Lang, H.; Bahadur, D. Dendrimer–Doxorubicin Conjugate for Enhanced Therapeutic Effects for Cancer. *J. Mater. Chem.* **2011**, *21* (15), 5729. https://doi.org/10.1039/c0jm04198j.

(58) Wei, H.; Cheng, S.-X.; Zhang, X.-Z.; Zhuo, R.-X. Thermo-Sensitive Polymeric Micelles Based on Poly(N-Isopropylacrylamide) as Drug Carriers. *Prog. Polym. Sci.* **2009**, *34* (9), 893–910. https://doi.org/10.1016/J.PROGPOLYMSCI.2009.05.002.

(59) Khoee, S.; Hemati, K. Synthesis of Magnetite/Polyamino-Ester Dendrimer Based on PCL/PEG Amphiphilic Copolymers via Convergent Approach for Targeted Diagnosis and Therapy. *Polym. (United Kingdom)* **2013**, *54* (21), 5574–5585. https://doi.org/10.1016/j.polymer.2013.07.074.

(60) Nigam, S.; Bahadur, D. Dendrimer-Conjugated Iron Oxide Nanoparticles as Stimuli-Responsive Drug Carriers for Thermally-Activated Chemotherapy of Cancer. *Colloids Surfaces B Biointerfaces* **2017**, *155*, 182–192. https://doi.org/10.1016/J.COLSURFB.2017.04.025.

(61) Liu, G.; Swierczewska, M.; Lee, S.; Chen, X. Functional Nanoparticles for Molecular Imaging Guided Gene Delivery. *Nano Today* **2010**, *5* (6), 524–539. https://doi.org/10.1016/J.NANTOD.2010.10.005.

(62) Mintzer, M. A.; Simanek, E. E. Nonviral Vectors for Gene Delivery. *Chem. Rev.* **2009**, *109* (2), 259–302. https://doi.org/10.1021/cr800409e.

(63) Wang, K.; Wang, K.; Shen, B.; Huang, T.; Sun, X.; Li, W.; Jin, G.; Li, L.; Bu, L.; Li, R.; et al. MR Reporter Gene Imaging of Endostatin Expression and Therapy. *Mol. Imaging Biol.* **2010**, *12* (5), 520–529. https://doi.org/10.1007/s11307-009-0286-0.

(64) Xiao, S.; Castro, R.; Rodrigues, J.; Shi, X.; Tomás, H. PAMAM Dendrimer/PDNA Functionalized-Magnetic Iron Oxide Nanoparticles for Gene Delivery. *J. Biomed. Nanotechnol.* **2015**, *11* (8), 1370–1384. https://doi.org/10.1166/jbn.2015.2101.

(65) Ch'ng, J. L.; Mulligan, R. C.; Schimmel, P.; Holmes, E. W. Antisense RNA Complementary to 3' Coding and Noncoding Sequences of Creatine Kinase Is a Potent Inhibitor of Translation in Vivo. *Proc. Natl. Acad. Sci. U. S. A.* **1989**, *86* (24), 10006–10010. https://doi.org/10.1073/PNAS.86.24.10006.

(66) Denhardt, D. T. Mechanism of Action of Antisense RNA. Sometime Inhibition of

Transcription, Processing, Transport, or Translationa. *Ann. N. Y. Acad. Sci.* **1992**, *660* (1), 70–76. https://doi.org/10.1111/j.1749-6632.1992.tb21059.x.

(67) Kim, S. H.; Mok, H.; Jeong, J. H.; Kim, S. W.; Park, T. G. Comparative Evaluation of Target-Specific GFP Gene Silencing Efficiencies for Antisense ODN, Synthetic SiRNA, and SiRNA Plasmid Complexed with PEI−PEG−FOL Conjugate. *Bioconjug. Chem.* **2006**, *17* (1), 241–244. https://doi.org/10.1021/BC050289F.

(68) Pan, B.; Cui, D.; Sheng, Y.; Ozkan, C.; Gao, F.; He, R.; Li, Q.; Xu, P.; Huang, T. Dendrimer-Modified Magnetic Nanoparticles Enhance Efficiency of Gene Delivery System. *Cancer Res.* **2007**, *67* (17), 8156–8163. https://doi.org/10.1158/0008-5472.CAN-06-4762.

(69) Zhang, Z.; Cao, X.; Zhao, X.; Withers, S. B.; Holt, C. M.; Lewis, A. L.; Lu, J. R. Controlled Delivery of Antisense Oligodeoxynucleotide from Cationically Modified Phosphorylcholine Polymer Films. *Biomacromolecules* **2006**, *7* (3), 784–791. https://doi.org/10.1021/BM050840B.

(70) Dykxhoorn, D. M.; Lieberman, J. The Silent Revolution: RNA Interference as Basic Biology, Research Tool, and Therapeutic. *Annu. Rev. Med.* **2005**, *56* (1), 401–423. https://doi.org/10.1146/annurev.med.56.082103.104606.

(71) Uprichard, S. L. The Therapeutic Potential of RNA Interference. *FEBS Lett.* **2005**, *579* (26), 5996–6007. https://doi.org/10.1016/j.febslet.2005.08.004.

(72) Gary, D. J.; Puri, N.; Won, Y.-Y. Polymer-Based SiRNA Delivery: Perspectives on the Fundamental and Phenomenological Distinctions from Polymer-Based DNA Delivery. *J. Control. Release* **2007**, *121* (1–2), 64–73. https://doi.org/10.1016/J.JCONREL.2007.05.021.

(73) Ikeda, Y.; Taira, K. Ligand-Targeted Delivery of Therapeutic SiRNA. *Pharm. Res.* **2006**, *23* (8), 1631–1640. https://doi.org/10.1007/s11095-006-9001-x.

(74) Taratula, O.; Garbuzenko, O.; Savla, R.; Andrew Wang, Y.; He, H.; Minko, T. Multifunctional Nanomedicine Platform for Cancer Specific Delivery of SiRNA by Superparamagnetic Iron Oxide Nanoparticles-Dendrimer Complexes. *Curr. Drug Deliv.* **2011**, *8* (1), 59–69.

(75) Dharap, S. S.; Minko, T. Targeted Proapoptotic LHRH-BH3 Peptide. *Pharm. Res.* **2003**, *20* (6), 889–896. https://doi.org/10.1023/A:1023839319950.

(76) Dharap, S. S.; Wang, Y.; Chandna, P.; Khandare, J. J.; Qiu, B.; Gunaseelan, S.; Sinko, P. J.; Stein, S.; Farmanfarmaian, A.; Minko, T. Tumor-Specific Targeting of an Anticancer Drug Delivery System by LHRH Peptide. *Proc. Natl. Acad. Sci. U. S. A.* **2005**, *102* (36), 12962–12967. https://doi.org/10.1073/pnas.0504274102.

(77) Unsoy, G.; Yalcin, S.; Khodadust, R.; Parsian, M.; Mutlu, P.; Bayanbold, K.-N.; Gunduz,

U. PAMAM Dedrimer Coated MNPs for SiRNA Delivery and Gene Silencing. *J. Cancer Stud. Ther.* **2014**, *1* (1), 1–5.

(78) Agrawal, A.; Min, D. H.; Singh, N.; Zhu, H.; Birjiniuk, A.; Von Maltzahn, G.; Harris, T. J.; Xing, D.; Woolfenden, S. D.; Sharp, P. A.; et al. Functional Delivery of SiRNA in Mice Using Dendriworms. *ACS Nano* **2009**, *3* (9), 2495–2504. https://doi.org/10.1021/nn900201e.

(79) Kesharwani, P.; Banerjee, S.; Gupta, U.; Mohd Amin, M. C. I.; Padhye, S.; Sarkar, F. H.; Iyer, A. K. PAMAM Dendrimers as Promising Nanocarriers for RNAi Therapeutics. *Mater. Today* **2015**, *18* (10), 565–572. https://doi.org/10.1016/J.MATTOD.2015.06.003.

(80) Li, J.; Liang, H.; Liu, J.; Wang, Z. Poly (Amidoamine) (PAMAM) Dendrimer Mediated Delivery of Drug and PDNA/SiRNA for Cancer Therapy. *Int. J. Pharm.* **2018**, *546* (1–2), 215–225. https://doi.org/10.1016/J.IJPHARM.2018.05.045.

(81) Dobson, J. Gene Therapy Progress and Prospects: Magnetic Nanoparticle-Based Gene Delivery. *Gene Ther.* **2006**, *13* (4), 283–287. https://doi.org/10.1038/sj.gt.3302720.

(82) Tschulik, K.; Compton, R. G. Nanoparticle Impacts Reveal Magnetic Field Induced Agglomeration and Reduced Dissolution Rates. *Phys. Chem. Chem. Phys.* **2014**, *16* (27), 13909–13913. https://doi.org/10.1039/C4CP01618A.

(83) Xie, J.; Chen, K.; Lee, H.; Xu, C.; Hsu, A. R.; Peng, S.; Chen, X.; Sun, S. Ultra-Small c(RGDyK)-Coated Fe3O4 Nanoparticles and Their Specific Targeting to Integrin α. *J. Am. Chem. Soc.* **2008**, *130*, 7542–7543.

(84) Yang, J.; Luo, Y.; Xu, Y.; Li, J.; Zhang, Z.; Wang, H.; Shen, M.; Shi, X.; Zhang, G. Conjugation of Iron Oxide Nanoparticles with RGD-Modified Dendrimers for Targeted Tumor MR Imaging. *ACS Appl. Mater. Interfaces* **2015**, *7* (9), 5420–5428. https://doi.org/10.1021/am508983n.

(85) Bumb, A.; Brechbiel, M. W.; Choyke, P. L.; Fugger, L.; Eggeman, A.; Prabhakaran, D.; Hutchinson, J.; Dobson, P. J. Synthesis and Characterization of Ultra-Small Superparamagnetic Iron Oxide Nanoparticles Thinly Coated with Silica. *Nanotechnology* **2008**, *19* (33). https://doi.org/10.1088/0957-4484/19/33/335601.

(86) Weibo Cai, †; Dong-Woon Shin, ‡; Kai Chen, †; Olivier Gheysens, †; Qizhen Cao, †; Shan X. Wang, ‡; Sanjiv S. Gambhir, †, A.; Xiaoyuan Chen*, †. Peptide-Labeled Near-Infrared Quantum Dots for Imaging Tumor Vasculature in Living Subjects. *Nano Lett.* **2006**, *6* (4), 669–676. https://doi.org/10.1021/NL052405T.

(87) Li, Z.-B.; Cai, W.; Cao, Q.; Chen, K.; Wu, Z.; He, L.; Chen, X. 64 Cu-Labeled Tetrameric and Octameric RGD Peptides for Small-Animal PET of Tumor a v b 3 Integrin Expression. *J Nucl Med* **2007**, *48*, 1162–1171. https://doi.org/10.2967/jnumed.107.039859.

(88) Zhu, J.; Xiong, Z.; Shen, M.; Shi, X. Encapsulation of Doxorubicin within Multifunctional Gadolinium-Loaded Dendrimer Nanocomplexes for Targeted Theranostics of Cancer Cells. *RSC Adv.* **2015**, *5* (38), 30286–30296. https://doi.org/10.1039/C5RA01215E.

(89) Percec, V.; Wilson, D. A.; Leowanawat, P.; Wilson, C. J.; Hughes, A. D.; Kaucher, M. S.; Hammer, D. A.; Levine, D. H.; Kim, A. J.; Bates, F. S.; et al. Self-Assembly of Janus Dendrimers into Uniform Dendrimersomes and Other Complex Architectures. *Science* **2010**, *328* (5981), 1009–1014. https://doi.org/10.1126/science.1185547.

(90) Filippi, M.; Catanzaro, V.; Patrucco, D.; Botta, M.; Tei, L.; Terreno, E. First in Vivo MRI Study on Theranostic Dendrimersomes. *J. Control. Release* **2017**, *248*, 45–52. https://doi.org/10.1016/j.jconrel.2017.01.010.

(91) Kamaly, N.; Miller, A. D. Paramagnetic Liposome Nanoparticles for Cellular and Tumour Imaging. *Int. J. Mol. Sci.* **2010**, *11* (4), 1759–1776. https://doi.org/10.3390/ijms11041759.

(92) Wang, Q.; Li, J.; An, S.; Chen, Y.; Jiang, C.; Wang, X. Magnetic Resonance-Guided Regional Gene Delivery Strategy Using a Tumor Stroma-Permeable Nanocarrier for Pancreatic Cancer. *Int. J. Nanomedicine* **2015**, *10*, 4479–4490. https://doi.org/10.2147/IJN.S84930.

(93) Tilcock, C.; Unger, E.; Cullis, P.; MacDougall, P. Liposomal Gd-DTPA: Preparation and Characterization of Relaxivity. *Radiology* **1989**, *171* (1), 77–80. https://doi.org/10.1148/radiology.171.1.2928549.

(94) Cheng, Z.; Thorek, D. L. J.; Tsourkas, A. Gadolinium-Conjugated Dendrimer Nanoclusters as a Tumor-Targeted T1 Magnetic Resonance Imaging Contrast Agent. *Angew. Chemie Int. Ed.* **2010**, *49* (2), 346–350. https://doi.org/10.1002/anie.200905133.

(95) Cheng, Z.; Thorek, D. L. J.; Tsourkas, A. Porous Polymersomes with Encapsulated Gd-Labeled Dendrimers as Highly Efficient MRI Contrast Agents. *Adv. Funct. Mater.* **2009**, *19* (23), 3753–3759. https://doi.org/10.1002/adfm.200901253.

(96) Chen, K.-J.; Wolahan, S. M.; Wang, H.; Hsu, C.-H.; Chang, H.-W.; Durazo, A.; Hwang, L.-P.; Garcia, M. A.; Jiang, Z. K.; Wu, L.; et al. A Small MRI Contrast Agent Library of Gadolinium(III)-Encapsulated Supramolecular Nanoparticles for Improved Relaxivity and Sensitivity. *Biomaterials* **2011**, *32* (8), 2160–2165. https://doi.org/10.1016/J.BIOMATERIALS.2010.11.043.

(97) Wiener, C.; Fauci, A. S.; Braunwald, E.; Kasper, D. L.; Hauser, S. L.; Longo, D. L.; Jameson, J. L.; Loscalzo, J. *Harrison's Principles of Internal Medicine, Self-Assessment and Board Review*, 18th ed.; McGraw Hill professional; McGraw-Hill Education: New york, 2008.

(98) Wang, H.; Chen, K.-J.; Wang, S.; Ohashi, M.; Kamei, K.; Sun, J.; Ha, J. H.; Liu, K.; Tseng, H.-R. A Small Library of DNA-Encapsulated Supramolecular Nanoparticles for

Targeted Gene Delivery. *Chem. Commun.* **2010**, *46* (11), 1851. https://doi.org/10.1039/b923711a.

(99) Wang, H.; Liu, K.; Chen, K.-J.; Lu, Y.; Wang, S.; Lin, W.-Y.; Guo, F.; Kamei, K.; Chen, Y.-C.; Ohashi, M.; et al. A Rapid Pathway Toward a Superb Gene Delivery System: Programming Structural and Functional Diversity into a Supramolecular Nanoparticle Library. *ACS Nano* **2010**, *4* (10), 6235–6243. https://doi.org/10.1021/nn101908e.

(100) Wang, S.; Chen, K.-J.; Wu, T.-H.; Wang, H.; Lin, W.-Y.; Ohashi, M.; Chiou, P.-Y.; Tseng, H.-R. Photothermal Effects of Supramolecularly Assembled Gold Nanoparticles for the Targeted Treatment of Cancer Cells. *Angew. Chemie Int. Ed.* **2010**, *49* (22), 3777–3781. https://doi.org/10.1002/anie.201000062.

(101) Lee, J.-H.; Chen, K.-J.; Noh, S.-H.; Garcia, M. A.; Wang, H.; Lin, W.-Y.; Jeong, H.; Kong, B. J.; Stout, D. B.; Cheon, J.; et al. On-Demand Drug Release System for In Vivo Cancer Treatment through Self-Assembled Magnetic Nanoparticles. *Angew. Chemie* **2013**, *125* (16), 4480–4484. https://doi.org/10.1002/ange.201207721.

(102) Tan, M.; Ye, Z.; Lindner, D.; Brady-Kalnay, S. M.; Lu, Z.-R. Synthesis and Evaluation of a Targeted Nanoglobular Dual-Modal Imaging Agent for MR Imaging and Image-Guided Surgery of Prostate Cancer. *Pharm. Res.* **2014**, *31* (6), 1469–1476. https://doi.org/10.1007/s11095-013-1008-5.

(103) Pilch, J.; Brown, D. M.; Komatsu, M.; Järvinen, T. A. H.; Yang, M.; Peters, D.; Hoffman, R. M.; Ruoslahti, E. Peptides Selected for Binding to Clotted Plasma Accumulate in Tumor Stroma and Wounds. *Proc. Natl. Acad. Sci. U. S. A.* **2006**, *103* (8), 2800–2804. https://doi.org/10.1073/pnas.0511219103.

(104) Tan, M.; Burden-Gulley, S. M.; Li, W.; Wu, X.; Lindner, D.; Brady-Kalnay, S. M.; Gulani, V.; Lu, Z.-R. MR Molecular Imaging of Prostate Cancer with a Peptide-Targeted Contrast Agent in a Mouse Orthotopic Prostate Cancer Model. *Pharm. Res.* **2012**, *29* (4), 953–960. https://doi.org/10.1007/s11095-011-0635-y.

(105) Sonmez, H.; Suer, S.; Karaarslan, I.; Baloglu, H.; Kokoglu, E. Tissue Fibronectin Levels of Human Prostatic Cancer, as a Tumor Marker. *Cancer Biochem Biophys* **1995**, *15* (2), 107–110.

(106) Tan, M.; Ye, Z.; Jeong, E. K.; Wu, X.; Parker, D. L.; Lu, Z. R. Synthesis and Evaluation of Nanoglobular Macrocyclic Mn(II) Chelate Conjugates as Non-Gadolinium(III) MRI Contrast Agents. *Bioconjug. Chem.* **2011**, *22* (5), 931–937. https://doi.org/10.1021/bc100573t.

(107) Su, H.; Wu, C.; Zhu, J.; Miao, T.; Wang, D.; Xia, C.; Zhao, X.; Gong, Q.; Song, B.; Ai, H. Rigid Mn(II) Chelate as Efficient MRI Contrast Agent for Vascular Imaging. *Dalt. Trans.* **2012**, *41* (48), 14480–14483. https://doi.org/10.1039/c2dt31696j.

(108) De Sá, A.; Bonnet, C. S.; Geraldes, C. F. G. C.; Tóth, É.; Ferreira, P. M. T.; André, J. P. Thermodynamic Stability and Relaxation Studies of Small, Triaza-Macrocyclic Mn(Ii) Chelates. *Dalt. Trans.* **2013**, *42* (13), 4522–4532. https://doi.org/10.1039/c2dt32496b.

(109) Bhyrappa, P.; Young, J. K.; Moore, J. S.; Suslick, K. S. Dendrimer-Metalloporphyrins: Synthesis and Catalysis. *J. Am. Chem. Soc.* **1996**, *118* (24), 5708–5711. https://doi.org/10.1021/ja953474k.

(110) Ding, L.; Lyu, Z.; Dhumal, D.; Kao, C.-L.; Bernard, M.; Peng, L. Dendrimer-Based Magnetic Resonance Imaging for Brain Cancer. *Sci. CHINA Mater.* **2018**. https://doi.org/10.1007/s11426-017-9082-5.

(111) Pan, D.; Schmieder, A.; Wickline, S.; Lanza, G. Manganese-Based MRI Contrast Agents: Past, Present and Future. *Tetrahedron* **2011**, *67* (44), 8431–8444. https://doi.org/10.1016/j.tet.2011.07.076.Manganese-based.

(112) Bertin, A.; Gallani, J. Development of a Dendritic Manganese-Enhanced Magnetic Resonance Imaging (MEMRI) Contrast Agent : Synthesis , Toxicity (in Vitro) and Relaxivity (in Vitro , in Vivo) Studies. *Bioconjugate Chem.* **2009**, *20* (4), 760–767.

(113) Zhu, J.; Gale, E. M.; Atanasova, I.; Rietz, T. A.; Caravan, P. Hexameric Mn ^{II} Dendrimer as MRI Contrast Agent. *Chem. - A Eur. J.* **2014**, *20* (44), 14507–14513. https://doi.org/10.1002/chem.201403883.

(114) Keshavarz, A.; Hajbabaei, S.; Sojoodi, J.; Mostafa, S.; Afshar, M. Mn2+ Negatively Charged Pegylated Dendrimer G2-Tryptophan: Novel Nano Magnetic Resonance Imaging Agent. *Adv. Appl. Physiol.* **2017**, *2* (1), 1–9. https://doi.org/10.11648/j.aap.20170201.11.

(115) Tan, M.; Wu, X.; Jeong, E.-K.; Chen, Q.; Parker, D.; Lu, Z.-R. An Effective Targeted Nanoglobular Manganese(II) Chelate Conjugate for Magnetic Resonance Molecular Imaging of Tumor Extracellular Matrix. *Mol. Pharmacol.* **2010**, *7* (4), 936–943. https://doi.org/10.1016/j.biopsych.2011.12.024.Depressive.

(116) Menjoge, A. R.; Kannan, R. M.; Tomalia, D. A. Dendrimer-Based Drug and Imaging Conjugates: Design Considerations for Nanomedical Applications. *Drug Discov. Today* **2010**, *15* (5–6), 171–185. https://doi.org/10.1016/j.drudis.2010.01.009.

(117) Jennings, L.; Long, N. Two Is Better than One'—probes for Dual-Modality Molecular Imaging. *Chem. Commun.* **2009**, *24*, 3511–3524. https://doi.org/10.1039/C5EW00289C.

(118) Yang, H.; Qin, C.; Yu, C.; Lu, Y.; Zhang, H.; Xue, F.; Wu, D.; Zhou, Z.; Yang, S. RGD-Conjugated Nanoscale Coordination Polymers for Targeted T_1 - and T_2 -Weighted Magnetic Resonance Imaging of Tumors in Vivo. *Adv. Funct. Mater.* **2014**, *24* (12), 1738–1747. https://doi.org/10.1002/adfm.201302433.

(119) Haribabu, V.; Farook, A. S.; Goswami, N.; Murugesan, R.; Girigoswami, A. Optimized Mn-Doped Iron Oxide Nanoparticles Entrapped in Dendrimer for Dual Contrasting Role

in MRI. *J. Biomed. Mater. Res. - Part B Appl. Biomater.* **2016**, *104* (4), 817–824. https://doi.org/10.1002/jbm.b.33550.

(120) Pradhan, P.; Giri, J.; Banerjee, R.; Bellare, J.; Bahadur, D. Preparation and Characterization of Manganese Ferrite-Based Magnetic Liposomes for Hyperthermia Treatment of Cancer. *J. Magn. Magn. Mater.* **2007**, *311* (1), 208–215. https://doi.org/10.1016/J.JMMM.2006.10.1179.

(121) Tang, Z. .; Sorensen, C. .; Klabunde, K. .; Hadjipanayis, G. . Preparation of Manganese Ferrite Fine Particles from Aqueous Solution. *J. Colloid Interface Sci.* **1991**, *146* (1), 38–52. https://doi.org/10.1016/0021-9797(91)90004-R.

(122) Wen, S.; Li, K.; Cai, H.; Chen, Q.; Shen, M.; Huang, Y.; Peng, C.; Hou, W.; Zhu, M.; Zhang, G.; et al. Multifunctional Dendrimer-Entrapped Gold Nanoparticles for Dual Mode CT/MR Imaging Applications. *Biomaterials* **2013**, *34* (5), 1570–1580. https://doi.org/10.1016/j.biomaterials.2012.11.010.

(123) Chen, Q.; Li, K.; Wen, S.; Liu, H.; Peng, C.; Cai, H.; Shen, M.; Zhang, G.; Shi, X. Targeted CT/MR Dual Mode Imaging of Tumors Using Multifunctional Dendrimer-Entrapped Gold Nanoparticles. *Biomaterials* **2013**, *34* (21), 5200–5209. https://doi.org/10.1016/j.biomaterials.2013.03.009.

(124) Li, K.; Wen, S.; Larson, A. C.; Shen, M.; Zhang, Z.; Chen, Q.; Shi, X.; Zhang, G. Multifunctional Dendrimer-Based Nanoparticles for in Vivo MR/CT Dual-Modal Molecular Imaging of Breast Cancer. *Int. J. Nanomedicine* **2013**, *8*, 2589–2600. https://doi.org/10.2147/IJN.S46177.

(125) Chen, Q.; Wang, H.; Liu, H.; Wen, S.; Peng, C.; Shen, M.; Zhang, G.; Shi, X. Multifunctional Dendrimer-Entrapped Gold Nanoparticles Modified with RGD Peptide for Targeted Computed Tomography/Magnetic Resonance Dual-Modal Imaging of Tumors. *Anal. Chem.* **2015**, *87* (7), 3949–3956. https://doi.org/10.1021/acs.analchem.5b00135.

(126) Cai, H.; Li, K.; Li, J.; Wen, S.; Chen, Q.; Shen, M.; Zheng, L.; Zhang, G.; Shi, X. Dendrimer-Assisted Formation of Fe<inf>3</Inf>O<inf>4</Inf>/Au Nanocomposite Particles for Targeted Dual Mode CT/MR Imaging of Tumors. *Small* **2015**, *11* (35), 4584–4593. https://doi.org/10.1002/smll.201500856.

(127) Luo, Y.; Zhao, L.; Li, X.; Yang, J.; Guo, L.; Zhang, G.; Shen, M.; Zhao, J.; Shi, X. The Design of a Multifunctional Dendrimer-Based Nanoplatform for Targeted Dual Mode SPECT/MR Imaging of Tumors. *J. Mater. Chem. B* **2016**, *4* (45), 7220–7225. https://doi.org/10.1039/c6tb02190e.

(128) Landmark, K. J.; Dimaggio, S.; Ward, J.; Kelly, Ḱ. C.; Vogt, S.; Hong, S.; Kotlyar, A.; Myc, A.; Thomas, T. P.; Penner-hahn, J. E.; et al. Synthesis, Characterization, and in Vitro Testing of Superparamagnetic Iron Oxide Nanoparticles Targeted Using Folic Acid-

Conjugated Dendrimers. *ACS Nano* **2008**, *2* (4), 773–783. https://doi.org/10.1021/nn800034w.

(129) Talanov, V. S.; Regino, C. A. S.; Kobayashi, H.; Bernardo, M.; Choyke, P. L.; Brechbiel, M. W. Dendrimer-Based Nanoprobe for Dual Modality Magnetic Resonance and Fluorescence Imaging. *Nano Lett.* **2006**, *6* (7), 1459–1463. https://doi.org/10.1021/nl060765q.

(130) Chen, J.; Sun, Y.; Chen, Q.; Wang, L.; Wang, S.; Tang, Y.; Shi, X.; Wang, H. Multifunctional Gold Nanocomposites Designed for Targeted CT/MR/Optical Trimodal Imaging of Human Non-Small Cell Lung Cancer Cells. *Nanoscale* **2016**, *8* (28), 13568–13573. https://doi.org/10.1039/c6nr03143a.

(131) Percec, V.; Glodde, M.; Johansson, G.; Balagurusamy, V. S. K.; Heiney, P. A. Transformation of a Spherical Supramolecular Dendrimer into a Pyramidal Columnar Supramolecular Dendrimer Mediated by the Fluorophobic Effect. *Angew. Chemie* **2003**, *115* (36), 4474–4478. https://doi.org/10.1002/ange.200351804.

(132) Percec, V.; Johansson, G.; Ungar, G.; Zhou, J. Fluorophobic Effect Induces the Self-Assembly of Semifluorinated Tapered Monodendrons Containing Crown Ethers into Supramolecular Columnar Dendrimers Which Exhibit a Homeotropic Hexagonal Columnar Liquid Crystalline Phase. *J. Am. Chem. Soc.* **1996**, *118* (41), 9855–9866. https://doi.org/10.1021/JA9615738.

(133) Liu, X.; Yuan, Y.; Bo, S.; Li, Y.; Yang, Z.; Zhou, X.; Chen, S.; Jiang, Z.-X. Monitoring Fluorinated Dendrimer-Based Self-Assembled Drug-Delivery Systems with ^{19}F Magnetic Resonance. *European J. Org. Chem.* **2017**, *2017* (30), 4461–4468. https://doi.org/10.1002/ejoc.201700566.

(134) Criscione, J. M.; Le, B. L.; Stern, E.; Brennan, M.; Rahner, C.; Papademetris, X.; Fahmy, T. M. Self-Assembly of PH-Responsive Fluorinated Dendrimer-Based Particulates for Drug Delivery and Noninvasive Imaging. *Biomaterials* **2009**, *30* (23–24), 3946–3955. https://doi.org/10.1016/J.BIOMATERIALS.2009.04.014.

(135) Martin, O. M.; Yu, L.; Mecozzi, S. Solution Self-Assembly and Solid State Properties of Fluorinated Amphiphilic Calix[4]Arenes. *Chem. Commun.* **2005**, *0* (39), 4964. https://doi.org/10.1039/b506781b.

(136) Kimura, A.; Narazaki, M.; Kanazawa, Y.; Fujiwara, H. 19F Magnetic Resonance Imaging of Perfluorooctanoic Acid Encapsulated in Liposome for Biodistribution Measurement. *Magn. Reson. Imaging* **2004**, *22* (6), 855–860. https://doi.org/10.1016/j.mri.2004.01.060.

(137) Pykett, I. L.; Rosen, B. R. Nuclear Magnetic Resonance: In Vivo Proton Chemical Shift Imaging. Work in Progress. *Radiology* **1983**, *149* (1), 197–201. https://doi.org/10.1148/radiology.149.1.6310682.

(138) Li, Y.; Xiao, K.; Luo, J.; Lee, J.; Pan, S.; Lam, K. S. A Novel Size-Tunable Nanocarrier System for Targeted Anticancer Drug Delivery. *J. Control. Release* **2010**, *144* (3), 314–323. https://doi.org/10.1016/j.jconrel.2010.02.027.

(139) Filippousi, M.; Papadimitriou, S. A.; Bikiaris, D. N.; Pavlidou, E.; Angelakeris, M.; Zamboulis, D.; Tian, H.; Van Tendeloo, G. Novel Core-Shell Magnetic Nanoparticles for Taxol Encapsulation in Biodegradable and Biocompatible Block Copolymers: Preparation, Characterization and Release Properties. *Int. J. Pharm.* **2013**, *448* (1), 221–230. https://doi.org/10.1016/j.ijpharm.2013.03.025.

(140) Bakewell, S. J.; Carie, A.; Costich, T. L.; Sethuraman, J.; Semple, J. E.; Sullivan, B.; Martinez, G. V.; Dominguez-Viqueira, W.; Sill, K. N. Imaging the Delivery of Drug-Loaded, Iron-Stabilized Micelles. *Nanomedicine Nanotechnology, Biol. Med.* **2017**, *13* (4), 1353–1362. https://doi.org/10.1016/j.nano.2017.01.009.

(141) Schleich, N.; Sibret, P.; Danhier, P.; Ucakar, B.; Laurent, S.; Muller, R. N.; Jérôme, C.; Gallez, B.; Préat, V.; Danhier, F. Dual Anticancer Drug/Superparamagnetic Iron Oxide-Loaded PLGA-Based Nanoparticles for Cancer Therapy and Magnetic Resonance Imaging. *Int. J. Pharm.* **2013**, *447* (1–2), 94–101. https://doi.org/10.1016/j.ijpharm.2013.02.042.

(142) Wang, J.; Gong, C.; Wang, Y.; Wu, G. Magnetic Nanoparticles with a PH-Sheddable Layer for Antitumor Drug Delivery. *Colloids Surfaces B Biointerfaces* **2014**, *118*, 218–225. https://doi.org/10.1016/j.colsurfb.2014.04.001.

(143) Yang, X.; Grailer, J. J.; Rowland, I. J.; Javadi, A.; Hurley, S. A.; Steeber, D. A.; Gong, S. Multifunctional SPIO/DOX-Loaded Wormlike Polymer Vesicles for Cancer Therapy and MR Imaging. *Biomaterials* **2010**, *31* (34), 9065–9073. https://doi.org/10.1016/j.biomaterials.2010.08.039.

(144) Patra, H. K.; Khaliq, N. U.; Romu, T.; Wiechec, E.; Borga, M.; Turner, A. P. F.; Tiwari, A. MRI-Visual Order-Disorder Micellar Nanostructures for Smart Cancer Theranostics. *Adv. Healthc. Mater.* **2014**, *3* (4), 526–535. https://doi.org/10.1002/adhm.201300225.

(145) Wang, H.; Wang, S.; Liao, Z.; Zhao, P.; Su, W.; Niu, R.; Chang, J. Folate-Targeting Magnetic Core-Shell Nanocarriers for Selective Drug Release and Imaging. *Int. J. Pharm.* **2012**, *430* (1–2), 342–349. https://doi.org/10.1016/j.ijpharm.2012.04.009.

(146) Ji, W.; Li, N.; Chen, D.; Jiao, Y.; Xu, Q.; Lu, J. A Hollow Porous Magnetic Nanocarrier for Efficient Near-Infrared Light- and PH-Controlled Drug Release. *RSC Adv.* **2014**, *4* (92), 51055–51061. https://doi.org/10.1039/C4RA07573K.

(147) Nasongkla, N.; Bey, E.; Ren, J.; Ai, H.; Khemtong, C.; Guthi, J. S.; Chin, S. F.; Sherry, A. D.; Boothman, D. A.; Gao, J. Multifunctional Polymeric Micelles as Cancer-Targeted, MRI-Ultrasensitive Drug Delivery Systems. *Nano Lett.* **2006**, *6* (11), 2427–2430. https://doi.org/10.1021/nl061412u.

(148) Gao, X.; Luo, Y.; Liao, C. Prostate Stem Cell Antigen-Targeted Nanoparticles with Dual Functional Properties : In Vivo Imaging and Cancer Chemotherapy. *Int. J. Nanomedicine* **2012**, *7*, 4037–4051.

(149) Chertok, B.; Moffat, B. A.; David, A. E.; Yu, F.; Bergemann, C.; Ross, B. D.; Yang, V. C. Iron Oxide Nanoparticles as a Drug Delivery Vehicle for MRI Monitored Magnetic Targeting of Brain Tumors. *Biomaterials* **2008**, *29* (4), 487–496. https://doi.org/10.1016/j.biomaterials.2007.08.050.

(150) Yang, H. W.; Hua, M. Y.; Liu, H. L.; Huang, C. Y.; Tsai, R. Y.; Lu, Y. J.; Chen, J. Y.; Tang, H. J.; Hsien, H. Y.; Chang, Y. S.; et al. Self-Protecting Core-Shell Magnetic Nanoparticles for Targeted, Traceable, Long Half-Life Delivery of BCNU to Gliomas. *Biomaterials* **2011**, *32* (27), 6523–6532. https://doi.org/10.1016/j.biomaterials.2011.05.047.

(151) Liao, J.; Wei, X.; Ran, B.; Peng, J.; Qu, Y.; Qian, Z. Polymer Hybrid Magnetic Nanocapsules Encapsulating IR820 and PTX for External Magnetic Field-Guided Tumor Targeting and Multifunctional Theranostics. *Nanoscale* **2017**, *9* (7), 2479–2491. https://doi.org/10.1039/C7NR00033B.

(152) Zhu, K.; Deng, Z.; Liu, G.; Hu, J.; Liu, S. Photoregulated Cross-Linking of Superparamagnetic Iron Oxide Nanoparticle (SPION) Loaded Hybrid Nanovectors with Synergistic Drug Release and Magnetic Resonance (MR) Imaging Enhancement. *Macromolecules* **2017**, *50* (3), 1113–1125. https://doi.org/10.1021/acs.macromol.6b02162.

(153) Asadi, H.; Khoee, S.; Deckers, R. Polymer-Grafted Superparamagnetic Iron Oxide Nanoparticles as a Potential Stable System for Magnetic Resonance Imaging and Doxorubicin Delivery. *RSC Adv.* **2016**, *6* (87), 83963–83972. https://doi.org/10.1039/C6RA20398A.

(154) Biswas, D.; Li, P.; Liu, D.; Oh, J. K. Enhanced Encapsulation of Superparamagnetic Fe_3O_4 in Acidic Core-Containing Micelles for Magnetic Resonance Imaging. *RSC Adv.* **2015**, *5* (130), 107938–107948. https://doi.org/10.1039/C5RA24582F.

(155) Feng, S. T.; Li, J.; Luo, Y.; Yin, T.; Cai, H.; Wang, Y.; Dong, Z.; Shuai, X.; Li, Z. P. PH-Sensitive Nanomicelles for Controlled and Efficient Drug Delivery to Human Colorectal Carcinoma LoVo Cells. *PLoS One* **2014**, *9* (6). https://doi.org/10.1371/journal.pone.0100732.

(156) Kuppusamy, P.; Li, H.; Ilangovan, G.; Cardounel, A. J.; Zweier, J. L.; Yamada, K.; Krishna, M. C.; Mitchell, J. B. Noninvasive Imaging of Tumor Redox Status and Its Modification by Tissue Glutathione Levels Noninvasive Imaging of Tumor Redox Status and Its Modification by Tissue. *Cancer Res.* **2002**, *62*, 307–312.

(157) Yu, J.; Li, X.; Luo, Y.; Lu, W.; Huang, J.; Liu, S. Poly(Ethylene Glycol) Shell-Sheddable

Magnetic Nanomicelle as the Carrier of Doxorubicin with Enhanced Cellular Uptake. *Colloids Surfaces B Biointerfaces* **2013**, *107*, 213–219. https://doi.org/10.1016/j.colsurfb.2013.02.009.

(158) Ding, M.; Zeng, X.; He, X.; Li, J.; Tan, H.; Fu, Q. Cell Internalizable and Intracellularly Degradable Cationic Polyurethane Micelles as a Potential Platform for Efficient Imaging and Drug Delivery. *Biomacromolecules* **2014**, *15* (8), 2896–2906. https://doi.org/10.1021/bm500506v.

(159) Kievit, F. M.; Gunn, J. W.; Lee, D. PEI-PEG-Chitosan Copolymer Coated Iron Oxide Nanoparticles for Safe Gene Delivery: Synthesis, Complexation, and Transfection. *Adv. Funct. Mater.* **2009**, *19* (14), 2244–2251. https://doi.org/10.1002/adfm.200801844.PEI-PEG-Chitosan.

(160) Kievit FM, Veiseh O, Fang C, Bhattarai N, Lee D, E. R. and Z. M. Chlorotoxin Labeled Magnetic Nanovectors for Targeted Gene Delivery to Glioma. *ACS Nano* **2010**, *4* (8), 4587–4594.

(161) Stephen, Z. R.; Dayringer, C. J.; Lim, J. J.; Revia, R. A.; Halbert, M. V.; Jeon, M.; Bakthavatsalam, A.; Ellenbogen, R. G.; Zhang, M. Approach to Rapid Synthesis and Functionalization of Iron Oxide Nanoparticles for High Gene Transfection. *ACS Appl. Mater. Interfaces* **2016**, *8* (10), 6320–6328. https://doi.org/10.1021/acsami.5b10883.

(162) Wang, C.; Ravi, S.; Martinez, G. V.; Chinnasamy, V.; Raulji, P.; Howell, M.; Davis, Y.; Mallela, J.; Seehra, M. S.; Mohapatra, S. Dual-Purpose Magnetic Micelles for MRI and Gene Delivery. *J. Control. Release* **2012**, *163* (1), 82–92. https://doi.org/10.1016/j.jconrel.2012.04.030.

(163) Lee, S. J.; Muthiah, M.; Lee, H. J.; Lee, H. J.; Moon, M. J.; Che, H. L.; Heo, S. U.; Lee, H. C.; Jeong, Y. Y.; Park, I. K. Synthesis and Characterization of Magnetic Nanoparticle-Embedded Multi-Functional Polymeric Micelles for MRI-Guided Gene Delivery. *Macromol. Res.* **2012**, *20* (2), 188–196. https://doi.org/10.1007/s13233-012-0023-4.

(164) Wan, Q.; Xie, L.; Gao, L.; Wang, Z.; Nan, X.; Lei, H.; Long, X.; Chen, Z.-Y.; He, C.-Y.; Liu, G.; et al. Self-Assembled Magnetic Theranostic Nanoparticles for Highly Sensitive MRI of Minicircle DNA Delivery. *Nanoscale* **2013**, *5* (2), 744–752. https://doi.org/10.1039/C2NR32438E.

(165) Lee, S. Y.; Yang, C. Y.; Peng, C. L.; Wei, M. F.; Chen, K. C.; Yao, C. J.; Shieh, M. J. A Theranostic Micelleplex Co-Delivering SN-38 and VEGF SiRNA for Colorectal Cancer Therapy. *Biomaterials* **2016**, *86*, 92–105. https://doi.org/10.1016/j.biomaterials.2016.01.068.

(166) Wang, C.; Hsu, C. H.; Li, Z.; Hwang, L. P.; Lin, Y. C.; Chou, P. T.; Lin, Y. Y. Effective Heating of Magnetic Nanoparticle Aggregates for in Vivo Nano-Theranostic Hyperthermia. *Int. J. Nanomedicine* **2017**, *12*, 6273–6287.

https://doi.org/10.2147/IJN.S141072.

(167) Xie, J.; Zhang, Y.; Yan, C.; Song, L.; Wen, S.; Zang, F.; Chen, G.; Ding, Q.; Yan, C.; Gu, N. High-Performance PEGylated Mn-Zn Ferrite Nanocrystals as a Passive-Targeted Agent for Magnetically Induced Cancer Theranostics. *Biomaterials* **2014**, *35* (33), 9126–9136. https://doi.org/10.1016/j.biomaterials.2014.07.019.

(168) Huang, X.; El-Sayed, I. H.; Qian, W.; El-Sayed, M. A. Cancer Cell Imaging and Photothermal Therapy in the Near-Infrared Region by Using Gold Nanorods. *J. Am. Chem. Soc.* **2006**, *128* (6), 2115–2120. https://doi.org/10.1021/ja057254a.

(169) Li, J.; Hu, Y.; Yang, J.; Wei, P.; Sun, W.; Shen, M.; Zhang, G.; Shi, X. Hyaluronic Acid-Modified Fe3O4at Au Core/Shell Nanostars for Multimodal Imaging and Photothermal Therapy of Tumors. *Biomaterials* **2015**, *38*, 10–21. https://doi.org/10.1016/j.biomaterials.2014.10.065.

(170) Dong, W.; Li, Y.; Niu, D.; Ma, Z.; Gu, J.; Chen, Y.; Zhao, W.; Liu, X.; Liu, C.; Shi, J. Facile Synthesis of Monodisperse Superparamagnetic Fe3O4 Core@hybrid@Au Shell Nanocomposite for Bimodal Imaging and Photothermal Therapy. *Adv. Mater.* **2011**, *23* (45), 5392–5397. https://doi.org/10.1002/adma.201103521.

(171) Chen, H.; Ren, X.; Paholak, H. J.; Burnett, J.; Ni, F.; Fang, X.; Sun, D. Facile Fabrication of Near-Infrared-Resonant and Magnetic Resonance Imaging-Capable Nanomediators for Photothermal Therapy. *ACS Appl. Mater. Interfaces* **2015**, *7* (23), 12814–12823. https://doi.org/10.1021/acsami.5b01991.

(172) Yang, J.; Lee, C. H.; Ko, H. J.; Suh, J. S.; Yoon, H. G.; Lee, K.; Huh, Y. M.; Haam, S. Multifunctional Magneto-Polymeric Nanohybrids for Targeted Detection and Synergistic Therapeutic Effects on Breast Cancer. *Angew. Chemie - Int. Ed.* **2007**, *46* (46), 8836–8839. https://doi.org/10.1002/anie.200703554.

(173) Liu, Y.; Yang, K.; Cheng, L.; Zhu, J.; Ma, X.; Xu, H.; Li, Y.; Guo, L.; Gu, H.; Liu, Z. PEGylated FePt@Fe2O3core-Shell Magnetic Nanoparticles: Potential Theranostic Applications and in Vivo Toxicity Studies. *Nanomedicine Nanotechnology, Biol. Med.* **2013**, *9* (7), 1077–1088. https://doi.org/10.1016/j.nano.2013.02.010.

(174) Tang, H.; Guo, Y.; Peng, L.; Fang, H.; Wang, Z.; Zheng, Y.; Ran, H.; Chen, Y. In Vivo Targeted, Responsive, and Synergistic Cancer Nanotheranostics by Magnetic Resonance Imaging-Guided Synergistic High-Intensity Focused Ultrasound Ablation and Chemotherapy. *ACS Appl. Mater. Interfaces* **2018**, *10* (18), 15428–15441. https://doi.org/10.1021/acsami.8b01967.

(175) Purushotham, S.; Chang, P. E. J.; Rumpel, H.; Kee, I. H. C.; Ng, R. T. H.; Chow, P. K. H.; Tan, C. K.; Ramanujan, R. V. Thermoresponsive Core-Shell Magnetic Nanoparticles for Combined Modalities of Cancer Therapy. *Nanotechnology* **2009**, *20* (30). https://doi.org/10.1088/0957-4484/20/30/305101.

(176) Zhen, Z.; Xie, J. Development of Manganese-Based Nanoparticles as Contrast Probes for Magnetic Resonance Imaging. *Theranostics* **2012**, *2* (1), 45–54. https://doi.org/10.7150/thno.3448.

(177) Tong, G.; Fang, Z.; Huang, G.; Jing, Y.; Dai, S.; Jiang, Q.; Zhang, C.; Feng, S.-T.; Li, Z.-P. Gadolinium/DOTA Functionalized Poly(Ethylene Glycol)-Block-Poly(Acrylamide-Co-Acrylonitrile) Micelles with Synergistically Enhanced Cellular Uptake for Cancer Theranostics. *RSC Adv.* **2016**, *6* (56), 50534–50542. https://doi.org/10.1039/C6RA04038A.

(178) Huang, S.; Cheng, Z.; Chen, Y.; Liu, B.; Deng, X.; Ma, P.; Lin, J. Multifunctional Polyelectrolyte Multilayers Coated onto Gd_2O_3:Yb^{3+},Er^{3+} @MSNs Can Be Used as Drug Carriers and Imaging Agents. *RSC Adv.* **2015**, *5* (52), 41985–41993. https://doi.org/10.1039/C5RA01750E.

(179) Tian, S.; Liu, G.; Wang, X.; Zhang, G.; Hu, J. PH-Responsive Tumor-Targetable Theranostic Nanovectors Based on Core Crosslinked (CCL) Micelles with Fluorescence and Magnetic Resonance (MR) Dual Imaging Modalities and Drug Delivery Performance. *Polymers (Basel).* **2016**, *8* (6), 1–18. https://doi.org/10.3390/polym8060226.

(180) Ho, L. C.; Hsu, C. H.; Ou, C. M.; Wang, C. W.; Liu, T. P.; Hwang, L. P.; Lin, Y. Y.; Chang, H. T. Unibody Core-Shell Smart Polymer as a Theranostic Nanoparticle for Drug Delivery and MR Imaging. *Biomaterials* **2015**, *37*, 436–446. https://doi.org/10.1016/j.biomaterials.2014.10.006.

(181) Yao, J.; Hsu, C.-H.; Li, Z.; Kim, T.; Hwang, L.-P.; Lin, Y.-C.; Lin, Y.-Y. Magnetic Resonance Nano-Theranostics for Glioblastoma Multiforme. *Curr. Pharm. Des.* **2015**, *21* (36), 5256–5266. https://doi.org/10.2174/1381612821666150923103307.

(182) Caltagirone, C.; Falchi, A. M.; Lampis, S.; Lippolis, V.; Meli, V.; Monduzzi, M.; Prodi, L.; Schmidt, J.; Sgarzi, M.; Talmon, Y.; et al. Cancer-Cell-Targeted Theranostic Cubosomes. *Langmuir* **2014**, *30* (21), 6228–6236. https://doi.org/10.1021/la501332u.

(183) Zhang, L.; Yang, Z.; Zhu, W.; Ye, Z.; Yu, Y.; Xu, Z.; Ren, J.; Li, P. Dual-Stimuli-Responsive, Polymer-Microsphere-Encapsulated CuS Nanoparticles for Magnetic Resonance Imaging Guided Synergistic Chemo-Photothermal Therapy. *ACS Biomater. Sci. Eng.* **2017**, *3* (8), 1690–1701. https://doi.org/10.1021/acsbiomaterials.7b00204.

(184) Li, M.; Li, L.; Zhan, C.; Kohane, D. S. Core-Shell Nanostars for Multimodal Therapy and Imaging. *Theranostics* **2016**, *6* (13), 2306–2313. https://doi.org/10.7150/thno.15843.

(185) Hu, D. R.; Chen, L. J.; Qu, Y.; Peng, J. R.; Chu, B. Y.; Shi, K.; Hao, Y.; Zhong, L.; Wang, M. Y.; Qian, Z. Y. Oxygen-Generating Hybrid Polymeric Nanoparticles with Encapsulated Doxorubicin and Chlorin E6 for Trimodal Imaging-Guided Combined Chemo-Photodynamic Therapy. *Theranostics* **2018**, *8* (6), 1558–1574. https://doi.org/10.7150/thno.22989.

(186) Wang, L.; Li, D.; Hao, Y.; Niu, M.; Hu, Y.; Zhao, H.; Chang, J.; Zhang, Z.; Zhang, Y. Gold Nanorod – Based Poly (Lactic-Co-Glycolic Acid) with Manganese Dioxide Core – Shell Structured Multifunctional Nanoplatform for Cancer Theranostic Applications. *Int. J. Nanomedicine* **2017**, *12*, 3059–3075. https://doi.org/10.2147/IJN.S128844.

(187) Liu, J.; Chen, Q.; Zhu, W.; Yi, X.; Yang, Y.; Dong, Z.; Liu, Z. Nanoscale-Coordination-Polymer-Shelled Manganese Dioxide Composite Nanoparticles: A Multistage Redox/PH/H2O2-Responsive Cancer Theranostic Nanoplatform. *Adv. Funct. Mater.* **2017**, *27* (10). https://doi.org/10.1002/adfm.201605926.

(188) Chen, Q.; Wang, X.; Wang, C.; Feng, L.; Li, Y.; Liu, Z. Drug-Induced Self-Assembly of Modified Albumins as Nano-Theranostics for Tumor-Targeted Combination Therapy. *ACS Nano* **2015**, *9* (5), 5223–5233. https://doi.org/10.1021/acsnano.5b00640.

(189) Sun, X.; Zhang, M.; Du, R.; Zheng, X.; Tang, C.; Wu, Y.; He, J.; Huang, W.; Wang, Y.; Zhang, Z.; et al. A Polyethyleneimine-Driven Self-Assembled Nanoplatform for Fluorescence and MR Dual-Mode Imaging Guided Cancer Chemotherapy. *Chem. Eng. J.* **2018**, *350* (March), 69–78. https://doi.org/https://doi.org/10.1016/j.cej.2018.05.157.

(190) Deng, X.; Dai, Y.; Liu, J.; Zhou, Y.; Ma, P.; Cheng, Z.; Chen, Y.; Deng, K.; Li, X.; Hou, Z.; et al. Multifunctional Hollow CaF2: Yb3+/Er3+/Mn2+-Poly(2-Aminoethyl Methacrylate) Microspheres for Pt(IV) pro-Drug Delivery and Tri-Modal Imaging. *Biomaterials* **2015**, *50* (1), 154–163. https://doi.org/10.1016/j.biomaterials.2015.01.040.

(191) Porsch, C.; Zhang, Y.; Östlund, Å.; Damberg, P.; Ducani, C.; Malmström, E.; Nyström, A. M. In Vitro Evaluation of Non-Protein Adsorbing Breast Cancer Theranostics Based on 19F-Polymer Containing Nanoparticles. *Part. Part. Syst. Charact.* **2013**, *30* (4), 381–390. https://doi.org/10.1002/ppsc.201300018.

(192) Boissenot, T.; Fattal, E.; Bordat, A.; Houvenagel, S.; Valette, J.; Chacun, H.; Gueutin, C.; Tsapis, N. Paclitaxel-Loaded PEGylated Nanocapsules of Perfluorooctyl Bromide as Theranostic Agents. *Eur. J. Pharm. Biopharm.* **2016**, *108*, 136–144. https://doi.org/10.1016/j.ejpb.2016.08.017.

(193) Quang, H. V.; Chang, C.; Song, P.; Hauge, E.; Kjems, J. Caveolae-Mediated Mesenchymal Stem Cell Labelling by PSS-Coated PLGA PFOB Nano-Contrast Agent for MRI. *Theranostics* **2018**, *8* (10), 2657–2671. https://doi.org/10.7150/thno.23206.

(194) Wijagkanalan, W.; Kawakami, S.; Hashida, M. Designing Dendrimers for Drug Delivery and Imaging: Pharmacokinetic Considerations. *Pharm. Res.* **2011**, *28* (7), 1500–1519. https://doi.org/10.1007/s11095-010-0339-8.

(195) Pharmacokinetics, C. P.-L. D.; Boyd, B. J.; Kaminskas, L. M.; Karellas, P.; Krippner, G.; Lessene, R.; Porter, C. J. H. Articles. **2006**.

(196) Leiro, V.; Garcia, J. P.; Tomás, H.; Pêgo, A. P. The Present and the Future of Degradable

Dendrimers and Derivatives in Theranostics. *Bioconjug. Chem.* **2015**, *26* (7), 1185–1197. https://doi.org/10.1021/bc5006224.

(197) Lee, S. J.; Jeong, J. R.; Shin, S. C.; Kim, J. C.; Chang, Y. H.; Chang, Y. M.; Kim, J. D. Nanoparticles of Magnetic Ferric Oxides Encapsulated with Poly(D,L Latide-Co-Glycolide) and Their Applications to Magnetic Resonance Imaging Contrast Agent. *J. Magn. Magn. Mater.* **2004**, *272–276* (III), 2432–2433. https://doi.org/10.1016/j.jmmm.2003.12.416.

(198) Kwon, H. Y.; Lee, J. Y.; Choi, S. W.; Jang, Y.; Kim, J. H. Preparation of PLGA Nanoparticles Containing Estrogen by Emulsification-Diffusion Method. *Colloids Surfaces A Physicochem. Eng. Asp.* **2001**, *182* (1–3), 123–130. https://doi.org/10.1016/S0927-7757(00)00825-6.

(199) Lemoine, D.; Francois, C.; Kedzierewicz, F.; Preat, V.; Hoffman, M.; Maincent, P. Stability Study of Nanoparticles of Poly(e-Caprolactone), Poly(D,L-Lactide) and Poly(D,L-Lactide-Co-Glycolide). *Biomaterials* **1996**, *17* (22), 2191–2197.

(200) Danhier, F. To Exploit the Tumor Microenvironment: Since the EPR Effect Fails in the Clinic, What Is the Future of Nanomedicine? *J. Control. Release* **2016**, *244* (Pt A), 108–121. https://doi.org/10.1016/j.jconrel.2016.11.015.

Chapter 6

Conclusions and Future Directions

Cancer theranostics has great potential for cancer detection and future therapy. It is minimally invasive and an inexpensive approach for the patients with minimum side effects on the healthy tissues. However, it is still a young platform, although rapidly growing. The thesis has addressed and developed different approaches to solve the difficulties and hurdles in this area.

In order to carry out personalized treatment clinicians need simultaneous information regarding the amount of drug release and condition of tumor site. Hence, the first project in the thesis proposes a way for the quantification of the drug release and simultaneous monitoring of the tumor site. A proof of concept experiment has been presented for drug delivery with dosage control using an alternating magnetic field (AMF). The controlled mild hyperthermia and quantification of released drug have been achieved by monitoring MRI longitudinal relaxation rate (R_1). The location of the liposomal sites could be tracked by the MRI transverse relaxation rate (R_2). The active targeting with bioconjugation or magnetofection in *in vivo* models could be tried in the future experiments.

However, the MRI detection sensitivity of liposomal nanoparticles suffers from various artifacts, poor contrast and resolution. Conventional MRI techniques based on relaxation parameters fails to eliminate artifacts and noise from the real signal. Thus, my second project has established a new technique by detecting the small changes in the local magnetic susceptibility associated with the paramagnetic nanoparticle by a non-linear technique that amplifies the small magnetic differences and significantly improves the contrast. An active-feedback field, coupled

with a new pulsing sequence and nonlinear fitting of temporal MRI signal have been used to develop a background-free high-contrast detection technique using the paramagnetic nanoparticles that could be targeted to tumors. *In vivo* mouse models have shown promising results to successfully detect nanoparticles, where other conventional methods have failed. This new method could potentially be applied with other paramagnetic nanoparticles to improve the contrast.

My first two projects deal with exogenous contrast agents like, gadolinium chelates or iron oxide nanoparticles. However, a risk-free endogenous contrast agent would be much more preferred for early tumor detection, since the metallic contrast agents have dosage limitations and safety concerns. Hence, a risk-free endogenous contrast agent has been developed in my third project. MR reporter gene ferritin has been used for this purpose. A replicon, a self-amplifying RNA derived from the RNA1 of Nodamura virus has been exploited to amplify the iron-binding protein ferritin. Contrast enhancement is shown for both *in vivo* and *in vitro* experiments and possible explanations have been discussed. A thorough time-point study in *in vitro* experiment could provide mechanistic details of this process.

In summary, I have addressed a few major concerns of theranostic approaches in my thesis such as monitoring of drug delivery process, development of high-contrast background-free MRI methods and designing a nontoxic MR contrast agent for early tumor detection. **Figure 6.1** highlights my findings for different aspects of this thesis. Furthermore, I have discussed the recent status and trends of theranostic for other nanoparticles. I have summarized different possibilities and future directions for this type of work. More statistical data should be taken for *in vivo* experiments. Active targeting strategy could be adopted to target tumor cells more effectively to

minimize possible side effects on the healthy tissues. Since the first part of my thesis uses liposomes, existing targeting strategies could be adopted. The second part of my thesis is about

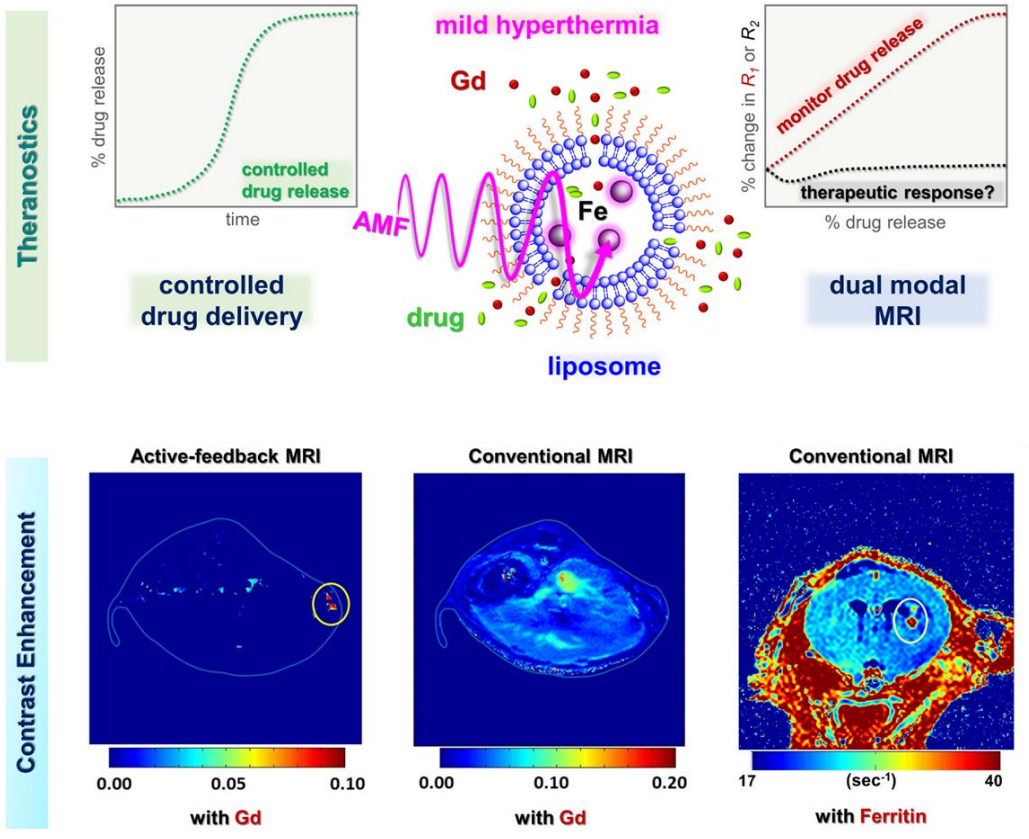

Figure 6.1. Research highlights: Summarizes the major findings in each project. Theranostic MRI approach for quantification of drug release with alternating magnetic field (AMF) and simultaneous site monitoring with liposomes are schematically shown in top diagram. Left figure in bottom indicates the successful detection of nanoparticles with background-free and high-contrast active-feedback MRI technique. Right most figure in bottom is illustrating the presence of high-contrast region for early tumor detection with amplified ferritin.

the use of a novel contrast agent Noda-ferritin. These constructs could be targeted by packaging the replicon inside a virus-like particle composed of the capsid protein of a well-studied plant virus Cowpea Chlorotic Mottle Virus, to pancreatic cancer, which is a silent killer and fourth leading cause of cancer-related death in both men and women in the US. Finally, I have used safe nanoparticles, biocompatible techniques and contrast agents for all my work to increase the

possibility of their early clinical acceptance. Some of them are already clinically approved, and others are generally considered safe for humans. Thus, early clinical trials of these new techniques and contrast agents are expected and I hope to see significant improvements in human cancer therapy by simultaneous detection, monitoring and treatment in a personalized way.